

**SPECTROSCOPIC STUDIES ON THE
INTERACTIONS OF BIOMIMETICS
WITH BIOLOGICAL MACROMOLECULES**

**THESIS
SUBMITTED FOR THE DEGREE OF
DOCTOR OF PHILOSOPHY (SCIENCE)**

**BY
RANAJAY SAHA**

**DEPARTMENT OF BIOCHEMISTRY
UNIVERSITY OF CALCUTTA**

2013

Dedicated To My Parents

Acknowledgements

One of the joys of carrying out a Ph.D. thesis is to look over the journey past and remember all the people who have helped and supported me all along this strenuous as well delightful passage.

Every successful venture is a process. In this process of accomplishment, first of all, I express my profound sense of gratitude to my supervisor and guide Dr. Samir Kumar Pal, for his constant guidance, support, motivation and untiring help during the course of my Ph.D. His in-depth knowledge on multidisciplinary field of science has been extremely beneficial for me and of immense help as well. My dissertation would not have completed within proper time if he would not have taken the pain of fixing instruments himself. I am extremely fortunate to have a supervisor who has left no stone unturned so that I could complete my Ph.D. thesis. He did never mind making sacrifices of all his leisure for our accomplishment and always available to answer our queries. The dissertation has gained substantiality due to his critical comments and constructive suggestions while pursuing each project work, His unflinching support, encouraging guidance and firm conviction has been always a source of inspiration for me and I will continue to follow his ideas in my future career.

I would remain grateful to Dr. Rajib Kumar Mitra, SNNCBS, India for many fruitful, enthusiastic and illuminating discussions during our collaborative research works. His critical remarks and suggestions have always been very helpful in improving my skills and for strengthening the manuscripts. I will always be indebted to him.

I want to sincerely acknowledge Prof. Satyajit Mayor, National Centre for Biological Sciences (TIFFR), India for fruitful collaborations. I always find his comments, questions and suggestions in the GFP manuscript very challenging and I always felt very relaxed after answering his concerns.

Dr. Achintya Singha, Bose Institute, India deserves special acknowledgement for helping me with Raman spectroscopy.

I am indebted to my many student colleagues for providing a stimulating and enriching environment. I thank Dr. Pramod Kumar Verma particularly with whom I started my research work; and many rounds of discussions on my project with him helped me a lot. I am ever indebted to Surajit for helping me with my experimental works. His suggestions have always been fruitful to my work. My special thanks go to Subrata and Nirmal who helped me out from many technical difficulties. My sincere appreciation goes to Dr. Abhinandan Mahal, Anupam, Soma, Samim, Nabarun, Susobhan, Siddhi, Dilip, Prasenjit and Soumendra da for providing a homely and cheerful environment, and also for assisting me in

research. A very special thanks to Soumik and Tanumoy with whom I shared many glorious moments over a long period of time. I will always miss their company in future.

I am obliged to the Director of S. N. Bose National Centre for Basic Sciences, Prof. Arup Kumar Raychaudhuri and all the faculty and staff members of the S. N. Bose centre whose activities at several instances have promoted my progress. I thank S. N. Bose National Centre for Basic Sciences for providing the research fellowship.

I am also grateful to all my school and college friends specially Sanjib, Bidyut, Arijit, Hardik and Amit for their constant inspiration and unconditional help whenever I needed. I am grateful to all my batchmates specially Ashutosh, Shinde and Kaloni for sharing many funny moments during this whole tenure. Besides, several people have knowingly and unknowingly helped me in the successful completion of this thesis.

Last but not the least, I would like to pay high regards to my beloved parents, for their devotions, sincere encouragement, support and inspiration throughout my research work that have made me more courageous, dedicated and patient. I owe everything to them and they are the reasons for what I am today. I feel myself very fortunate to have them as parents. My sincere gratitude goes to my elder sister Ranjita, my brother-in-law Nitai and little sweet nephew Sarthak. It is their unconditional love, well wishes and confidence on me that have made this thesis a success.

Dated:

*Department of Chemical, Biological
and Macromolecular Sciences,
S. N. Bose National Centre for Basic Sciences,
Block JD, Sec III, Salt Lake, Kolkata 700098, India.*

(Ranajay Saha)

Table of Contents

	Page
Chapter 1: Introduction	
1.1. Scope of the Spectroscopic Studies on the Interactions of Biomimetics with Biological Macromolecules	1
1.2. Objective	4
1.3. Summary of the Work Done	6
1.3.1. Structural Characterization and Crucial Ultrafast Dynamical Events in Biomimetic Self-assembly	6
1.3.1.1. Microstructure, Morphology and Ultrafast Dynamics of a Novel Edible Microemulsion	6
1.3.2. Ultrafast Spectroscopic Studies on the Molecular Interaction of Biologically Relevant Small Molecules with Biomimetic Self-assembly	6
1.3.2.1. Structural and Dynamical Characterization of Unilamellar AOT Vesicles in Aqueous Solutions and their Efficacy as Potential Drug Delivery Vehicle	6
1.3.2.2. Nanostructure, Solvation Dynamics and Nanotemplating of Plasmonically Active SERS Substrate in Reverse Vesicles	7
1.3.3. Spectroscopic Studies on the Decisive Ultrafast Dynamical Events in Biological Macromolecules	8
1.3.3.1. Light Driven Ultrafast Electron Transfer in Oxidative Redding of Green Fluorescent Proteins	8
1.3.4. Ultrafast Spectroscopic Studies on the Electron Transfer Dynamics in a Protein Under Nanoscopic Confinement of a Biomimetic Self-assembly	8

	Page
1.3.4.1. Protein-Cofactor Binding and Ultrafast Electron Transfer in Riboflavin Binding Protein under the Spatial Confinement of Nanoscopic Reverse Micelles	8
1.3.5. Spectroscopic Studies on the Molecular Recognition of a Fluorescence-modified Protein by a Model Receptor	9
1.3.5.1. Molecular Recognition of a Model Globular Protein Apomyoglobin by Synthetic Receptor Cyclodextrin: Effect of Fluorescence Modification of the Protein and Cavity Size of the Receptor in the Interaction	9
1.4. Plan of Thesis	10
References	11

Chapter 2: An Overview of Experimental Techniques and Systems

2.1. Steady-state and Dynamical Tools	18
2.1.1. Solvation Dynamics	18
2.1.1.1. Theory	18
2.1.1.2. Experimental Methods	23
2.1.2. Fluorescence Anisotropy	26
2.1.2.1. Theory	27
2.1.2.2. Experimental Methods	29
2.1.3. Estimation of Microviscosity from Stokes-Einstein-Debye Equation	31
2.1.4. Arrhenius Theory of Activation Energy	32
2.1.5. Förster Resonance Energy Transfer (FRET)	34
2.1.6. Photoinduced Electron Transfer (PET)	37
2.1.6.1. Theory	38
2.1.6.2. Experimental Methods	39
2.1.7. Surface Enhanced Raman Scattering (SERS)	39
2.1.7.1. Mechanism of SERS	40

	Page	
2.1.8.	Excited State Proton Transfer (ESPT)	41
2.1.9.	In Vitro Drug Release Study	42
2.1.10.	Phase Behaviour Study of Microemulsion (ME)	43
2.1.11.	Determination of the Distribution of Butyl Lactate between the Aqueous Phase and the Oil Phase	44
2.1.12.	Molecular Modelling Study	44
2.1.13.	Quantum Yield Calculation	44
2.2.	Systems	45
2.2.1.	Organized Assemblies (Biomimetics)	45
2.2.1.1.	Microemulsions (MEs)	45
2.2.1.2.	Vesicle	47
2.2.1.3.	Reverse Vesicle (RV)	48
2.2.1.4.	Cyclodextrin (CyD)	49
2.2.2.	Proteins	50
2.2.2.1.	Riboflavin Binding Protein (RBP)	50
2.2.2.2.	Green fluorescence Protein (GFP)	51
2.2.2.3.	mEos2 Protein	52
2.2.2.4.	Apomyoglobin Protein (Apo-Mb)	54
2.2.3.	Molecular Probes	55
2.2.3.1.	4-(dicyanomethylene)-2-methyl-6-(p-dimethylaminostyryl) -4H-pyran (DCM)	55
2.2.3.2.	p-Benzoquinone (BQ)	55
2.2.3.3.	Tryptophan [(2S)-2-Amino-3-(1H-Indol-3-yl) Propanoic acid]	55
2.2.3.4.	Rifampicin [3-[[4-Methyl-1-Piperazinyl]-Imino]-Methyl]-Rifamycin]	56
2.2.3.5.	Riboflavin (Rf)	56
2.2.3.6.	2'-(4-Hydroxyphenyl)-5-(4-Methyl-1-Piperazinyl) -2,5'-Bi-1H-Benzimidazole Trihydrochloride Hydrate,	

	Page
Hoechst 33258 (H258)	58
2.2.3.7. Dansyl Chloride [5-(Dimethylamino)naphthalene-1-sulfonyl chloride]	58
2.2.3.8. Ethidium Bromide (EB)	58
2.2.3.9. Crystal Violet (CV)	58
References	59

Chapter 3: Instrumentation and Sample Preparation

3.1. Instrumental Setup	72
3.1.1. Steady-state UV-Vis Absorption and Emission Measurement	72
3.1.2. Circular Dichroism (CD) Measurement	73
3.1.3. Time Correlated Single Photon Counting (TCSPC) Technique	75
3.1.4. Femtosecond-resolved Fluorescence Up-conversion Technique	77
3.1.5. Transmission Electron Microscope (TEM)	78
3.1.6. Dynamic Light Scattering (DLS) Measurement	79
3.1.7. Density and Sound Velocity Measurement	81
3.1.8. X-ray Diffraction (XRD) Measurement	82
3.1.9. Fourier Transform Infrared (FTIR) Measurement	83
3.1.10. Laser Raman Spectroscopy	84
3.1.11. Conductivity Measurement	86
3.1.12. Refractive Indices Measurement	87
3.1.13. Viscosity Measurement	88
3.2. Sample Preparation	89
3.2.1. Chemicals Used	89
3.2.2. Preparation of Vesicle Solution	90
3.2.3. Preparation of Microemulsion (ME)	90
3.2.4. Preparation of Reverse vesicle (RV)	91
3.2.5. Nanoparticle Synthesis in Reverse Vesicle	91
3.2.6. Preparation of Protein and Probe Solutions	91

	Page
3.2.7. Determination of Thermodynamics of Binding	92
References	93
Chapter 4: Structural Characterization and Crucial Ultrafast Dynamical Events in Biomimetic Self-assembly	
4.1. Introduction	95
4.2. Results and Discussion	97
4.2.1. Microstructure, Morphology and Ultrafast Dynamics of a Novel Edible Microemulsion	97
4.3. Conclusion	111
References	113
Chapter 5: Ultrafast Spectroscopic Studies on the Molecular Interaction of Biologically Relevant Small Molecules with Biomimetic Self-assembly	
5.1. Introduction	118
5.2. Results and Discussion	119
5.2.1. Structural and Dynamical Characterization of Unilamellar AOT Vesicles in Aqueous Solutions and their Efficacy as Potential Drug Delivery Vehicle	119
5.2.2. Nanostructure, Solvation Dynamics and Nanotemplating of Plasmonically Active SERS Substrate in Reverse Vesicles	132
5.3. Conclusion	142
References	144
Chapter 6: Spectroscopic Studies on the Decisive Ultrafast Dynamical Events in Biological Macromolecules	
6.1. Introduction	152
6.2. Results and Discussion	153
6.2.1. Light Driven Ultrafast Electron Transfer in Oxidative	

	Page
Redding of Green Fluorescent Proteins	153
6.2.1.1. An Ultrafast View of the Photoconversion Process in EGFP	153
6.2.1.2. The Anionic State of Glu222 Facilitates Excited State Proton Transfer in EGFP	159
6.2.1.3. A Central Role for the Anionic State of Glu222 in Facilitating ET-Dependent Photoconversion in EGFP	160
6.2.1.4. The Role of ET in Other PCFPs	162
6.3. Conclusion	166
References	167

**Chapter 7: Ultrafast Spectroscopic Studies on the Electron
Transfer Dynamics in a Protein Under Nanoscopic
Confinement of a Biomimetic Self-assembly**

7.1. Introduction	170
7.2. Results and Discussion	171
7.2.1. Protein-Cofactor Binding and Ultrafast Electron Transfer in Riboflavin Binding Protein under the Spatial Confinement of Nanoscopic Reverse Micelles	171
7.3. Conclusion	182
References	183

**Chapter 8: Spectroscopic Studies on the Molecular
Recognition of a Fluorescence-modified
Protein by a Model Receptor**

8.1. Introduction	188
8.2. Results and Discussion	190
8.2.1 Molecular Recognition of a Model Globular Protein Apomyoglobin by Synthetic Receptor Cyclodextrin: Effect of Fluorescence Modification of the Protein and Cavity Size	

	Page
of the Receptor in the Interaction	190
8.3. Conclusion	200
References	201
List of Publications	206

Chapter 1

Introduction

1.1. Scope of the Spectroscopic Studies on the Interactions of Biomimetics with Biological Macromolecules:

Studies in dilute solution have yielded essential information about the biophysical properties of macromolecules like proteins. However, the cellular milieu is rich in diversity of both simple and complex molecules, and also quite crowded. For example, in *E. coli*, the cytoplasm is estimated to contain 300-400 mg mL⁻¹ of proteins, nucleic acids, and various small molecules, which can take up to 40% of the total cellular volume [1, 2]. This is called the excluded volume effect, where a significant fraction of the intracellular space is inaccessible to other macromolecules, as a result, effective concentration, or thermodynamic activity, or chemical potential of macromolecules increase by several orders of magnitude, and hence the thermodynamic driving force for them to react [3]. Consequently, this altered environment has been shown to affect the equilibria and rates of many molecular processes, including diffusion [4], association and dissociation [5], protein folding [6, 7] and stability [8]. Studying the nature and magnitude of these changes should improve our understanding of how biological macromolecules function in their native environments.

A type of crowding called confinement refers to situations in which macromolecules find themselves inside small compartments [2, 9-13]. Such compartments include those created by cytoskeletal structures [14, 15] or by the central cage of the chaperonin proteins [16-18] inside which newly synthesized proteins can fold, protected from crowding enhanced, non-productive aggregation with other folding chains. When considering these factors it is reasonable to assume that proteins may experience different energy landscapes when folding *in vivo* than in bulk, and these differences may constitute a significant piece of the folding puzzle. Confining proteins or in general biomacromolecules inside artificially created hosts is an effective approach for mimicking cellular confinement [19]. Such practice facilitates controlled study of various biological phenomena attached with the protein function. Currently, considerable efforts are focused on the engineering of molecular

systems that mimic functional aspects of cells [20]. A common feature of many cell function mimics is the containment of a small, aqueous volume enabling the creation of synthetic cell-like systems [21]. Accordingly, folding in nanopores can be a useful caricature of the more complex situations that the polypeptide chain encounters under cellular conditions. Eggers and Valentine showed that the melting temperature of α -lactalbumin increases by nearly 30 °C relative to the bulk value on encapsulation in the nanopores of silica glass. Wei *et al.* [22] have developed techniques for encapsulating proteins in mesoporous host materials with tunable pore sizes, while Kumar and Chaudhari [23] have immobilized proteins in the spaces between two parallel layers of α -zirconium. Very recently, confinement-induced stability of helices in carbon nanotube has been described by the interplay of several factors that include protein sequence, solvent conditions, strength of nanotube peptide interactions, and the nanotube diameter [24]. There are also many experimental and theoretical studies examining how confinement affects the intrinsic properties of the protein [25-36]. The common observation from most of these studies is that confinement could stabilize the folded state of proteins [8, 13, 37, 38]. However, confinement induced destabilization of protein is also realized in literature. Simplified coarse-grained bead models using implicit solvent shows that β -hairpin and small protein structures are stabilized by moderate confinement and are unexpectedly destabilized in the limiting case of overconfinement [39, 40]. $A\beta_{21-30}$ shows differences in structure and dynamics of the decapeptide depending upon the hydrophilic and hydrophobic character of the confinement, at the extreme confinement conditions [33]. The idea that confinement may shift the equilibrium between two states of a molecule with different shapes was first investigated by Minton [41]. Minton [42] found that a molecule that switches between a spherical shape and a cubic shape when confined in a cage will have an equilibrium constant significantly different from that in bulk solution because the volumes accessible to the two shapes are very different.

Thus the effect of macromolecular confinement on protein structure is quite complex and diverse; and despite numerous studies cited above fundamental gaps remain in our understanding of the effects of confinement on biomolecular systems. Most importantly, the dynamic behavior of various biomimicking systems and the ultrafast dynamics of protein molecules in such biologically relevant environment is still worthy in the present literature.

In this respect, time-resolved fluorescence spectroscopy is an efficient tool to study such ultrafast processes and has been useful in providing data on protein structure and dynamics quite efficiently [43-46]. The focus of this thesis is to explore the effect of confinement on the structure, dynamics and reactivity of biomolecules using various biomimicking self-assemblies. The study of dynamic behavior of the biomimicking self-assemblies is also the part of our research focus. Surfactant based vesicles [47, 48], microemulsions (MEs) [49, 50], and various cyclic oligosaccharides [51, 52] etc. have been a convenient choice for similar studies and also have been explored here as a biomimicking confinement. In our study conventional organic chromophores have been employed to unravel picosecond-resolved solvation dynamics of water in biomimicking self-assemblies. Within the scope of the thesis, we investigate the efficacy of the biomimicking systems as a drug delivery vehicle and also as a template for metal nanoparticle (NP) synthesis. In another aspect of our study, we examine the role of ultrafast electron transfer (ET) in oxidative redding of green fluorescent proteins (GFPs) using femtosecond and picosecond-resolved fluorescence spectroscopy. We investigate how hydration and surface charge of the confinement affect the ultrafast ET dynamics of riboflavin binding protein (RBP) to the bound cofactor riboflavin (Rf, vitamin B2), an important metabolic process, in anionic sodium bis(2-ethylhexyl) sulfosuccinate (AOT) reverse micelles (RMs) and cationic hexadecyltrimethylammonium bromide (CTAB) RMs of various hydrations. Our study also addresses the consequence of attachment of a fluoroprobe at the protein surface, in the molecular recognition of a model globular protein apomyoglobin (Apo-Mb) by selectively small model receptor cyclodextrin (CyD) of various cavity sizes. The experimental tools used for studying the dynamical processes involve solvation dynamics, temporal fluorescence anisotropy, photoinduced electron transfer (PET), and Förster resonance energy transfer (FRET). The different experimental techniques employed for our study includes steady-state UV-Vis absorption and fluorescence spectroscopy, picosecond and femtosecond-resolved fluorescence spectroscopy, Fourier transform infrared spectroscopy (FTIR), Raman spectroscopy, X-ray diffraction (XRD), high-resolution transmission electron microscopy (HRTEM), dynamic light scattering (DLS) and circular dichroism (CD) spectroscopy etc.

1.2. Objective:

The dynamical coupling between biomolecules and their hydration water is long recognized as a major determinant of protein stability [53-55] and macromolecular functions such as mediating molecular recognition [43, 56, 57], ligand binding [58, 59] and accelerating enzymatic catalysis [60-62]. A thorough knowledge of the water dynamics in biomimicking systems can find immense use in modulation of the biomolecular function in cell-like environment. Surfactant based MEs are well known biomimicking systems for such studies [49, 50]. In one of our studies we have proposed a new ME system from pharmaceutically acceptable components tween 80/butyl lactate/isopropyl myristate (IPM)/water [63]. Conductivity, viscosity, ultrasonic compressibility and sound velocity measurements have been employed to investigate the gradual changes occurring in the microstructure of the MEs with increasing water content. The picosecond-resolved solvation dynamics of the probe 4-(dicyanomethylene)-2-methyl-6-(p-dimethylaminostyryl)-4H-pyran (DCM) has been successfully applied to study the solvent relaxation dynamics of water in such altered environments, with changing structural transition of the biomimicking MEs, at various water surfactant concentrations.

Vesicles have considerable structural similarity with biological membranes and serve as an excellent mimic to cellular confinement [64]. The interaction of various model drugs and biologically relevant small molecules with various biomimetic systems could prolong our understanding on the characteristics of biological macromolecules in real cellular environment. In this respect one of our study explores the structural and dynamical characteristics of AOT vesicles using various spectroscopic techniques [65]. Picosecond-resolved and polarization gated spectroscopy have been used to study the solvation dynamics and microviscosity at the surface of the vesicles. Within the scope of the present study we have also explored the drug delivery potentiality of AOT vesicles employing *in vitro* dialysis bag method. Our study on biomimetics self-assemblies has been further extended to vesicle structures forming in oil continuous media, typically known as reverse vesicle (RV). The study of RVs is of great fundamental interest since knowledge about molecular bilayers, which play an important role in living cells, can be obtained through a thoroughly new viewpoint. In this respect we study the structural and dynamical characteristics of RVs using

electron microscopic techniques, including steady-state and time-resolved fluorescence spectroscopy [66]. Our study also evaluates RVs to be a template for metal NP synthesis and investigates the scattering (surface enhanced Raman scattering, SERS) cross-section of the as prepared NP clusters in the RV template, useful for ultrasensitive detection of molecular analytes in solution.

Fluorescent proteins undergoing green to red (G/R) photoconversion have proved to be potential tools for investigating dynamic processes in living cells and for photo-localization nanoscopy [67, 68]. Despite the obvious value of photoconversion of fluorescent proteins, key photochemical reaction during light induced G/R photoconversion of fluorescent proteins remains unclear. In one of our study using femtosecond and picosecond-resolved fluorescence spectroscopy, we capture the fast dynamics of the ET process and explore the nature of the specific ground and excited states that participate in the ET process leading to the photoconversion of GFP [69].

ET is crucial to life and is ubiquitous in enzymatic catalysis [70-72], especially in enzymes with redox reactions [73]. Flavoproteins with flavin chromophores are examples of such enzymes and are involved in various catalytic processes [74, 75]. The understanding of ET reaction dynamics of flavins in proteins and their redox reactions in cell-like confinement is crucial to the enzyme function. In one of our study, we investigate the effect of confinement on the ultrafast ET dynamics of RBP to the bound cofactor Rf, an important metabolic process, in anionic AOT-RMs of various hydrations [76]. In addition to excluded volume effect, various nonspecific interactions like ionic charge of the confining surface can influence the biochemical reactions in the confined environment of the cell. To this end, we have studied the ET dynamics of RBP-Rf complex under the confinement of a cationic CTAB-RMs with similar water pool size to the anionic AOT-RMs, towards simulating equal restricted volume effect.

Visualization of the *in vitro* complex cellular processes involving proteins requires the use of spectroscopically distinguishable fluorescent reporters often realized by labelling of the protein. In one of our study we address the consequence of attachment of a fluorophore at the protein surface, in the molecular recognition of a model globular protein Apo-Mb by selectively small model receptor CyD [77]. A detailed study using both steady-state and

picosecond-resolved fluorescence spectroscopy well illustrates the molecular recognition of the protein depending on the hydrophobic cavity size of the synthetic receptor CyD.

1.3. Summary of the Work Done:

1.3.1. Structural Characterization and Crucial Ultrafast Dynamical Events in Biomimetic Self-assembly:

1.3.1.1. Microstructure, Morphology and Ultrafast Dynamics of a Novel Edible Microemulsion [63]: An edible ME composing of tween 80/butyl lactate/IPM/water has been formulated. Pseudo-ternary phase diagram of the system contains a large single isotropic region. The phase behavior of the system is also studied at low pH (2.6) and in 0.9% NaCl solution. Conductivity, viscosity, ultrasonic velocity and compressibility study find consistent result in the structural transition (from water in oil (w/o) to bicontinuous and from bicontinuous to oil in water (o/w)) behavior of the ME. DLS study reveals the size of the MEs. The absorption and steady-state emission spectra of DCM successfully probes the polarity of the ME at its solvation shell and shows the efficacy of hosting model drug molecules. The rotational anisotropy of the dye has been studied to ascertain the geometrical restriction of the probe molecule. Picosecond-resolved fluorescence spectroscopy applies well to study the relaxation dynamics of water in the solvation shell of the MEs. The study finds strong correlation in the relaxation dynamics of water with the structure of host assembly and offers an edible ME system which could act as a potential drug delivery system and nontoxic nano-template for other applications.

1.3.2. Ultrafast Spectroscopic Studies on the Molecular Interaction of Biologically Relevant Small Molecules with Biomimetic Self-assembly:

1.3.2.1. Structural and Dynamical Characterization of Unilamellar AOT Vesicles in Aqueous Solutions and their Efficacy as Potential Drug Delivery Vehicle [65]: Aerosol OT (AOT) is well known to form nanometre sized aqueous droplets in organic solvents and used in several contemporary applications including templates of NP synthesis. However, the detailed structural characterization of AOT in aqueous media is relatively less attended.

In this study, we have used DLS technique for the structural characterization of AOT in aqueous solutions and found to have a monodispersed, unilamellar vesicles (~140 nm diameter). The efficacy of the vesicles to host both charged drugs like H258 (2'-(4-Hydroxyphenyl)-5-(4-Methyl-1-Piperazinyl)-2,5'-Bi-1H-Benzimidazole Trihydrochloride Hydrate), EtBr (ethidium bromide) and hydrophobic drug like DCM has also been investigated using FRET. Picosecond-resolved and polarization gated spectroscopy have been used to study the solvation dynamics and microviscosity at the surface of the biomimicking AOT vesicles. We have also performed concentration and temperature dependent studies in order to confirm the stability of the vesicles in aqueous phase. The drug release profile of the vesicles has been studied through *in vitro* dialysis method. The study explores the hydrogen bonded structure and dynamics at the interface of the AOT vesicle, which is similar to the environment around cell. The non-toxic, monodispersed vesicles in aqueous media with a noteworthy stability in wide range of AOT concentration and temperature, capable of hosting drugs of various natures (both hydrophobic and charged) simultaneously for many codelivery applications with controlled drug release profile may find its applications in drug delivery.

1.3.2.2. Nanostructure, Solvation Dynamics and Nanotemplating of Plasmonically Active SERS Substrate in Reverse Vesicles [66]: RVs are the organic counterparts to vesicles and are spherical containers in oils consisting of an oily core surrounded by reverse bilayers with water layers present in between. In this work, we present a facile route for forming stable RV from non-toxic surfactants and oil components. The RV formation is characterized by DLS, and further confirmed by transmission electron microscopic (TEM) techniques. The water channels present in between the bilayers are found to be a potential template for inorganic NP synthesis. Both UV-Vis absorption spectroscopy and TEM study reveal successful formation of highly clustered silver NPs within the water layers of the RVs. XRD analyzes the crystalline nature of the NPs. FTIR spectroscopy shows the signature of different kinds of water molecules in between the RV bilayers. The dynamical description of the templating water, dictating the controlled formation of the NPs in RV, is well revealed in the picosecond-resolved solvation dynamics study of a hydrophilic fluorescence probe H258. The rotational anisotropy study successfully describes geometrical restriction of the probe molecule in RV. Notably, this study provides the first proof-of-concept data for the

ability of RV to be a template of synthesizing metal NPs. The as-prepared NP clusters are evaluated to be potential SERS substrate in solution using crystal violet as a model analyte.

1.3.3. Spectroscopic Studies on the Decisive Ultrafast Dynamical Events in Biological Macromolecules:

1.3.3.1. Light Driven Ultrafast Electron Transfer in Oxidative Redding of Green Fluorescent Proteins [69]: Fluorescent proteins undergoing green to red (G/R) photoconversion have proved to be potential tools for investigating dynamic processes in living cells and for photo-localization nanoscopy. However, the photochemical reaction during light induced G/R photoconversion of fluorescent proteins remains unclear. In this study, we report the direct observation of ultrafast time-resolved ET during the photoexcitation of the fluorescent proteins enhanced GFP (EGFP) and mEos2 in presence of electron acceptor, *p*-benzoquinone (BQ). Our results show that in the excited state, the neutral EGFP chromophore accepts electrons from an anionic electron donor, Glu222, and G/R photoconversion is facilitated by ET to nearby electron acceptors. By contrast, mEos2 fails to produce the red emitting state in the presence of BQ; ET depletes the excited state configuration en route to the red-emitting fluorophore. These results show that ultrafast ET plays a pivotal role in multiple photoconversion mechanisms and provide a method to modulate the G/R photoconversion process.

1.3.4. Ultrafast Spectroscopic Studies on the Electron Transfer Dynamics in a Protein Under Nanoscopic Confinement of a Biomimetic Self-assembly:

1.3.4.1. Protein-Cofactor Binding and Ultrafast Electron Transfer in Riboflavin Binding Protein under the Spatial Confinement of Nanoscopic Reverse Micelles [76]: We study the effect of confinement on the ultrafast ET dynamics of RBP to the bound cofactor Rf, an important metabolic process, in anionic AOT-RMs of various hydrations. Notably, in addition to excluded volume effect, various nonspecific interactions like ionic charge of the confining surface can influence the biochemical reactions in the confined environment of the cell. To this end, we have also studied the ET dynamics of RBP-Rf

complex under the confinement of a cationic CTAB-RMs with similar water pool size to the anionic AOT-RMs, towards simulating equal restricted volume effect. It has been found that spatial confinement of RBP in AOT-RM of $w_0 = 10$ ($w_0 = [\text{water}]/[\text{surfactant}]$) leads to loss of its tertiary structure and hence vitamin binding capacity. Although, RBP regains its binding capacity and tertiary structure in AOT-RMs of $w_0 \geq 20$ due to its complete hydration, the ultrafast ET from RBP to Rf merely occurs in such systems. However, to our surprise the ET process is found to occur in CTAB-RMs of similar volume restriction. It is found that under the spatial confinement of anionic AOT-RMs, the isoalloxazine ring of Rf is improperly placed in the protein nanospace, so that ET between RBP and Rf is not permitted. This anomaly in the binding behavior of Rf to RBP in AOT-RMs is believed to be the influence of repulsive potential of the anionic AOT-RMs surface to the protein. Our finding thus suggests that under similar size restriction both the hydration and surface charge of the confining volume could have major implication in the intra-protein ET dynamics in real cellular environments.

1.3.5. Spectroscopic Studies on the Molecular Recognition of a Fluorescence-modified Protein by a Model Receptor:

1.3.5.1. Molecular Recognition of a Model Globular Protein Apomyoglobin by Synthetic Receptor Cyclodextrin: Effect of Fluorescence Modification of the Protein and Cavity Size of the Receptor in the Interaction [77]: Labelling of proteins with some extrinsic probe is unavoidable in molecular biology research. Particularly, spectroscopic studies in the optical region, require fluorescence modification of native proteins, by attaching polycyclic aromatic fluoroprobe with the proteins under investigation. Our present study aims to address the consequence of attachment of a fluoroprobe at the protein surface, in the molecular recognition of the protein by selectively small model receptor. A spectroscopic study involving Apo-Mb and CyD of various cavity sizes as model globular protein and synthetic receptors, respectively, using steady-state and picosecond-resolved techniques, is detailed here. A study involving FRET between intrinsic amino acid tryptophan (donor) and *N, N*-dimethyl naphthalene moiety (acceptor) of the extrinsic dansyl probes at the surface of Apo-Mb, precisely monitor changes in donor acceptor distance as a consequence of interaction of the protein with CyD having different cavity sizes (β and γ

variety). Molecular modelling studies on the interaction of tryptophan and dansyl probe with β -CyD is reported here, and found to be consistent with the experimental observations. In order to investigate structural aspects of the interacting protein, we have used CD spectroscopy. Temperature dependent CD studies explore the change in secondary structure of Apo-Mb in association with CyD, before and after fluorescence modification of the protein. Overall, the study well exemplifies approaches to protein recognition by CyD as a synthetic receptor and offers a cautionary note on the use of hydrophobic fluorescent labels for proteins in biochemical studies involving recognition of molecules.

1.4. Plan of Thesis:

The plan of the thesis is as follows:

Chapter 1: This chapter gives a brief introduction to the scope and motivation behind the thesis work. A brief summary of the work done is also included in this chapter.

Chapter 2: This chapter provides a brief overview of the steady-state and dynamical tools, the structural aspects of biologically important systems (proteins, biomimetics etc.) and probes used in the experiments.

Chapter 3: Details of instrumentation, data analysis and experimental procedures have been discussed in this chapter.

Chapter 4: In this chapter ultrafast dynamical events in biomimetic self-assembly has been discussed. The structural characterization of the self-assembly is also elaborated.

Chapter 5: Studies on the molecular interaction of biologically relevant small molecules with biomimetic self-assembly has been examined.

Chapter 6: Decisive ultrafast dynamical events in biological macromolecules has been discussed in this chapter.

Chapter 7: In this chapter ultrafast spectroscopic studies on the electron transfer dynamics in a protein under nanoscopic confinement of a self-assembled biomimetics has been discussed.

Chapter 8: Spectroscopic studies on molecular recognition of a fluorescence-modified protein by a model receptor is discussed in this chapter.

References:

- [1] S.B. Zimmerman, S.O. Trach, Estimation of macromolecule concentrations and excluded volume effects for the cytoplasm of *Escherichia coli*, *J. Mol. Biol.* 222 (1991) 599.
- [2] R.J. Ellis, A.P. Minton, Cell biology: Join the crowd, *Nature* 425 (2003) 27.
- [3] A.P. Minton, The effect of volume occupancy upon the thermodynamic activity of proteins: Some biochemical consequences, *Mol. Cell. Biochem.* 55 (1983) 119.
- [4] M. Weiss, M. Elsner, F. Kartberg, T. Nilsson, Anomalous subdiffusion is a measure for cytoplasmic crowding in living cells, *Biophys. J.* 87 (2004) 3518.
- [5] D. Miyoshi, S. Matsumura, S.-i. Nakano, N. Sugimoto, Duplex dissociation of telomere DNAs induced by molecular crowding, *J. Am. Chem. Soc.* 126 (2003) 165.
- [6] J. Martin, F.-U. Hartl, The effect of macromolecular crowding on chaperonin-mediated protein folding, *Proc. Natl. Acad. Sci. U.S.A.* 94 (1997) 1107.
- [7] X. Ai, Z. Zhou, Y. Bai, W.-Y. Choy, ¹⁵N NMR spin relaxation dispersion study of the molecular crowding effects on protein folding under native conditions, *J. Am. Chem. Soc.* 128 (2006) 3916.
- [8] A.P. Minton, The influence of macromolecular crowding and macromolecular confinement on biological reactions in physiological media, *J. Biol. Chem.* 276 (2001) 10577.
- [9] M.A. Griffin, M. Friedel, J.E. Shea, Effects of frustration, confinement, and surface interactions on the dimerization of an off-lattice β -barrel protein, *J. Chem. Phys.* 123 (2005) 174707.
- [10] M. Friedel, D.J. Sheeler, J.E. Shea, Effects of confinement and crowding on the thermodynamics and kinetics of folding of a minimalist β -barrel protein, *J. Chem. Phys.* 118 (2003) 8106.
- [11] J. Mittal, R.B. Best, Thermodynamics and kinetics of protein folding under confinement, *Proc. Natl. Acad. Sci. U.S.A.* 105 (2008) 20233.
- [12] D. Lucent, V. Vishal, V.S. Pande, Protein folding under confinement: A role for solvent, *Proc. Natl. Acad. Sci. U.S.A.* 104 (2007) 10430.
- [13] H.-X. Zhou, Protein folding in confined and crowded environments, *Arch. Biochem. Biophys.* 469 (2008) 76.

- [14] A.A. Simpson, Y. Tao, P.G. Leiman, M.O. Badasso, Y. He, P.J. Jardine, N.H. Olson, M.C. Morais, S. Grimes, D.L. Anderson, T.S. Baker, M.G. Rossmann, Structure of the bacteriophage ϕ 29 DNA packaging motor, *Nature* 408 (2000) 745.
- [15] J. Mathé, A. Aksimentiev, D.R. Nelson, K. Schulten, A. Meller, Orientation discrimination of single-stranded DNA inside the α -hemolysin membrane channel, *Proc. Natl. Acad. Sci. U.S.A.* 102 (2005) 12377.
- [16] A. Brinker, G. Pfeifer, M.J. Kerner, D.J. Naylor, F.U. Hartl, M. Hayer-Hartl, Dual function of protein confinement in chaperonin-assisted protein folding, *Cell* 107 (2001) 223.
- [17] F.U. Hartl, M. Hayer-Hartl, Molecular chaperones in the cytosol: From nascent chain to folded protein, *Science* 295 (2002) 1852.
- [18] A. Jewett, J.-E. Shea, Reconciling theories of chaperonin accelerated folding with experimental evidence, *Cell. Mol. Life Sci.* 67 (2010) 255.
- [19] S. Hudson, J. Cooney, E. Magner, Proteins in mesoporous silicates, *Angew. Chem., Int. Ed.* 47 (2008) 8582.
- [20] A. Pohorille, D. Deamer, Artificial cells: Prospects for biotechnology, *Trends Biotechnol.* 20 (2002) 123.
- [21] M.J. Doktycz, M.L. Simpson, Nano-enabled synthetic biology, *Mol. Syst. Biol.* 3 (2007) 125.
- [22] Y. Wei, J. Xu, Q. Feng, H. Dong, M. Lin, Encapsulation of enzymes in mesoporous host materials via the nonsurfactant-templated sol-gel process, *Mater. Lett.* 44 (2000) 6.
- [23] C.V. Kumar, A. Chaudhari, Proteins immobilized at the galleries of layered α -zirconium phosphate: Structure and activity studies, *J. Am. Chem. Soc.* 122 (2000) 830.
- [24] E.P. O'Brien, G. Stan, D. Thirumalai, B.R. Brooks, Factors governing helix formation in peptides confined to carbon nanotubes, *Nano Lett.* 8 (2008) 3702.
- [25] J. Jarvet, J. Danielsson, P. Damberg, M. Oleszczuk, A. Gräslund, Positioning of the alzheimer A β (1–40) peptide in SDS micelles using NMR and paramagnetic probes, *J. Biomol. NMR* 39 (2007) 63.
- [26] R.W. Peterson, K. Anbalagan, C. Tommos, A.J. Wand, Forced folding and structural analysis of metastable proteins, *J. Am. Chem. Soc.* 126 (2004) 9498.

- [27] A. Baumketner, A. Jewett, J.E. Shea, Effects of confinement in chaperonin assisted protein folding: Rate enhancement by decreasing the roughness of the folding energy landscape, *J. Mol. Biol.* 332 (2003) 701.
- [28] A. Bhattacharya, Robert B. Best, J. Mittal, Smoothing of the GB1 hairpin folding landscape by interfacial confinement, *Biophys. J.* 103 (2012) 596.
- [29] H.-X. Zhou, G. Rivas, A.P. Minton, Macromolecular crowding and confinement: Biochemical, biophysical, and potential physiological consequences, *Annu. Rev. Biophys.* 37 (2008) 375.
- [30] A. Malik, J. Kundu, S.K. Mukherjee, P.K. Chowdhury, Myoglobin unfolding in crowding and confinement, *J. Phys. Chem. B* 116 (2012) 12895.
- [31] J. Tian, A.E. Garcia, Simulation studies of protein folding/unfolding equilibrium under polar and nonpolar confinement, *J. Am. Chem. Soc.* 133 (2011) 15157.
- [32] E.J. Sorin, V.S. Pande, Nanotube confinement denatures protein helices, *J. Am. Chem. Soc.* 128 (2006) 6316.
- [33] J.S. Rao, L. Cruz, Effects of confinement on the structure and dynamics of an intrinsically disordered peptide: A molecular-dynamics study, *J. Phys. Chem. B* 117 (2013) 3707.
- [34] S.S. Mandal, S. Bhaduri, H. Amenitsch, A.J. Bhattacharyya, Synchrotron small-angle X-ray scattering studies of hemoglobin nonaggregation confined inside polymer capsules, *J. Phys. Chem. B* 116 (2012) 9604.
- [35] B. Chen, W. Qi, X. Li, C. Lei, J. Liu, Heated proteins are still active in a functionalized nanoporous support, *Small* 9 (2013) 2228.
- [36] D.B. Gornowich, G.J. Blanchard, Enhancement of enzyme activity by confinement in an inverse opal structure, *J. Phys. Chem. C* 116 (2012) 12165.
- [37] M.S. Cheung, D. Klimov, D. Thirumalai, Molecular crowding enhances native state stability and refolding rates of globular proteins, *Proc. Natl. Acad. Sci. U.S.A.* 102 (2005) 4753.
- [38] H.-X. Zhou, Helix formation inside a nanotube: Possible influence of backbone-water hydrogen bonding by the confining surface through modulation of water activity, *J. Chem. Phys.* 127 (2007) 245101.

- [39] D.K. Klimov, D. Newfield, D. Thirumalai, Simulations of β -hairpin folding confined to spherical pores using distributed computing, *Proc. Natl. Acad. Sci. U.S.A.* 99 (2002) 8019.
- [40] H.-X. Zhou, Polymer models of protein stability, folding, and interactions, *Biochemistry* 43 (2004) 2141.
- [41] A.P. Minton, Confinement as a determinant of macromolecular structure and reactivity, *Biophys. J.* 63 (1992) 1090.
- [42] A.P. Minton, Effect of a concentrated "inert" macromolecular cosolute on the stability of a globular protein with respect to denaturation by heat and by chaotropes: A statistical-thermodynamical model, *Biophys. J.* 78 (2000) 101.
- [43] S.K. Pal, A.H. Zewail, Dynamics of water in biological recognition, *Chem. Rev.* 104 (2004) 2099.
- [44] L. Zhang, L. Wang, Y.-T. Kao, W. Qiu, Y. Yang, O. Okobiah, D. Zhong, Mapping hydration dynamics around a protein surface, *Proc. Natl. Acad. Sci. U.S.A.* 104 (2007) 18461.
- [45] W. Qiu, Y.-T. Kao, L. Zhang, Y. Yang, L. Wang, W.E. Stites, D. Zhong, A.H. Zewail, Protein surface hydration mapped by site-specific mutations, *Proc. Natl. Acad. Sci. U.S.A.* 103 (2006) 13979.
- [46] R. Biswas, S.K. Pal, Caging enzyme function: α -chymotrypsin in reverse micelle, *Chem. Phys. Lett.* 387 (2004) 221.
- [47] Q. Chen, K.G. Rausch, H. Schönherr, G.J. Vancso, α -Chymotrypsin-catalyzed reaction confined in block-copolymer vesicles, *ChemPhysChem* 11 (2010) 3534.
- [48] Q. Chen, H. Schönherr, G.J. Vancso, Block-copolymer vesicles as nanoreactors for enzymatic reactions, *Small* 5 (2009) 1436.
- [49] J.H. Tian, A.E. Garcia, Simulations of the confinement of ubiquitin in self-assembled reverse micelles, *J. Chem. Phys.* 134 (2011) 225101.
- [50] A.V. Martinez, S.C. DeSensi, L. Dominguez, E. Rivera, J.E. Straub, Protein folding in a reverse micelle environment: The role of confinement and dehydration, *J. Chem. Phys.* 134 (2011) 055107.
- [51] W. Oi, M. Isobe, A. Hashidzume, A. Harada, Macromolecular recognition: Discrimination between human and bovine serum albumins by cyclodextrins, *Macromol. Rapid Commun.* 32 (2011) 501.

- [52] H.S. Samra, F. He, A. Bhambhani, J.D. Pipkin, R. Zimmerer, S.B. Joshi, C.R. Middaugh, The effects of substituted cyclodextrins on the colloidal and conformational stability of selected proteins, *J. Pharm. Sci.* 99 (2010) 2800.
- [53] M.S. Cheung, A.E. García, J.N. Onuchic, Protein folding mediated by solvation: Water expulsion and formation of the hydrophobic core occur after the structural collapse, *Proc. Natl. Acad. Sci. U.S.A.* 99 (2002) 685.
- [54] I. Daidone, M.B. Ulmschneider, A. Di Nola, A. Amadei, J.C. Smith, Dehydration-driven solvent exposure of hydrophobic surfaces as a driving force in peptide folding, *Proc. Natl. Acad. Sci. U.S.A.* 104 (2007) 15230.
- [55] S.J. Kim, B. Born, M. Havenith, M. Gruebele, Real-time detection of protein-water dynamics upon protein folding by terahertz absorption spectroscopy, *Angew. Chem. Int. Ed.* 47 (2008) 6486.
- [56] D. Zhong, S.K. Pal, A.H. Zewail, Femtosecond studies of protein-DNA binding and dynamics: Histone I, *ChemPhysChem* 2 (2001) 219.
- [57] Y. Levy, J.N. Onuchic, Water mediation in protein folding and molecular recognition, *Ann. Rev. Biophys. Biomol. Struct.* 35 (2006) 389.
- [58] J.R.H. Tame, S.H. Sleight, A.J. Wilkinson, J.E. Ladbury, The role of water in sequence-independent ligand binding by an oligopeptide transporter protein, *Nat. Struct. Mol. Biol.* 3 (1996) 998.
- [59] D.N. Dubins, R. Filfil, R.B. Macgregor, T.V. Chalikian, Role of water in protein-ligand interactions: Volumetric characterization of the binding of 2'-CMP and 3'-CMP to ribonuclease A, *J. Phys. Chem. B* 104 (1999) 390.
- [60] F. Garczarek, K. Gerwert, Functional waters in intraprotein proton transfer monitored by FTIR difference spectroscopy, *Nature* 439 (2006) 109.
- [61] P. Shrimpton, R.K. Allemann, Role of water in the catalytic cycle of *E. coli* dihydrofolate reductase, *Protein Sci.* 11 (2002) 1442.
- [62] Y. Pocker, Water in enzyme reaction: Biophysical aspects of hydration-dehydration processes, *Cell. Mol. Life Sci.* 57 (2000) 1008.
- [63] R. Saha, S. Rakshit, R.K. Mitra, S.K. Pal, Microstructure, morphology, and ultrafast dynamics of a novel edible microemulsion, *Langmuir* 28 (2012) 8309.

- [64] T. Sheynis, J. Sykora, A. Benda, S. Kolusheva, M. Hof, R. Jelinek, Bilayer localization of membrane-active peptides studied in biomimetic vesicles by visible and fluorescence spectroscopies, *Eur. J. Biochem.* 270 (2003) 4478.
- [65] R. Saha, P.K. Verma, R.K. Mitra, S.K. Pal, Structural and dynamical characterization of unilamellar AOT vesicles in aqueous solutions and their efficacy as potential drug delivery vehicle, *Colloids Surf., B* 88 (2011) 345.
- [66] R. Saha, S. Rakshit, D. Majumdar, A. Singha, R. Mitra, S. Pal, Nanostructure, solvation dynamics, and nanotemplating of plasmonically active SERS substrate in reverse vesicles, *J. Nanopart. Res.* 15 (2013) 1576.
- [67] E. Betzig, G.H. Patterson, R. Sougrat, O.W. Lindwasser, S. Olenych, J.S. Bonifacino, M.W. Davidson, J. Lippincott-Schwartz, H.F. Hess, Imaging intracellular fluorescent proteins at nanometer resolution, *Science* 313 (2006) 1642.
- [68] J. Wiedenmann, G.U. Nienhaus, Live-cell imaging with EosFP and other photoactivatable marker proteins of the GFP family, *Expert Rev. Proteomics* 3 (2006) 361.
- [69] R. Saha, P.K. Verma, S. Rakshit, S. Saha, S. Mayor, S.K. Pal, Light driven ultrafast electron transfer in oxidative redding of green fluorescent proteins, *Sci. Rep.* 3 (2013) 1580.
- [70] V. Balzani, Electron transfer in chemistry, Wiley-VCH, Weinheim, Germany, 2001.
- [71] D.S. Bendall, Protein electron transfer, Bios Scientific, Oxford, U.K., 1996.
- [72] J. Stubbe, W.A. van der Donk, Protein radicals in enzyme catalysis, *Chem. Rev.* 98 (1998) 705.
- [73] M. Sinnott, Comprehensive biological catalysis: A mechanistic reference, Academic, San Diego, 1998.
- [74] S. Ghisla, P. Kroneck, P. Macheroux, H. Sund, Flavins and flavoproteins, Agency for Scientific Pub, Berlin, 1999.
- [75] F. Müller, Chemistry and biochemistry of flavoenzymes, CRC Press, Boca Raton, Florida, 1991.
- [76] R. Saha, S. Rakshit, P.K. Verma, R.K. Mitra, S.K. Pal, Protein-cofactor binding and ultrafast electron transfer in riboflavin binding protein under the spatial confinement of nanoscopic reverse micelles, *J. Mol. Recognit.* 26 (2013) 59.

[77] R. Saha, S. Rakshit, S.K. Pal, Molecular recognition of a model globular protein apomyoglobin by synthetic receptor cyclodextrin: Effect of fluorescence modification of the protein and cavity size of the receptor in the interaction *J. Mol. Recognit.* 26 (2013) 568.

Chapter 2

An Overview of Experimental Techniques and Systems

In order to investigate the various processes involved in the course of study on the interaction of biomimetics with biological macromolecules, different steady-state and dynamical tools have been employed. These include solvation dynamics, fluorescence anisotropy, Förster resonance energy transfer (FRET), determination of activation energy using Arrhenius theory, excited state proton transfer (ESPT), photoinduced electron transfer (PET), surface enhanced Raman scattering (SERS), *in vitro* drug release study, densimetric and acoustic measurements. In this chapter, brief discussions about these tools and an overview of various systems used in our studies have been provided.

2.1. Steady-state and Dynamical Tools:

2.1.1. Solvation Dynamics:

2.1.1.1. Theory: Solvation dynamics refer to the process of reorganization of solvent dipoles around a dipole created instantaneously or an electron/proton injected suddenly in a polar liquid. In order to understand the meaning and scope of solvation dynamics, let us first visualize the physical essence of the dynamical process involved for a solute molecule in a polar solvent [1-3]. A change in the probe (solute) is made at time $t = 0$, by an excitation pulse, which leads to the creation of a dipole. This dipole gives rise to an instantaneous electric field on the solvent molecules. The interaction of permanent dipoles of the solvent with the instantaneously created electric field, shifts the free energy minimum of the solvent to a non-zero value of the polarization. The solvent motion is crucial (Figure 2.1). Since the probe is excited instantaneously (a Franck-Condon transition as far as the nuclear degrees of freedom are concerned), the solvent molecules at $t = 0$ find themselves in a relatively high-energy configuration. Subsequently, the solvent molecules begin to move and rearrange themselves to reach their new equilibrium positions (Figure 2.2). The nuclear motion involved can be broadly classified into rotational and translational motions.

When the solvent is bulk water, rotational motion would also include hindered rotation and libration, while translation would include the intermolecular vibration due to the extensive hydrogen bonding. The two specific motions, libration and intermolecular vibration, are relatively high in frequency and are expected to play a dominant role in the initial part of solvation [4]. The molecular motions involved are shown schematically in

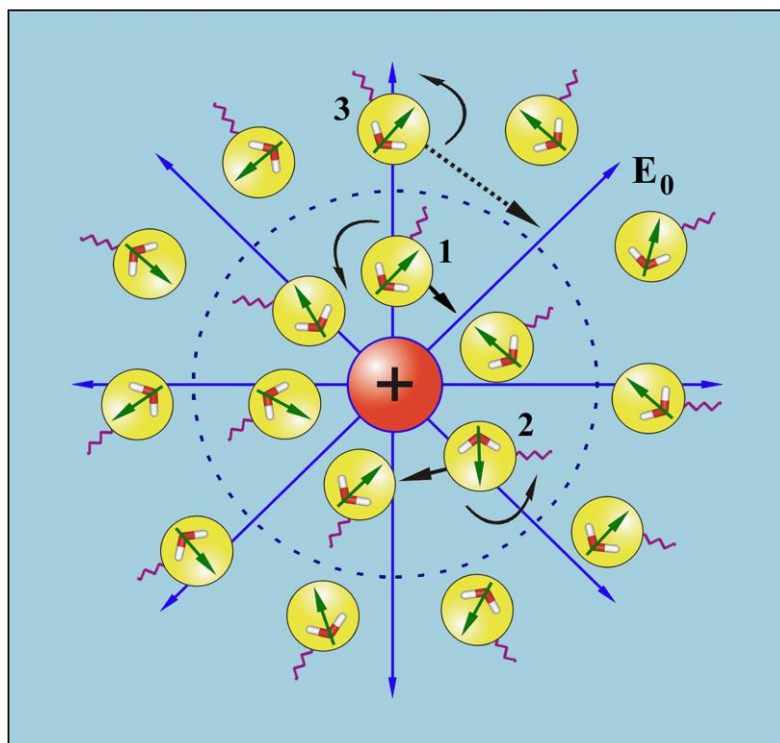


Figure 2.1. Schematic illustration of solvation of an ion (or dipole) by water. The neighboring molecules (numbered 1 and 2) can either rotate or translate to attain the minimum energy configuration. On the other hand, distant water molecule 3 can only rotate to attain minimum energy configuration. The field is shown as E_0 . The springs connected to the molecules are meant to denote hydrogen bonding.

Figure 2.1, and in Figure 2.3 we show a typical solvation time correlation function. For clarity, we approximate the motions responsible for the decay in different regions.

A simple way to address the dynamics of polar solvation is to start with the following expression for the solvation energy, $E_{\text{solv}}(t)$ [5],

$$E_{\text{solv}}(t) = -\frac{1}{2} \int d\mathbf{r} \mathbf{E}_0(\mathbf{r}) \cdot \mathbf{P}(\mathbf{r}, t) \quad (2-1)$$

where $\mathbf{E}_0(\mathbf{r})$ is the instantaneously created, position-dependent electric field from the ion or the dipole of the solute and $\mathbf{P}(\mathbf{r},t)$ is the position and time-dependent polarization.

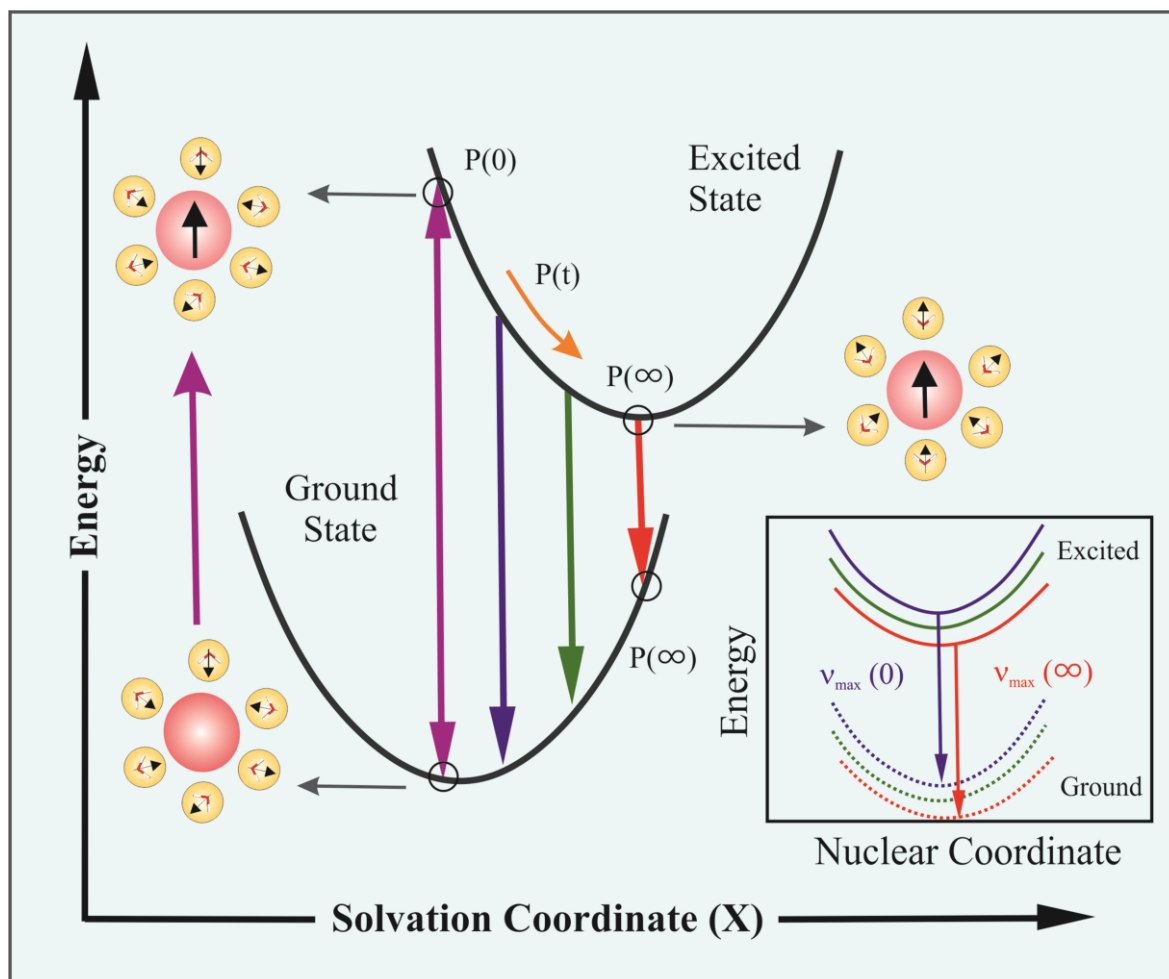


Figure 2.2. Schematic representation of the potential energy surfaces involved in solvation dynamics showing the water orientational motions along the solvation coordinate together with instantaneous polarization P . In the inset we show the change in the potential energy along the intramolecular nuclear coordinate. As solvation proceeds the energy of the solute comes down giving rise to a red shift in the fluorescence spectrum. Note the instantaneous P , e.g., $P(\infty)$, on the two connected potentials.

The latter is defined by the following expression,

$$\mathbf{P}(\mathbf{r},t) = \int d\Omega \mu(\Omega) \rho(\mathbf{r},\Omega,t) \quad (2-2)$$

where $\mu(\Omega)$ is the dipole moment vector of a molecule at position \mathbf{r} , and $\rho(\mathbf{r},\Omega,t)$ is the position, orientation and time-dependent density. Therefore, the time dependence of the solvation energy is determined by the time dependence of polarization that is in turn

determined by the time dependence of the density. If the perturbation due to the probe on dynamics of bulk water is negligible, then the time dependence of polarization is dictated by the natural dynamics of the liquid.

The theoretical analysis of the time-dependent density is usually carried out using a molecular hydrodynamic approach that is based on the basic conservation (density,

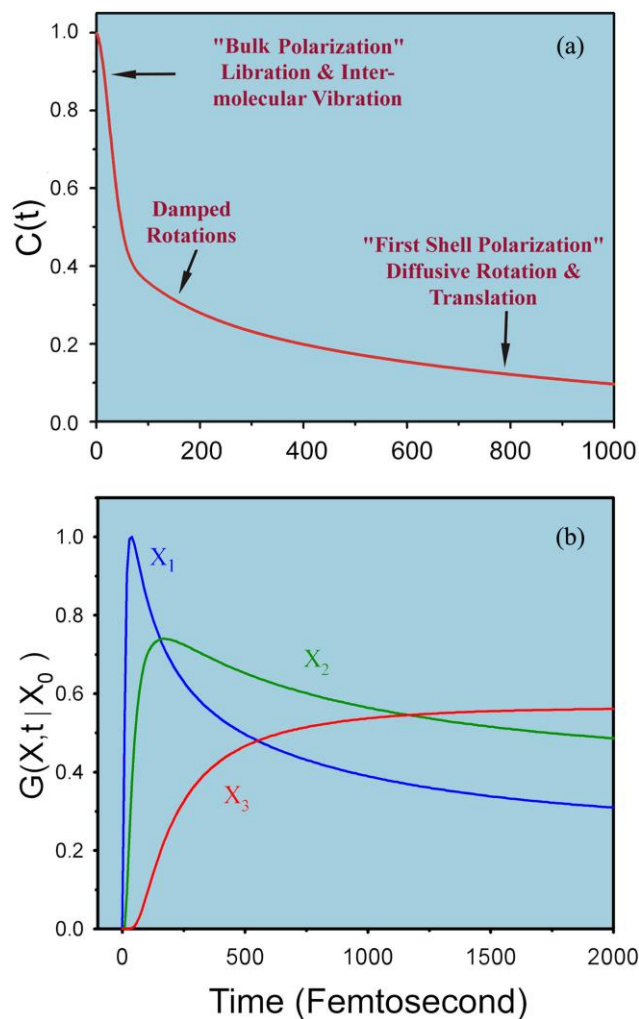


Figure 2.3. (a) A typical solvation time correlation function for water is shown here. The time correlation function exhibits three distinct regions: The initial ultrafast decay, an intermediate decay of about 200 fs and the last slow decay with time constant of 1 ps. The physical origin of each region is indicated on the plot itself; see text. (b) Green's function $G(X, t | X_0)$ for population relaxation along the solvation coordinate (X) is plotted against time in femtosecond. In G , X_0 is the initial position at $t = 0$. This Figure shows the position and time dependence of the population fluorescence intensity. At early times (when the population is at X_1) there is ultrafast rise followed by an ultrafast decay. At intermediate times (when the population is at X_2) there is a rise followed by a slow decay as shown by the green line. At long times when the population is nearly relaxed (position X_3 , red line) we see only a rise.

momentum and energy) laws and includes the effects of intermolecular (both spatial and orientational) correlations. The latter provides the free energy surface on which solvation proceeds. The equation of motion of the density involves both orientational and translational motions of the solvent molecules. The details of the theoretical development are reported in literature [1]; here we shall present a simple physical picture of the observed biphasic solvation dynamics.

Within linear response theory, the solvation correlation function is directly related to the solvation energy as,

$$C(t) = \frac{\langle \delta E(0) \cdot \delta E(t) \rangle}{\langle \delta E^2 \rangle} = \frac{\langle E(t) \rangle - \langle E(\infty) \rangle}{\langle E(0) \rangle - \langle E(\infty) \rangle} \quad (2-3)$$

where δE is the fluctuation of solvation energy from the average, equilibrium value. Note that the equality in equation (2-3) indicates the direct relation for the average of the fluctuations over the equilibrium distribution (left) and the non-equilibrium function (right) which relates to observables; without $\langle E(\infty) \rangle$ the correspondence is clear, and $\langle E(\infty) \rangle$ is rigorously the result of the equilibrium term in the numerator and for normalization in the denominator.

The ultrafast component in the solvation time correlation function (see Figure 2.3(a)), originates from the initial relaxation in the steep collective solvation potential. The collective potential is steep because it involves the total polarization of the system [1, 3]. This initial relaxation couples mainly to the hindered rotation (i.e., libration) and the hindered translation (i.e., the intermolecular vibration), which are the available high frequency modes of the solvent; neither long amplitude rotation nor molecular translation are relevant here. The last part in the decay of the solvation correlation function involves larger amplitude rotational and translational motions of the nearest neighbor molecules in the first solvation shell. In the intermediate time, one gets contributions from the moderately damped rotational motions of water molecules. In a sense, with the above description one recovers the famous Onsager's "inverse snow-ball" picture of solvation [6]. The slowest time constant is ~ 1 ps, which is determined by the individual rotational and translational motions of the molecules in the "first solvation shell" nearly close to the

probe. The femtosecond component is dominated by the high frequency hindered rotational and translational (vibration) polarization [7].

Figure 2.2 shows a schematic of the solvation potential and the orientational motions for the water molecules involved. From the shape of the potential, it can be seen that the transient behavior for the population during solvation should be a decay function on the blue edge of the spectrum and a rise function on the red edge. These wavelength-dependent features can be explained nicely within a generalized model of relaxation in which a Gaussian wave packet relaxes on a harmonic surface. The relaxation is non-exponential and a Green's function can describe the approach of the wave packet along the solvation coordinate, X , to its equilibrium value. For the general non-Markovian case it is given by [8],

$$G(X, t|X_0) = \frac{1}{\sqrt{2\pi\langle X^2 \rangle [1 - C^2(t)]}} \exp \left[-\frac{[X - X_0 C(t)]^2}{2\langle X^2 \rangle [1 - C^2(t)]} \right] \quad (2-4)$$

where $\langle X^2 \rangle$ is the equilibrium mean square fluctuation of the polarization coordinate in the excited state surface, $C(t)$ is the solvation correlation function described in equation (2-3) and X_0 is the initial value of the packet on the solvation coordinate. Equation (2-4) describes the motion of the wave packet (polarization density) beginning at $t = 0$ (X_0) as a delta function and according to the solvation time correlation function. As $t \rightarrow \infty$, $C(t) \rightarrow 0$ and we recover the standard Gaussian distribution. Initially, ($t \rightarrow 0$), the exponential is large, so the decay is ultrafast, but at long times, the relaxation slows down, ultimately to appear as a rise. In Figure 2.3(b), we present calculations of $G(X, t|X_0)$ at different positions along the solvation coordinate giving decays at X_1 and X_2 , but with different time constants, and a rise at X_3 , as demonstrated experimentally.

2.1.1.2. Experimental Methods: In order to study solvation stabilization of a probe in an environment, a number of fluorescence transients are taken at different wavelengths across the emission spectrum of the probe. As described earlier, blue and red ends of the emission spectrum are expected to show decay and rise, respectively in the transients. The observed fluorescence transients are fitted by using a nonlinear least square fitting procedure to a function

$$\left(X(t) = \int_0^t E(t')R(t-t')dt' \right) \quad (2-5)$$

comprising of convolution of the instrument response function (IRF) ($E(t)$) with a sum of exponentials

$$\left(R(t) = A + \sum_{i=1}^N B_i \exp(-t/\tau_i) \right) \quad (2-6)$$

with pre-exponential factors (B_i), characteristic lifetimes (τ_i) and a background (A). Relative concentration in a multi-exponential decay is finally expressed as;

$$\alpha_n = \frac{B_n}{\sum_{i=1}^N B_i}. \quad (2-7)$$

The relative contribution of a particular decay component (f_n) in the total fluorescence is defined as,

$$f_n = \frac{\tau_n B_n}{\sum_{i=1}^N B_i \tau_i} \times 100. \quad (2-8)$$

The quality of the curve fitting is evaluated by reduced chi-square (0.9-1.1) and residual data. The purpose of the fitting is to obtain the decays in an analytical form suitable for further data analysis.

To construct time resolved emission spectra (TRES) we follow the technique described in references [9, 10]. As described above, the emission intensity decays are analyzed in terms of the multi-exponential model,

$$I(\lambda, t) = \sum_{i=1}^N \alpha_i(\lambda) \exp(-t/\tau_i(\lambda)) \quad (2-9)$$

where $\alpha_i(\lambda)$ are the pre-exponential factors, with $\sum \alpha_i(\lambda) = 1.0$. In this analysis we compute a new set of intensity decays, which are normalized so that the time-integrated intensity at each wavelength is equal to the steady-state intensity at that wavelength. Considering $F(\lambda)$ to be the steady-state emission spectrum, we calculate a set of $H(\lambda)$ values using,

$$H(\lambda) = \frac{F(\lambda)}{\int_0^{\infty} I(\lambda, t) dt} \quad (2-10)$$

which for multiexponential analysis becomes,

$$H(\lambda) = \frac{F(\lambda)}{\sum_i \alpha_i(\lambda)\tau_i(\lambda)} \quad (2-11)$$

Then, the appropriately normalized intensity decay functions are given by,

$$I(\lambda, t) = H(\lambda)I(\lambda, t) = \sum_{i=1}^N \alpha'_i(\lambda) \exp\left(-t/\tau_i(\lambda)\right) \quad (2-12)$$

where $\alpha'_i(\lambda) = H(\lambda)\alpha_i(\lambda)$. The values of $I(\lambda, t)$ are used to calculate the intensity at any wavelength and time, and thus the TRES. The values of the emission maxima and spectral width are determined by nonlinear least-square fitting of the spectral shape of the TRES. The spectral shape is assumed to follow a lognormal line shape [9],

$$I(\bar{\nu}) = I_0 \exp\left\{-\left[\ln 2 \left(\frac{\ln(\alpha+1)}{b}\right)^2\right]\right\} \quad (2-13)$$

with $\alpha = \frac{2b(\bar{\nu} - \bar{\nu}_{\max})}{\Delta} - 1$ where I_0 is amplitude, $\bar{\nu}_{\max}$ is the wavenumber of the emission

maximum and spectral width is given by, $\Gamma = \Delta \frac{\sinh(b)}{b}$. The terms b and Δ are asymmetry and width parameters, respectively and equation (2-9) reduces to a Gaussian function for $b = 0$.

The time-dependent fluorescence Stokes shifts, as estimated from TRES are used to construct the normalized spectral shift correlation function or the solvent correlation function $C(t)$ and is defined as,

$$C(t) = \frac{\bar{\nu}(t) - \bar{\nu}(\infty)}{\bar{\nu}(0) - \bar{\nu}(\infty)} \quad (2-14)$$

where, $\bar{\nu}(0)$, $\bar{\nu}(t)$ and $\bar{\nu}(\infty)$ are the emission maxima (in cm^{-1}) of the TRES at time zero, t and infinity, respectively. The $\bar{\nu}(\infty)$ value is considered to be the emission frequency beyond which insignificant or no spectral shift is observed. The $C(t)$ function represents the temporal response of the solvent relaxation process, as occurs around the probe following its photoexcitation and the associated change in the dipole moment.

In order to further investigate possible heterogeneity in the positional distribution of fluoroprobes at the interfaces of biomimicking self-assemblies we follow time-resolved

area normalized emission spectroscopy (TRANES), which is a well-established technique [11, 12] and is a modified version of TRES. TRANES were constructed by normalizing the area of each spectrum in TRES such that the area of the spectrum at time t is equal to the area of the spectrum at $t = 0$. A useful feature of this method is the presence of an isoemissive point in the spectra involve emission from two species, which are kinetically coupled either irreversibly or reversibly or not coupled at all.

2.1.2. Fluorescence Anisotropy: Anisotropy is defined as the extent of polarization of the emission from a fluorophore. Anisotropy measurements are commonly used in biochemical applications of fluorescence. It provides information about the size and shape of proteins or the rigidity of various molecular environments. Anisotropy measurements have also been used to measure protein-protein associations, fluidity of membranes and for immunoassays of numerous substances. These measurements are based on the principle of photoselective excitation of those fluorophore molecules whose absorption transition dipoles are parallel to the electric vector of polarized excitation light. In an isotropic solution, fluorophores are oriented randomly. However, upon selective excitation, partially oriented population of fluorophores with polarized fluorescence emission results. The relative angle between the absorption and emission transition dipole moments determines the maximum measured anisotropy (r_0). The fluorescence anisotropy (r) and polarization (P) are defined by,

$$r = \frac{I_{\parallel} - I_{\perp}}{I_{\parallel} + 2I_{\perp}} \quad (2-15)$$

$$\text{and } P = \frac{I_{\parallel} - I_{\perp}}{I_{\parallel} + I_{\perp}} \quad (2-16)$$

where I_{\parallel} and I_{\perp} are the fluorescence intensities of vertically and horizontally polarized emission when the fluorophore is excited with vertically polarized light. Polarization and anisotropy are interrelated as,

$$r = \frac{2P}{3 - P} \quad (2-17)$$

$$\text{and } P = \frac{3r}{2 + r} \quad (2-18)$$

Although polarization and anisotropy provides the same information, anisotropy is preferred since the latter is normalized by total fluorescence intensity ($I_T = I_{\parallel} + 2I_{\perp}$) and in case of multiple emissive species anisotropy is additive while polarization is not. Several phenomena, including rotational diffusion and energy transfer, can decrease the measured anisotropy to values lower than maximum theoretical values. Following a pulsed excitation the fluorescence anisotropy, $r(t)$ of a sphere is given by,

$$r(t) = r_0 \exp(-t/\tau_{\text{rot}}) \quad (2-19)$$

where r_0 is the anisotropy at time $t = 0$ and τ_{rot} is the rotational correlation time of the sphere.

2.1.2.1. Theory: For a radiating dipole the intensity of light emitted is proportional to the square of the projection of the electric field of the radiating dipole onto the transmission axis of the polarizer. The intensity of parallel and perpendicular projections are given by,

$$I_{\parallel}(\theta, \psi) = \cos^2 \theta \quad (2-20)$$

$$I_{\perp}(\theta, \psi) = \sin^2 \theta \sin^2 \psi \quad (2-21)$$

where θ and ψ are the orientational angles of a single fluorophore relative to the z and y-axis, respectively (Figure 2.4a). In solution, fluorophores remain in random distribution and the anisotropy is calculated by excitation photoselection. Upon photoexcitation by polarized light, the molecules having absorption transition moments aligned parallel to the electric vector of the polarized light have the highest probability of absorption. For the excitation polarization along z-axis, all molecules having an angle ψ with respect to the y-axis will be excited. The population will be symmetrically distributed about the z-axis. For experimentally accessible molecules, the value of ψ will be in the range from 0 to 2π with equal probability. Thus, the ψ dependency can be eliminated.

$$\langle \sin^2 \psi \rangle = \frac{\int_0^{2\pi} \sin^2 \psi d\psi}{\int_0^{2\pi} d\psi} = \frac{1}{2} \quad (2-22)$$

$$\text{and } I_{\parallel}(\theta) = \cos^2 \theta \quad (2-23)$$

$$I_{\perp}(\theta) = \frac{1}{2} \sin^2 \theta \quad (2-24)$$

Consider a collection of molecules oriented relative to the z-axis with probability $f(\theta)$. Then, measured fluorescence intensities for this collection after photoexcitation are,

$$I_{\parallel} = \int_0^{\pi/2} f(\theta) \cos^2 \theta d\theta = k \langle \cos^2 \theta \rangle \quad (2-25)$$

$$I_{\perp} = \frac{1}{2} \int_0^{\pi/2} f(\theta) \sin^2 \theta d\theta = \frac{k}{2} \langle \sin^2 \theta \rangle \quad (2-26)$$

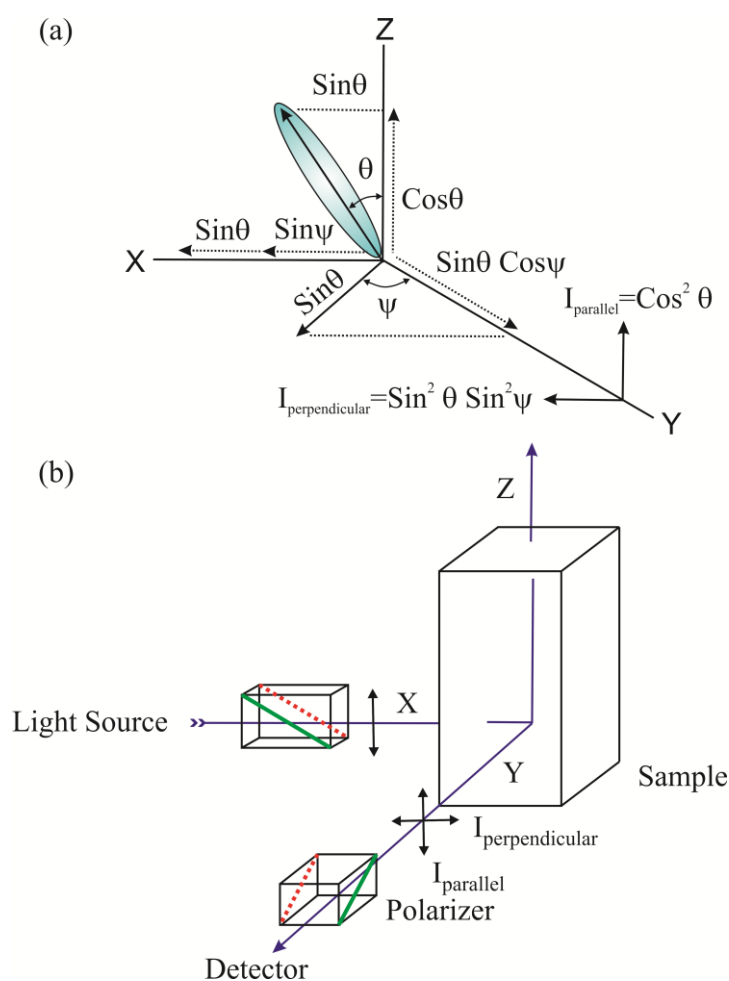


Figure 2.4. (a) Emission intensity of a single fluorophore (blue ellipsoid) in a coordinate system. (b) Schematic representation of the measurement of fluorescence anisotropy.

where $f(\theta)d\theta$ is the probability that a fluorophore is oriented between θ and $\theta+d\theta$ and is given by,

$$f(\theta)d\theta = \cos^2 \theta \sin \theta d\theta \quad (2-27)$$

k is the instrumental constant. Thus, the anisotropy (r) is defined as,

$$r = \frac{3\langle \cos^2 \theta \rangle - 1}{2} \quad (2-28)$$

when $\theta = 54.7^\circ$ i.e. when $\cos^2\theta = 1/3$, the complete loss of anisotropy occurs. Thus, the fluorescence taken at $\theta = 54.7^\circ$ with respect to the excitation polarization is expected to be free from the effect of anisotropy and is known as magic angle emission. For collinear absorption and emission dipoles, the value of $\langle \cos^2\theta \rangle$ is given by the following equation,

$$\langle \cos^2 \theta \rangle = \frac{\int_0^{\pi/2} \cos^2 \theta f(\theta) d\theta}{\int_0^{\pi/2} f(\theta) d\theta} \quad (2-29)$$

Substituting equation (2-27) in equation (2-29) one can get the value of $\langle \cos^2\theta \rangle = 3/5$ and anisotropy value to be 0.4 (from equation (2-28)). This is the maximum value of anisotropy obtained when the absorption and emission dipoles are collinear and when no other depolarization process takes place. However, for most fluorophore, the value of anisotropy is less than 0.4 and it is dependent on the excitation wavelength. It is demonstrated that as the displacement of the absorption and emission dipole occurs by an angle γ relative to each other, it causes further loss of anisotropy (reduction by a factor 2/5) [10] from the value obtained from equation (2-28). Thus, the value of fundamental anisotropy, r_0 is given by,

$$r_0 = \frac{2}{5} \left(\frac{3 \cos^2 \gamma - 1}{2} \right) \quad (2-30)$$

For any fluorophore randomly distributed in solution, with one-photon excitation, the value of r_0 varies from -0.20 to 0.40 for γ values varying from 90° to 0° .

2.1.2.2. Experimental Methods: For time resolved anisotropy ($r(t)$) measurements (Figure 2-4b), emission polarization is adjusted to be parallel and perpendicular to that of the excitation polarization. Spencer and Weber [13] have derived the relevant equations for the time dependence of $I_{\parallel}(t)$ (equation (2-31)) and $I_{\perp}(t)$ (equation (2-32)) for single rotational and fluorescence relaxation times, τ_{rot} and τ_f , respectively,

$$I_{\parallel}(t) = \exp(-t/\tau_f)(1 + 2r_0 \exp(-t/\tau_{rot})) \quad (2-31)$$

$$I_{\perp}(t) = \exp(-t/\tau_f)(1 - r_0 \exp(-t/\tau_{rot})) \quad (2-32)$$

The total fluorescence is given by,

$$F(t) = I_{\parallel}(t) + 2I_{\perp}(t) = 3 \exp(-t/\tau_f) = F_0 \exp(-t/\tau_f) \quad (2-33)$$

The time dependent anisotropy, $r(t)$ is given by,

$$r(t) = \frac{I_{\parallel}(t) - I_{\perp}(t)}{I_{\parallel}(t) + 2I_{\perp}(t)} = r_0 \exp(-t/\tau_{rot}) \quad (2-34)$$

$F(t)$ depends upon τ_f and $r(t)$ depends upon τ_{rot} so that these two lifetimes can be separated. This separation is not possible in steady-state measurements. It should be noted that the degree of polarization (P) is not independent of τ_f and is therefore not as useful quantity as r . For reliable measurement of $r(t)$, three limiting cases can be considered.

- (a) If $\tau_f < \tau_{rot}$, the fluorescence decays before the anisotropy decays, and hence only r_0 can be measured.
- (b) If $\tau_{rot} < \tau_f$, in contrast to steady-state measurements, τ_{rot} can be measured in principle. The equations (2-31) and (2-32) show that the decay of the parallel and perpendicular components depends only upon τ_{rot} . The only experimental disadvantage of this case is that those photons emitted after the period of a few times τ_{rot} can not contribute to the determination of τ_{rot} , but provided the signal-to-noise ratio is favorable, this need not be of great concern.
- (c) If $\tau_{rot} \approx \tau_f$, then it becomes the ideal situation since almost all photons are counted within the time (equal to several rotational relaxation times) in which $r(t)$ shows measurable changes.

For systems with multiple rotational correlation times, $r(t)$ is given by,

$$r(t) = r_0 \sum_i \beta_i e^{-t/\tau_i} \quad (2-35)$$

where $\sum_i \beta_i = 1$. It should be noted that the instrument monitoring the fluorescence, particularly the spectral dispersion element, responds differently to different polarizations of light, thus emerging the need for a correction factor. For example, the use of diffraction gratings can yield intensities of emission, which depend strongly upon orientation with

respect to the plane of the grating. It is inevitably necessary when using such instruments to correct for the anisotropy in response. This instrumental anisotropy is usually termed as G-factor (grating factor) and is defined as the ratio of the transmission efficiency for vertically polarized light to that for horizontally polarized light ($G = I_{\parallel}/I_{\perp}$). Hence, values of fluorescence anisotropy, $r(t)$ corrected for instrumental response, would be given by [10],

$$r(t) = \frac{I_{\parallel}(t) - GI_{\perp}(t)}{I_{\parallel}(t) + 2GI_{\perp}(t)} \quad (2-36)$$

The G-factor at a given wavelength can be determined by exciting the sample with horizontally polarized excitation beam and collecting the two polarized fluorescence decays, one parallel and other perpendicular to the horizontally polarized excitation beam. G-factor can also be determined following longtime tail matching technique [10]. If $\tau_{\text{rot}} < \tau_r$, it can be seen that the curves for $I_{\parallel}(t)$ and $I_{\perp}(t)$ should become identical. If in any experiment they are not, it can usually be assumed that this is due to a non-unitary G-factor. Hence normalizing the two decay curves on the tail of the decay eliminates the G-factor in the anisotropy measurement.

2.1.3. Estimation of Microviscosity from Stokes-Einstein-Debye Equation: The interfacial microviscosity, η_m as experienced by probe molecule in the biomimicking systems like vesicles can be estimated from the time-resolved fluorescence anisotropy using the modified Stokes-Einstein-Debye equation (SED) [14, 15],

$$\tau_r = \frac{\eta_m V_h}{k_B T} \quad (2-37)$$

where k_B is the Boltzmann constant, T is the absolute temperature. Hydrodynamic volume of the probe (V_h) can be calculated as:

$$V_h = V_m f C \quad (2-38)$$

where f is the shape factor ($f = 1$ for a spherical probe) and C represents solute-solvent coupling constant ($C = 1$ for “stick” condition and $C < 1$ for “slip” condition) and V_m is the molecular volume of the probe [16]. In case of $f = C = 1$, equation (2-37) reduces to the original simple SED equation,

$$\tau_r = \frac{\eta_m V_m}{k_B T} \quad (2-39)$$

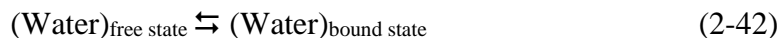
For probe molecules with prolate ellipsoid shape, the value of f is calculated using the equation [14, 15],

$$f = \frac{2}{3} \frac{1-p^4}{[(2-p^2)p^2(1-p^2)^{-1/2} \ln \frac{1+(1-p^2)^{1/2}}{p}] - p^2} \quad (2-40)$$

where p is the axial ratio (ratio of minor axis to major axis) of the prolate ellipsoid. The energy barrier, E_η for the viscous flow is estimated according to the relation [17],

$$\eta_m = \eta_0 \exp\left(\frac{E_\eta}{RT}\right) \quad (2-41)$$

2.1.4. Arrhenius Theory of Activation Energy: The dynamics of solvation at a biomolecular interface can be exploited to give information about the energetics of the participating water molecules [5]. Water present at the surface of biomolecules or biomimicking systems can broadly be distinguished as bound type (water hydrogen bonded to the interface, BW) and free type water (FW). In the water layer around the surface, the interaction with water involves hydrogen bonding to the polar and charged groups of the surface. When strongly bonded to the biomacromolecules or biomimicking surfaces, the water molecules cannot contribute to solvation dynamics because they can neither rotate nor translate. However, hydrogen bonding is transient and there exists a dynamic equilibrium between the free and the bound water molecules. The potential of the interaction can be represented by a double-well structure to symbolize the processes of bond breaking and bond forming. In general, the bonded water molecules become free by translational and rotational motions. The equilibrium between bound and free water can be written as [18-20],



Using the dynamic exchange model, an expression for this equilibrium can be derived. In a coupled diffusion-reaction equation the rate constant k_\pm can be written as,

$$k_\pm = 0.5[-B \pm (B^2 - 4D_R k_{bf})^{1/2}] \quad (2-43)$$

where $B = 2D_R + k_{bf} + k_{fb}$ and D_R is the rotational diffusion constant, k_{bf} is the rate constant of the bound to free transition and k_{fb} is that of the reverse process. Typically, the rate

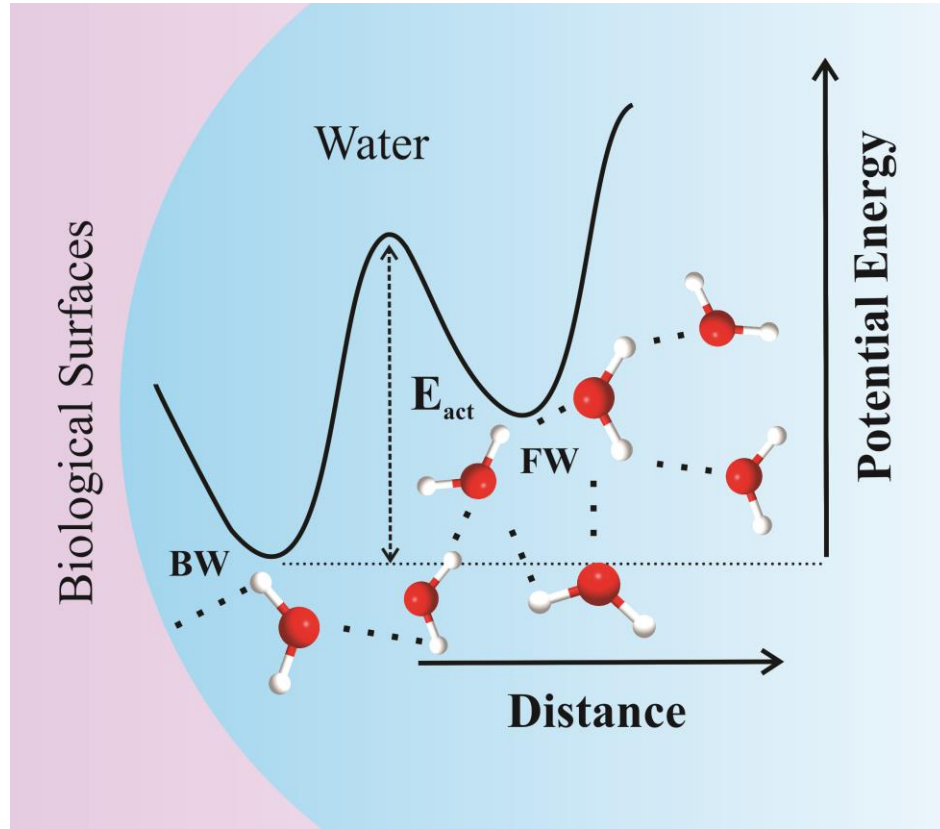


Figure 2.5. Schematic representation of different types of water molecules (BW and FW) present at various bimolecular interfaces and the corresponding activation energy barrier.

constant of free to bound reaction, is larger than that for the reverse process. It can be shown that, when the rates of interconversion between “bound” and “free” water molecules are small as compared to $2D_R$, then,

$$\tau_{\text{slow}}^{-1} \approx k_{bf}^{-1} \quad (2-44)$$

and from the activated complex theory one can have,

$$k_{bf} = (k_B T/h) \exp(-\Delta G^0 / RT) \quad (2-45)$$

If the transition process (2-42) follows a typical Arrhenius type of energy barrier crossing model, one can write,

$$\tau_{\text{slow}}^{-1} \approx k_{bf} = A \exp(-E_{\text{act}} / RT) \quad (2-46)$$

where ‘ E_{act} ’ is the activation energy for the transition process and ‘ A ’ is the pre-exponential factor. A plot of $\ln(1/\tau_{slow})$ against $1/T$ produces a straight line and from the slope of the line E_{act} can be calculated. The temperature dependence of the solvation follows the Arrhenius equation and yields the activation energy needed for the conversion of bound and free forms [20].

2.1.5. Förster Resonance Energy Transfer (FRET): FRET is an electrodynamic phenomenon involving the non-radiative transfer of the excited state energy from the donor dipole (D) to an acceptor dipole (A) in the ground state (Figure 2.6a). FRET has got wide applications in all fluorescence applications including medical diagnostics, DNA analysis and optical imaging. Since FRET can measure the size of a protein molecule or the thickness of a membrane, it is also known as ‘spectroscopic ruler’ [21]. FRET is very often used to measure the distance between two sites on a macromolecule [22]. Basically, FRET is of two types: (i) Homo-molecular FRET and (ii) Hetero-molecular FRET. In the former case the same fluorophore acts both as energy donor and acceptor, while in the latter case two different molecules act as donor and acceptor.

Each donor-acceptor (D-A) pair participating in FRET is characterized by a distance known as Förster distance (R_0) i.e., the D-A separation at which energy transfer is 50% efficient. The R_0 value ranges from 20 to 60 Å. The rate of resonance energy transfer (k_T) from donor to an acceptor is given by [10],

$$k_T = \frac{1}{\tau_D} \left(\frac{R_0}{r} \right)^6 \quad (2-47)$$

where τ_D is the lifetime of the donor in the absence of acceptor and r is the donor to acceptor (D-A) distance. The rate of transfer of donor energy depends upon the extent of overlap of the emission spectrum of the donor with the absorption spectrum of the acceptor ($J(\lambda)$), the quantum yield of the donor (Q_D), the relative orientation of the donor and acceptor transition dipoles (κ^2) and the distance between the donor and acceptor molecules (r) (Figure 2.6b). In order to estimate FRET efficiency of the donor and hence to determine distances between donor-acceptor pairs, the methodology described below is followed [10]. R_0 is given by,

$$R_0 = 0.211 [\kappa^2 n^{-4} Q_D J(\lambda)]^{1/6} \quad (\text{in } \text{Å}) \quad (2-48)$$

where n is the refractive index of the medium, Q_D is the quantum yield of the donor and $J(\lambda)$ is the overlap integral. κ^2 is defined as,

$$\kappa^2 = (\cos\theta_T - 3\cos\theta_D \cos\theta_A)^2 = (\sin\theta_D \sin\theta_A \cos\phi - 2\cos\theta_D \cos\theta_A)^2 \quad (2-49)$$

where θ_T is the angle between the emission transition dipole of the donor and the absorption transition dipole of the acceptor, θ_D and θ_A are the angles between these dipoles and the vector joining the donor and acceptor and ϕ is angle between the planes of the donor and acceptor (Figure 2.6b). κ^2 value can vary from 0 to 4. For collinear and parallel transition dipoles, $\kappa^2 = 4$; for parallel dipoles, $\kappa^2 = 1$; and for perpendicularly oriented dipoles, $\kappa^2 = 0$. For donor and acceptors that randomize by rotational diffusion prior to energy transfer, the magnitude of κ^2 is assumed to be $2/3$. However, in systems where there is a definite site of attachment of the donor and acceptor molecules, to get physically relevant results, the value of κ^2 has to be estimated from the angle between the donor emission and acceptor absorption dipoles [23]. $J(\lambda)$, the overlap integral, which expresses the degree of spectral overlap between the donor emission and the acceptor absorption, is given by,

$$J(\lambda) = \frac{\int_0^{\infty} F_D(\lambda) \epsilon_A(\lambda) \lambda^4 d\lambda}{\int_0^{\infty} F_D(\lambda) d\lambda} \quad (2-50)$$

where $F_D(\lambda)$ is the fluorescence intensity of the donor in the wavelength range of λ to $\lambda+d\lambda$ and is dimensionless. $\epsilon_A(\lambda)$ is the extinction coefficient (in $M^{-1}cm^{-1}$) of the acceptor at λ . If λ is in nm, then $J(\lambda)$ is in units of $M^{-1}cm^{-1}nm^4$.

Once the value of R_0 is known, the efficiency of energy transfer can be calculated. The efficiency of energy transfer (E) is the fraction of photons absorbed by the donor which are transferred to the acceptor and is defined as,

$$E = \frac{k_T(r)}{\tau_D^{-1} + k_T(r)} \quad (2-51)$$

$$\text{Or, } E = \frac{R_0^6}{r^6 + R_0^6} \quad (2-52)$$

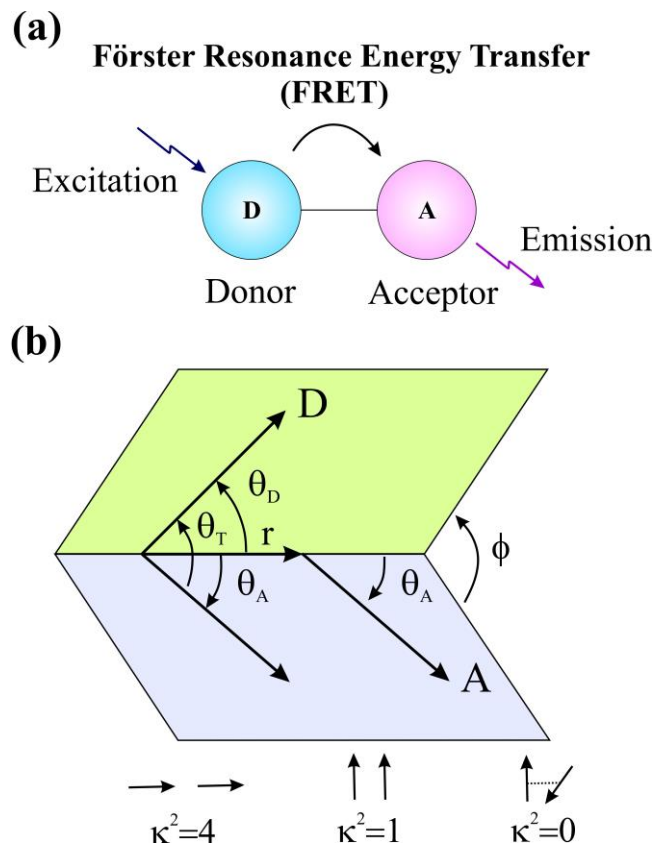


Figure 2.6. (a) Schematic illustration of the Förster resonance energy transfer (FRET) process. (b) Dependence of the orientation factor κ^2 on the directions of the emission and absorption dipoles of the donor and acceptor, respectively.

For D-A systems decaying with multiexponential lifetimes, E is calculated from the amplitude weighted lifetimes $\langle \tau \rangle = \sum_i \alpha_i \tau_i$ of the donor in absence (τ_D) and presence (τ_{DA}) of the acceptor as,

$$E = 1 - \frac{\tau_{DA}}{\tau_D} \quad (2-53)$$

The D-A distances can be measured using equations (2-52) and (2-53).

Distance distribution between donor and acceptor was estimated according to the procedure described in the literature [10, 24]. The observed fluorescence transients of the donor molecules in absence of acceptor were fitted using a nonlinear least-squares fitting procedure (software SCIENTIST) to the following function,

$$I_D(t) = \int_0^t E(t') p(t' - t) dt' \quad (2-54)$$

which comprises the convolution of the instrument response function (IRF) ($E(t)$) with exponential ($p(t) = \sum_i \alpha_{Di} \exp(-t/\tau_{Di})$). The convolution of the distance distribution function $P(r)$ in the fluorescence transients of donor in presence of acceptor in the system under studies is estimated using the same software (SCIENTIST) in the following way.

The intensity decay of D-A pair, spaced at a distance r , is given by

$$I_{DA}(r, t) = \sum_i \alpha_{Di} \exp \left[-\frac{t}{\tau_{Di}} - \frac{t}{\tau_{Di}} \left(\frac{R_0}{r} \right)^6 \right] \quad (2-55)$$

and the intensity decay of the sample considering $P(r)$ is given by

$$I_{DA}(t) = \int_{r=0}^{\infty} P(r) I_{DA}(r, t) dr \quad (2-56)$$

Where $P(r)$ consist of the following terms:

$$P(r) = \frac{1}{\sigma\sqrt{2\pi}} \exp \left[-\frac{1}{2} \left(\frac{\bar{r} - r}{\sigma} \right)^2 \right] \quad (2-57)$$

In this equation \bar{r} is the mean of the Gaussian with a standard deviation of σ . Usually distance distributions are described by the full width at half maxima (hw). This half width is given by $hw = 2.354\sigma$.

2.1.6. Photoinduced Electron Transfer (PET): Electron transfer (ET) reactions are of fundamental importance to both chemistry and biology and can be interpreted by the classical ET theory developed by Marcus [25]. In simple terms, an ET reaction involves the transfer of an electron from a ‘donor’ to an ‘acceptor’. ET reactions can occur both thermally and photochemically. The latter reactions are referred to as PET reactions. In PET reactions, absorption of light activates the donor or acceptor for ET. According to Rabinowich [26] “an electronically excited molecule has an increased tendency to give away an electron, as well as the capacity to replace the one which was removed from its normal level”. Absorption of a photon activates molecules to undergo redox reactions, the activation being equal to the excitation energy of the molecule. The photosynthetic reaction centre use this mode of molecular activation in order to convert solar energy to chemical energy via charge separation [27].

2.1.6.1. Theory: PET involves the use of visible or UV light to initiate electron transfer from a donor (D) to an acceptor (A) molecule. The first step of the reaction is the absorption of light by either a donor, the acceptor or a ground-state complex between the donor and acceptor, often referred to as a charge transfer complex. These possibilities are shown in equations (2-58) to (2-60).



The transferred electron, in principle, can get back to the donor, through a process known as back electron transfer (BET). BET regenerates the donor and acceptor molecules in their ground states and can be described as



The molecule, which gets excited by absorbing light, is referred to as the ‘sensitizer’ and the other molecule is referred to as the ‘quencher’. The excited state involved can be the singlet or the triplet state of the molecule.

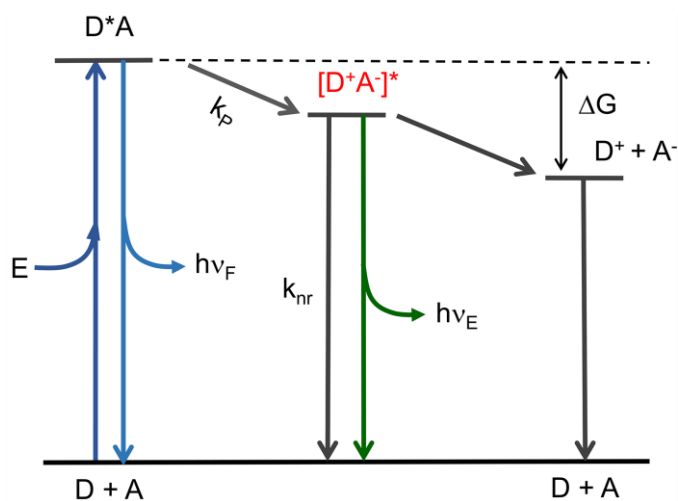


Figure 2.7. Energy diagram for photoinduced electron transfer (PET). The excited molecule is assumed to be the electron donor. ν_F and ν_E are emission from the fluorophore and exciplex, respectively.

The ET reaction described above proceeds in several discrete steps. For example, consider a general reaction taking place in solution, where the reactants are free to move around. The interaction between the excited acceptor and ground state donor or vice versa

creates a series of short-lived intermediates, each possessing a unique geometry and electronic distribution. The excited acceptor and ground state donor molecules diffuse towards each other by a series of one-dimensional random steps leading to the formation of an encounter complex. Further diffusion towards each other leads to the formation of a collision complex. In excited state ET reactions, a collision complex can be visualized as an ensemble consisting of the sensitizer and the quencher surrounded by several layers of solvent molecules. The sensitizer and the quencher are said to be contained within a solvent cage, at a centre-to-centre distance (d_{cc}) of $\sim 7 \text{ \AA}$. The lifetimes of these complexes are usually in the 10^{-9} to 10^{-10} s range. Electron transfer within the collision complex or encounter complex with a rate k_P , leads to the formation of contact ion pair (CIP) or exciplex (Figure 2.7). This complex may emit as an exciplex ($h\nu_E$) or be quenched and return to the ground state (Figure 2.7).

The important part of this process is the decrease in total energy of the charge transfer complex. The energy decreases because the ability to donate or accept electrons changes when a fluorophore is in the excited state. Excitation provides the energy to drive charge separation. D and A do not form a complex when both are in the ground state because this is energetically unfavorable. The energy released by electron transfer can also change if the ions become solvated and/or separated in a solvent with a high dielectric constant.

2.1.6.2. Experimental Methods: In order to study PET fluorescence decay transients of the donor molecule were taken in presence and absence of the quencher molecules. The observed decay transients were multiexponentially fitted by using the nonlinear least square fitting procedure (mentioned earlier) to determine the ultrafast time scale of the reaction. The apparent rate constants, k_{nr} , for the nonradiative processes were determined by comparing the lifetimes of donor in the absence (τ_0) and in the presence (τ) of the acceptor, using the relation

$$k_{nr} = 1/\langle\tau\rangle - 1/\langle\tau_0\rangle \quad (2-62)$$

2.1.7. Surface Enhanced Raman Scattering (SERS): Inelastic light scattering by a molecule with the quantized vibrational signature is the physical phenomenon behind Raman spectroscopy [28]. Despite the rich information offered by regular Raman

spectroscopy, it has not been the primary choice as a handy analytical tool comparable to Fourier-transform infrared (FTIR) or UV-Vis spectroscopy due to the inherent limitation, “feeble signal” [29]. The weak signal in Raman spectroscopy is due to the extremely small Raman scattering cross section for most molecules except some special cases of resonating molecular structures. For example, the benzene molecule, which is a relatively strong Raman scatterer, exhibits a scattering cross section of $2.8 \times 10^{-29} \text{ cm}^2 \text{ molecule}^{-1} \text{ sr}^{-1}$ (where ‘sr’ denotes squared radian) [30], which is 12-14 orders of magnitude lower than typical fluorescence cross sections.

The accidental discovery of SERS in 1974 led to major advancements in the field of spectroscopy. Fleischmann *et al.*, observed that the Raman signal from pyridine molecules adsorbed on a roughened silver electrode surfaces was 10^5 - 10^6 times stronger compared to the bulk pyridine. Martin Fleischman explained this phenomenon to be an

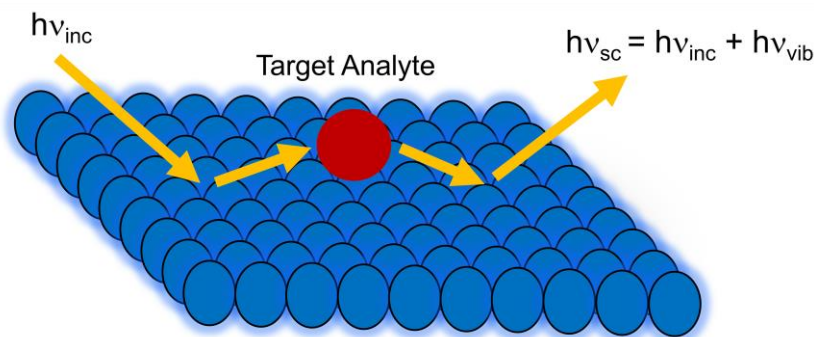


Figure 2.8. Electromagnetic enhancement of surface enhanced Raman scattering.

after-effect of the large number of scattering molecules present on the surface [31]. The discovery of SERS has opened a promising way to overcome the traditionally low sensitivity problem in Raman spectroscopy. SERS is utilized as a sensitive technique for chemical and bioanalytical sensing and imaging [32-35]. It is a breakthrough that the employment of surface enhancement has solved the low intensity problem of Raman scattering and made it possible to work as a more satisfying surface technique.

2.1.7.1. Mechanism of SERS: What mechanism causes the enhancement of Raman spectra of molecules located near a metal? This issue has recently been discussed in many theoretical and experimental works and reviews [29, 36, 37]. However, a clearer

understanding of this signal magnification came from the electromagnetic enhancement effect. The electromagnetic component of the enhancement results from an increased field at the metallic NP surface. The field enhancement involves the creation of a surface plasmon on the substrate surface, which transfers energy through an electric field to the target molecules allowing otherwise inaccessible vibrational structure to be determined (Figure 2.8) [38]. It has been observed that aggregates of metallic NPs generate very intense enhanced Raman signals at the junction between two NPs, called ‘hot spots’ [39-41]. Therefore, aggregates of metallic NPs i.e., metal NP clusters are great candidates for SERS substrates and an active area of research.

2.1.8. Excited State Proton Transfer (ESPT): The transfer of a proton from one group to another is a fundamental chemical reaction that occurs throughout chemistry and biology [42, 43]. In a typical ESPT reaction, $AH^+ + B \rightarrow A + BH^+$, where A and B denote different molecular species for intermolecular, or different sites of a single molecular species for intramolecular proton transfer process (Figure 2.9). Proton-transfer reactions are catalyzed by many enzymes [44, 45], while in respiratory complexes the coupling of proton and electron transfer results in movement of protons across a membrane and the establishment of a proton gradient that can then be used for the synthesis of ATP [46, 47]. The rate of proton transfer depends on many parameters like the energy required to bring the reactants together, the magnitude of the barrier that must be crossed (or potentially tunneled through) during the actual proton-transfer process, and the energy required to separate the products of the reaction [48]. Once the reactants are properly positioned, proton transfer ability is controlled by the factors that influence the nature of hydrogen-bonding interactions [49], such as the dielectric of the local environment, the distance between donor and acceptor groups, and their relative pK_a values. These factors can help reduce the barrier between donor and acceptor groups, as discussed on the role of low-barrier hydrogen bonds, for example, enzyme catalysis [50, 51].

ESPT reactions in solution provide useful models for proton transfer in general [52-54]. Owing to the light mass of the proton, the transfer process usually occurs on an ultrafast timescale. The development of short-pulse lasers has enabled the direct

measurement of ESPT reactions and made it possible to investigate their mechanisms in greater detail [55-57].

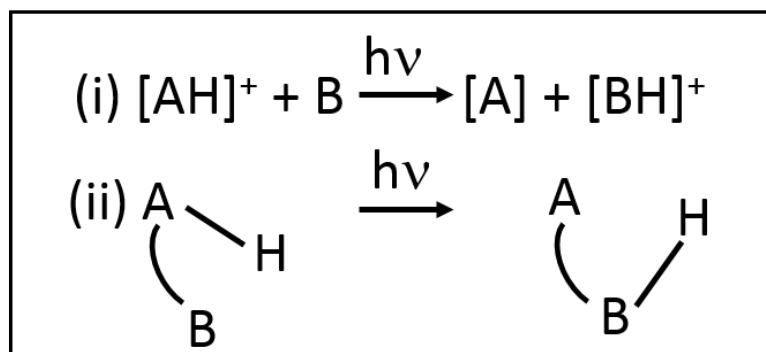


Figure 2.9. Schematic diagram showing (i) intermolecular and (ii) intramolecular proton transfer reaction.

2.1.9. In Vitro Drug Release Study: In the light of wide versatility of applications, controlled release profile of therapeutic drug is an obvious characteristics of drug delivery vehicles for the exploitation of the modern concept of therapeutic treatment that can maintain drug concentration in the blood or in targeted tissues at a desired value for a considerable period of time [58, 59] rendering a control on the drug release rate and duration [60]. For this purpose, in general, controlled release systems (CRS) initially releases the dose contained in parts so as to rapidly achieve at the drug effective therapeutic concentration. Such drug release kinetics follows a well-defined behavior in order to supply the maintenance dose enabling the attainment of the desired drug concentration. *In vitro* release was determined by the dialysis bag method [61]. To perform the study, 1-1.5 ml of the sample solution (like vesicle) containing the drug was taken in a dialysis bag and was tightly sealed. The sealed dialysis bag was then introduced into 40-50 ml of *in vitro* release buffer of proper pH. The whole system was then incubated at 37 °C under stirring condition at a constant speed. Aliquots of 2 ml were withdrawn from the release medium at selected time intervals for 24 hr and replaced with equal volume of fresh buffer to keep the release medium volume constant. The released amount of the drug in each aliquot was then determined from the absorbance value and the percentage released in the bulk was calculated as a function of incubation time. Control experiments were done

by taking only the drug solution in the dialysis bag against the release medium under identical experimental condition.

A typical profile of the first order exponential controlled release of the drug [62, 63] follows the relation,

$$Q = Q_0 - be^{-Kt} \quad (2-63)$$

where Q is the cumulative percent of drug released at time t, b is a constant and K is the rate constant of drug release.

The mechanism of drug release can be analyzed by a relationship proposed by Peppas et al. [64]:

$$\frac{M_t}{M} = kt^n \quad (2-64)$$

where M_t/M is the fraction of drug released at time t, k is a kinetic constant relative to the properties of the matrix and the drug (structural and geometric characteristics) and n is the diffusional exponent, which depends upon the release mechanism and geometry of the device. It has been shown that this relation can adequately describe the release of drugs or other solutes from slabs, cylinders and spheres, regardless of the release mechanism [64].

2.1.10. Phase Behaviour Study of Microemulsion (ME): A simple pseudoternary system with water, oil (an alkane), non-ionic surfactant and a cosurfactant can form a ME at appropriate conditions. In our study the pseudo-ternary phase diagrams were constructed to investigate the concentration ranges of components for identifying the existence of ME regions by water titration method, using oil (IPM), surfactant (Tween 80), cosurfactant (butyl lactate) and double distilled water at room temperature with constant surfactant/cosurfactant wt. ratio (1:1). IPM was mixed with Tween 80/butyl lactate mixture; water was then added drop wise (10 μ l) using micropipette until a transparent and homogeneous dispersion converts to turbid mixture. Appearance of turbidity was considered as an indication of phase separation. The ME regions were identified as optically transparent and isotropic mixtures. Pseudo-ternary phase diagrams of the system were also constructed at acidic pH (sodium citrate buffer, pH 2.6) and 0.9% NaCl solution.

2.1.11. Determination of the Distribution of Butyl Lactate between the Aqueous Phase and the Oil Phase: In one of our study distribution of butyl lactate between the aqueous phase and the oil phase was determined by measuring the emission spectra of DCM in different solutions of IPM-butyl lactate mixture [65]. With gradual addition of butyl lactate to IPM (oil) the emission peak of DCM undergoes red shift due to the increased polarity of the medium. A standard curve was plotted with X-axis being the volume of butyl lactate present in the mixture and Y-axis is the emission peak of DCM in the medium. To estimate the distribution of butyl lactate between the aqueous and oil phase a calculated amount of butyl lactate was added containing DCM to a 1:1 (2 ml each) mixture of IPM and water. Next the system was vortexed for 4 hour and then equilibrated whereupon it separated into oil and water phases distinctly. The oil phase was then extracted from the mixture and the emission peak of DCM was measured. Comparing this result with the standard curve the amount of butyl lactate distributed in IPM was quantified.

2.1.12. Molecular Modelling Study: For the molecular modeling studies we used commercially available ChemBio3D ultra (from CambridgeSoft™) software following the procedure reported earlier [66, 67]. The force field employed for these calculations is MM2 with default parameters provided with the software. Conjugate gradient methods were used to search for geometry-optimized structures with a convergence criterion of 0.0001 kcal Å⁻¹. The minimized energy structures of the various complexes as investigated in the present study were obtained by first geometry optimizing each component of the complex in vacuum. These geometry-optimized components were then brought together in a face to face orientation and to within Van der Waals radii and re-optimized. Relative binding energies were determined by subtracting the sum of the geometry-optimized energies of the isolated components from the total energy obtained for the geometry-optimized complex [68].

2.1.13. Quantum Yield Calculation: Quantum yield of the dye H258 in sodium bis(2-ethylhexyl) sulfosuccinate (AOT) vesicle was calculated according to the following equation using ethanol as a reference standard,

$$Q = Q_R \left(\frac{I}{I_R} \right) \left(\frac{OD_R}{OD} \right) \left(\frac{n^2}{n_R^2} \right) \quad (2-65)$$

where Q denotes quantum yield, OD is optical density at the excitation wavelength of 375 nm, I is the integrated fluorescence intensity and n is the refractive indices of H258 in respective solutions. Considering the Q_R of H258 in ethanol to be 0.50 [69], the Q of H258 in AOT vesicle was measured [70].

2.2. Systems:

2.2.1. Organized Assemblies (Biomimetics): Amphiphilic molecules, such as surfactants, aggregate to form various macromolecular assemblies. In our study organized assemblies like MEs, reversed MEs/RMs, vesicles, and RVs along with cyclic oligosaccharides like cyclodextrins have been used as the biomimicking confinement.

2.2.1.1. Microemulsions (MEs): MEs are isotropic and thermodynamically stable dispersed micro-heterogeneous systems composed of water, oil and amphiphile that brings down the water/oil interfacial tension (IFT), γ , to a very low value [71, 72]. There are

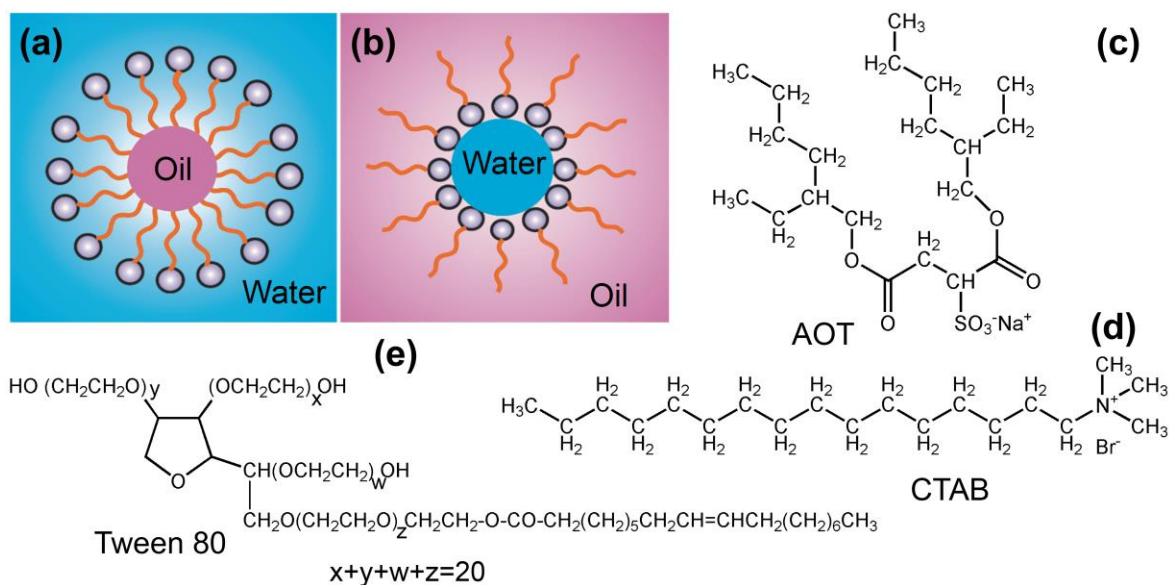


Figure 2.10. Schematic representation of the (a) oil-in-water (o/w) and (b) water-in-oil (w/o) microemulsion. Chemical structure of (c) Sodium bis(2-ethylhexyl) sulfosuccinate (AOT) (d) Hexadecyltrimethylammonium bromide (CTAB) and (e) Polyoxyethylenesorbitan monooleate (Tween 80).

two important parameters which describe the ability and effectiveness of a surfactant to form MEs, the spontaneous curvature H_0 and the flexibility of the surfactant film,

described by the bending moduli κ and $\bar{\kappa}$ (these values show how difficult it is to deform the amphiphilic film) [73, 74]. When H_0 is positive, the surfactant film is convex toward the water and promotes the formation of an oil-in-water (o/w) ME (Figure 2.10a). If H_0 is close to zero, then flat domains are formed (such as bicontinuous structures and lamellar liquid crystals). When H_0 is negative, the surfactant film is convex toward the oil, favoring water-in-oil (w/o) ME (Figure 2.10b). The value of H_0 is affected by the nature of the surfactant and the length of the alcohol chain [74]. Alcohols can modify the H_0 value when its penetration into the interface is important enough to increase interface flexibility (alcohol as cosurfactant), or it can change the polarity of polar and apolar phases (alcohol as cosolvent).

Surfactants, can also form reverse micelles (RMs) in organic media. RM is somewhat like w/o ME, where, amount of water present is significantly low that satisfies the hydration of the hydrophilic head group [71]. In fact the distinction between RM and w/o ME is not very sharp and also quite controversial. In this thesis we consider w/o ME and RM to be synonymous. RMs with water nanopools resemble the water pockets found in various bioaggregates such as proteins, membranes and mitochondria. Thus, RM systems are excellent biomimetics for exploration of biological membranes and biologically confined water molecules [75-77]. Aqueous RMs are generally characterized by the degree of hydration (w_0), which is the ratio of molar concentration of water to that of surfactant, where the radius of the water pool is proportional to the w_0 values. Shapes and sizes of the surfactant aggregates depend strongly on the type and concentration of the surfactant, and on the nature of counterion and external solvent. The AOT-alkane-water system is interesting as the solution is homogeneous and optically transparent over a wide range of temperature, pressure and pH. AOT is a double tailed anionic surfactant (Figure 2.10c for structure). The AOT-RM can compartmentalize a large amount of water in its central core, and the nanoscale aggregation process is fairly well-characterized with respect to size and shape at various water contents. The critical micelle concentration (CMC) of AOT in hydrocarbon solvent is about 0.1 mM [78]. In liquid alkanes, AOT-RMs ($w_0 = 0$) are completely associated and each micelle contains 23 monomers. The structures of these RMs are slightly asymmetric and are of round cylindrical nature. Spherical RMs are generally formed by surfactants with high values of the packing parameter, $\theta > 3$. AOT-

RMs can dissolve large amounts of water, being able to reach w_0 values as large as 40-60, depending on the surrounding non-polar organic medium and temperature [79]. In contrast to AOT which does not require any cosurfactant to form RMs, single tailed cationic surfactant like hexadecyltrimethylammonium bromide (CTAB) (Figure 2.10d for structure) do not form RMs in the absence of cosurfactant [80]. RMs based on the cationic surfactant CTAB have been extensively used as host for different enzymes [81]. These systems offer the possibility to compare the enzymatic activities performed in a cationic RM with those performed in the well-known systems AOT/hydrocarbon/water RMs [82]. Besides these ionic surfactants several nonionic surfactants can also form RM. Tween 80 (Figure 2.10e for structure) is a nonionic surfactant with excellent emulsifying and wetting properties. The Tween 80 molecule has a multi-headed structure, with four extended hydrophilic moieties, one of which has a tagged alkyl chain. It is an odorless and taste-less material, generally regarded as nontoxic and non-irritant, and hence is widely used as an emulsifier, solubiliser and a wetting agent in food, cosmetics, and in pharmaceutical applications [83].

2.2.1.2. Vesicle: Amphiphilic molecules, because of their solubility properties, aggregate into molecularly ordered structures, which often take the form of bilayers. When these bilayers curve and close, the resulting aggregates are called vesicles. The presence of a solvent inner reservoir (in most cases water) enclosed inside bilayers of amphiphiles, in turn comprised of a solvophobic (hydrophobic) middle shell and solvophilic (hydrophilic) layers on both sides, are the key morphological characteristics of a vesicular structure (Figure 2.11). This vesicle phase can consist of unilamellar vesicles (ULVs) or multilamellar vesicles (MLVs). When the Amphiphilic molecules in addition are phospholipids, the vesicles are known as liposomes. Formation of vesicles depends on a number of factors such as amphiphilicity, as well as generalized geometric parameters of the constituent amphiphiles [84]. It is important to keep in mind that all vesicular characteristics like overall size, membrane mechanical stability, bilayer width, fluidity and permeability, outer and inner layer functionalities and consequently the ability to encapsulate and release hydrophobic and hydrophilic molecules of interest are determined by the chemical characteristics of the constituting amphiphile and therefore can be tuned accordingly by

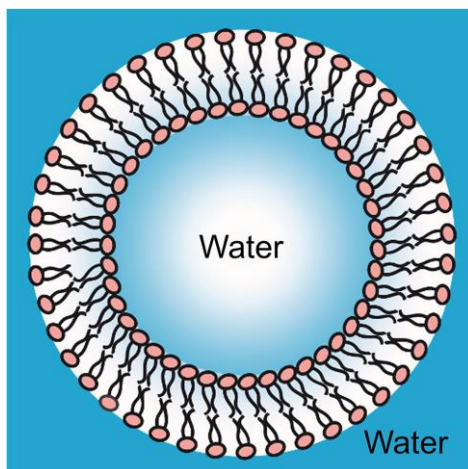


Figure 2.11. Schematic representation of a vesicle structure.

synthesis [85]. Bhattacharyya *et al.* [86, 87] demonstrated that the solvation dynamics in lipid vesicles is biexponential with one component of a few hundred picoseconds and another of several thousand picoseconds. The slow solvation dynamics clearly demonstrates that the motion of the water molecules is highly constrained in the vesicles and is similar to the water molecules present in the immediate vicinity of biomolecules also called “biological water” [5]. The similarities of vesicles with cellular membranes have made them model systems for investigating phenomena and behavioral characteristics found in biological systems [88, 89].

2.2.1.3. Reverse Vesicle (RV): Contrary to normal vesicles formed in water, the closed bimolecular layers can be also formed in nonpolar media. The self-organizing structure is named “reverse vesicles” [90-94]. (Figure 2.12). With a nonpolar organic solvent being the continuous medium, amphiphilic molecules in RVs self-assemble in an opposite way compared to their counterparts in water. That is, within the molecular bilayer the hydrophobic parts of the molecules stay outside while their hydrophilic parts are hidden inside the bilayer (Figure 2.12). As a unique type of reverse supramolecular self-assemblies, the study of RVs is of great fundamental interest. Also, RVs possess potential for a range of applications. For example, the highly restricted two-dimensional water channels within the molecular bilayers of RVs can trap guest molecules such as enzymes [95] and inorganic ions [96], making them ideal candidates for micro- or nano-reaction centers for biological tests and for synthesis of inorganic nanomaterials.

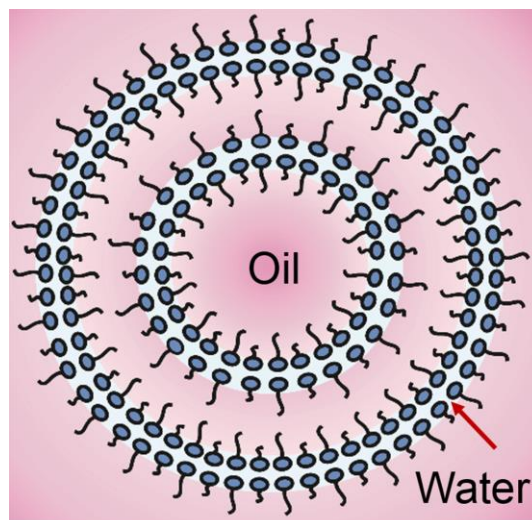


Figure 2.12. Schematic representation of a reverse vesicle structure.

2.2.1.4. Cyclodextrin (CyD): CyDs are molecular receptors of major importance in supramolecular chemistry [97]. They are cyclic nonreducing oligosaccharides composed of several glucopyranose units linked together via α -(1-4) glycoside bonds. CyD is obtained from the enzymatic activity of bacterial enzymes on starch molecules [97, 98]. The CyD members composed of 6, 7, and 8 glucopyranose units are called α -, β -, and γ -CyDs, respectively. As can be seen in Figure 2.13, the structure of this sugar in solution is truncated cone shaped with the hydroxyl groups on the outside and the ether like oxygen atoms in the inside [97]. The exterior polar groups allow CyD to dissolve in water while retaining a central nonpolar cavity. The cavity forms a hydrophobic matrix that enables CyDs to form inclusion complexes with hydrophobic guest molecules [97, 99] and thus they are specially well suited for practical applications in many industrial areas [100-102], in particular in food and pharmaceutical chemistry. Besides, there is a wide range of effects of CyDs on chemical properties of proteins such as aggregation suppression and protection against degradation or alteration of function [103, 104]. In fact depending on CyD and peptide, both stabilization and destabilization against proteolytic and chemical degradation might happen [105-109]. The hydrophobic core of CyD molecules interact with the hydrophobic residues in proteins. The main interaction mode has been shown to be the inclusion of aromatic side chains into the CyD cavity [105, 110]. Since CyDs interact

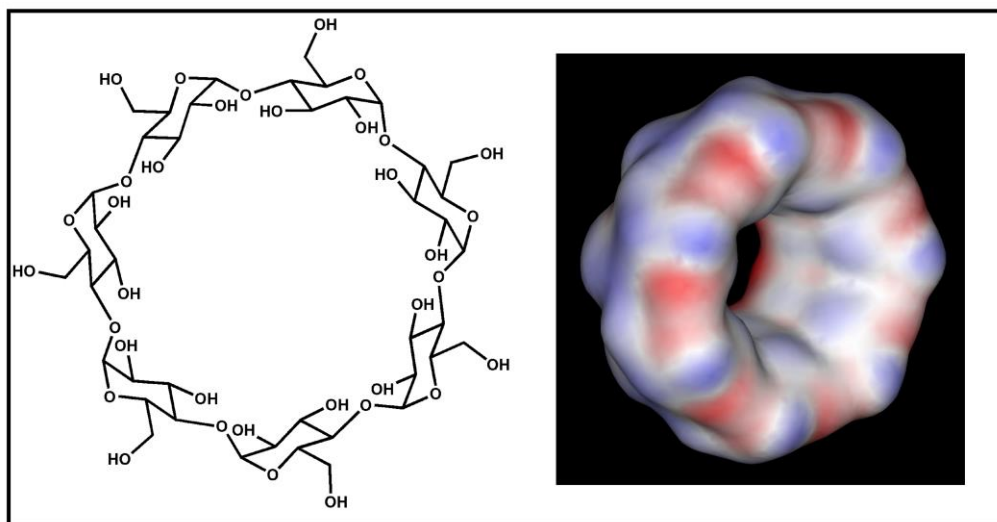


Figure 2.13. Schematic representation of a β -cyclodextrin molecule. The truncated cone structure is illustrated in the right part of the figure.

selectively with hydrophobic compounds of a size and shape matching their cavity to form inclusion complexes in aqueous media, they are considered simple biomimetic compounds [107, 111-114].

2.2.2. Proteins: Four types of model proteins; riboflavin binding proteins (RBP), enhanced green fluorescence proteins (EGFP), mEos2 and apomyoglobin (Apo-Mb) have been used in our studies.

2.2.2.1. Riboflavin Binding Protein (RBP): RBP is a monomeric globular protein extracted from chicken egg white having molecular weight of 30 kDa [115]. The molecule is a three-dimensional ellipsoid of dimensions $50 \times 40 \times 35 \text{ \AA}$ and comprises a single polypeptide chain of 219 amino acids, nine disulfide bridges, six α -helices, and four series of discontinuous areas of β structure [116, 117]. The primary function of RBP is to deliver riboflavin (Rf) to the developing embryo in mammals. The ligand-binding domain of RBP is a hydrophobic cleft, 20 \AA wide and 15 \AA deep. The binding of Rf occurs in the cleft with the isoalloxazine ring stacked between the parallel planes of tryptophan 156 (Trp156) and tyrosine 75 (Tyr75) (Figure 2.14) [117]. The isoalloxazine ring of flavins is amphipathic: the xylene portion is hydrophobic, and the pyrimidine moiety is hydrophilic. The X-ray structure reveals that the major interactions of the isoalloxazine ring with the protein are

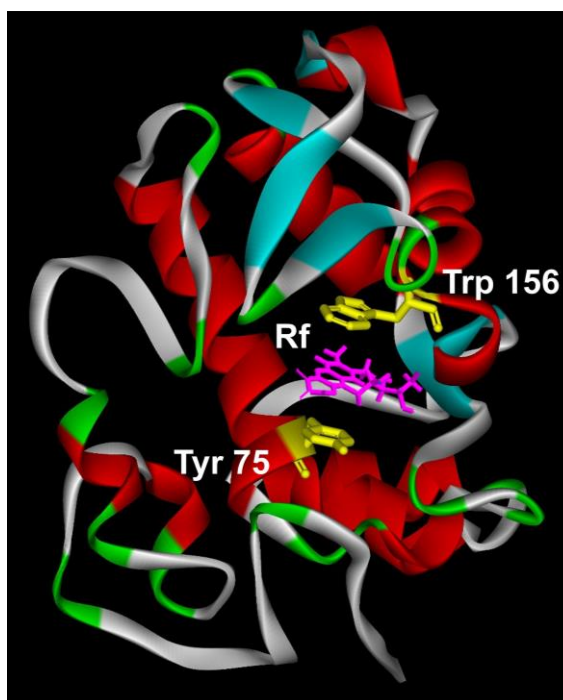


Figure 2.14. X-ray crystallographic structure of riboflavin binding protein (RBP) depicting the riboflavin binding domain. Structural data is obtained in personal communication with Prof. H. L. Monaco.

hydrophobic, and the xylene moiety is buried most deeply in the protein [117]. Complexation of Rf with RBP in buffer is found to quench both the fluorescence of Rf and Trp fluorescence of protein. The quenching of Trp fluorescence is both static and dynamic in nature [118]. However, the quenching of Rf upon binding with RBP is a consequence of ultrafast ET to the flavin chromophore (Rf) in the excited electronic state from nearby tryptophan or tyrosine residues present in RBP [116, 119-121].

2.2.2.2. Green Fluorescent Protein (GFP): GFP, a bioluminescent protein from the jellyfish *Aequorea victoria*, has revolutionized our ability to visualize the key molecular events that occur within living cells [122]. The protein is intensely fluorescent, with a quantum efficiency of approximately 80% [122]. The intrinsic fluorescence of the protein is due to a unique covalently attached chromophore, which is formed post-translationally within the protein upon cyclization and oxidation of residues Ser65-Tyr66-Gly67, leading to the formation of the p-hydroxybenzylidene-imidazolinone chromophore [122]. Enhanced green fluorescent protein (EGFP) is among the brightest and most photostable of

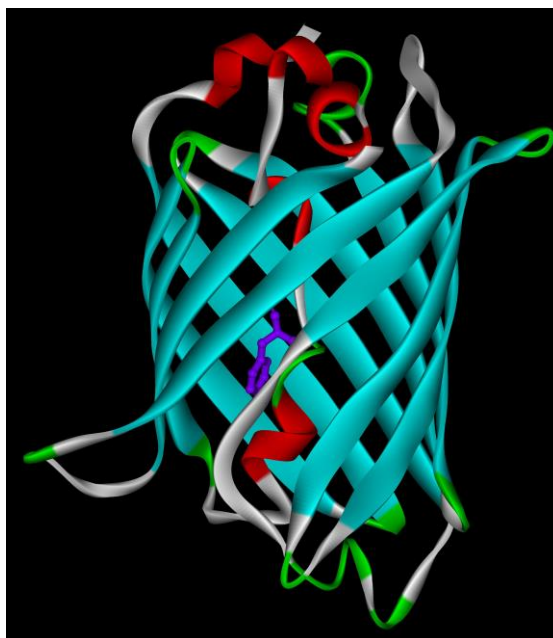


Figure 2.15. X-ray crystallographic structure (PDB code: 1EMA) of green fluorescent protein showing 11 β -strands forming a hollow cylinder through which is threaded a helix bearing the chromophore, shown in ball-and-stick (violet colored) representation.

the *Aequorea*-based fluorescent proteins which substitutes threonine for serine at position 65 (S65T) and phenylalanine for leucine at position 64 (F64L) in the amino acid sequence of the wild-type protein [123]. The GFP chromophore is protectively housed along a coaxial helix threaded through the center of an 11-stranded β -barrel consisting of 238 amino acids (Figure 2.15) [124, 125]. The chromophore is covalently anchored and effectively secluded from the aqueous solvent surrounding the protein [125]. Additionally, noncovalent coupling of the chromophore to the protein backbone is facilitated via an extended hydrogen-bonded network. Following photoexcitation this aromatic chromophore undergoes ESPT, producing a brightly fluorescent anion with green emission [56].

2.2.2.3. mEos2 Protein: Development in the field of super-resolution fluorescence microscopy techniques such as photoactivation localization microscopy (PALM) [126], stimulated emission depletion (STED) microscopy [127], and stochastic optical reconstruction microscopy (STORM) [128] spearheaded the search for brighter, more stable, and less phototoxic photoactivatable fluorescent proteins (PA-FPs) that can be photoconverted from one emission wavelength to another upon stimulation with an appropriate wavelength [129]. Among the most recently developed fluorescent proteins

displaying a photoswitchable behavior, McKinney *et al.* [130] reported an improvement in mEosFP, a green-to-red converter, called mEos2, which has overcome the temperature sensitivity of mEos. mEos2 alleviated the maturation problems of EosFP and has yielded the best localization precision achieved thus far for a PAFP (~10 nm in one dimension) [130]. mEos2 exhibits a well-defined tetramer structure (Figure 2.16). It consists of four classical β cans, which contact one another to form two types of interfaces [131]. Simultaneous mutations of I102N and Y189A completely removes the oligomerization tendency of mEos2 and enhances the brightness [131]. The green form of mEos2 arises via autocatalytic maturation in the dark, yielding a cis-coplanar two ring chromophore chemically identical to that found in GFP. Irradiation with near-UV light causes conversion of the green to the red emitting state [130]. The red chromophore in

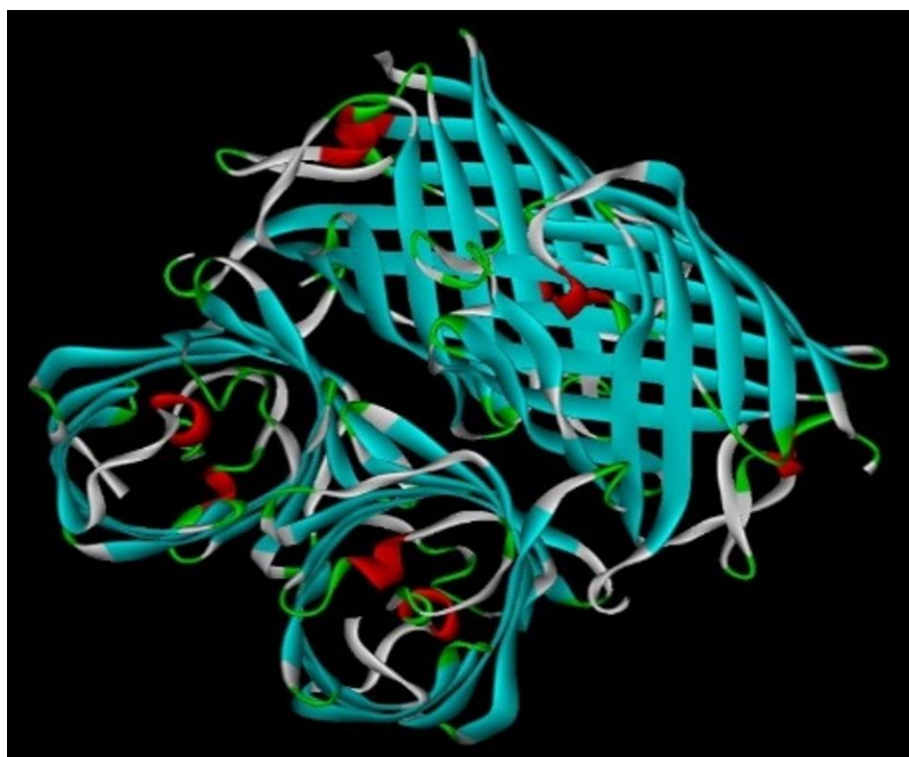


Figure 2.16. X-ray crystallographic structure (PDB code: 3S05) of the mEos2 protein.

mEos2, with excitation and emission maxima at 571 (with a vibronic sideband at 533 nm) and 580 nm (with a vibronic band at 630 nm), respectively, is generated by cleavage of a peptide backbone. The break occurs between His-62 $N\alpha$ - $C\alpha$ bond with concomitant

extension of the conjugated π electron system in the interior of the β -barrel without disruption of the tertiary structure [132].

2.2.2.4. Apomyoglobin Protein (Apo-Mb): Myoglobin, a member of the hemoprotein family, is a well-known protein which binds a protoporphyrin IX iron complex via noncovalent interactions [133, 134]. The essential role of myoglobin is storage of oxygen during periods of rest until required for oxidative phosphorylation. The X-ray crystallographic analysis indicates that myoglobin is a relatively compact globular protein, which consists of eight-helices and heme as a prosthetic group (Figure 2.17) [135, 136]. It has a total of 153 amino acids, two of which are intrinsic tryptophans (trp7 and trp14). The inside and outside surfaces of the protein are well defined [136]. The interior consists

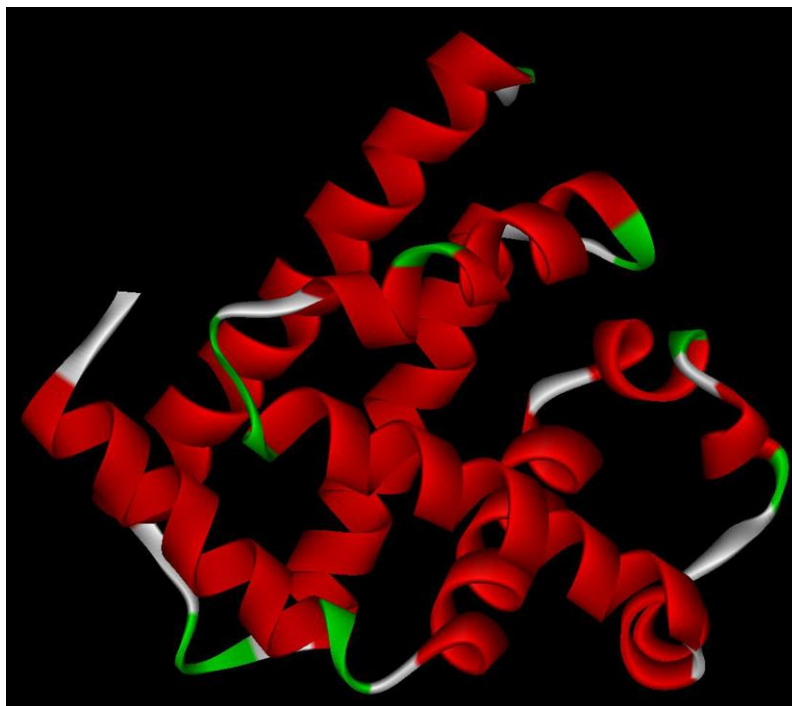


Figure 2.17. X-ray crystallographic structure (PDB code: 1MBN) of the apomyoglobin protein.

almost entirely of nonpolar residues including leucine, valine, methionine, and phenylalanine. Polar residues such as aspartate, glutamate, lysine, and arginine are absent from the interior protein surface. In fact, two histidines are the only polar residues which play an integral role in the binding of heme oxygen. The outside of the protein has both polar and nonpolar residues. The apo form of the protein is used in order to avoid a

multitude of problems associated with the heme prosthetic group, which is not covalently bound to the holoprotein.

2.2.3. Molecular Probes: In this section we will discuss about the different probe molecules that have been used in the course of study.

2.2.3.1. 4-(dicyanomethylene)-2-methyl-6-(p-dimethylaminostyryl)-4H-pyran (DCM):

The laser dye DCM (Figure 2.18A), is completely insoluble in water, and has selective binding affinity to micelle [137], RM [138] and vesicle [86] surfaces. The dye is completely hydrophobic (nonpolar) in the ground state. However, photoexcitation increases dipole moment of the probe making it polar and hence increases its hydrophilicity in the excited state. Thus photoexcited DCM molecule diffuses from the surfactant water interfaces (relatively nonpolar) towards more polar bulk water phase revealing a fluorescence emission signature (temporal line width) of the excursion through multiple environments in the excited state [139]. The molar extinction coefficient value of DCM in methanol is $42,000 \text{ M}^{-1} \text{ cm}^{-1}$ at 468.5 nm and the emission peak is at 630 nm [140].

2.2.3.2. p-Benzoquinone (BQ): BQ (Figure 2.18B) is a well-known probe for electron accepting and shuttling for any electron rich material/compound, which readily accepts electron and adapted to the resonance species hydroquinone [141]. Large doses could induce local irritation, clonic convulsions, decreased blood pressure and death due to paralysis of the medullary centres.

2.2.3.3. Tryptophan [(2S)-2-Amino-3-(1H-indol-3-yl) propanoic acid]: Tryptophan (Figure 2.18C) is one of the 22 standard amino acids and an essential amino acid in the human diet. Only the L-stereoisomer of tryptophan is found in enzymes and proteins. However, the D-stereoisomer is occasionally found in naturally produced peptides. Tryptophan has large bulky aromatic side chain. Tryptophan is significantly more polar than other aromatic amino acids, because of the nitrogen of the tryptophan indole ring. Tryptophan is rare amino acid and has a single codon. It absorbs light at 280 nm. The molar extinction coefficient value of tryptophan in water is $5,579 \text{ M}^{-1} \text{ cm}^{-1}$ at 278 nm. The

fluorescence emission peak of tryptophan dissolved in water is ~355 nm and the quantum yield of this molecule is 0.14 [142].

2.2.3.4. Rifampicin [3-[[4-Methyl-1-piperazinyl)-imino]-methyl]-rifamycin]:

Rifampicin (Figure 2.18D) is an antibiotic drug of the rifamycin group. Rifampicin is a first line anti-tuberculosis drug which is active against *Mycobacterium tuberculosis* as well as few other Mycobacterial species [143]. It can be used alone or in combination with other drugs like, isoniazid and pyrazinamide for the treatment of tuberculosis. It is a potent inhibitor for DNA dependent RNA synthesis from bacteria. Rifampicin absorbs light at 228 nm, 333 nm and 473 nm. Its solubility in water is 1.3 mg ml⁻¹ at pH 4.3. The molar extinction coefficient of Rifampicin at 473 nm is 15286 M⁻¹ cm⁻¹.

2.2.3.5. Riboflavin (Rf): Rf (Figure 2.18E) is well known as vitamin B₂. It is the central component of the cofactors FAD and FMN, and is therefore required by all flavo-proteins. As such, vitamin B₂ is required for a wide variety of cellular processes. It plays a key role in energy metabolism, and for the metabolism of fats, carbohydrates and proteins. Milk, cheese, leafy green vegetables, liver, kidneys, legumes, tomatoes, yeast and mushrooms are good source of Rf, but exposure to light destroys Rf. Rf is very important for the preservation of food in right light condition [144]. The photochemical reactions of Rf are well understood [145]. It has already been demonstrated that the intramolecular ET process is responsible for the photoreduction of the chromophore [146, 147]. It has been proposed that two photoproducts, Lumichrome and Lumiflavin are generated via an intermediate compound deuteroflavin during the photodeterioration of the Rf chromophore in presence of oxygen [147]. The role of proton transfer from the ribityl chain to the side nitrogen moiety for the generation of the photoproduct is also identified. In a recent study, it has been established that Rf is a potential photosensitizer and the activated triplet state in the molecule is concluded to be responsible for the photosensitization [148, 149]. It is to be noted that the photoproducts of Rf are also very hazardous for the biological activity as they degrade important amino acids including the tryptophan and tyrosin. Rf has two distinct absorption bands at 445 nm and 375 nm with extinction coefficient of 12200 M⁻¹ cm⁻¹ at 450 nm [118, 150]. The emission peak of Rf in buffer is 520 nm [120].

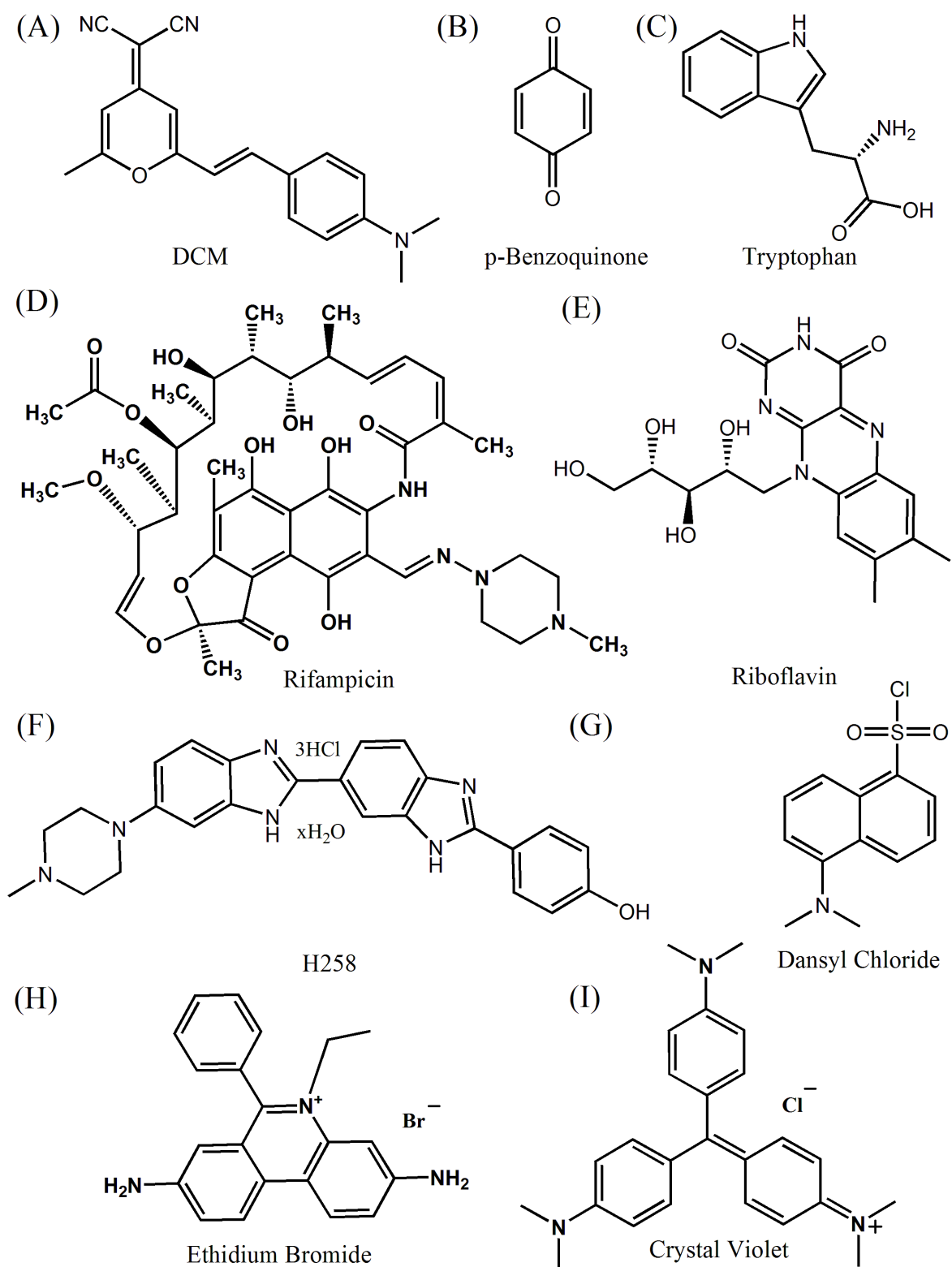


Figure 2.18. Molecular structure of (A) DCM, (B) p-Benzoquinone, (C) Tryptophan, (D) Rifampicin, (E) Riboflavin, (F) H258, (G) Dansyl Chloride, (H) Ethidium Bromide and (I) Crystal Violet.

2.2.3.6. [2'-(4-Hydroxyphenyl)-5-(4-methyl-1-piperazinyl)-2,5'-bi-1H-benzimidazole trihydrochloride hydrate], Hoechst 33258 (H258): The commercially available probe H258 (Figure 2.18F) is widely used as fluorescent cytological stain of DNA. Since it has affinity for the double stranded DNA. H258 is soluble in water. In bulk water the absorption peak and emission peaks of H258 are at 366 and 500 nm [151], respectively and it is sensitive to the polarity of the medium. The significant solvchromic effect (solvation) in the absorption and emission spectra of H258 makes the dye an attractive solvation probe for microenvironments [152].

2.2.3.7. Dansyl Chloride [5-(Dimethylamino)naphthalene-1-sulfonyl chloride]: Dansyl chloride (Figure 2.18G) is one of the widely used extrinsic fluorescent probes in biological labeling [153, 154]. The reactive free amino groups of amino acids (lysine and arginine) react with dansyl chloride in their deprotonated form as a nucleophile and fluoresce at green region of the visible spectrum. Protein-dansyl conjugates are sensitive to their immediate environment. This, in combination with their ability to accept energy (by FRET) from the amino acid tryptophan, allows this labeling technique to be used in investigating protein folding and dynamics [155].

2.2.3.8. Ethidium Bromide (EtBr): EtBr is a well-known fluorescent probe (Figure 2.18H) for DNA, which readily intercalates into the DNA double helix [156]. Compared to bulk water, the emission intensity and lifetime of EtBr increases significantly when EtBr intercalates into the double helix of DNA [157]. This remarkable fluorescence enhancement of EtBr is utilized to study the motion of DNA segments, and the interaction of DNA with surfactants and drug [158]. Absorption maxima of EtBr in aqueous solution are at 285 nm and 480 nm, after excitation EtBr emits orange light with wavelength maxima at 620 nm [159].

2.2.3.9. Crystal Violet (CV): CV is a triarylmethane dye (Figure 2.18I), used as a staining material. It can bind to the negatively charged phosphate backbone of DNA and negatively charged amino acids of proteins. It is highly soluble in water and other polar solvents. Its concentration is determined using extinction coefficient, $112,000 \text{ M}^{-1}\text{cm}^{-1}$ at 509 nm [160]. CV is a well-known probe for the detection of SERS enhancement [161].

References:

- [1] B. Bagchi, R. Biswas, Polar and nonpolar solvation dynamics, ion diffusion and vibrational relaxation: Role of biphasic solvent response in chemical dynamics, *Adv. Chem. Phys.* 109 (1999) 207.
- [2] G.R. Fleming, M. Cho, Chromophore-solvent dynamics, *Ann. Rev. Phys. Chem.* 47 (1996) 109.
- [3] B. Bagchi, Dynamics of solvation and charge transfer reactions in dipolar liquids, *Ann. Rev. Phys. Chem.* 40 (1989) 115.
- [4] R. Jimenez, G.R. Fleming, P.V. Kumar, M. Maroncelli, Femtosecond solvation dynamics of water, *Nature* 369 (1994) 471.
- [5] S.K. Pal, J. Peon, B. Bagchi, A.H. Zewail, Biological water: Femtosecond dynamics of macromolecular hydration, *J. Phys. Chem. B* 106 (2002) 12376.
- [6] L. Onsager, Comments on "effects of phase density on the ionization process and electron localization in fluids" by J. Jortner and A. Gathon, *Can. J. Chem.* 55 (1977) 1819.
- [7] R.M. Stratt, M. Maroncelli, Nonreactive dynamics in solution: The emerging molecular view of solvation dynamics and vibrational relaxation, *J. Phys. Chem.* 100 (1996) 12981.
- [8] J.T. Hynes, Outer-sphere electron transfer reactions and frequency-dependent friction, *J. Phys. Chem.* 90 (1986) 3701.
- [9] M.L. Horng, J.A. Gardecki, A. Papazyan, M. Maroncelli, Subpicosecond measurements of polar solvation dynamics: Coumarin 153 revisited, *J. Phys. Chem.* 99 (1995) 17311.
- [10] J.R. Lakowicz, Principles of fluorescence spectroscopy, 3rd ed., Springer, New York, 2006.
- [11] N. Periasamy, A.S.R. Koti, Time resolved fluorescence spectroscopy: TRES and TRANES, *Proc. Indian Natn. Sci. Acad.* 69A (2003) 41.
- [12] A.S.R. Koti, M.M.G. Krishna, N. Periasamy, Time-resolved area-normalized emission spectroscopy (TRANES): A novel method for confirming emission from two excited states, *J. Phys. Chem. A* 105 (2001) 1767.
- [13] R.D. Spencer, G. Weber, Measurements of subnanosecond fluorescence lifetimes with a cross-correlation phase fluorometer, *Ann. N. Y. Acad. Sci* 158 (1969) 361.

- [14] L. A. Philips, S. P. Webb, J. H. Clark, High-pressure studies of rotational reorientation dynamics: The role of dielectric friction, *J. Chem. Phys.* 83 (1985) 5810.
- [15] B. Kalman, N. Clarke, L. B. A. Johansson, Dynamics of a new fluorescent probe, 2,5,8,11-tetra-tert-butylperylene in solution, cubic lyotropic liquid crystals, and model membranes, *J. Phys. Chem.* 93 (1989) 4608.
- [16] N. Ito, O. Kajimoto, K. Hara, Picosecond time-resolved fluorescence depolarization of p-terphenyl at high pressures, *Chem. Phys. Lett.* 318 (2000) 118.
- [17] R. Zana, Microviscosity of aqueous surfactant micelles: Effect of various parameters, *J. Phys. Chem. B* 103 (1999) 9117.
- [18] B. Bagchi, Water dynamics in the hydration layer around proteins and micelles, *Chem. Rev.* 105 (2005) 3197.
- [19] P. Grigolini, M. Maestro, A two-state stochastic model for the dynamics of constrained water in reversed micelles, *Chem. Phys. Lett.* 127 (1986) 248.
- [20] N. Nandi, B. Bagchi, Dielectric relaxation of biological water, *J. Phys. Chem. B* 101 (1997) 10954.
- [21] L. Stryer, Fluorescence energy transfer as a spectroscopic ruler, *Ann. Rev. Biochem.* 47 (1978) 819.
- [22] P.K. Verma, S.K. Pal, Ultrafast resonance energy transfer in bio-molecular systems, *Eur. Phys. J. D* 60 (2010) 137.
- [23] D. Banerjee, S.K. Pal, Simultaneous binding of minor groove binder and intercalator to dodecamer DNA: Importance of relative orientation of donor and acceptor in FRET, *J. Phys. Chem. B* 111 (2007) 5047.
- [24] S. Batabyal, T. Mondol, S.K. Pal, Picosecond-resolved solvent reorganization and energy transfer in biological and model cavities, *Biochimie* 95 (2013) 1127.
- [25] R.A. Marcus, Electron-transfer reactions in chemistry-theory and experiment, *Rev. Mod. Phys.* 65 (1993) 599.
- [26] E.J. Rabinowitch, Photosynthesis and related processes, Interscience Publishers, Inc., New York, 1945.
- [27] G.J. Kavarnos, Fundamentals of photoinduced electron transfer, Wiley-VCH, New York, 1993.

- [28] C.V. Raman, K.S. Krishnan, Polarisation of scattered light-quanta, *Nature* 122 (1928) 169.
- [29] H. Ko, S. Singamaneni, V.V. Tsukruk, Nanostructured surfaces and assemblies as SERS media, *Small* 4 (2008) 1576.
- [30] V.V. Tsukruk, S. Singamaneni, Scanning probe microscopy of soft matter, Wiley-VCH Verlag GmbH & Co. KGaA, 2011.
- [31] M. Fleischmann, P.J. Hendra, A.J. McQuillan, Raman spectra of pyridine adsorbed at a silver electrode, *Chem. Phys. Lett.* 26 (1974) 163.
- [32] S.E.J. Bell, N.M.S. Sirimuthu, Surface-enhanced Raman spectroscopy (SERS) for sub-micromolar detection of DNA/RNA mononucleotides, *J. Am. Chem. Soc.* 128 (2006) 15580.
- [33] K. Kneipp, H. Kneipp, I. Itzkan, R.R. Dasari, M.S. Feld, Ultrasensitive chemical analysis by Raman spectroscopy, *Chem. Rev.* 99 (1999) 2957.
- [34] Y. Wang, J.L. Seebald, D.P. Szeto, J. Irudayaraj, Biocompatibility and biodistribution of surface-enhanced Raman scattering nanoprobe in Zebrafish embryos: *In vivo* and multiplex imaging, *ACS Nano* 4 (2010) 4039.
- [35] S. Schultz, D.R. Smith, J.J. Mock, D.A. Schultz, Single-target molecule detection with nonbleaching multicolor optical immunolabels, *Proc. Natl. Acad. Sci. U.S.A.* 97 (2000) 996.
- [36] A. Campion, P. Kambhampati, Surface-enhanced Raman scattering, *Chem. Soc. Rev.* 27 (1998) 241.
- [37] K. Kneipp, H. Kneipp, I. Itzkan, R.R. Dasari, M.S. Feld, Surface-enhanced Raman scattering and biophysics, *J. Phys.: Condens. Matter* 14 (2002) R597.
- [38] M. Moskovits, Surface roughness and the enhanced intensity of Raman scattering by molecules adsorbed on metals, *J. Chem. Phys.* 69 (1978) 4159.
- [39] U. Kreibig, M. Vollmer, Optical properties of metal clusters, Springer, Berlin, 1995.
- [40] D.-F. Zhang, Q. Zhang, L.-Y. Niu, L. Jiang, P.-G. Yin, L. Guo, Self-assembly of gold nanoparticles into chain-like structures and their optical properties, *J. Nanopart. Res.* 13 (2011) 3923.

- [41] M. Muniz-Miranda, C. Gellini, P.R. Salvi, M. Innocenti, M. Pagliai, V. Schettino, Fabrication of nanostructured silver substrates for surface-enhanced Raman spectroscopy, *J. Nanopart. Res.* 13 (2011) 5863.
- [42] R.P. Bell, *The proton in chemistry*, 2nd ed., Chapman and Hall, London, 1973.
- [43] J.T. Hynes, J.P. Klinman, H.-H. Limbach, R.L. Schowen, *Hydrogen transfer reactions*, Wiley-VCH Verlag GmbH & Co. KGaA, 2007.
- [44] J.P. Richard, T.L. Amyes, Proton transfer at carbon, *Curr. Opin. Chem. Biol.* 5 (2001) 626.
- [45] S.Y. Reece, J.M. Hodgkiss, J. Stubbe, D.G. Nocera, Proton-coupled electron transfer: The mechanistic underpinning for radical transport and catalysis in biology, *Philos. Trans. R. Soc. Lond. B Biol. Sci.* 361 (2006) 1351.
- [46] J.P. Hosler, S. Ferguson-Miller, D.A. Mills, Energy transduction: Proton transfer through the respiratory complexes, *Annu. Rev. Biochem.* 75 (2006) 165.
- [47] R.H. Fillingame, Coupling H⁺ transport and ATP synthesis in F1F0-ATP synthases: Glimpses of interacting parts in a dynamic molecular machine, *J. Exp. Biol.* 200 (1997) 217.
- [48] A.J. Kresge, What makes proton transfer fast, *Acc. Chem. Res.* 8 (1975) 354.
- [49] G. Jeffrey, *An introduction to hydrogen bonding*, Oxford University Press, New York, 1997.
- [50] W.W. Cleland, P.A. Frey, J.A. Gerlt, The low barrier hydrogen bond in enzymatic catalysis, *J. Biol. Chem.* 273 (1998) 25529.
- [51] S.-o. Shan, D. Herschlag, The change in hydrogen bond strength accompanying charge rearrangement: Implications for enzymatic catalysis, *Proc. Natl. Acad. Sci. U.S.A.* 93 (1996) 14474.
- [52] D. Stoner-Ma, A.A. Jaye, K.L. Ronayne, J. Nappa, S.R. Meech, P.J. Tonge, An alternate proton acceptor for excited-state proton transfer in green fluorescent protein: Rewiring GFP, *J. Am. Chem. Soc.* 130 (2008) 1227.
- [53] D. Huppert, P. Leiderman, M. Ben-Ziv, L. Genosar, L. Cohen, Excitation wavelength dependence of the proton-transfer reaction of the green fluorescent protein, *J. Phys. Chem. B* 109 (2005) 4241.

- [54] L.M. Tolbert, K.M. Solntsev, Excited-state proton transfer: From constrained systems to “super” photoacids to superfast proton transfer, *Acc. Chem. Res.* 35 (2001) 19.
- [55] M. Kondo, I.A. Heisler, D. Stoner-Ma, P.J. Tonge, S.R. Meech, Ultrafast dynamics of protein proton transfer on short hydrogen bond potential energy surfaces: S65T/H148D GFP, *J. Am. Chem. Soc.* 132 (2009) 1452.
- [56] M. Chattoraj, B.A. King, G.U. Bublitz, S.G. Boxer, Ultra-fast excited state dynamics in green fluorescent protein: Multiple states and proton transfer, *Proc. Natl. Acad. Sci. U.S.A.* 93 (1996) 8362.
- [57] S.P. Webb, L.A. Philips, S.W. Yeh, L.M. Tolbert, J.H. Clark, Picosecond kinetics of the excited-state, proton-transfer reaction of 1-naphthol in water, *J. Phys. Chem.* 90 (1986) 5154.
- [58] R.S. Langer, D.L. Wise, Medical applications of controlled release, applications and evaluation, CRC Press, Boca Raton, Florida, 1984.
- [59] M. Grassi, PhD Thesis, Department of Chemical Engineering (DICAMP), University of Trieste, VIII Ciclo, 1996.
- [60] J.R. Robinson, V.H.L. Lee, Controlled drug delivery, Marcel Dekker, Inc., New York, Basel, 1987.
- [61] J.A. Omotosho, T.L. Whateley, A.T. Florence, Methotrexate transport from the internal phase of multiple w/o/w emulsions, *J. Microencapsul.* 6 (1989) 183.
- [62] H. Dai, Q. Chen, H. Qin, Y. Guan, D. Shen, Y. Hua, Y. Tang, J. Xu, A temperature-responsive copolymer hydrogel in controlled drug delivery, *Macromolecules* 39 (2006) 6584.
- [63] L. Zhang, X. Sun, Z.-R. Zhang, An investigation on liver-targeting microemulsions of norcantharidin, *Drug Delivery* 12 (2005) 289.
- [64] P.L. Ritger, N.A. Peppas, A simple equation for description of solute release I. Fickian and non-fickian release from non-swellable devices in the form of slabs, spheres, cylinders or discs, *J. Controlled Release* 5 (1987) 23.
- [65] R. Saha, S. Rakshit, R.K. Mitra, S.K. Pal, Microstructure, morphology, and ultrafast dynamics of a novel edible microemulsion, *Langmuir* 28 (2012) 8309.

- [66] R.W. Larsen, R. Jasuja, R.K. Hetzler, P.T. Muraoka, V.G. Andrada, D.M. Jameson, Spectroscopic and molecular modeling studies of caffeine complexes with DNA intercalators, *Biophys. J.* 70 (1996) 443.
- [67] S. Banerjee, P. Verma, R. Mitra, G. Basu, S. Pal, Probing the interior of self-assembled caffeine dimer at various temperatures, *J. Fluoresc.* 22 (2012) 753.
- [68] R. Saha, S. Rakshit, S.K. Pal, Molecular recognition of a model globular protein apomyoglobin by synthetic receptor cyclodextrin: Effect of fluorescence modification of the protein and cavity size of the receptor in the interaction *J. Mol. Recognit.* 26 (2013) 568.
- [69] H. Gorner, Direct and sensitized photoprocesses of bis-benzimidazole dyes and the effect of surfactant and DNA, *Photochem. Photobiol.* 73 (2001) 339.
- [70] R. Saha, P.K. Verma, R.K. Mitra, S.K. Pal, Structural and dynamical characterization of unilamellar AOT vesicles in aqueous solutions and their efficacy as potential drug delivery vehicle, *Colloids Surf., B* 88 (2011) 345.
- [71] M. Fanun, *Microemulsions: Properties and applications*, CRC Press, Boca Raton, Florida, 2009.
- [72] M. Shevachman, A. Shani, N. Garti, Formation and investigation of microemulsions based on jojoba oil and nonionic surfactants, *J. Am. Oil Chem. Soc.* 81 (2004) 1143.
- [73] R. Strey, Microemulsion microstructure and interfacial curvature, *Colloid Polym. Sci.* 272 (1994) 1005.
- [74] M. Gradzielski, Effect of the cosurfactant structure on the bending elasticity in nonionic oil-in-water microemulsions, *Langmuir* 14 (1998) 6037.
- [75] K. Bhattacharyya, Solvation dynamics and proton transfer in supramolecular assemblies, *Acc. Chem. Res.* 36 (2003) 95.
- [76] B. Cohen, D. Huppert, K.M. Kyril M. Solntsev, Y. Tsfadia, E. Nachliel, M. Gutman, Excited state proton transfer in reverse micelles, *J. Am. Chem. Soc.* 124 (2002) 7539.
- [77] W.D. Van Horn, M.E. Ogilvie, P.F. Flynn, Reverse micelle encapsulation as a model for intracellular crowding, *J. Am. Chem. Soc.* 131 (2009) 8030.

- [78] Y.-C. Jean, H.J. Ache, Determination of critical micelle concentrations in micellar and reversed micellar systems by positron annihilation techniques, *J. Am. Chem. Soc.* 100 (1978) 984.
- [79] T.K. Jain, M. Varshney, A. Maitra, Structural studies of Aerosol OT reverse micellar aggregates by FT-IR spectroscopy, *J. Phys. Chem.* 93 (1989) 7409.
- [80] P.K. Das, A. Chaudhuri, S. Saha, A. Samanta, First simultaneous estimates of the water pool core size and the interfacial thickness of a cationic water-in-oil microemulsion by combined use of chemical trapping and time-resolved fluorescence quenching, *Langmuir* 15 (1999) 4765.
- [81] R. Hilhorst, C. Laane, C. Veeger, Enzymatic conversion of apolar compounds in organic media using an NADH-regenerating system and dihydrogen as reductant, *FEBS Lett.* 159 (1983) 225.
- [82] Y.L. Khmeinitzky, A.V. Kabanov, N.L. Klyachko, A.V. Levashov, K. Martinek, Structure and reactivity in reverse micelles, M.P. Pileni (Ed.), Elsevier, Amsterdam, 1989.
- [83] R.C. Rowe, P.J. Sheskey, A.J. Owen, Handbook of pharmaceutical excipients, American Pharmaceutical Association, London, UK, 2005.
- [84] K. Edwards, M. Almgren, Surfactant-induced leakage and structural change of lecithin vesicles: Effect of surfactant headgroup size, *Langmuir* 8 (1992) 824.
- [85] S. Pispas, Vesicular structures in mixed block copolymer/surfactant solutions, *Soft Matter* 7 (2011) 8697.
- [86] S.K. Pal, D. Sukul, D. Mandal, K. Bhattacharyya, Solvation dynamics of DCM in lipid, *J. Phys. Chem. B* 104 (2000) 4529.
- [87] A. Datta, S.K. Pal, D. Mandal, K. Bhattacharyya, Solvation dynamics of coumarin 480 in vesicles, *J. Phys. Chem. B* 102 (1998) 6114.
- [88] M. Antonietti, S. Förster, Vesicles and liposomes: A self-assembly principle beyond lipids, *Adv. Mater.* 15 (2003) 1323.
- [89] F.E. Antunes, E.F. Marques, M.G. Miguel, B. Lindman, Polymer-vesicle association, *Adv. Colloid Interface Sci.* 147-148 (2009) 18.
- [90] S.-H. Tung, H.-Y. Lee, S.R. Raghavan, A facile route for creating “reverse” vesicles: Insights into “reverse” self-assembly in organic liquids, *J. Am. Chem. Soc.* 130 (2008) 8813.

- [91] H. Kunieda, K. Nakamura, U. Olsson, B. Lindman, Spontaneous formation of reverse vesicles, *J. Phys. Chem.* 97 (1993) 9525.
- [92] H. Li, X. Xin, T. Kalwarczyk, E. Kalwarczyk, P. Niton, R. Hołyst, J. Hao, Reverse vesicles from a salt-free cationic surfactant system: A confocal fluorescence microscopy study, *Langmuir* 26 (2010) 15210.
- [93] S. Rangelov, M. Almgren, K. Edwards, C. Tsvetanov, Formation of normal and reverse bilayer structures by self-assembly of nonionic block copolymers bearing lipid-mimetic units, *J. Phys. Chem. B* 108 (2004) 7542.
- [94] X.-N. Xu, L. Wang, Z.-T. Li, Reverse vesicles formed by hydrogen bonded arylamide-derived triammonium cyclophanes and hexaammonium capsule, *Chem. Commun.* (2009) 6634.
- [95] A. Sánchez-Ferrer, F. Garcia-Carmona, Reverse vesicles as a new system for studying enzymes in organic solvents, *Biochem. J.* 285 (1992) 373.
- [96] H. Li, J. Hao, Z. Wu, Phase behavior and properties of reverse vesicles in salt-free cationic surfactant mixtures, *J. Phys. Chem. B* 112 (2008) 3705.
- [97] J. Szejtli, Introduction and general overview of cyclodextrin chemistry, *Chem. Rev.* 98 (1998) 1743.
- [98] B.A. van der Veen, J.C.M. Uitdehaag, B.W. Dijkstra, L. Dijkhuizen, Engineering of cyclodextrin glycosyltransferase reaction and product specificity, *Biochim. Biophys. Acta* 1543 (2000) 336.
- [99] W. Saenger, Cyclodextrin inclusion compounds in research and industry, *Angew. Chem., Int. Ed.* 19 (1980) 344.
- [100] A.R. Hedges, Industrial applications of cyclodextrins, *Chem. Rev.* 98 (1998) 2035.
- [101] I.T. Horváth, P.T. Anastas, Innovations and green chemistry, *Chem. Rev.* 107 (2007) 2169.
- [102] J. Szejtli, Utilization of cyclodextrins in industrial products and processes, *J. Mater. Chem.* 7 (1997) 575.
- [103] M. Khajepour, T. Troxler, V. Nanda, J.M. Vanderkooi, Melittin as model system for probing interactions between proteins and cyclodextrins, *Proteins: Struct., Funct., Bioinf.* 55 (2004) 275.

- [104] X.-r. Qin, H. Abe, H. Nakanishi, NMR and CD studies on the interaction of Alzheimer β -amyloid peptide (12–28) with β -cyclodextrin, *Biochem. Biophys. Res. Commun.* 297 (2002) 1011.
- [105] F.L. Aachmann, D.E. Otzen, K.L. Larsen, R. Wimmer, Structural background of cyclodextrin–protein interactions, *Protein Eng.* 16 (2003) 905.
- [106] A. Cooper, Effect of cyclodextrins on the thermal stability of globular proteins, *J. Am. Chem. Soc.* 114 (1992) 9208.
- [107] R. Breslow, S.D. Dong, Biomimetic reactions catalyzed by cyclodextrins and their derivatives, *Chem. Rev.* 98 (1998) 1997.
- [108] J. Horský, J. Pitha, Inclusion complexes of proteins: Interaction of cyclodextrins with peptides containing aromatic amino acids studied by competitive spectrophotometry, *J. Inclusion Phenom. Macrocyclic Chem.* 18 (1994) 291.
- [109] V. Yeguas, M. Altarsha, G. Monard, R. López, M.F. Ruiz-López, Peptide binding to β -cyclodextrins: Structure, dynamics, energetics, and electronic effects, *J. Phys. Chem. A* 115 (2011) 11810.
- [110] K. Matsubara, Y. Ando, T. Irie, K. Uekama, Protection afforded by maltosyl- β -cyclodextrin against α -chymotrypsin-catalyzed hydrolysis of a luteinizing hormone-releasing hormone agonist, buserelin acetate, *Pharm. Res.* 14 (1997) 1401.
- [111] J. Szejtli, Cyclodextrins and their inclusion complexes, Akademiai Kiado, Budapest (Hungary), 1982.
- [112] W. Oi, M. Isobe, A. Hashidzume, A. Harada, Macromolecular recognition: Discrimination between human and bovine serum albumins by cyclodextrins, *Macromol. Rapid Commun.* 32 (2011) 501.
- [113] A. Harada, Large ring molecules, Wiley & Sons, Chichester, U.K., 1996.
- [114] A. Hashidzume, A. Harada, Recognition of polymer side chains by cyclodextrins, *Polym. Chem.* 2 (2011) 2146.
- [115] J. Becvar, G. Palmer, The binding of flavin derivatives to the riboflavin-binding protein of egg white. A kinetic and thermodynamic study, *J. Biol. Chem.* 257 (1982) 5607.
- [116] D. Zhong, A.H. Zewail, Femtosecond dynamics of flavoproteins: Charge separation and recombination in riboflavine (vitamin B₂)-binding protein and in glucose oxidase enzyme, *Proc. Natl. Acad. Sci. U.S.A.* 98 (2001) 11867.

- [117] H.L. Monaco, Crystal structure of chicken riboflavin-binding protein, *Embo J.* 16 (1997) 1475.
- [118] R. Saha, S. Rakshit, P.K. Verma, R.K. Mitra, S.K. Pal, Protein-cofactor binding and ultrafast electron transfer in riboflavin binding protein under the spatial confinement of nanoscopic reverse micelles, *J. Mol. Recognit.* 26 (2013) 59.
- [119] N. Mataga, H. Chosrowjan, Y. Shibata, F. Tanaka, Y. Nishina, K. Shiga, Dynamics and mechanisms of ultrafast fluorescence quenching reactions of flavin chromophores in protein nanospace, *J. Phys. Chem. B* 104 (2000) 10667.
- [120] S. Rakshit, R. Saha, P.K. Verma, R.K. Mitra, S.K. Pal, Ultrafast electron transfer in riboflavin binding protein in macromolecular crowding of nano-sized micelle, *Biochimie* 94 (2012) 2673.
- [121] A. Lukacs, R.-K. Zhao, A. Haigney, R. Brust, G.M. Greetham, M. Towrie, P.J. Tonge, S.R. Meech, Excited state structure and dynamics of the neutral and anionic flavin radical revealed by ultrafast transient mid-IR to visible spectroscopy, *J. Phys. Chem. B* 116 (2012) 5810.
- [122] R.Y. Tsien, The green fluorescent protein, *Annu. Rev. Biochem* 67 (1998) 509.
- [123] G.H. Patterson, S.M. Knobel, W.D. Sharif, S.R. Kain, D.W. Piston, Use of the green fluorescent protein and its mutants in quantitative fluorescence microscopy, *Biophys. J.* 73 (1997) 2782.
- [124] A.B. Cubitt, R. Heim, S.R. Adams, A.E. Boyd, L.A. Gross, R.Y. Tsien, Understanding, improving and using green fluorescent proteins, *Trends Biochem. Sci.* 20 (1995) 448.
- [125] M. Ormö, A.B. Cubitt, K. Kallio, L.A. Gross, R.Y. Tsien, S.J. Remington, Crystal structure of the *Aequorea victoria* green fluorescent protein, *Science* 273 (1996) 1392.
- [126] E. Betzig, G.H. Patterson, R. Sougrat, O.W. Lindwasser, S. Olenych, J.S. Bonifacino, M.W. Davidson, J. Lippincott-Schwartz, H.F. Hess, Imaging intracellular fluorescent proteins at nanometer resolution, *Science* 313 (2006) 1642.
- [127] K.I. Willig, R.R. Kellner, R. Medda, B. Hein, S. Jakobs, S.W. Hell, Nanoscale resolution in GFP-based microscopy, *Nat. Methods* 3 (2006) 721.
- [128] M.J. Rust, M. Bates, X. Zhuang, Sub-diffraction-limit imaging by stochastic optical reconstruction microscopy (STORM), *Nat. Methods* 3 (2006) 793.

- [129] P. Annibale, M. Scarselli, A. Kodiyan, A. Radenovic, Photoactivatable fluorescent protein mEos2 displays repeated photoactivation after a long-lived dark state in the red photoconverted form, *J. Phys. Chem. Lett.* 1 (2010) 1506.
- [130] S.A. McKinney, C.S. Murphy, K.L. Hazelwood, M.W. Davidson, L.L. Looger, A bright and photostable photoconvertible fluorescent protein, *Nat. Methods* 6 (2009) 131.
- [131] M. Zhang, H. Chang, Y. Zhang, J. Yu, L. Wu, W. Ji, J. Chen, B. Liu, J. Lu, Y. Liu, J. Zhang, P. Xu, T. Xu, Rational design of true monomeric and bright photoactivatable fluorescent proteins, *Nat. Methods* 9 (2012) 727.
- [132] H. Mizuno, T.K. Mal, K.I. Tong, R. Ando, T. Furuta, M. Ikura, A. Miyawaki, Photo-induced peptide cleavage in the green-to-red conversion of a fluorescent protein, *Mol. Cell* 12 (2003) 1051.
- [133] E. Antonini, M. Brunori, Hemoglobin and myoglobin in their reactions with ligands, North-Holland Pub. Co., 1971.
- [134] T. Hayashi, Y. Hisaeda, New functionalization of myoglobin by chemical modification of heme-propionates, *Acc. Chem. Res.* 35 (2001) 35.
- [135] J.C. Kendrew, H.C. Watson, B.E. Strandberg, R.E. Dickerson, D.C. Phillips, V.C. Shore, A partial determination by X-ray methods, and its correlation with chemical data, *Nature* 190 (1961) 666.
- [136] T. Takano, Structure of myoglobin refined at 2.0 Å resolution. I. Crystallographic refinement of metmyoglobin from sperm whale, *J. Mol. Biol.* 110 (1977) 537.
- [137] S.K. Pal, D. Sukul, D. Mandal, S. Sen, K. Bhattacharyya, Solvation dynamics of DCM in micelles, *Chem. Phys. Lett.* 327 (2000) 91.
- [138] S.K. Pal, D. Mandal, D. Sukul, K. Bhattacharyya, Solvation dynamics of 4-(dicyanomethylene)-2-methyl-6-(p-dimethylaminostyryl)-4H-pyran (DCM) in a microemulsion, *Chem. Phys. Lett.* 312 (1999) 178.
- [139] R. Sarkar, A.K. Shaw, M. Ghosh, S.K. Pal, Ultrafast photoinduced deligation and ligation dynamics: DCM in micelle and micelle-enzyme complex, *J. Photochem. Photobiol., B* 83 (2006) 213.
- [140] M. Meyer, J.C. Mialocq, B. Perly, Photoinduced intramolecular charge transfer and trans-cis isomerization of the DCM styrene dye: Picosecond and nanosecond laser

spectroscopy, high-performance liquid chromatography, and nuclear magnetic resonance studies, *J. Phys. Chem.* 94 (1990) 98.

[141] C. Burda, T.C. Green, S. Link, M.A. El-Sayed, Electron shuttling across the interface of CdSe nanoparticles monitored by femtosecond laser spectroscopy, *J. Phys. Chem. B* 103 (1999) 1783.

[142] P.G. Wu, L. Brand, Resonance energy transfer: Methods and applications, *Anal. Biochem.* 218 (1994) 1.

[143] J.W. Long, Essential guide to prescription drugs 1992, HarperCollins Publishers, New York, 1991.

[144] O.W. Parks, C. Allen, Photodegradation of riboflavin to lumichrome in milk exposed to sunlight, *J. Dairy Sci.* 60 (1977) 1038.

[145] W.J. Nickerson, G. Strauss, The photochemical cleavage of water by riboflavin, *J. Am. Chem. Soc.* 82 (1960) 5007.

[146] W.M. Moore, J.T. Spence, F.A. Raymond, S.D. Colson, Photochemistry of riboflavin. I. The hydrogen transfer process in the anaerobic photobleaching of flavins, *J. Am. Chem. Soc.* 85 (1963) 3367.

[147] B. Holmström, G. Oster, Riboflavin as an electron donor in photochemical reactions, *J. Am. Chem. Soc.* 83 (1961) 1867.

[148] M. Halwer, The photochemistry of riboflavin and related compounds, *J. Am. Chem. Soc.* 73 (1951) 4870.

[149] E. Silva, Biological implications of aerobically obtained riboflavin-sensitized photoproducts of tryptophan, *J. Photochem. Photobiol., B* 14 (1992) 142.

[150] M.G. Duyvis, R. Hilhorst, C. Laane, D.J. Evans, D.J.M. Schmedding, Role of riboflavin in beer flavor instability: Determination of levels of riboflavin and its origin in beer by fluorometric apoprotein titration, *J. Agric. Food Chem.* 50 (2002) 1548.

[151] R. Saha, S. Rakshit, D. Majumdar, A. Singha, R. Mitra, S. Pal, Nanostructure, solvation dynamics, and nanotemplating of plasmonically active SERS substrate in reverse vesicles, *J. Nanopart. Res.* 15 (2013) 1576.

[152] D. Banerjee, S.S. Sinha, S.K. Pal, Interplay between hydration and electrostatic attraction in ligand binding: Direct observation of hydration barrier at reverse micellar interface, *J. Phys. Chem. B* 111 (2007) 14239.

- [153] D. Zhong, S.K. Pal, A.H. Zewail, Femtosecond studies of protein-DNA binding and dynamics: Histone I, *ChemPhysChem* 2 (2001) 219.
- [154] S.K. Pal, J. Peon, A.H. Zewail, Biological water at the protein surface: Dynamical solvation probed directly with femtosecond resolution, *Proc. Natl. Acad. Sci. U.S.A.* 99 (2002) 1763.
- [155] T. Mondol, S. Batabyal, A. Mazumder, S. Roy, S.K. Pal, Recognition of different DNA sequences by a DNA-binding protein alters protein dynamics differentially, *FEBS Lett.* 586 (2012) 258.
- [156] D.P. Millar, R.J. Robbins, A.H. Zewail, Torsion and bending of nucleic acids studied by subnanosecond time-resolved fluorescence depolarization of intercalated dyes, *J. Chem. Phys.* 76 (1982) 2080.
- [157] J. Olmsted, D.R. Kearns, Mechanism of ethidium bromide fluorescence enhancement on binding to nucleic acids, *Biochemistry* 16 (1977) 3647.
- [158] R. Sarkar, S.K. Pal, Ligand-DNA interaction in a nanocage of reverse micelle, *Biopolymers* 83 (2006) 675.
- [159] S.K. Pal, D. Mandal, K. Bhattacharyya, Photophysical processes of ethidium bromide in micelles and reverse micelles, *J. Phys. Chem. B* 102 (1998) 11017.
- [160] H. Langhals, Color chemistry. Synthesis, properties and applications of organic dyes and pigments. 3rd revised edition. By Heinrich Zollinger, *Angew. Chem. Int. Ed.* 43 (2004) 5291.
- [161] M.V. Cañamares, C. Chenal, R.L. Birke, J.R. Lombardi, DFT, SERS, and single-molecule SERS of crystal violet, *J. Phys. Chem. C* 112 (2008) 20295.

Chapter 3

Instrumentation and Sample Preparation

In this chapter the details of instrumental setup and sample preparation techniques used in our studies have been described.

3.1. Instrumental Setups:

3.1.1. Steady-state UV-Vis Absorption and Emission Measurement: Steady-state UV-Vis absorption and emission spectra of the probe molecules were measured with Shimadzu UV-2450 spectrophotometer and Jobin Yvon Fluoromax-3 fluorimeter, respectively. Schematic ray diagrams of these two instruments are shown in Figures 3.1 and 3.2.

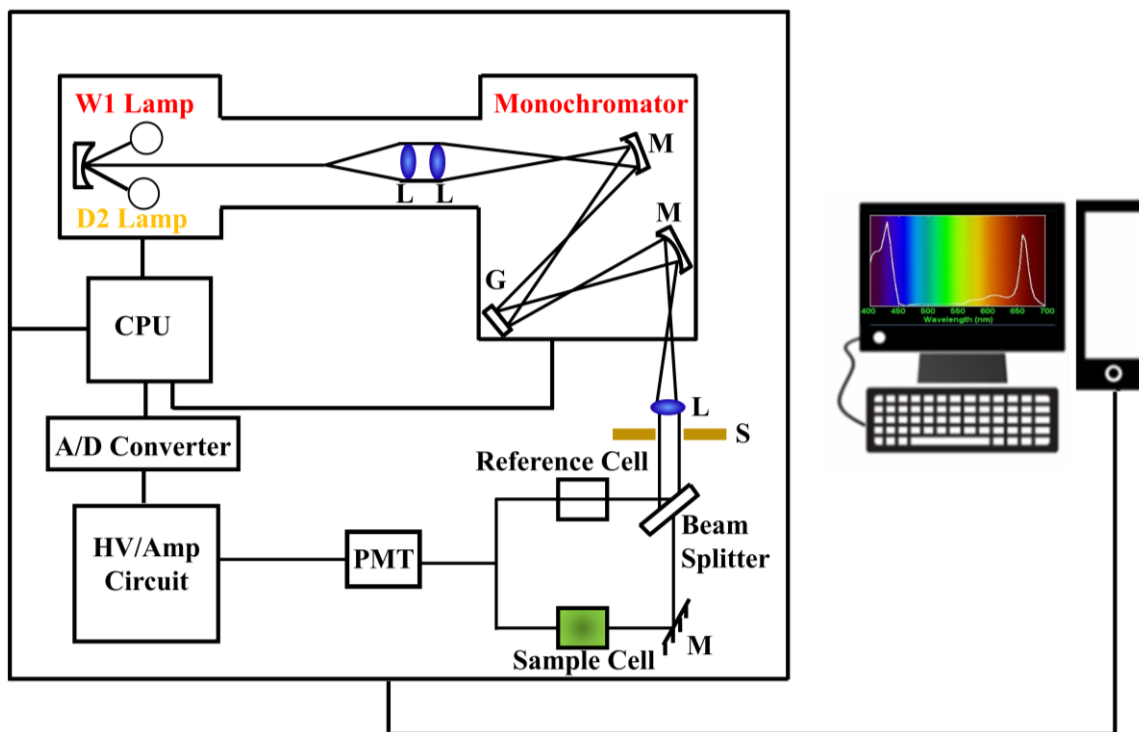


Figure 3.1. Schematic ray diagram of an absorption spectrophotometer. Tungsten halogen (W1) and deuterium lamps (D2) are used as light sources in the visible and UV regions, respectively. M, G, L, S, PMT designate mirror, grating, lens, shutter and photomultiplier tube, respectively. CPU, A/D converter and HV/amp indicate central processing unit, analog to digital converter and high-voltage/amplifier circuit, respectively.

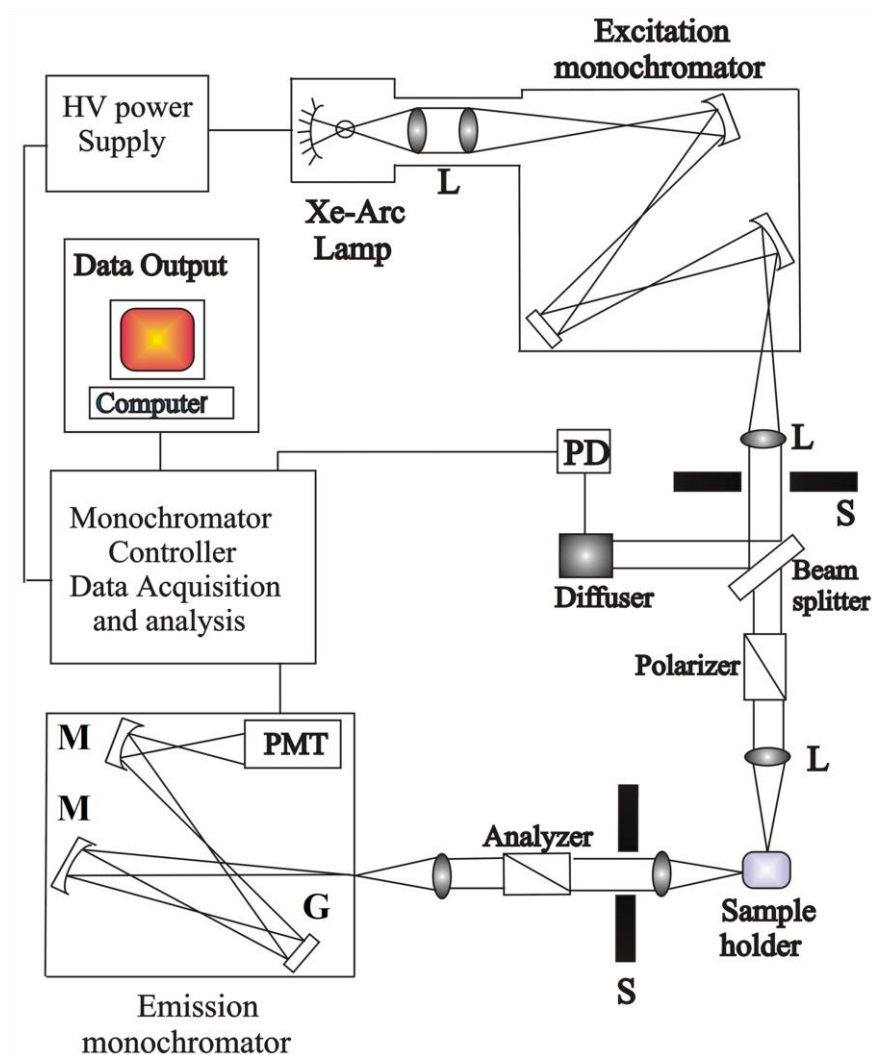


Figure 3.2. Schematic ray diagram of an emission spectrofluorimeter. M, G, L, S, PMT and PD represent mirror, grating, lens, shutter, photomultiplier tube and reference photodiode, respectively.

3.1.2. Circular Dichroism (CD) Measurement: CD is a form of spectroscopy based on the differential absorption of left and right-handed circularly polarized light. It can be used to determine the structure of macromolecules (including the secondary structure of proteins and the handedness of DNA). The CD measurements were done in a JASCO spectropolarimeter with a temperature controller attachment (Peltier) (Figure 3.3). The CD spectra were acquired using quartz cells of 0.1 and 1.0 cm path length. For proteins, the typical concentration used for CD measurements were within 10 μM .

The working principle of CD measurement is as follows: when a plane polarized light passes through an optically active substance, not only do the left (L) and right (R)

circularly polarized light rays travel at different speeds, $c_L \neq c_R$, but these two rays are absorbed to different extents, i.e., $A_L \neq A_R$. The difference in the absorbance of the left and right circularly polarized light, i.e., $\Delta A = A_L - A_R$, is defined as circular dichroism [1]. CD spectroscopy follows Beer-Lambert law. If I_0 is the intensity of light incident on the cell, and I , that of emergent light, then absorbance is given by,

$$A = \log_{10} \left(\frac{I_0}{I} \right) = \epsilon c l \quad (3-1)$$

where, A is proportional to concentration (c) of optically active substance and optical path length (l). If ' c ' is in moles L^{-1} and ' l ' is in cm, then ϵ is called the molar absorptivity or molar extinction coefficient. In an optically active medium, two absorbances, A_L and A_R are considered, where $A_L = \log_{10} (I_0/I_L)$ and $A_R = \log_{10} (I_0/I_R)$. At the time of incidence on the sample, intensity of left and right circularly polarized light are same, i.e., $I_0 = I_L = I_R$. Any micrograph passes periodically changing light through the medium, oscillating between left and right circular polarization, and the difference in absorbances are recorded directly [2].

$$\Delta A = A_L - A_R = \log_{10} \left(\frac{I_0}{I_L} \right) - \log_{10} \left(\frac{I_0}{I_R} \right) = \log_{10} \left(\frac{I_R}{I_L} \right) \quad (3-2)$$

or
$$\Delta A = (\Delta \epsilon) c l \quad (3-3)$$

As seen from equation (3-2), I_0 does not appear in this final equation, so there is no need for a reference beam. The instruments are, therefore, of single beam type. Most of the CD spectropolarimeters, although they measure differential absorption, produce a CD spectrum in units of ellipticity (θ) expressed in millidegrees versus λ , rather than ΔA versus λ . The relation between ellipticity and CD is given by,

$$\theta = \frac{2.303 \times 180 \times (A_L - A_R)}{4\pi} \text{ degrees} \quad (3-4)$$

To compare the results from different samples, optical activity is computed on a molar or residue basis. Molar ellipticity, $[\theta]$ is defined as,

$$[\theta] = \frac{\theta}{c l} \quad (3-5)$$

where, ' θ ' is in degrees, ' c ' is in moles L^{-1} and ' l ' is in cm. The unit of molar ellipticity is $\text{deg M}^{-1} \text{cm}^{-1}$.

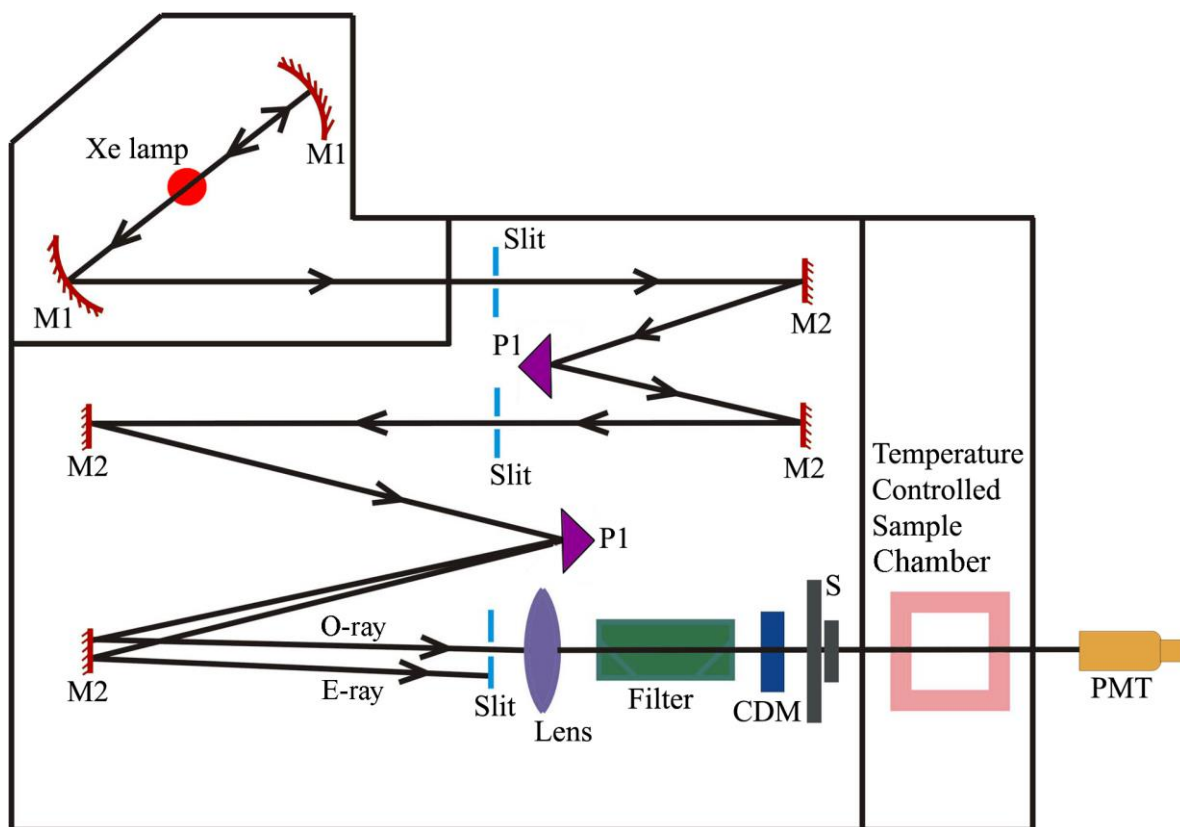


Figure 3.3. Schematic ray diagram of a circular dichroism (CD) spectropolarimeter. M1, M2, P1, S, PMT, CDM, O-ray and E-ray represent concave mirror, plain mirror, reflecting prism, shutter, photomultiplier tube, CD-modulator, ordinary ray and extraordinary ray, respectively.

3.1.3. Time-Correlated Single Photon Counting (TCSPC) Technique: All the picosecond-resolved fluorescence transients were recorded using TCSPC technique. The schematic block diagram of a TCSPC system is shown in Figure 3.4. TCSPC setup from Edinburgh instruments, U.K., was used during fluorescence decay acquisitions. The instrument response functions (IRFs) of the laser sources at different excitation wavelengths varied between 70 ps to 80 ps. The fluorescence from the sample was detected by a photomultiplier after dispersion through a grating monochromator [3]. For all

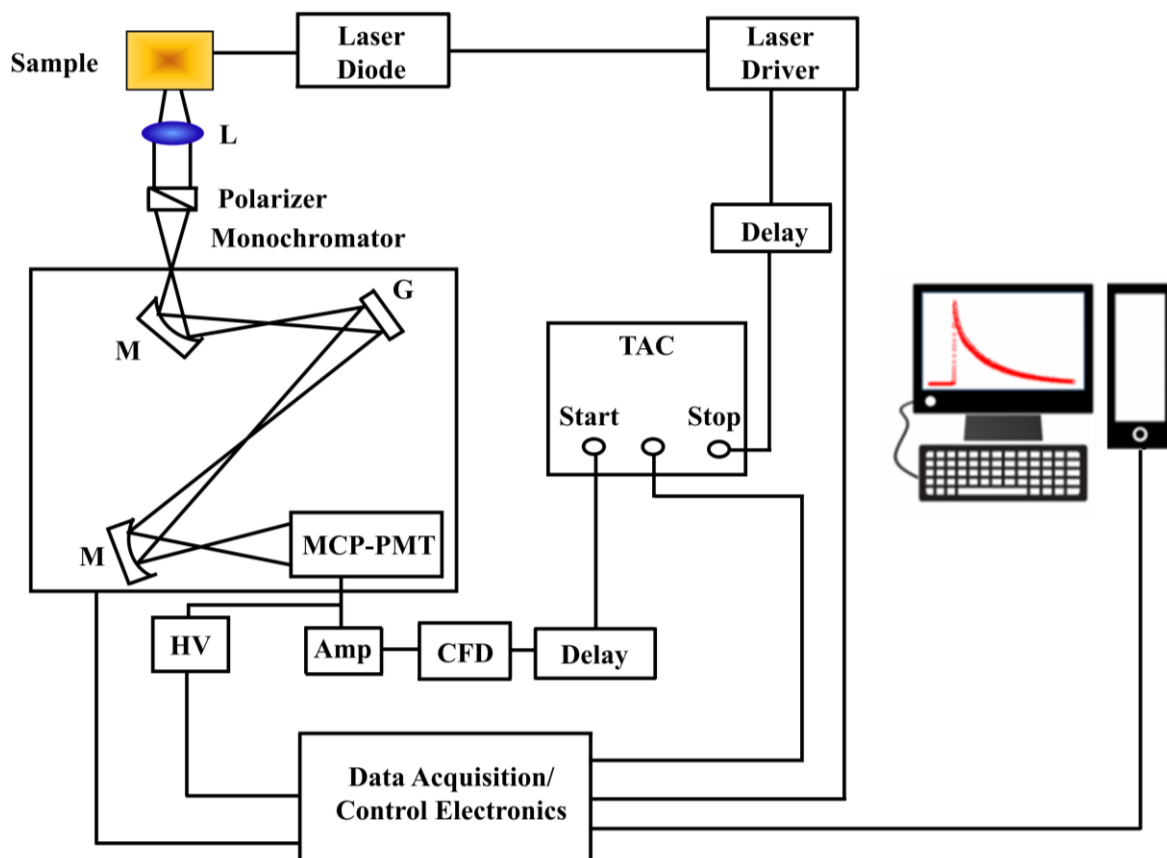


Figure 3.4. Schematic ray diagram of a time correlated single photon counting (TCSPC) spectrophotometer. A signal from microchannel plate photomultiplier tube (MCP-PMT) is amplified (Amp) and connected to start channel of time to amplitude converter (TAC) via constant fraction discriminator (CFD) and delay. The stop channel of the TAC is connected to the laser driver via a delay line. L, M, G and HV represent lens, mirror, grating and high voltage source, respectively.

transients, the polarizer in the emission side was adjusted to be at 54.7° (magic angle) with respect to the polarization axis of excitation beam. In order to measure anisotropy, fluorescent transients were taken with emission polarizer aligned in parallel and perpendicular directions with respect to vertical polarization of excitation light. For tryptophan excitation of protein, femtosecond-coupled TCSPC setup were employed in which the sample was excited by the third harmonic laser beam (300 nm) of the 900 nm (0.5 nJ per pulse) using a mode-locked Ti-sapphire laser with an 80 MHz repetition rate (Tsunami, Spectra Physics), pumped by a 10 W Millennia (Spectra Physics) followed by a pulse-peaker (rate 8 MHz) and a third harmonic generator (Spectra-Physics, model 3980). The third harmonic beam was used for excitation of the sample inside the TCSPC

instrument (IRF = 70 ps) and the second harmonic beam was collected as for the start pulse.

3.1.4. Femtosecond-resolved Fluorescence Up-conversion Technique: The femtosecond-resolved fluorescence spectroscopy was carried out using a femtosecond

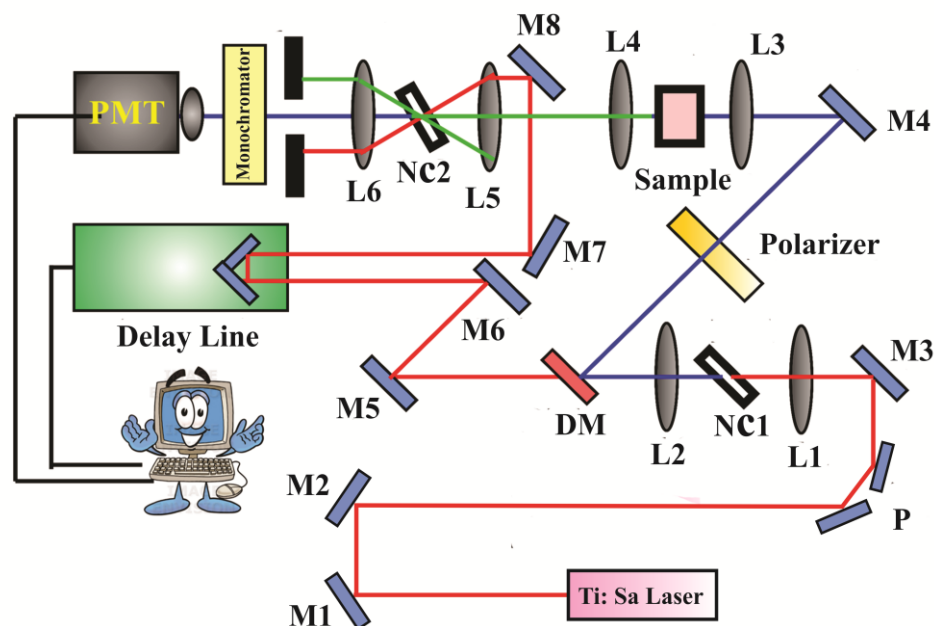


Figure 3.5. Schematic diagram of a femtosecond fluorescence up-conversion experimental setup. A BBO crystal (NC1) is used for second harmonic generation, which provides a pump beam in the UV region. Another BBO crystal (NC2) generates the up-conversion signal of pump and probe beams. L and M indicate lenses and mirrors, respectively. M1-M3 and M5-M8 are IR mirrors whereas M4 is a UV mirror. DM is dichroic mirror and P is periscope.

up-conversion setup (FOG 100, CDP, Figure 3.5) in which the sample was excited at 390 nm, using the second harmonic of a mode-locked Ti-sapphire laser with 80 MHz repetition rate (Tsunami, Spectra Physics), pumped by 10 W Millennia (Spectra Physics). The fundamental beam was passed through a periscopic arrangement (P) (Figure 3.5) before getting frequency doubled in a nonlinear crystal, NC1 (1 mm BBO, $\theta = 25^\circ$, $\phi = 90^\circ$). This beam was then sent into a rotating circular cell of 1 mm thickness containing the sample via a dichroic mirror (DM), a polarizer and a mirror (M4). The resulting fluorescence emission was collected, refocused with a pair of lenses (L4 and L5) and mixed with the fundamental beam (780 nm) coming through a delay line to yield an upconverted photon signal in a nonlinear crystal, NC2 (0.5 mm BBO (β -barium borate), $\theta = 10^\circ$, $\phi = 90^\circ$). The

upconverted light was dispersed in a double monochromator and detected using photon counting electronics. The instrument response time was determined from the cross-correlation function due to sum frequency generation between gate and excitation pulses. The cross-correlation function was obtained using the Raman scattering from water, displaying a full width at half maximum of approximately (FWHM) of 165 fs. The observed femtosecond-resolved decays were fitted using a Gaussian shape for the exciting pulse.

3.1.5. Transmission Electron Microscope (TEM): A FEI TecnaiTF-20 field-emission high-resolution TEM (Figure 3.6) equipped with an energy dispersive X-ray (EDAX)

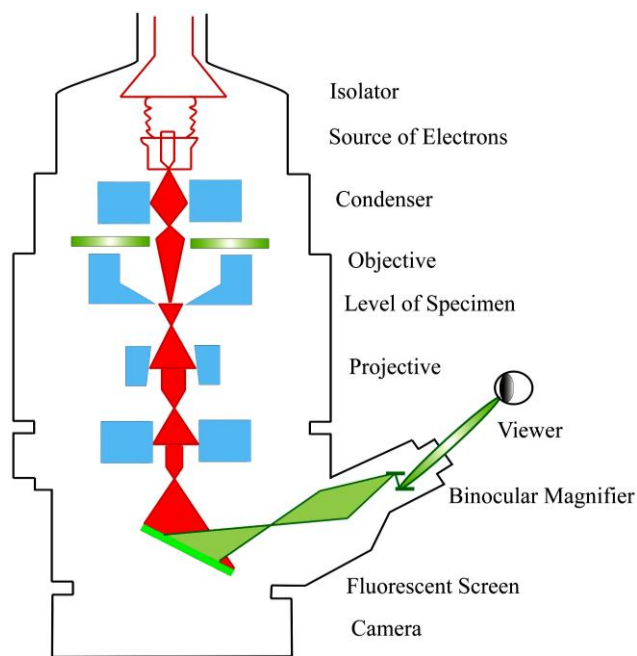


Figure 3.6. Schematic diagram of a typical transmission electron microscope (TEM). After the transmission of electron beam through a specimen, the magnified image is formed either in the fluorescent screen or can be detected by a CCD camera.

spectrometer was used to characterize the microscopic structures of samples and to analyze their elemental composition. The sizes of the nanoparticles were determined from the TEM images obtained at 200 kV acceleration voltage of the microscope. The imaging of the reverse vesicle solutions were conducted at 120 kV. Samples for TEM were prepared by placing a drop of the colloidal solution on a carbon-coated copper grid and allowing the film to evaporate overnight at room-temperature.

3.1.6. Dynamic Light Scattering (DLS): DLS, also known as photon correlation spectroscopy (PCS) or quasi-elastic light scattering (QELS) is one of the most popular techniques used to determine the hydrodynamic size of the particles. DLS measurements were performed on a Nano S Malvern instrument, (U.K.) employing a 4 mW He-Ne laser ($\lambda = 632.8 \text{ nm}$) and equipped with a thermostatted sample chamber. The instrument allows DLS measurements in which all the scattered photons are collected at 173° scattering angle

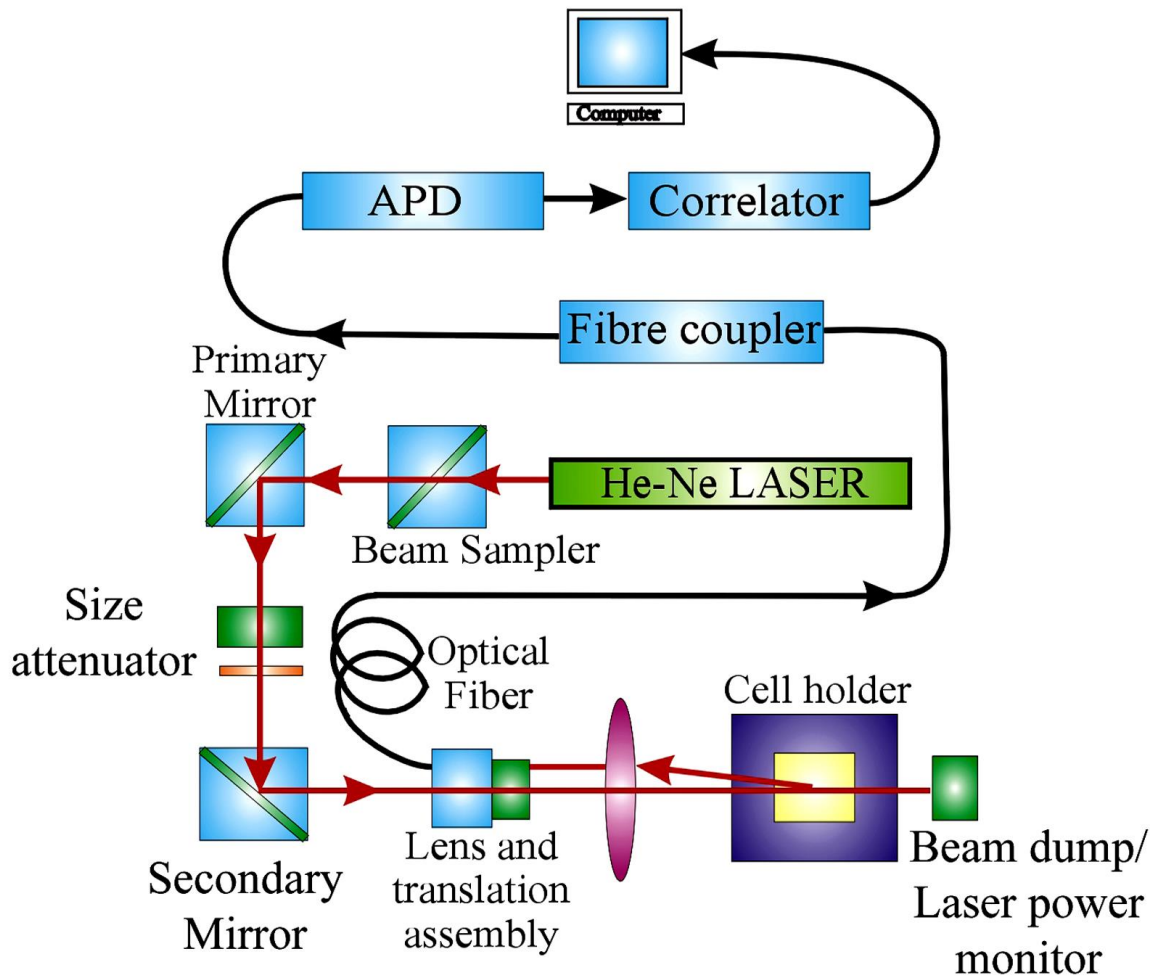


Figure 3.7. Schematic ray diagram of dynamic Light Scattering (DLS) instrument. The avalanche photo diode (APD) is connected to preamplifier/amplifier assembly and finally to correlator. It has to be noted that lens and translational assembly, laser power monitor, size attenuator, laser are controlled by the computer.

(Figure 3.7). The instrument measures the time dependent fluctuation in intensity of light scattered from the particles in solution at a fixed scattering angle [4]. The ray diagram of the DLS setup is shown in Figure 3.7.

It has been seen that particles in dispersion are in a constant, random Brownian motion and this causes the intensity of scattered light to fluctuate as a function of time. The correlator used in a DLS instrument constructs the intensity autocorrelation function $G(\tau)$ of the scattered intensity,

$$G(\tau) = \langle I(t)I(t + \tau) \rangle \quad (3-6)$$

where τ is the time difference (the sample time) of the correlator. For a large number of monodisperse particles in Brownian motion, the correlation function (given the symbol G) is an exponential decaying function of the correlator time delay τ ,

$$G(\tau) = A[1 + B\exp(-2\Gamma\tau)] \quad (3-7)$$

where A is the baseline of the correlation function, B is the intercept of the correlation function. Γ is the first cumulant and is related to the translational diffusion coefficient as, $\Gamma = Dq^2$, where q is the scattering vector and its magnitude is defined as,

$$q = \left(\frac{4\pi n}{\lambda_0} \right) \sin\left(\frac{\theta}{2}\right) \quad (3-8)$$

where n is the refractive index of dispersant, λ_0 is the wavelength of the laser and θ , the scattering angle. For polydisperse samples, the equation can be written as,

$$G(\tau) = A \left[1 + B |g^{(1)}(\tau)|^2 \right] \quad (3-9)$$

where the correlation function $g^{(1)}(\tau)$ is no longer a single-exponential decay and can be written as the Laplace transform of a continuous distribution $G(\Gamma)$ of decay times,

$$g^{(1)}(\tau) = \int_0^{\infty} G(\Gamma) \exp(-\Gamma\tau) d\Gamma \quad (3-10)$$

The scattering intensity data in DLS were processed using the instrumental software to obtain the hydrodynamic diameter (d_H) and the size distribution of the scatterer in each sample. In a typical size distribution graph from the DLS measurement, X-axis shows a distribution of size classes in nm, while the Y-axis shows the relative intensity of the scattered light. The diffusion coefficient (D) can be calculated using d_H of the particle by using the Stoke-Einstein relation,

$$D = \frac{k_B T}{3\pi\eta d_H} \quad (3-11)$$

where k_B , T , d_H , and η are Boltzmann constant, temperature in Kelvin, hydrodynamic diameter and viscosity, respectively.

3.1.7. Density and Sound Velocity Measurement: The density and sound velocity measurements were done in DSA 5000 from Anton Paar. The instrument measures density and sound velocity with accuracies of 5×10^{-3} and 1×10^{-6} , respectively. The density and

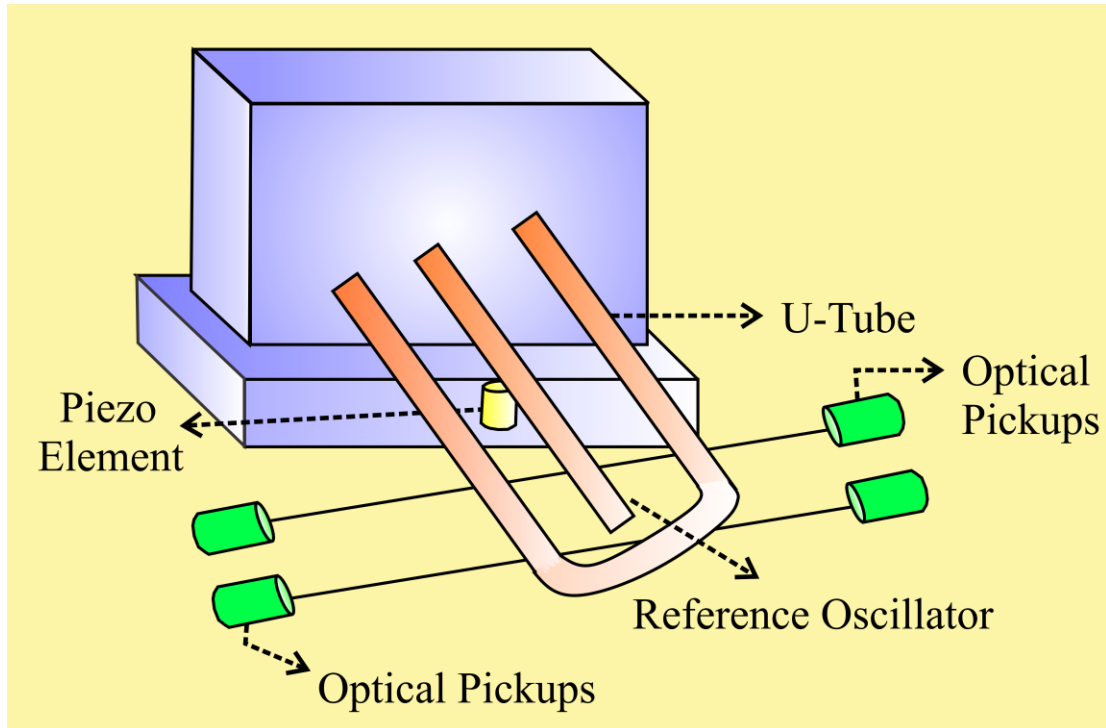


Figure 3.8. Schematic representation of the densimeter.

velocity are measured according to the following measuring principle. A U-shaped glass tube of known volume and mass is filled with the liquid sample and excited electronically by a Piezo element (Figure 3.8). The U-tube is kept oscillating continuously at the characteristic frequency f . Optical pick-ups record the oscillation period P as $P = 1/f$. This frequency is inversely proportional to the density ρ of the filled-in sample. The reference oscillator speeds up the measurements when aiming at various measuring temperatures.

The density is calculated as,

$$\rho = AxP^2 - B \quad (3-12)$$

where and A, B are parameters. Once the instrument has been adjusted with air and water, the density of the sample can be determined. Adiabatic compressibility (β) of the solutions can be determined by solution density (ρ) and the sound velocity (u) and applying Laplace's equation,

$$\beta = \frac{1}{\rho \times u^2} \quad (3-13)$$

3.1.8. X-ray Diffraction (XRD) Measurement: XRD is a popular and powerful technique for determining crystal structure of crystalline materials. By examining the diffraction pattern, one can identify the crystalline phase of the material. Small angle scattering is

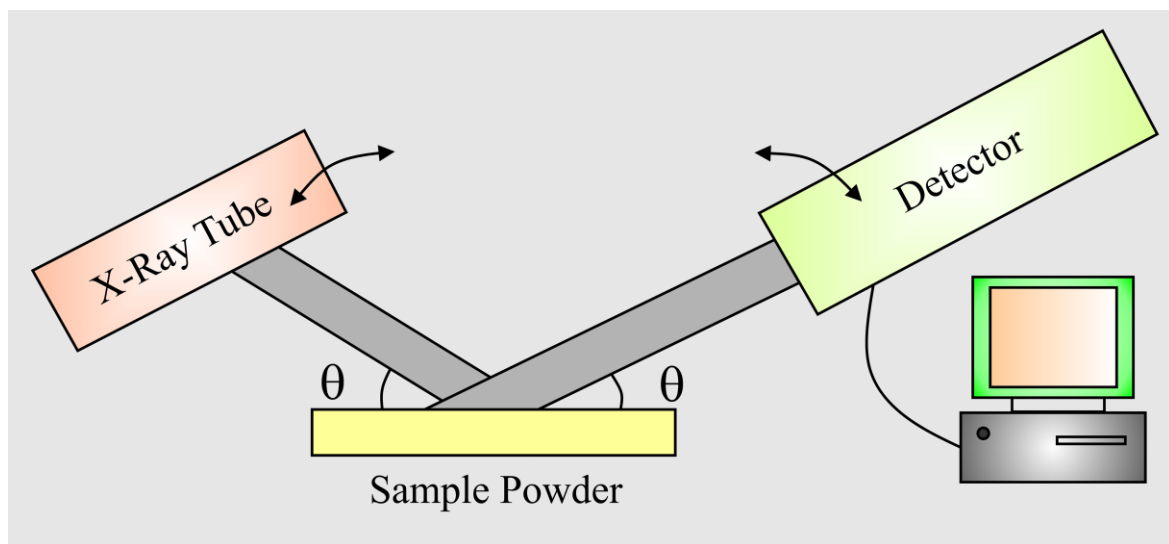


Figure 3.9. Schematic diagram of X-ray diffraction (XRD) instrument. By varying the angle θ , the Bragg's law conditions, $n\lambda = 2d\sin\theta$ are satisfied by different d -spacings in polycrystalline materials. Plotting the angular positions and intensities of the resultant diffracted peaks of radiation produces a pattern, which is characteristic of the sample.

useful for evaluating the average interparticle distance while wide-angle diffraction is useful for refining the atomic structure of nanoclusters. The widths of the diffraction lines are closely related to strain, defect size and distribution in nanocrystals. As the size of the nanocrystals decreases, the line width is broadened due to loss of long-range order relative to the bulk. This XRD line width can be used to estimate the size of the particle by using the Debye-Scherrer formula,

$$D = \frac{0.9\lambda}{\beta \cos \theta} \quad (3-14)$$

where, D is the nanocrystal diameter, λ is the wavelength of light, β is the full-width half-maximum (FWHM) of the peak in radians, and θ is the Bragg angle. XRD measurements were performed on a PANalytical XPERT-PRO diffractometer (Figure 3.9) equipped with Cu $K\alpha$ radiation ($\lambda = 1.5418 \text{ \AA}$ at 40 mA, 45 kV) [5]. XRD patterns were obtained by employing a scanning rate of $0.02^\circ \text{ s}^{-1}$ in the 2θ range from 15° to 90° . The nanoparticles (NPs) were ultracentrifuged and dried to get the XRD pattern.

3.1.9. Fourier Transform Infrared (FTIR) Measurement: FTIR spectroscopy is a technique that can provide very useful information about functional groups in a sample. An infrared spectrum represents the fingerprint of a sample with absorption peaks which correspond to the frequencies of vibrations between the bonds of the atoms making up the material. Because each different material is a unique combination of atoms, no two

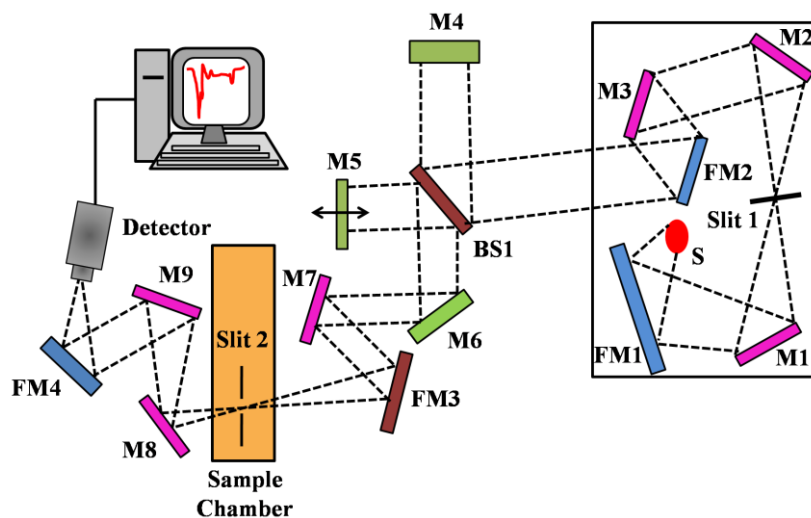


Figure 3.10. Schematic of Fourier Transform Infrared (FTIR) spectrometer. It is basically a Michelson interferometer in which one of the two fully-reflecting mirrors is movable, allowing a variable delay (in the travel-time of the light) to be included in one of the beams. M , FM and $BS1$ represent the mirror, focusing mirror and beam splitter, respectively. $M5$ is a moving mirror.

compounds produce the exact same infrared spectrum. Therefore, infrared spectroscopy can result in a positive identification (qualitative analysis) of every different kind of material. In addition, the size of the peaks in the spectrum is a direct indication of the

amount of material present. The two-beam Michelson interferometer is the heart of FTIR spectrometer. It consists of a fixed mirror (M4), a moving mirror (M5) and a beam-splitter (BS1), as illustrated in Figure 3.10. The beam-splitter is a laminate material that reflects and transmits light equally. The collimated IR beam from the source is partially transmitted to the moving mirror and partially reflected to the fixed mirror by the beam-splitter. The two IR beams are then reflected back to the beam-splitter by the mirrors. The detector then monitors the transmitted beam from the fixed mirror and reflected beam from the moving mirror, simultaneously. The two combined beams interfere constructively or destructively depending on the wavelength of the light (or frequency in wavenumbers) and the optical path difference introduced by the moving mirror. The resulting signal is called an interferogram which has the unique property that every data point (a function of the moving mirror position) which makes up the signal has information about every infrared frequency which comes from the source. Because the analyst requires a frequency spectrum (a plot of the intensity at each individual frequency) in order to make identification, the measured interferogram signal cannot be interpreted directly. A means of “decoding” the individual frequencies is required. This can be accomplished via a well-known mathematical technique called the Fourier transformation. This transformation is performed by the computer which then presents the user with the desired spectral information for analysis. In our study FTIR measurements were performed on a JASCO FTIR-6300 spectrometer (transmission mode) using CaF₂ window.

3.1.10. Laser Raman Spectroscopy: Raman spectroscopy is a useful technique for the identification of a wide range of substances-solids, liquids, and gases. It is a straightforward, non-destructive technique requiring no sample preparation. Raman spectroscopy involves illuminating a sample with monochromatic light and using a spectrometer to examine light scattered by the sample.

At the molecular level photons can interact with matter by absorption or scattering processes. Scattering may occur either elastically, or inelastically. The elastic process is termed Rayleigh scattering, whilst the inelastic process is termed Raman scattering. The electric field component of the scattering photon perturbs the electron cloud of the molecule and may be regarded as exciting the system to a ‘virtual’ state. Raman scattering occurs when the system exchanges energy with the photon, and the system subsequently

decays to vibrational energy levels above or below that of the initial state. The frequency shift corresponding to the energy difference between the incident and scattered

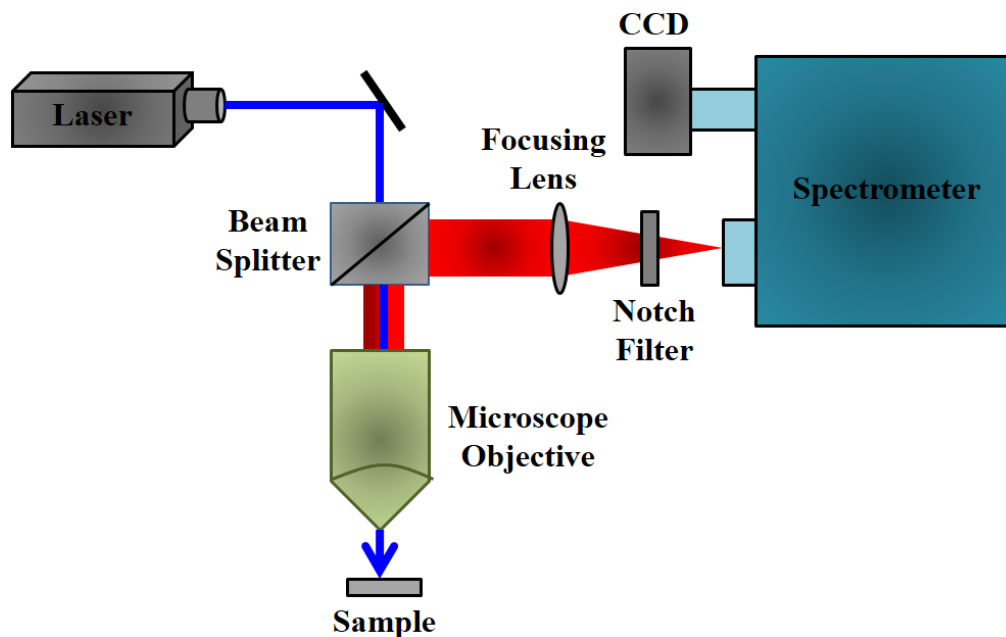


Figure 3.11. Schematic diagram of a Raman spectrometer.

photon is termed the Raman shift. Depending on whether the system has lost or gained vibrational energy, the Raman shift occurs either as an up or down-shift of the scattered photon frequency relative to that of the incident photon. The down-shifted and up-shifted components are called, the Stokes and anti-Stokes lines, respectively. A plot of detected number of photons versus Raman shift from the incident laser energy gives a Raman spectrum. Different materials have different vibrational modes, and therefore characteristic Raman spectra. This makes Raman spectroscopy a useful technique for material identification. There is one important distinction to make between the Raman spectra of gases and liquids, and those taken from solids - in particular, crystals. For gases and liquids it is meaningful to speak of the vibrational energy levels of the individual molecules which make up the material. Crystals do not behave as if composed of molecules with specific vibrational energy levels, instead the crystal lattice undergoes vibration. These macroscopic vibrational modes are called phonons.

In most of the Raman spectrometer, lasers are used as a photon source due to their highly monochromatic nature, and high beam fluxes (Figure 3.11). This is necessary as the

Raman effect is weak, typically the Stokes lines are $\sim 10^5$ times weaker than the Rayleigh scattered component. In the visible spectral range, Raman spectrometers use notch filters to cut out the signal from a very narrow range centred on the frequency corresponding to the laser radiation. Most Raman spectrometers for material characterization use a microscope to focus the laser beam to a small spot ($< 1\text{--}100\ \mu\text{m}$ diameter). Light from the sample passes back through the microscope optics into the spectrometer. Raman shifted radiation is detected with a charge-coupled device (CCD) detector, and a computer is used for data acquisition and curve fitting. These factors have helped Raman spectroscopy to become a very sensitive and accurate technique.

In our study [5] Raman experiments were performed in a back scattering geometry by using a LabRAM HR, JobinYvon fitted with a Peltier-cooled CCD detector. An air cooled argon ion laser with a wavelength of 488 nm was used as the excitation light source. The laser power was 17 mW at the sample and the integration time was 1 second with a double accumulation for each measurement. 2-4 μl of 560 μM CV ethanol solution was added in the substrate solutions, and SERS measurements were started after 5 minute of incubation.

3.1.11. Conductivity Measurement: Conductivity is the ability of a material to conduct current. Positive and negative ions in a solution will move to the oppositely charged electrode when an electric charge is applied to the solution, thus conducting current (Figure 3.12). In addition to the current applied, ion movement is affected by the solvent properties (temperature, viscosity) and the physical properties of the ion (size, charge, concentration etc.). As temperature increases, ions move faster and conduct more current. As viscosity increases, the ions move slower and conduct less current. In theory, a conductivity measuring cell consists of two, 1-cm square electrode surfaces spaced 1 cm apart. The cell constant (K) is determined by the cell length (L) and cross-sectional area (A) ($K = L / A$). Cells with larger/smaller electrodes or electrodes spaced at a different distance are characterized by a different cell constant. Since the cell's physical configuration significantly affects the conductivity measurement, it must be multiplied by the conductance to obtain the actual conductivity reading. For most uses, the actual cell

constant (K) of a specific cell is determined by comparing the measurement of a standard solution of known specific conductivity (e.g., 0.01 M KCl) to the measured conductance.

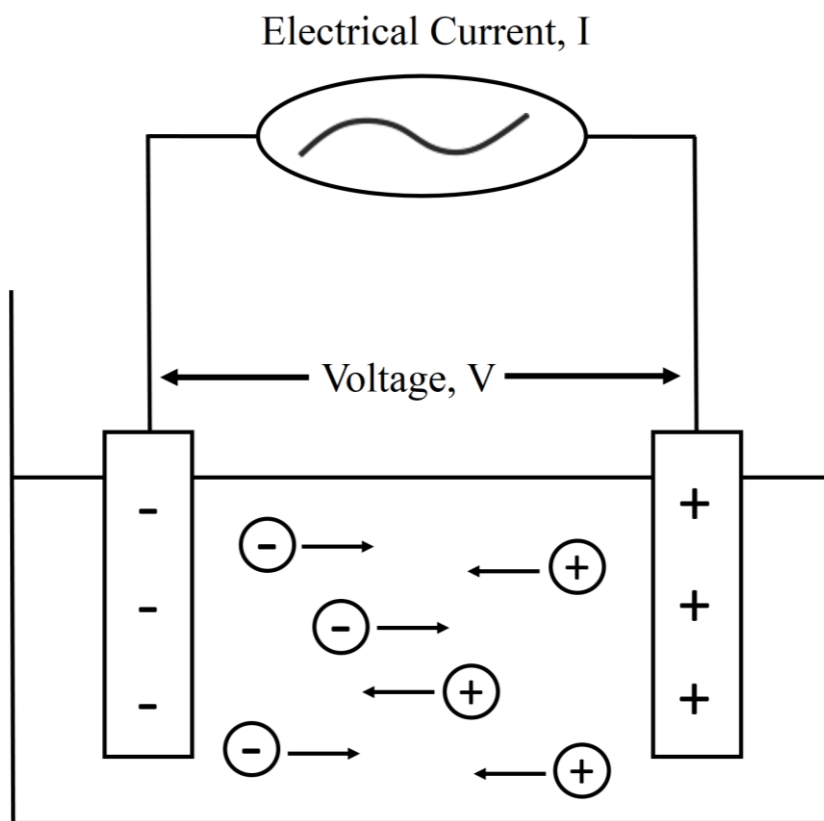


Figure 3.12. Schematic representation of ion migration in solution.

In our study the electrical conductivity of the microemulsion (ME) was measured using a Sension378 conductivity meter (Hach Company, Loveland, CO) at room temperature. Since the MEs were based on nonionic components and there is no considerable dependence of phase behavior on salinity, solution of 0.9% NaCl was used as the titrant in place of pure water. Measurement of conductivity was carried out with an absolute accuracy up to $\pm 0.5\%$.

3.1.12. Refractive Indices Measurement: Refractive indices of the solutions were measured by using a Rudolph J357 automatic refractometer. The instrument measures the refractive indices using sodium D-line of wavelength 589.3 nm with accuracies ± 0.00004 . The measurement of the refractive index of the sample is based on the determination of the critical angle of total reflection. A light source, usually a long-life LED, is focused onto a

prism surface via a lens system. Due to the focusing of light to a spot at the prism surface, a wide range of different angles is covered. As shown in the Figure 3.13, the measured

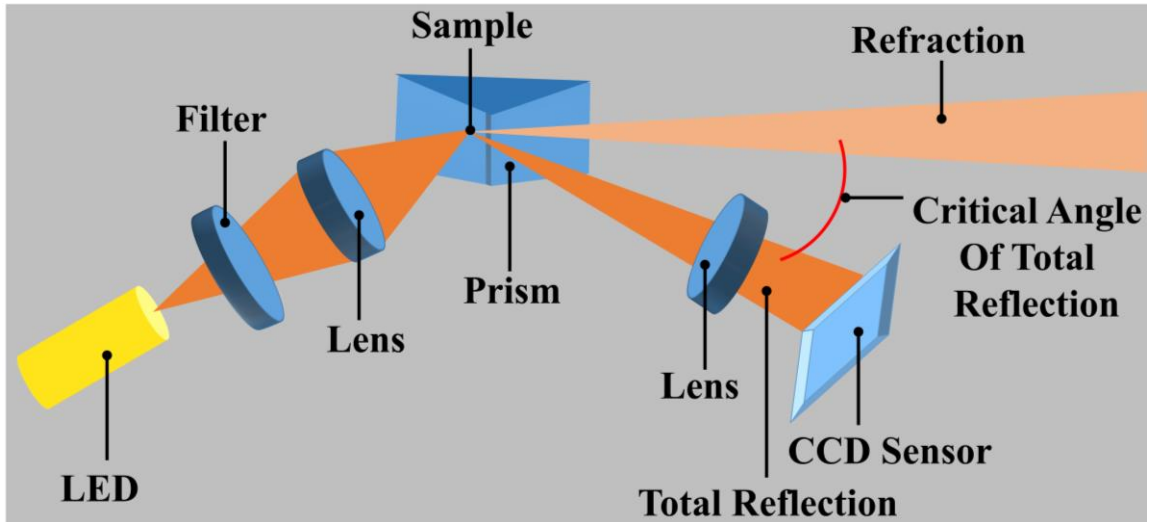


Figure 3.13. Schematic representation of the refractometer.

sample is in direct contact with the measuring prism. Depending on its refractive index, the incoming light below the critical angle of total reflection is partly transmitted into the sample, whereas for higher angles of incidence the light is totally reflected. This dependence of the reflected light intensity from the incident angle is measured with a high-resolution sensor array. From the video signal taken with the CCD sensor the refractive index of the sample can be calculated.

3.1.13. Viscosity Measurement: Viscosity of the solutions were measured by measuring the flow times in a calibrated Ostwald viscometer having 100-s efflux time for water. In a typical experiment the time taken for a liquid to flow between the two marks in an Ostwald viscometer (A→B, Figure 3.14) is a function of both viscosity and density. The relationship between dynamic viscosity and density is called kinematic viscosity and is defined as,

$$\text{Kinematic Viscosity} = [\text{Dynamic Viscosity}]/\text{Density} \quad (3-15)$$

An Ostwald viscometer is normally supplied with a viscometer constant which can be used to calculate viscosity. However, if that is not available, the viscosity of the test fluid can be

compared with one whose viscosity is known (e.g., water) and the viscosity is calculated using the following equation,

$$\eta = \eta_w \frac{t \times \rho}{t_w \times \rho_w} \quad (3-16)$$

where η denotes viscosity, ρ is density and t being the time of flow of the respective systems.

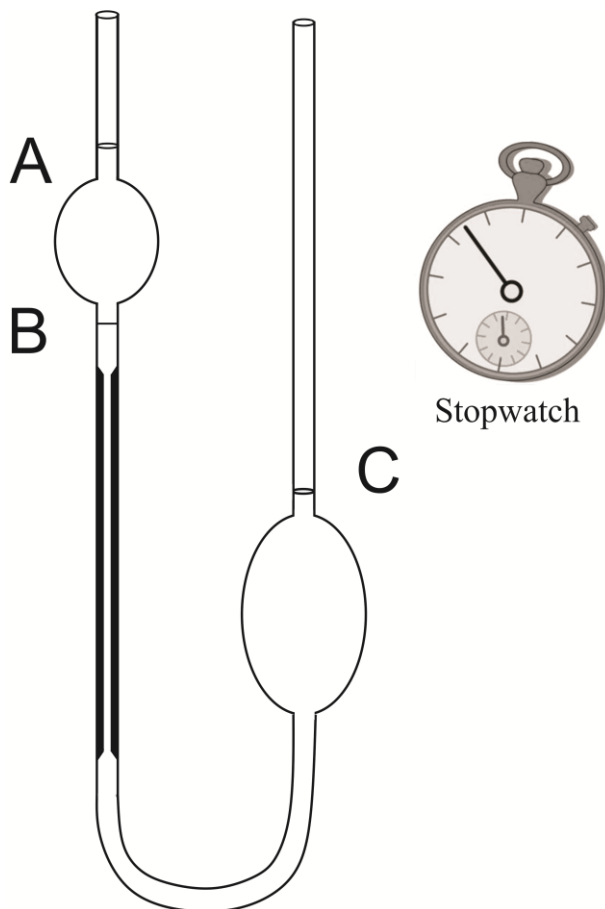


Figure 3.14. Schematic representation of Ostwald viscometer.

3.2. Sample Preparation: In this section the different sample preparation methods have been discussed.

3.2.1. Chemicals Used: The chemicals, spectroscopic probes, and proteins were procured from the following sources. Double distilled water was used to prepare all the aqueous solutions. The chemicals isopropyl myristate (IPM), polyoxyethylenesorbitan monooleate

(Tween 80), silver nitrate (AgNO_3), sodium borohydride (NaBH_4), rifampicin was purchased from Sigma Aldrich. The probes 2'-(4-Hydroxyphenyl)-5-(4-Methyl-1-Piperazinyl)-2,5'-Bi-1H-Benzimidazole Trihydrochloride Hydrate (H258), ethidium bromide (EtBr) and dansyl chloride (DC) was purchased from Molecular probes. 4-(dicyanomethylene)-2-methyl-6-(p-dimethylamino-styryl)-4H-pyran (DCM) and hexadecyltrimethylammonium bromide (CTAB) was obtained from Fluka. Sodium citrate, β -Cyclodextrin (β -CyD) and γ -CyD was purchased from Aldrich. The chemicals crystal violet (CV), sodium bis(2-ethylhexyl) sulfosuccinate (AOT), lyophilized riboflavin binding protein (RBP, Apo form from chicken egg white), di-sodium hydrogen phosphate, sodium dihydrogen phosphate, sodium acetate, acetic acid, riboflavin (Rf, Vitamin B2) and apomyoglobin (Apo-Mb from horse skeletal muscle) was obtained from Sigma. Butyl lactate and isooctane was procured from Spectrochem. Sodium chloride and citric acid was obtained from Merck. Ammonium molybdate was purchased from SRL (analytical grade). *p*-Benzoquinone (BQ) was from Alfa Aesar. EGFP was obtained from MC4100 *Escherichia coli* (*E. coli*) cells containing pEGFP (Clontech), as described in the reference [6]. The plasmid pRSETA harboring mEos2 was transformed into *E. coli* BL21DE3 cells and mEos2 was obtained from the protein purification facility at the Centre for Cellular and Molecular Platforms (Bangalore, India). All the chemicals and the proteins were of highest purity available and used without further purification.

3.2.2. Preparation of Vesicle Solution: Transparent solutions of vesicles were prepared by adding calculated amount of AOT surfactant to water followed by gentle stirring [7]. For vesicles containing probe molecules the respective probe was added before stirring the solutions. Prior to all the measurements, the AOT/water solutions were filtered with a Whatman syringe filter (pore size of 0.2 micrometre).

3.2.3. Preparation of Microemulsion (ME): ME solutions of specific wt. fraction of water to oil (X_w) were prepared by adding calculated volume of water and IPM (oil) to solutions containing constant Tween 80/butyl lactate wt. ratio (1:1) [8]. The solution mixtures were then vortexed to get the transparent solutions of ME. AOT Reverse micellar (RM) solutions were prepared by adding requisite volumes of water into a given volume of AOT solution (100 mM) in isooctane with gentle stirring to achieve RMs with required

degree of hydration, w_0 (= [water]/[surfactant]) [9]. For CTAB-RM preparation hexanol was additionally added as a cosurfactant in 1:9 ratios (v/v) to the isoctane solution [9]. For encapsulation of protein in the RM, buffer solutions of the proteins were used as the aqueous phase of the RM.

3.2.4. Preparation of Reverse Vesicle (RV): For the preparation of RVs, o/w ME comprising of tween 80, butyl lactate, and IPM, with wt. fraction of water being, $X_w = 0.37$, was prepared. The wt. ratio of tween 80 and butyl lactate was maintained at 1:1. Next 13.3 μl of the ME was added to 2 ml of IPM. The solution was then vortexed for 15 minutes to get a transparent solution of RV [5].

3.2.5. Nanoparticle Synthesis in Reverse Vesicle (RV): 200 mM aqueous solution of AgNO_3 was used as the aqueous phase to prepare ME with $X_w = 0.37$. 13.3 μl of this ME was then added to 2 ml of IPM and was allowed to stir for 15 minutes to get a transparent solution of RV containing silver ions. After that 2.5 mg of NaBH_4 was added to the RV solutions and was allowed to stir overnight (12 hours) to get RV containing silver NPs [5].

3.2.6. Preparation of Protein and Probe Solutions: Aqueous stock solutions of RBP were prepared in a phosphate buffer (10 mM) at pH 7.0 using double distilled water [9]. Concentration of RBP in buffer was determined using the extinction coefficient value of $49000 \text{ M}^{-1} \text{ cm}^{-1}$ at 280 nm [10]. Rf concentration was calculated from its absorbance using the extinction coefficient value of $12200 \text{ M}^{-1} \text{ cm}^{-1}$ at 450 nm [10]. We have used 15 μM RBP and 7.5 μM Rf solutions for all the spectroscopic studies.

EGFP and mEos2 solutions were prepared in either phosphate buffer solution (10 mM, pH 7.0) or sodium acetate buffer solution (10 mM, pH 3.0 and pH 4.2) [11]. For picosecond measurements we used 0.5 μM EGFP and 2 mM BQ solutions. To get sufficient photon count in femtosecond up-conversion measurements we used 14.5 μM EGFP, with concentration of BQ being 57 mM. In picosecond-resolved studies of mEos2 (0.67 μM) the concentration of BQ was 2.6 mM.

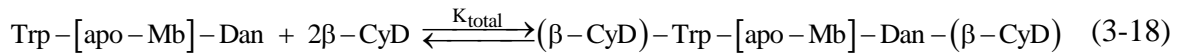
Aqueous stock solutions of Apo-Mb were prepared in phosphate buffer (10 mM) at pH 7.5 [12]. The working concentration of the protein was 1.66 μM , far below the aggregation concentration of the protein [13, 14]. Labeling of Apo-Mb with dansyl

chloride was done by incubating 1.66 μM of the protein in 10 mM phosphate buffer at pH 7.5, with 10-fold molar excess of dansyl chloride (in acetonitrile) at 4°C, for overnight stirring. The reaction was quenched by adding tris-HCl, pH 7.5. It was then dialyzed against 10 mM phosphate buffer, pH 7.5 [15]. The reactive groups of amino acids (lysine, arginine) react with dansyl chloride in their deprotonated form as a nucleophile. Since the pK_a of arginine ($\text{pK}_a = 12.48$) is greater than that of lysine ($\text{pK}_a = 10.5$), at pH 7.5 lysine is favorably dansylated [16, 17].

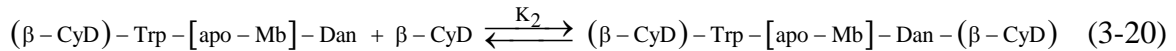
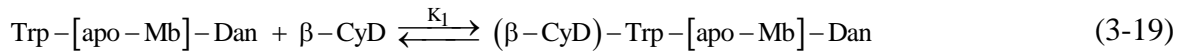
3.2.7. Determination of Thermodynamics of Binding: In order to establish the stoichiometric compositions of the inclusion complexes of a ligand to its receptor, and to determine the thermodynamic energy parameters associated with the binding, Benesi-Hildebrand method [18] was applied employing following equation:

$$\frac{1}{I_F - I_F^0} = \frac{1}{I_F' - I_F^0} + \frac{1}{K_i (I_F' - I_F^0) [\text{CyD}]} \quad (3-17)$$

Where I_F^0 , I_F , and I_F' are the integrated fluorescence intensities of the ligand in the absence, at intermediate and at infinite concentrations of the receptor, K_i being the binding constant. Linearity in this plot suggests 1:1 stoichiometry of the binding. In our study [12] the inclusion of tryptophan (Trp) with β -CyD led us to estimate the overall equilibrium constant (K_{total}) for dansyl bound apomyoglobin (Dan. Apo-Mb) association with β -CyD dictated by the reaction



This equilibrium can be split into two steps in which $(\beta - \text{CyD}) - \text{Trp} - [\text{Apo-Mb}] - \text{Dan}$ and $(\beta - \text{CyD}) - \text{Trp} - [\text{Apo-Mb}] - \text{Dan} - (\beta - \text{CyD})$ are formed in individual steps with association constants K_1 and K_2 , estimated from equation (3-17), respectively



According to multiple equilibria model [19, 20], the K_{total} was estimated from the product of the stepwise constants K_1 and K_2 , determined from equation (3-17).

References:

- [1] A. Rodger, B. Nordén, Circular dichroism and linear dichroism, Oxford University Press, 1997.
- [2] N. Berova, K. Nakanishi, R.W. Woody, Circular dichroism: Principles and applications, Wiley, 2000.
- [3] D.V. O'Conner, D. Philips, Time correlated single photon counting, Academic Press, London, 1984.
- [4] R. Pecora, Dynamic light scattering: Applications of photon correlation spectroscopy, Springer, 1985.
- [5] R. Saha, S. Rakshit, D. Majumdar, A. Singha, R. Mitra, S. Pal, Nanostructure, solvation dynamics, and nanotemplating of plasmonically active SERS substrate in reverse vesicles, *J. Nanopart. Res.* 15 (2013) 1576.
- [6] A.M. Saxena, J.B. Udgaonkar, G. Krishnamoorthy, Protein dynamics control proton transfer from bulk solvent to protein interior: A case study with a green fluorescent protein, *Protein Sci.* 14 (2005) 1787.
- [7] R. Saha, P.K. Verma, R.K. Mitra, S.K. Pal, Structural and dynamical characterization of unilamellar AOT vesicles in aqueous solutions and their efficacy as potential drug delivery vehicle, *Colloids Surf., B* 88 (2011) 345.
- [8] R. Saha, S. Rakshit, R.K. Mitra, S.K. Pal, Microstructure, morphology, and ultrafast dynamics of a novel edible microemulsion, *Langmuir* 28 (2012) 8309.
- [9] R. Saha, S. Rakshit, P.K. Verma, R.K. Mitra, S.K. Pal, Protein-cofactor binding and ultrafast electron transfer in riboflavin binding protein under the spatial confinement of nanoscopic reverse micelles, *J. Mol. Recognit.* 26 (2013) 59.
- [10] M.G. Duyvis, R. Hilhorst, C. Laane, D.J. Evans, D.J.M. Schmedding, Role of riboflavin in beer flavor instability: Determination of levels of riboflavin and its origin in beer by fluorometric apoprotein titration, *J. Agric. Food Chem.* 50 (2002) 1548.
- [11] R. Saha, P.K. Verma, S. Rakshit, S. Saha, S. Mayor, S.K. Pal, Light driven ultrafast electron transfer in oxidative redding of green fluorescent proteins, *Sci. Rep.* 3 (2013) 1580.

- [12] R. Saha, S. Rakshit, S.K. Pal, Molecular recognition of a model globular protein apomyoglobin by synthetic receptor cyclodextrin: Effect of fluorescence modification of the protein and cavity size of the receptor in the interaction *J. Mol. Recognit.* 26 (2013) 568.
- [13] O. Tcherkasskaya, O.B. Ptitsyn, Molten globule versus variety of intermediates: Influence of anions on pH-denatured apomyoglobin, *FEBS Lett.* 455 (1999) 325.
- [14] J.A. Stevens, J.J. Link, Y.-T. Kao, C. Zang, L. Wang, D. Zhong, Ultrafast dynamics of resonance energy transfer in myoglobin: Probing local conformation fluctuations, *J. Phys. Chem. B* 114 (2010) 1498.
- [15] U. Banik, N.C. Mandal, B. Bhattacharyya, S. Roy, A fluorescence anisotropy study of tetramer-dimer equilibrium of lambda repressor and its implication for function, *J. Biol. Chem.* 268 (1993) 3938.
- [16] R.P. Haugland, Handbook of fluorescent probes and research chemicals, 7th ed., Molecular Probes, Eugene, OR, 1996.
- [17] T. Mondol, S. Batabyal, A. Mazumder, S. Roy, S.K. Pal, Recognition of different DNA sequences by a DNA-binding protein alters protein dynamics differentially, *FEBS Lett.* 586 (2012) 258.
- [18] H.A. Benesi, J.H. Hildebrand, A spectrophotometric investigation of the interaction of iodine with aromatic hydrocarbons, *J. Am. Chem. Soc.* 71 (1949) 2703.
- [19] M.T. Beck, I. Nagypál, Chemistry of complex equilibria, Ellis Horwood, 1990.
- [20] E.A. Hoffmann, I. Nagypál, Response reactions: Equilibrium coupling, *J. Phys. Chem. B* 110 (2006) 10581.

Chapter 4

Structural Characterization and Crucial Ultrafast Dynamical Events in Biomimetic Self-assembly

4.1. Introduction:

In chemical and biological environments, water exists mainly as interfacial water, which is located in the close vicinity of different type of interfaces and is mostly confined in cellular cavities and interstitial voids. These environments may contain from millions to only a few tens of water molecules. The attractive/repulsive interaction between the interface and water molecules, as well as the geometrical constraint by the environment, causes significant changes in local and long-range water structure. As a result, chemistry in aqueous biomolecular systems and in organized molecular assemblies differs markedly from that in a homogeneous fluid medium [1-4]. Nature uses this difference exceptionally efficiently to carry out various chemical processes [1, 2, 5]. Water molecules confined in organized assemblies (reverse micelles, micelles, vesicles) and various biological macromolecules (such as protein surface or DNA) strongly influence the structure, function and dynamics of biomolecules [6]. Surfactant based microemulsion (ME) systems are well known biomimicking systems for such studies [7, 8].

The structure of ME can be idealized as a set of interfaces dividing polar and nonpolar domains. Depending on the composition of the system the microstructure of a ME may exist as water-in-oil (w/o) droplets, oil-in-water (o/w) droplets, or a bicontinuous structure. Various spectroscopic techniques like small angle X-ray scattering (SAXS), dynamic light scattering (DLS), pulsed-gradient-spin-echo (PGSE) nuclear magnetic resonance spectroscopy and others have been employed for structural identification of these systems [9-12]. Moreover, there is a growing interest to study the behavior of water molecules in such organized assemblies. Pharmaceuticals have displayed enhanced structural and conformational stability and slow diffusivity [13] and certain enzymes manifest enhanced activity at certain levels of hydration [13] in ME system. Garti and coworkers have employed the sub-zero differential scanning calorimetry (DSC) to study

the nature of the water and its thermal behavior in ME systems [14]. Water confined in reverse micelles has been detailed by Amararene *et al.* using acoustic and densimetric experiments [15]. Nuclear magnetic resonance (NMR) studies have successively reported the diffusive property of water in these types of nanoconfining environments. With this background the dynamics of water in such nanocavity seems interesting and can be studied using various techniques like solvation dynamics.

Our study attempts to construct a novel ME system comprising of pharmaceutically acceptable components tween 80/butyl lactate/isopropyl myristate (IPM)/water [16-18]. The pseudo-ternary phase diagram has been constructed for the chosen system at a constant surfactant/cosurfactant wt. ratio of 1:1. Conductivity, viscosity, ultrasonic compressibility and sound velocity measurements are employed to investigate the gradual changes occurring in the microstructure of the MEs with increasing water content. The bound property of water at the surfactant water interface has successfully been studied by the solvation probe 4-(dicyanomethylene)-2-methyl-6-(p-dimethylaminostyryl)-4H-pyran (DCM); using picosecond time-resolved fluorescence spectroscopy technique. To ascertain the geometrical restriction of the probe at the interface, rotational relaxation dynamics of the dye in different ME systems have also been determined. In relation to the microenvironment polarity, the steady-state absorption and emission data of DCM at the interface has been monitored as a function of water concentration. The focus of this study is formulation and physicochemical characterization of the ME formed using pharmaceutically acceptable components in a wide composition range in order to obtain information on self-organized structures. The study focuses to find correlation in the water relaxation dynamics with the structure of the host assembly. It is believed that the findings would show the convenience of characterizing ME systems from a physicochemical and spectroscopic point of view and improve our understanding of the microstructure of such biomimicking ME systems. This will serve as a basis for further investigations of ME systems useful in drug delivery and nontoxic nano-template for other applications.

4.2. Results and Discussion:

4.2.1. Microstructure, Morphology and Ultrafast Dynamics of a Novel Edible Microemulsion [19]:

Figure 4.1 shows the pseudo-ternary phase diagram of the system composed of Tween 80/butyl lactate/IPM/water at room temperature. The phase behavior, as shown in Figure 4.1, manifests a large single phase isotropic ME region, formed spontaneously at room temperature coupled with a two phase region appearing along the oil-water axis. The isotropic mixtures of ME remain stable without any phase separation upon prolonged standing. For potential pharmaceutical application, the ME system should be stable

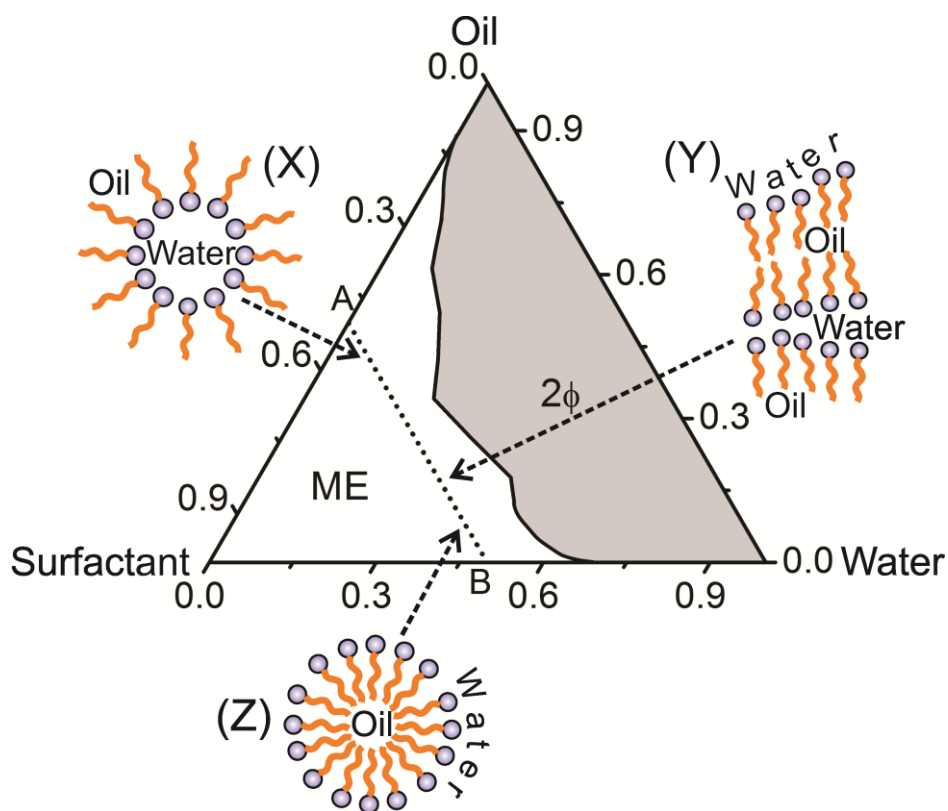


Figure 4.1. Pseudo-ternary phase diagram of tween 80/butyl lactate/IPM/water ME system. (2Φ) Two phase region, (ME) single phase region, (X) w/o ME, (Y) bicontinuous ME, (Z) o/w ME. The dotted line AB represents the dilution line along which all the experiments are carried out.

at various physiologically relevant environments, and to check that we observe the phase behavior at pH = 2.6 and also in 0.9% salt concentration. It is found that the phase

behavior of the system remains almost unaltered at pH 2.6 (Figure 4.2a) as well as in 0.9% salt concentration (Figure 4.2b) revealing the stability of the system in such environments. Considering the finite possibility of butyl lactate being hydrolysed to form n-butanol at *in vivo* low pH of the stomach, which may in turn affect the stability of the ME system, we construct the phase behavior of the system at various pH using n-butanol as the

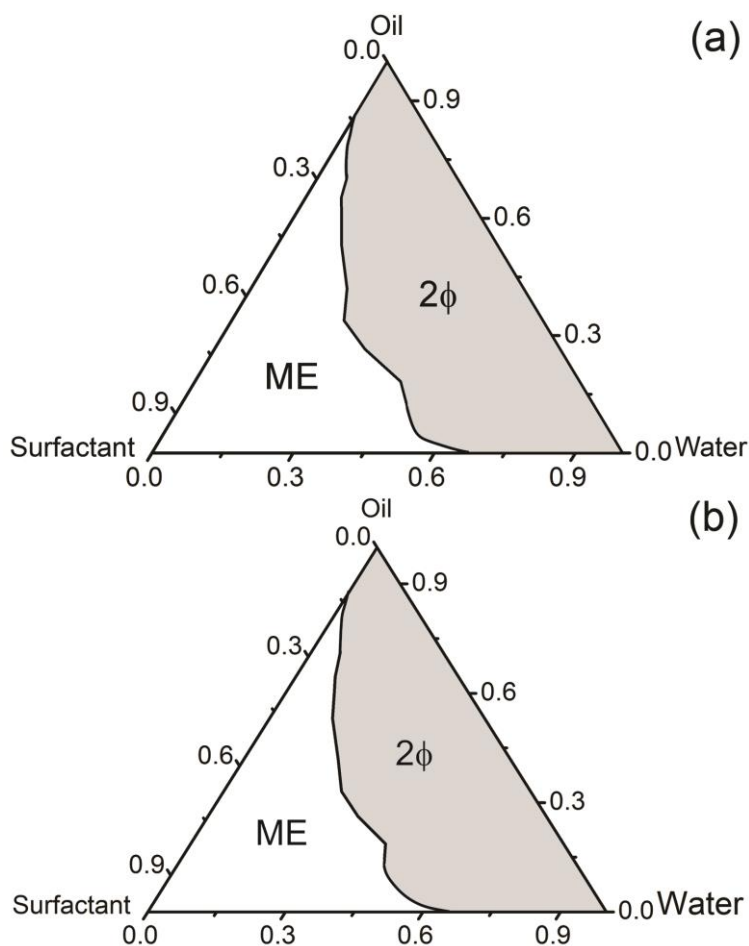


Figure 4.2. Pseudo-ternary phase diagram of tween 80/butyl lactate/IPM/water ME system (a) at pH 2.6 and (b) at 0.9% NaCl. (2Φ) Two phase region, (ME) single phase region.

cosurfactant and only marginal change in the phase behavior is observed when butyl lactate is replaced by n-butanol. This firmly affirms that possible formation of n-butanol does hardly affect the stability of the ME. This study further adds up to the potentiality of the ME system in pharmaceutical applications. Notably, the line AB in Figure 4.1 shows the experimental path along which the measurement of physical properties is carried out.

Line AB corresponds to a fixed surfactant-cosurfactant wt. ratio of 1, with wt. fraction each in the total system being 0.25. The wt. fraction of water (denoted by X_w) and oil varies through the line AB.

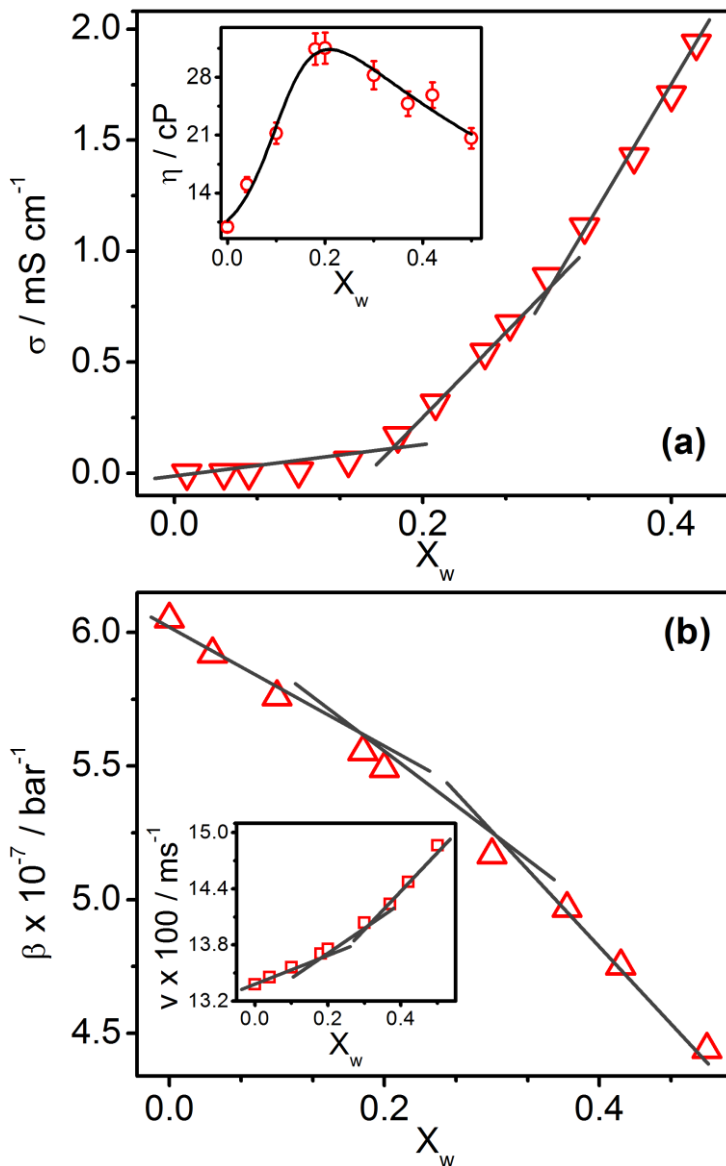


Figure 4.3. (a) Variation of electrical conductivity (σ) along the dilution line AB ($X_w = \text{wt. fraction of water}$), the inset shows the respective variation in viscosity (η). (b) Variation of ultrasonic compressibility (β) along the dilution line AB, the inset shows the respective variation in ultrasonic velocity (v).

It is well known that in nonionic MEs at low water contents, discrete reverse micelles (w/o) are formed within a continuous oil phase and the system shows electrical

conductivity (σ) similar to that of the oil phase [20, 21]. Conversely, systems with high water content, forming normal micelles (o/w) within a continuous aqueous phase, shows σ similar to that of pure water [20, 22]. We measure σ as a function of X_w to identify the microstructure type of the ME phase in the present investigation. Figure 4.3a is a representative σ vs. X_w profile for the studied ME system along the dilution line AB of Figure 4.1. The curve can be divided into three distinct segments. In the oil rich region σ is very low and increases marginally with X_w . The poor conductivity of the system in this region is due to the closed domains of water present in w/o MEs. The low conductive oil continuous phase in this region prevents continuous migration of the charge carriers and hence explains the low conductivity of the water droplets (w/o). On further addition of water σ increases and two sharp transition points are obtained at $X_w = 0.18$ and 0.30 . The transition at $X_w = 0.18$ could be correlated with the formation of bicontinuous ME where various interconnected surfactant domains form a network of conductive channel allowing effective transport of charge carriers and relatively higher values of σ can be realized [23]. The change in the slope of σ beyond $X_w = 0.30$ can be interpreted as a structural transition to o/w droplets. This transition takes place as at high X_w the aqueous phase becomes the continuous phase with surfactant coated oil droplets dispersed into it and a significant connectivity between aqueous domains is established.

The structural transition in ME essentially involves droplet association i.e., clustering and fusion. It must, therefore, have a direct influence on the internal structure and hence viscosity. Figure 4.3a (inset) shows the dynamic viscosity of the ME system along the dilution line AB. Bell shaped viscosity profile with flattened maxima is obtained as has earlier been reported using nonionic surfactants, tween 60/ethanol/R(+)-limonene/water/propylene glycol [24]; brij-35/butanol/eucalyptus oil/water [25]. The low initial viscosity of the system is attributed to the negligible interactions between the isolated ‘hard sphere-like’ water globules dispersed in the continuous oil medium [26]. With gradual addition of water, dispersed water droplets grow and the enhanced attractive interaction between them leads to the formation of water clusters. The increase in the viscosity in oil-rich MEs is thus derived from an increase in the dispersed droplet sizes and the enhanced attractive interactions between the droplets [27]. At the threshold composition such clustering leads to the formation of bicontinuous structure wherein the

infinite radius of curvature of the aggregate results in the maximum viscosity of the system. In our study the maximum of viscosity occurs at $X_w = 0.20$ wherein a bicontinuous ME is realized. Further addition of water causes a decrease in viscosity indicating that water, which is the least viscous component of the ME system, becomes the outer phase eventually forming o/w MEs. In this aqueous-rich region, viscosity gradually decreases expectedly due to a dilution effect of the o/w ME droplets. The viscosity data thus corroborates with the conductivity data and specify that with increasing water, the oil-continuous ME transforms into a bicontinuous form at $X_w = 0.20$ and with further addition of water ultimately it transforms into the water continuous structure.

Ultrasonic velocity (v) in the ME system as a function of X_w is displayed in Figure 4.3b, inset. ' v ' increases with the addition of water with small changes in the slope at two X_w values of ~ 0.18 and 0.30 , suggesting structural evolution at these concentrations. We also measure isentropic compressibility, β for all these systems and the results are shown in Figure 4.3b. A consistent decrease of β is observed with increasing water content with sharp changes in slope identified at X_w values of about 0.18 and 0.30 . The decrease in β with increasing X_w is expected, as the system becomes more water like with increasing X_w . The higher compressibility of the system at low water content is in well agreement with the viscosity behavior of the system which suggests hard sphere-like character of the water globules in oil continuous medium (w/o) [26]. The observed experimental trend of β with distinct changes in the slope, suggests the deviation of elastic properties of water in the ME system correlating the different structural identity of the MEs. Such finding is well in agreement with conductivity and viscosity behavior of the system with structural transition at ~ 0.18 and 0.30 wt. fraction of water.

Size characterization of the resulting ME is also essential in ensuring safe and efficient dosage. Monitoring of changes in the size distribution can provide valuable information for optimizing the formulation. Figure 4.4, inset shows a typical DLS curve for the ME system along the dilution line AB with X_w being 0.42 . The curve is single modal and the peak is rather narrow, indicating the low polydispersity of the sample. Figure 4.4 summarizes the effect of sample composition on the droplet size of MEs. In general, the droplet size is small, ranging from 4.7 to 10.3 nm. This is in line with previously published data [28, 29]. For w/o ME, "lipodynamic" diameter increases

expectedly with increasing water content indicating larger size of the water pool at higher X_w [29]. However, for o/w MEs the droplet size remains fairly constant with added water confirming their formation in the studied range of X_w . Notably the uncertain shape distribution of bicontinuous MEs prevents one to measure its size by DLS, which assumes aggregate shape as circular in size measurement.

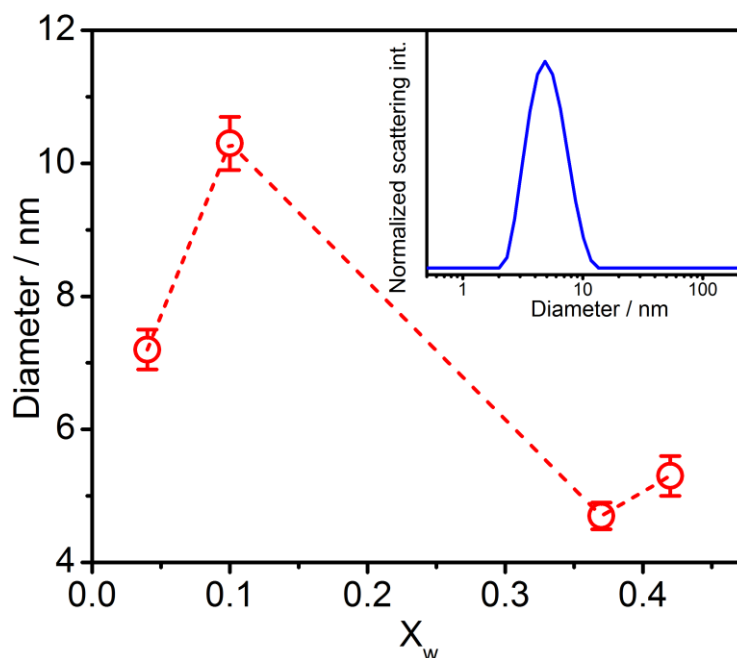


Figure 4.4. Diameter of MEs at various X_w values ($X_w =$ wt. fraction of water). The dotted line is guide to the eye. The inset shows a typical dynamic light scattering curve for the ME with $X_w = 0.42$.

We investigate the microenvironment characteristics of the domains in MEs using steady-state and time-resolved spectroscopic technique in order to understand the properties of water/oil molecules solubilized into the core. This knowledge is very useful to apply MEs as solubilizing media or as a template in a processes running on the interface between oil and water. The steady-state absorption and emission features are presented in Figure 4.5. In IPM, DCM exhibits an absorption peak at 455 nm (Figure 4.5a). But in MEs with $X_w = 0.04$ the absorption peak is red shifted to 465 nm (Figure 4.5a). The difference of the absorption spectra of DCM in MEs with that of DCM in IPM exhibits a negative absorption or depletion at 455 nm and a distinct peak at 510 nm (Figure 4.5a, inset). The negative absorption at 455 nm clearly indicates that upon addition of surfactants and water,

the population of DCM in the bulk IPM decreases. On the other hand, the emergence of the positive absorption peak at 510 nm indicates that in the presence of surfactants and water, the DCM molecules migrate to a highly polar region, which is presumably due to the

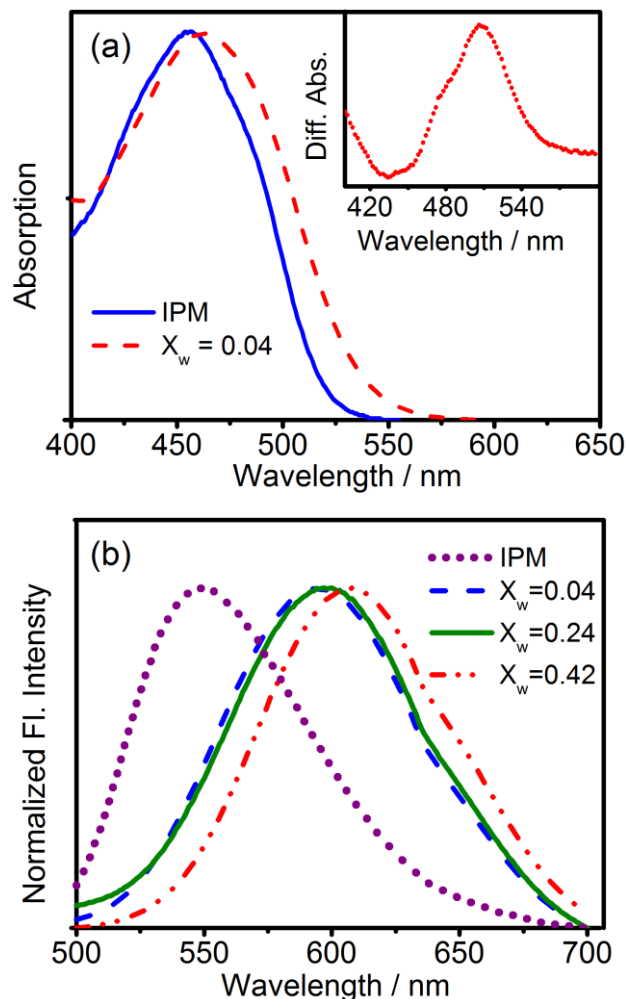


Figure 4.5. (a) Absorption spectra of DCM in $X_w = 0.04$ ME and in pure IPM, the inset shows the difference spectra (in arbitrary unit) between DCM in IPM with that of $X_w = 0.04$ ME. (b) Steady-state emission spectra of DCM excited at 409 nm in IPM and in MEs.

influence of the ME. The fluorescence spectra of DCM strongly depends on the polarity of the medium [30] and hence could act as a good reporter for the microenvironment of ME. Figure 4.5b is a representative illustration of the steady-state emission spectra of DCM at various X_w values excited at 409 nm. The corresponding emission peaks (λ_{\max}) are presented in Table 4.1. As is evidenced from the table, the emission peaks are significantly red shifted compared to DCM in IPM ($\lambda_{\max} = 548$ nm). It is known that in pure

hydrocarbon (e.g. isooctane) the emission peak of DCM is 530 nm and it is significantly red shifted to ~620 nm in polar solvent like methanol [30]. The red shifted emission peaks in the range of 596-608 nm (Table 4.1) strongly suggests the presence of a considerable fraction of DCM molecules at the surfactant-water interface of the ME where the microenvironment polarity is expected to be lower compared to that of the water present at the central core of the nanoscopic domain [31]. It could be noted that the emission peak of

Table 4.1. Steady-state fluorescence peak (λ_{\max}), fittings parameters of the solvent correlation function ($C(t)$) for the probe DCM in microemulsions of various X_w values. ^m

Wt. fraction of water (X_w)	Fluorescence peak, λ_{\max} (nm)	a_1 (%)	τ_1 (ns)	a_2 (%)	τ_2 (ns)	$\langle\tau_s\rangle$ (ns)	$\Delta\nu$ (cm ⁻¹)
0.04	596	50	0.15	50	2.06	1.11	1165
0.10	596	56	0.18	44	1.82	0.92	1071
0.20	600	48	0.14	52	1.91	1.06	1060
0.24	600	52	0.17	48	1.62	0.87	1016
0.37	605	56	0.13	44	1.39	0.68	1115
0.42	608	65	0.11	35	0.84	0.37	1073

^m τ_i represents the solvent correlation time constant, a_i represents its relative contribution and $\langle\tau_s\rangle$ is the average solvation time constant. $\Delta\nu$ represents fluorescence Stokes shift.

DCM appears at different wavelengths at different structural domains of the ME (Table 4.1). This observation supports our earlier observation regarding the existence of different structural entity at various X_w values and reveals the different micro-polarity experienced by the probe at respective aggregates. The minor red shift of the emission peak on going from $X_w = 0.37$ to 0.42 for o/w ME is notable and is discussed latter.

The probe DCM has previously been used to report the solvation dynamics of various organized nano assemblies [32, 33]. Here, we study the solvation dynamics of the probe in the ME system and investigate in details the effect of confinement on water relaxation dynamics with different structures of identical composing elements. Figure 4.6a and Figure 4.7 shows the decay transients of DCM at three selected wavelengths of 540 (at the blue end of the spectrum), 600 (around the peak position), and 670 nm (at the red end of the spectrum) for ME of different hydration level (X_w). It is evidenced from the figures that the decay pattern is strongly wavelength dependent for all the systems studied. For example, at $X_w = 0.04$ (Figure 4.6a) the blue end (540 nm) decays with the fitted four-exponential time constants of 0.07 ns (62%), 0.35 ns (22%), 1.19 ns (14%) and 3.57 ns

(2%). The transients get slower with increasing wavelength. For the extreme red wavelength (670 nm), a distinct rise component of 0.07 ns is produced along with the

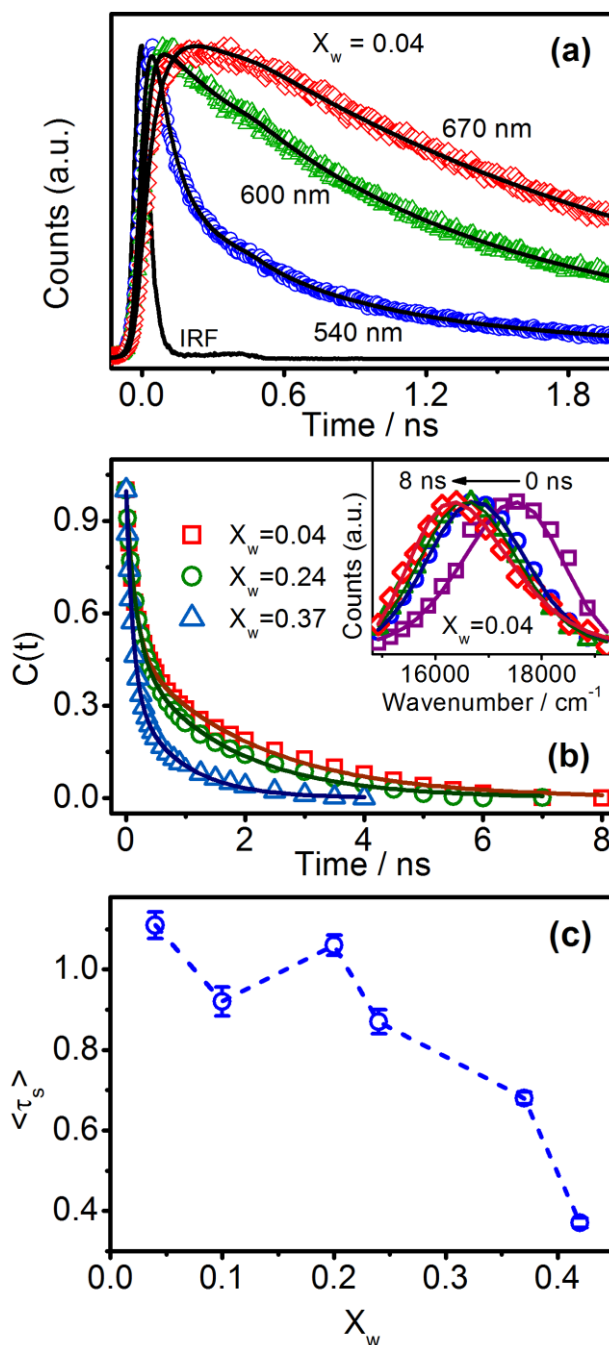


Figure 4.6. (a) Fluorescence decay transients of DCM in ME with $X_w = 0.04$. (b) Solvent correlation function, $C(t)$ of DCM in different MEs. The solid lines denote the best fit to biexponential decay. Time-resolved emission spectra (TRES) of DCM in ME with $X_w = 0.04$ are shown in the inset. (c) The average solvation time ($\langle \tau_s \rangle = a_1 \tau_1 + a_2 \tau_2$) for DCM in MEs of various X_w values. The dotted line is guide to the eye.

decay components of 1.93 ns and 4.3 ns. The presence of faster decay components at the blue end and a rise component at the red wavelength is indicative of solvation of the probe in the ME system.

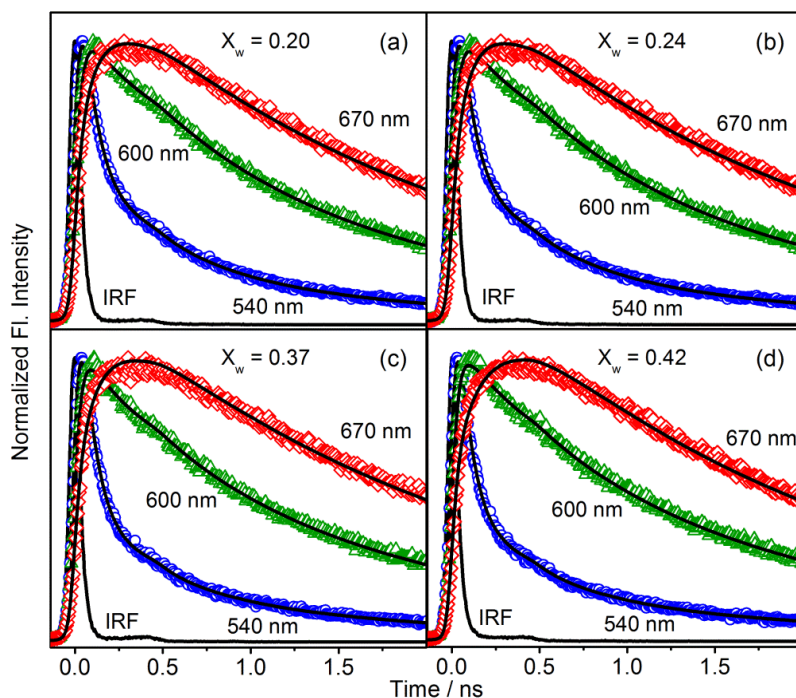


Figure 4.7. Fluorescence decay transients of DCM in microemulsions of different X_w values.

Using the decay transients at different wavelengths, we construct the time-resolved emission spectra (TRES) for different X_w values (inset of Figure 4.6b and Figure 4.8). A representative TRES for DCM with $X_w = 0.04$ is presented in the inset of Figure 4.6b wherein a significant dynamic fluorescence Stokes shift of 1165 cm^{-1} in 8 ns is observed. Similar Stokes shift for other systems are also listed in Table 4.1. The solvent correlation function, $C(t)$ obtained for all these systems are fitted with bi-exponential decay functions based on the core-shell model [34, 35] and the fitted parameters are presented in Table 4.1. The core-shell model is based on the fact that at least two distinctly different kinds of water molecules are present at the interface of MEs, that is, interfacial (shell) water molecules directly hydrogen bonded to the surfactant headgroups, which displays modified properties compared with bulk water and very slow relaxation dynamics (in the order of nanoseconds), and interior (core) or bulk-like water, which are not directly hydrogen

bonded to the surfactant headgroups but have properties slightly different from bulk water [34, 35]. Note that both these two types of water molecules relax at a time scale slower than that of bulk water (of the order of sub picoseconds [36]), which is probably due to the interaction of the surfactant headgroup with water. It is evident from Table 4.1 that for all the ME structures one of the solvation time constants is of the order of some hundreds of picoseconds, while the other is of the order of a few nanoseconds. It could be mentioned here that both the observed time constants are orders of magnitude slower than the sub-picosecond solvation time constant of bulk water [36]. It is now important to discard any possibility of the observed solvation dynamics by the oil itself since the probe is highly soluble in IPM. Unlike the ME systems, we do not observe any rise component in the decay transient of IPM/DCM system, which clearly indicates the lack of any “slow” solvation present in such system. It has to be mentioned here that a possibility of slow solvation dynamics may arise from the butyl lactate water mixture. We have determined the distribution of butyl lactate between oil phase and water phase and the molar ratio of butyl lactate in oil phase to water is found to be ~ 14.3 . To eliminate the possibility of a probable contribution of butyl lactate/water system towards the observed slow dynamics, we measure the decay transients of a saturated (4.2%, v/v) [37] butyl lactate/water solution. The observed dynamics is rather faster and hardly contribute to the observed slower dynamics of ME systems. The observed slow and relatively fast components for the MEs thus might generate out of the relaxation process by the interfacial bound type and free type water molecules; respectively present in the interface of ME structure. A similar two-component model consisting of a shell of interfacial water molecules and a bulk-like core has previously been applied to explore the slow dynamics of the water molecules inside various self-assembly like micelles [38], reverse micelles [39] and lamellar structures [40]. Notably over the past few years a significant number of studies has been directed towards understanding the water relaxation dynamics in ternary systems with varying parameters like surfactant charge [38], effect of counter ion [41], surfactant hydration [40, 42], micellar size [42-44], morphology of the aggregate [40, 44] etc. However time-resolved solvation dynamics studies led by Levinger *et al.* [45] show that the solvent reorganization in quaternary micellar systems is significantly slower than in ternary micellar systems, indicating that the probe molecule is located at the micellar interface regardless of alkanol

or surfactant. Their study concludes that the environment sensed by the probe C343 in different studied reverse micelles is the same despite the differences in the surfactant or cosurfactant used to make the reverse micelles. Bhattacharyya and coworkers [46] studied the solvation dynamics of 4-aminophthalimide in w/o ME of Triton X-100 in mixed solvents. Their study finds the bimodal solvation response of surrounding water molecules. Despite all these efforts, a detailed systematic investigation of water relaxation dynamics

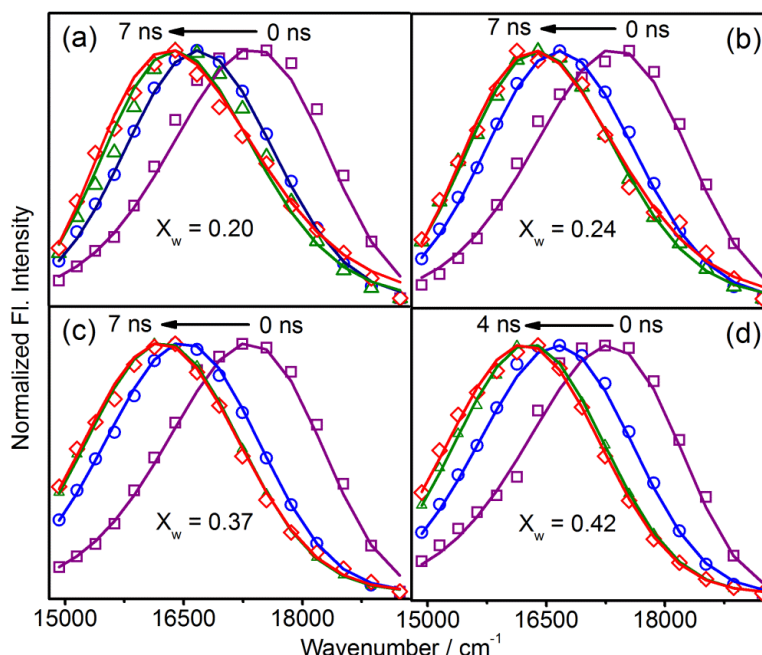


Figure 4.8. Time-resolved emission spectra (TRES) of DCM in microemulsions of various X_w values.

for quaternary ME of different structural identity with similar composing elements is still lacking and is one of our major concerns in the present study.

Let's compare the solvation dynamics in different nano assemblies. The slow relaxation dynamics of water as obtained in different structures of ME in the present study have been summarized in Table 4.1 and Figure 4.6b. As observed from the table, for w/o ME at low water content ($X_w = 0.04$) the decay consists of a slow time constant of 2.06 ns and a relatively faster time constant of 0.15 ns. At higher water content ($X_w = 0.10$) the decay of $C(t)$ is still bi-exponential, but relatively faster and consists of a component of 1.82 ns and 0.18 ns with increased contribution of the faster moving bulk water. This observation is justifiable in view of the larger size of the ME for $X_w = 0.10$ compared to

$X_w = 0.04$ (Figure 4.4), resulting an increase in the curvature of the surfactant film and hence a greater fraction of water interacts with the interface leading to a relatively faster relaxation [44, 47]. In the present study the time scale obtained for DCM solvation in w/o ME is consistent with that obtained for the same probe in AOT/n-haptane ME with $w_0 = 20$, where $w_0 = [\text{water}]/[\text{surfactant}]$ [33]. It is to be remembered that the size of AOT reverse ME at $w_0 = 20$ is comparable [39] to the size range found for the w/o system studied here (Figure 4.4). In the oil-in-water ME system ($X_w = 0.37$ and 0.42) it can be observed that (Table 4.1) the water relaxation dynamics gets significantly affected with increasing X_w . The average solvation time ($\langle \tau_s \rangle = a_1 \tau_1 + a_2 \tau_2$) for $X_w = 0.37$ is 0.68 ns whereas it decreases to 0.37 ns for $X_w = 0.42$. Observing their comparable size (Figure 4.4), at first, it seems quite contradictory in view of our earlier discussion on water dynamics in w/o system. However it should be noted that the λ_{max} value for $X_w = 0.42$ is red shifted compared to that of $X_w = 0.37$ (Table 4.1), suggesting that in o/w ME with $X_w = 0.42$ the location of the probe is shifted little towards the bulk water compared to that of $X_w = 0.37$ and this difference in location is manifested with significantly higher contribution of bulk water with overall faster dynamics of solvation for the latter. At this stage we would like to compare the dynamics of solvation between the two micellar entities just discussed. In many ways the solvation dynamics of water in o/w ME resembles to that of w/o. First, the overall solvation dynamics are significantly slower than those in the bulk water [36] and other polar solvents like methanol, acetonitrile, ethylene glycol etc [48]. Second, both the $C(t)$ functions can be fitted well to bi-exponential decays. Despite

Table 4.2. Fluorescence anisotropy data ($r(t)$) for DCM in MEs at different X_w values. ^m

Wt. fraction of water (X_w)	$r(0)$	a_{fast} (%)	τ_{fast} (ns)	a_{slow} (%)	τ_{slow} (ns)	$\langle \tau_r \rangle$ (ns)
0.04	0.27	14	0.07	86	1.26	1.09
0.10	0.30	24	0.07	76	1.29	0.99
0.20	0.26	07	0.08	93	0.99	0.93
0.24	0.30	14	0.05	86	1.06	0.92
0.37	0.31	25	0.03	75	1.30	0.98
0.42	0.30	20	0.04	80	1.03	0.83

^m τ_i represents the anisotropy time constant and a_i represents its relative weight in the total anisotropy.

the similarities the most striking difference is that water dynamics is much faster in the o/w ME compared to w/o (Figure 4.6c) revealing the confinement of water in the interior of

w/o reverse ME system with restricted translational and rotational motion resulting in a substantially slower dynamics. Now looking into the solvation time components of bicontinuous ME (Table 4.1) one can similarly see bi-exponential decay of $C(t)$ with slower relaxation dynamics compared to bulk water. It should be noted here that the structural nature of bicontinuous ME is much complex and quite difficult to predict. The uncertainty lies in its shape, aggregation stability, dimension etc. From Table 4.1 and Figure 4.6c it is evident that with increasing water content the overall dynamics gets faster at and beyond $X_w \sim 0.2$, which is quite consistent with the conductivity, viscosity and sound velocity measurements. The faster solvation time for $X_w = 0.24$ compared to $X_w = 0.20$ is believed to be due to the transition of water in oil reverse bicontinuous to oil in water bicontinuous ME making the overall dynamics faster with the probe being present in water continuous region of the latter.

To ascertain the geometrical restriction of the probe in the interfacial region, we measure the time-resolved anisotropy of the probe in selected MEs of different structural identity. Typical anisotropy decays are shown in Figure 4.9. As observed in Figure 4.9 and Table 4.2, all the anisotropy decay transients can be fitted bi-exponentially. The rotational time constants observed (Table 4.2) are of the order of hundreds of picoseconds (τ_{fast}) and a few nanoseconds (τ_{slow}), which are in the same order of magnitude as previously reported for micelles [49] with the same probe molecules. The observed τ_{fast} and τ_{slow} could be correlated to the wobbling motion and lateral diffusion of the probe molecule, respectively [50, 51]. It could be noted that the time components obtained in this study are significantly slower than the picosecond time scale reported in bulk water [52] indicating a hindered rotation of the probe in the ME. This shows that the dye experiences higher microviscosity in MEs in comparison to that in bulk water and illustrates the residence of the probe in the interfacial layer of the ME. It could be noted that the $r(0)$ (anisotropy at time zero) values reported in the present systems are smaller than the ideal value of 0.4 (Table 4.2). The limited resolution of our picoseconds-resolved experimental setup (~ 80 ps instrument response function, IRF) is unable to detect the ultrafast components of the rotational motion, which eventually reduces the $r(0)$ values. We plot the average rotational time

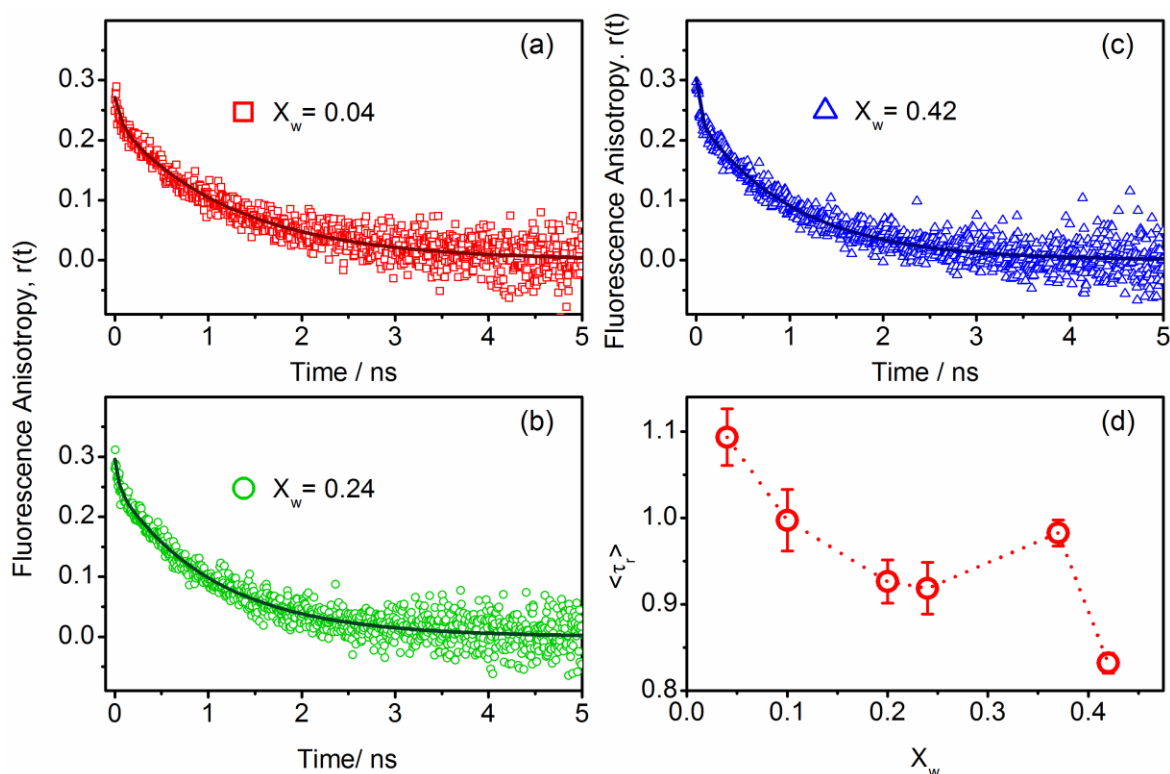


Figure 4.9. Time-resolved fluorescence anisotropy decay, $r(t)$, of DCM in MEs with (a) $X_w = 0.04$ (b) $X_w = 0.24$ (c) $X_w = 0.42$. (d) The average rotational anisotropy ($\langle \tau_r \rangle = a_{fast}\tau_{fast} + a_{slow}\tau_{slow}$) values for DCM in MEs of various X_w values. The dotted line is guide to the eye.

against X_w (Figure 4.9d). The figure resembles the solvation profile wherein $\langle \tau_s \rangle$ decreases with increasing X_w . The decreased $\langle \tau_r \rangle$ with increasing X_w indicates progressive release of restriction on the probe which eventually ease the translational and rotational motion of the probe molecule and hence decreasing $\langle \tau_s \rangle$.

4.3. Conclusion:

A novel tween based edible microemulsion (ME) has been formulated. A large single phase region is obtained in the pseudo-ternary phase diagram of the system. The phase behavior of the system remains almost unaltered at low pH (2.6) and in 0.9% salt concentration which provides a good opportunity for this system to use in drug delivery applications. The pseudo-ternary system is found to undergo phase transitions from w/o to bicontinuous and from bicontinuous to o/w ME along water dilution line. The transitions are identified at two distinct X_w values (water wt. fraction) using conductivity, viscosity, ultrasonic compressibility and velocity studies. Micropolarity of the ME environments are

successfully probed by the solvatochromic dye DCM. Both steady-state absorption and emission spectra show the dye to reside in the surfactant water interface of the MEs and suggests the efficacy of the MEs to host the model drug/ligand DCM. The significant rotational hindrance of the dye in time-resolved fluorescence anisotropy study, further confirms its presence at the interface. The dynamical solvation of water in the ME has been unveiled using picosecond time-resolved fluorescence spectroscopy. The study finds strong correlation in the relaxation dynamics of water with the structure of host assembly and offers an edible ME system which could act as a potential drug delivery system and nontoxic nano-template for other applications.

References:

- [1] G.W. Robinson, S.B. Singh, M.W. Evans, Water in biology, chemistry and physics, World Scientific, Singapore, 1996.
- [2] M.M. Teeter, Water-protein interactions: Theory and experiment, *Ann. Rev. Biophys. Chem.* 20 (1991) 577.
- [3] R.K. Mitra, S.S. Sinha, P.K. Verma, S.K. Pal, Modulation of dynamics and reactivity of water in reverse micelles of mixed surfactants, *J. Phys. Chem. B* 112 (2008) 12946.
- [4] R.K. Mitra, P.K. Verma, D. Banerjee, S.K. Pal, Hydrogen bonding barrier crossing dynamics at bio-mimicking surfaces, K.-L. Han, G.-J. Zhao (Eds.), Hydrogen bonding and transfer in the excited state, John Wiley, Chippenham, 2010.
- [5] M. Sundaralingam, Y.C. Sekharudu, Water-inserted alpha-helical segments implicate reverse turns as folding intermediates, *Science* 244 (1989) 1333.
- [6] N. Nandi, K. Bhattacharyya, B. Bagchi, Dielectric relaxation and solvation dynamics of water in complex chemical and biological systems, *Chem. Rev.* 100 (2000) 2013.
- [7] J.H. Tian, A.E. Garcia, Simulations of the confinement of ubiquitin in self-assembled reverse micelles, *J. Chem. Phys.* 134 (2011) 225101.
- [8] A.V. Martinez, S.C. DeSensi, L. Dominguez, E. Rivera, J.E. Straub, Protein folding in a reverse micelle environment: The role of confinement and dehydration, *J. Chem. Phys.* 134 (2011) 055107.
- [9] P.A. Reynolds, E.P. Gilbert, J.W. White, High internal phase water-in-oil emulsions and related microemulsions studied by small angle neutron scattering. 2. The distribution of surfactant, *J. Phys. Chem. B* 105 (2001) 6925.
- [10] J.-W. Benjamins, K. Thuresson, T. Nylander, Formation of a liquid crystalline phase from phosphatidylcholine at the oil-aqueous interface, *Langmuir* 21 (2005) 2804.
- [11] O. Söderman, M. Nydén, NMR in microemulsions. NMR translational diffusion studies of a model microemulsion, *Colloids Surf., A* 158 (1999) 273.

- [12] M. Giustini, G. Palazzo, G. Colafemmina, M.D. Monica, M. Giomini, A. Ceglie, Microstructure and dynamics of the water-in-oil CTAB/n-pentanol/n-hexane/water microemulsion: A spectroscopic and conductivity study, *J. Phys. Chem.* 100 (1996) 3190.
- [13] M. Maestro, Enzymatic activity in reverse micelles-some modellistic considerations on bell-shaped curves, *J. Mol. Liq.* 42 (1989) 71.
- [14] N. Garti, A. Aserin, I. Tiunova, S. Ezrahi, Sub-zero temperature behavior of water in non-ionic microemulsions, *J. Therm. Anal. Calorim.* 51 (1998) 63.
- [15] A. Amararene, M. Gindre, J.-Y.L. Hue´rou, C. Nicot, W. Urbach, M. Waks, Water confined in reverse micelles: Acoustic and densimetric studies, *J. Phys. Chem. B* 101 (1997) 10751.
- [16] R.C. Rowe, P.J. Sheskey, S.C. Owen, Handbook of pharmaceutical excipients, Pharmaceutical Press and American Pharmacists Association, London, 2006.
- [17] Isopropyl Myristate; Tolerance Exemption, Environmental protection agency: 40 CFR Part 180, Federal Register: February 1, 1995, <http://www.epa.gov/fedrgstr/EPA-PEST/1995/February/Day-01/pr-126.html>.
- [18] L.d. Campo, A. Yaghmur, N. Garti, M.E. Leser, B. Folmer, O. Glatter, Five-component food-grade microemulsions: Structural characterization by SANS, *J. Colloid Interface Sci.* 274 (2004) 251.
- [19] R. Saha, S. Rakshit, R.K. Mitra, S.K. Pal, Microstructure, morphology, and ultrafast dynamics of a novel edible microemulsion, *Langmuir* 28 (2012) 8309.
- [20] S. Ezrahi, E. Wachtel, A. Aserin, N. Garti, Structural polymorphism in a four-component nonionic microemulsion, *J. Colloid Interface Sci.* 191 (1997) 277.
- [21] J.F. Billman, E.W. Kaler, Structure and phase behavior in four-component nonionic microemulsions, *Langmuir* 7 (1991) 1609.
- [22] A. Arvidsson, O. Söderman, The microemulsion phase in the didecyldimethylammonium bromide/dodecane/water system. Phase diagram, microstructure, and nucleation kinetics of excess oil phase, *Langmuir* 17 (2001) 3567.
- [23] F. Podlogar, M.B. Rogač, M. Gašperlin, The effect of internal structure of selected water-tween 40-imwitor 308-IPM microemulsions on ketoprofene release, *Int. J. Pharm.* 302 (2005) 68.

- [24] A. Yagmur, A. Aserin, B. Antalek, N. Garti, Microstructure considerations of new five-component Winsor IV food-grade microemulsions studied by pulsed gradient spin-echo NMR, conductivity, and viscosity, *Langmuir* 19 (2003) 1063.
- [25] R.K. Mitra, B.K. Paul, Physicochemical investigations of microemulsification of eucalyptus oil and water using mixed surfactants (AOT + brij-35) and butanol, *J. Colloid Interface Sci.* 283 (2005) 565.
- [26] M. Gradzielski, H. Hoffman, Rheological Properties of Microemulsions, P. Kumar, K.L. Mittal (Eds.), Handbook of microemulsion science and technology, Marcel Dekker, New York, 1999, 161.
- [27] Z. Saidi, C. Mathew, J. Peyrelasse, C. Boned, Percolation and critical exponents for the viscosity of microemulsions, *Phys. Rev. A* 42 (1990) 872.
- [28] O. Rojas, J. Koetz, S. Kosmella, B. Tiersch, P. Wacker, M. Kramer, Structural studies of ionic liquid-modified microemulsions, *J. Colloid Interface Sci.* 333 (2009) 782.
- [29] M.A. Polizelli, V.R.N. Telis, L.Q. Amaral, E. Feitosa, Formation and characterization of soy bean oil/surfactant/water microemulsions, *Colloids Surf., A* 281 (2006) 230.
- [30] M. Meyer, J.C. Mialocq, Ground state and singlet excited state of laser dye DCM: Dipole moments and solvent induced spectral shifts, *Opt. Commun.* 64 (1987) 264.
- [31] C.D. Geddes, J.R. Lakowicz, Reviews in fluorescence, Springer, Maryland, USA, 2005.
- [32] R. Saha, P.K. Verma, R.K. Mitra, S.K. Pal, Structural and dynamical characterization of unilamellar AOT vesicles in aqueous solutions and their efficacy as potential drug delivery vehicle, *Colloids Surf., B* 88 (2011) 345.
- [33] S.K. Pal, D. Mandal, D. Sukul, K. Bhattacharyya, Solvation dynamics of 4-(dicyanomethylene)-2-methyl-6-(p-dimethylaminostyryl)-4H-pyran (DCM) in a microemulsion, *Chem. Phys. Lett.* 312 (1999) 178.
- [34] I.R. Piletic, D.E. Moilanen, D.B. Spry, N.E. Levinger, M.D. Fayer, Testing the core/shell model of nanoconfined water in reverse micelles using linear and nonlinear IR spectroscopy, *J. Phys. Chem. A* 110 (2006) 4985.
- [35] J. Faeder, B.M. Ladanyi, Molecular dynamics simulations of the interior of aqueous reverse micelles, *J. Phys. Chem. B* 104 (2000) 1033.

- [36] R. Jimenez, G.R. Fleming, P.V. Kumar, M. Maroncelli, Femtosecond solvation dynamics of water, *Nature* 369 (1994) 471.
- [37] M. Goral, D.G. Shaw, A. Maczynski, B. Wisniewska-Gocłowska, IUPAC-NIST solubility data series. 88. esters with water-revised and updated. part 3. C(7) to C(9) esters, *J. Phys. Chem. Ref. Data* 39 (2010) 023102.
- [38] Y. Tamoto, H. Segawa, H. Shirota, Solvation dynamics in aqueous anionic and cationic micelle solutions: Sodium alkyl sulfate and alkyltrimethylammonium bromide, *Langmuir* 21 (2005) 3757.
- [39] R.K. Mitra, S.S. Sinha, S.K. Pal, Temperature-dependent solvation dynamics of water in AOT/isooctane reverse micelles, *Langmuir* 24 (2008) 49.
- [40] P.K. Verma, R. Saha, R.K. Mitra, S.K. Pal, Slow water dynamics at the surface of macromolecular assemblies of different morphologies, *Soft Matter* 6 (2010) 5971.
- [41] M.R. Harpham, B.M. Ladanyi, N.E. Levinger, The effect of the counterion on water mobility in reverse micelles studied by molecular dynamics simulations, *J. Phys. Chem. B* 109 (2005) 16891.
- [42] M. Kumbhakar, S. Nath, T. Mukherjee, H. Pal, Solvation dynamics in triton-X-100 and triton-X-165 micelles: Effect of micellar size and hydration *J. Chem. Phys.* 121 (2004) 6026.
- [43] D.M. Willard, R.E. Riter, N.E. Levinger, Dynamics of polar solvation in lecithin/water/cyclohexane reverse micelles, *J. Am. Chem. Soc.* 120 (1998) 4151.
- [44] D.M. Willard, N.E. Levinger, Influence of morphology on polar solvation dynamics in lecithin reverse micelles, *J. Phys. Chem. B.* 104 (2000) 11075.
- [45] E.M. Corbeil, N.E. Levinger, Dynamics of polar solvation in quaternary microemulsions, *Langmuir* 19 (2003) 7264.
- [46] D. Mandal, A. Datta, S.K. Pal, K. Bhattacharyya, Solvation dynamics of 4-aminophthalimide in water-in-oil microemulsion of triton X-100 in mixed solvents, *J. Phys. Chem. B* 102 (1998) 9070.
- [47] D.E. Moilanen, E.E. Fenn, D. Wong, M.D. Fayer, Water dynamics in large and small reverse micelles: From two ensembles to collective behavior, *J. Chem. Phys.* 131 (2009) 014704.

- [48] P.v.d. Meulen, H. Zhang, A.M. Jonkman, M. Glasbeek, Subpicosecond solvation relaxation of 4-(dicyanomethylene)-2-methyl-6-(p-(dimethylamino)styryl)-4h-pyran in polar liquids, *J. Phys. Chem.* 100 (1996) 5367.
- [49] R.K. Mitra, S.S. Sinha, S.K. Pal, Temperature dependent hydration at micellar surface: Activation energy barrier crossing model revisited, *J. Phys. Chem. B* 111 (2007) 7577.
- [50] G. Lipari, A. Szabo, Model-free approach to the interpretation of nuclear magnetic resonance relaxation in macromolecules. 1. Theory and range of validity, *J. Am. Chem. Soc.* 104 (1982) 4546.
- [51] C.C. Wang, R. Pecora, Time-correlation functions for restricted rotational diffusion, *J. Chem. Phys.* 72 (1980) 5333.
- [52] D. Banerjee, P.K. Verma, S.K. Pal, Temperature-dependent femtosecond-resolved hydration dynamics of water in aqueous guanidinium hydrochloride solution, *Photochem. Photobiol. Sci.* 8 (2009) 1441.

Chapter 5

Ultrafast Spectroscopic Studies on the Molecular Interaction of Biologically Relevant Small Molecules with Biomimetic Self-assembly

5.1. Introduction:

In recent years, it has become increasingly clear that there are important differences between protein conformational dynamics *in vivo* and *in vitro*, mostly due to the different environment. The cellular environment is crowded with lipids, carbohydrates and other protein molecules, whereas the buffers used for *in vitro* experiments are usually at the infinite dilution limit. Moreover, in such crowded environment, biomolecules find themselves inside a small compartments or pores with dimensions comparable to the size of large macromolecules created by the cytoskeletal structures or by the central cage of the chaperonin proteins [1-3]. This altered environment is dynamically different from *in vitro* dilute solutions and could have significant influence on the structure, function and dynamics of biomolecules. The interaction of various model drugs and biologically relevant small molecules with various biomimicking self-assemblies could prolong our understanding on the characteristics of biological macromolecules in real cellular environment.

Vesicles have considerable structural similarity with biological membranes including high encapsulation property, permeability and have widely been used in several applications including biomimicking [4], drug delivery [5], synthesis of nanoparticle (NPs) [6], biochemical catalysis [7], cosmetics [7] etc. Preparation of vesicles involves rather simple and straightforward approach. In one of the methods it is formed by phospholipids that usually require some additional energy like ultrasonication [8]. The vesicles thus obtained are metastable and easy to fuse. On the other hand, the spontaneous formation of thermodynamically stable, long lived vesicles has been realized in a variety of aqueous surfactant solutions [9-21]. Out of these Aerosol OT (sodium bis(2-ethylhexyl)

sulfosuccinate, AOT) is a well-studied surfactant, which forms reverse micelles (RMs) of well-defined structure in organic oil [22]. It is a versatile double tailed medicinal surfactant [23] which is known as a transdermal drug delivery vehicle in normal micellar form [24]. By virtue of its nontoxicity, spontaneously formed and thermodynamically stable long lived AOT vesicles in unilamellar form might establish a potential application. Although the detailed phase diagram of AOT-water system is available in literature [25, 26], a comprehensive understanding of the structure and dynamics of the vesicle-forming water-rich region needs to be extensively studied as only a handful of reports are available in the literature that relate various morphologies and mechanical properties of AOT vesicle [27, 28]. Moreover, complete characterization of the aggregate structure in aqueous solution (unilamellar or multilamellar) including dynamical states of water in such systems at different temperatures have not yet been attempted. Much like the above “normal” vesicles in water, one can also find their counterparts in organic, nonpolar “oils”, and these are termed “reverse” vesicles (RVs) [29-32]. With a nonpolar organic solvent being the continuous medium, amphiphilic molecules in RVs self-assemble in an opposite way with hydrophilic parts inside and hydrophobic parts outside. The study of RVs is of great fundamental interest since knowledge about molecular bilayers, which play an important role in living cells, can be obtained through a thoroughly new viewpoint.

In this chapter, we have reported our study on the structural and dynamical states of water in various biomimicking vesicle systems using numerous spectroscopic techniques. We have studied the interaction of various model drugs with the vesicles. Within the scope of the study we have also explored the drug delivery potentiality of AOT vesicles and found RVs to be a potential template for metal NP synthesis useful for ultrasensitive detection of molecular analytes.

5.2. Results and Discussion:

5.2.1. Structural and Dynamical Characterization of Unilamellar AOT Vesicles in Aqueous Solutions and their Efficacy as Potential Drug Delivery Vehicle [33]:

In order to measure the size of the self-aggregate of AOT in dilute aqueous solution, dynamic light scattering (DLS) measurements are carried out at three different AOT concentrations (9, 14 and 18 mM; inset of Figure 5.1a) and at various temperatures. A

representative intensity distribution curve for 18 mM AOT solution is presented in Figure 5.1a which indicates an aggregate size of ~140 nm. Similar size distribution is obtained with 9 and 14 mM AOT concentrations. It can be emphasized here that the distribution profile is unimodal in both intensity ($\propto d^6$) distribution as well as in volume ($\propto d^3$) distribution profile (d being the diameter of particles) with relatively low (~0.2) polydispersity index (PDI), suggesting the existence of aggregates of uniform sizes. Here the higher hydrodynamic diameter with unimodal size distribution indicates the formation of AOT vesicles, rather self-assembly of AOT molecules to form micelles. The previously reported CVC (critical vesicle concentration) of 7.8 mM [27, 34] and CMC (critical micelle concentration) of 2.66 mM [35-37] strongly suggests the preferential formation of vesicles in the studied concentration range. An important question is worth introducing here is whether the vesicles are unilamellar or multilamellar. It is known that geometrical properties of multilamellar vesicles (MLV) depend upon the concentration of the vesicle forming amphiphile and increase in amphiphile concentration adds up new layers in MLV resulting in a concentration dependent growth of vesicle size [38]. The uniformity in the concentration independent size distribution of vesicles in the present study confirms the unilamellar vesicle (ULV) formation. Temperature dependent DLS study (inset of Figure 5.1a) shows a single monodispersed (with low PDI) peak with a slight decrease in the vesicle size with temperature. Shedding of water molecules from hydration layer, as has also been observed in micelles at higher temperature [39] is an obvious reason for this change, moreover, the increased contribution of faster moving bulk water [40] (which extends from fs to ps) at higher temperature also limits the estimation of hydration layer by slow DLS (which extends from ns to ms) technique to a smaller value. It is also to be noted here that self-assembled structures (like micelles, RMs, vesicles etc.) retain a dynamic equilibrium in solution which manifests dynamic exchange of solutes (amphiphiles), and is a function of temperature and solvent properties. Exclusion of water from the vesicle-pool during the dynamic exchange of solutes at higher temperature might be one of the reasons for this change. Thus the change in the vesicle size is a cumulative approach and its reversibility provides evidence of the very physical nature of the size reduction. The overall retention

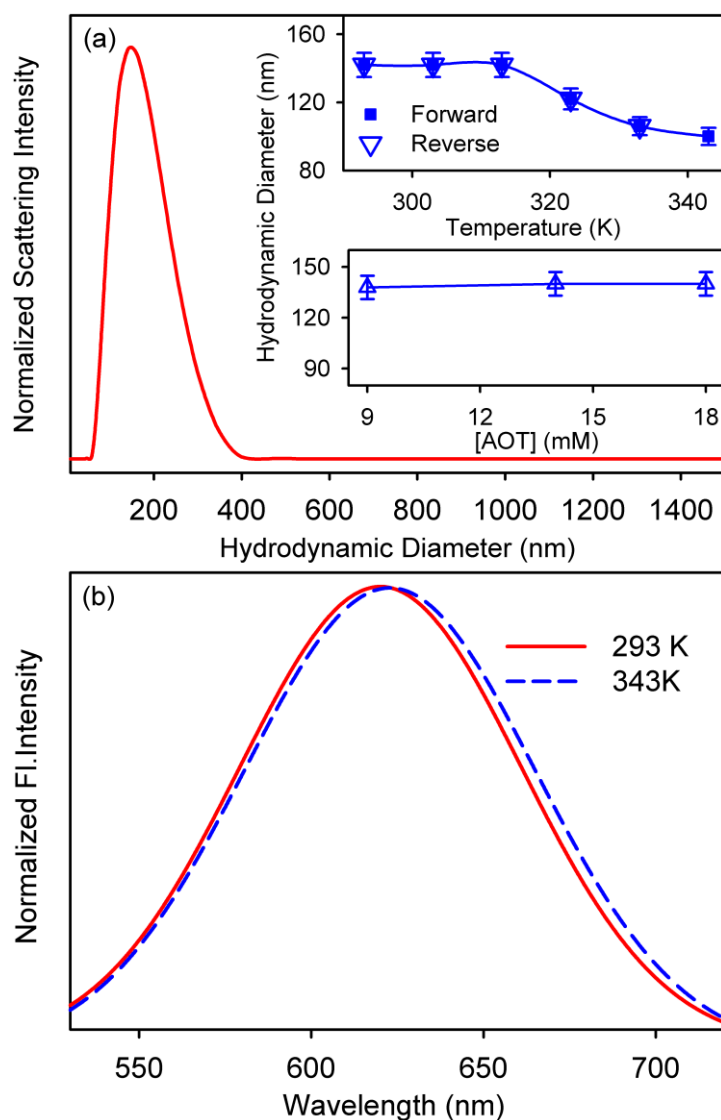


Figure 5.1. (a) A typical dynamic light scattering (DLS) signal of 18 mM AOT/water vesicle at 293 K. Change in hydrodynamic diameter of 18 mM AOT/water vesicles at different temperatures in both forward and reverse mode have been shown in the inset. The concentration independent vesicle diameter is shown in another inset. (b) Emission spectrum of DCM excited at 375 nm in 18 mM AOT/water vesicle at 293 K and 343 K.

of size and monodispersity provides evidence of existence of only vesicle structures even at elevated temperatures.

The aging effect on the size of the vesicles is examined by DLS experiment. Freshly prepared vesicles show a diameter of about ~140 nm and it remains unchanged even after 15 days with an almost unchanged PDI value (~0.2) (Table 5.1). The transparency of the solution is also found to be retained with aging confirming the stability of the ULV with time, which is a prerequisite for a potential drug delivery vehicle.

Table 5.1. *Hydrodynamic Diameter of 18 mM AOT/water vesicle at different time intervals.*

Day	Hydrodynamic Diameter (nm)
1	140
3	141
6	140
9	138
12	140
15	141

As the vesicles are non-fluorescent, the spectroscopic study is probed by 4-(dicyanomethylene)-2-methyl-6-(p-dimethylaminostyryl)-4H-pyran (DCM). Figure 5.1b depicts the fluorescence spectra of DCM in 18 mM AOT vesicle, excited at 375 nm, at 293 and 343 K. The emission peak, which is obtained at 620 nm at 293 K, is consistent with the value found for DCM in Triton X-100, cetyltrimethylammonium bromide and sodium dodecyl sulfate (SDS) micelles [41]. The position of the emission maximum of DCM in AOT vesicle is found to be similar to that in highly polar solvents, e.g. methanol, formamide etc [42, 43]. It may be recalled here that in pure hydrocarbon (e.g. n-heptane) DCM exhibits very weak emission with quantum yield of 0.01 and emission maximum at 530 nm [44]. The emission quantum yield of DCM is also known to increase with increase in solvent polarity and is 0.44 in methanol [45]. The red shifted emission maximum (620 nm) and relatively high quantum yield (0.36) value of DCM in AOT vesicles suggest that DCM molecules stay in the polar interface of the vesicles instead of the dry hydrocarbon layer. The insignificant red shift (~2 nm) (Figure 5.1b) in the peak position of the probe at higher temperature signifies that the microenvironment of the probe does not change appreciably with temperature and it resides in the interface only.

To probe the dynamics of water entrapped in the AOT vesicles we study the picosecond-resolved fluorescence spectroscopy of the solvation probe, DCM. The fluorescence decay transients of DCM in AOT vesicles at three representative wavelengths at 293 K are presented in Figure 5.2a. It is evident from the figure that the decay patterns are strongly wavelength dependent. At 560 nm, the transient decays fast with time components of 140 ps (60%), 670 ps (30%) and 1680 ps (10%). For the extreme red wavelength (680 nm), a distinct rise component of 210 ps is obtained along with decay components of 995 ps and 1800 ps. The presence of faster decay components at the blue

end and a rise component at the red wavelength is indicative of solvation in the vesicles. As the temperature is increased to 343 K, the transients still show wavelength dependency, however, with a decrease in the time constants, indicating increased mobility of the solvating species at elevated temperatures.

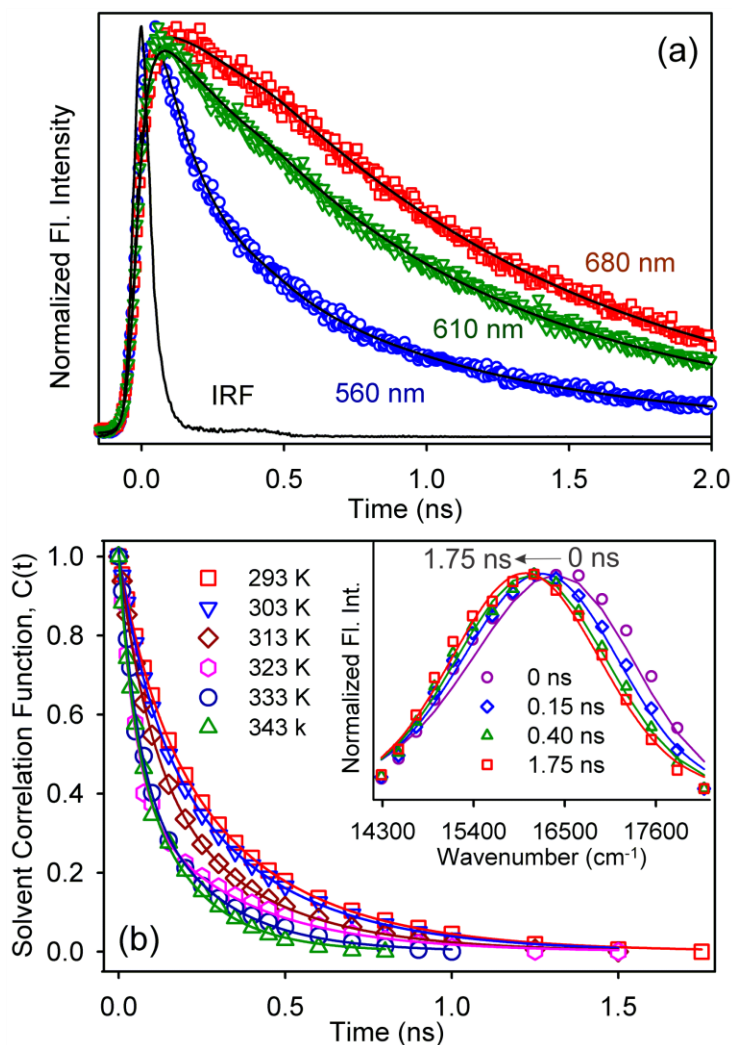


Figure 5.2. (a) Fluorescence decays of DCM in 18 mM AOT/water vesicle at 293 K, at 560, 610 and 680 nm. (b) Solvent correlation function, $C(t)$ of DCM in 18 mM AOT/water vesicle at 293, 303, 313, 323, 333 and 343 K. The solid lines denote the best fit to biexponential decay. Time-resolved emission spectra of DCM in 18 mM AOT/water vesicle at 293 K are shown in the inset.

The time-resolved emission spectra (TRES) of DCM in AOT vesicles are constructed at different temperatures following the procedure given in the previous section. A typical TRES for DCM in AOT vesicle as obtained at 293 K is depicted in the inset of

Figure 5.2b. The $C(t)$ curves obtained at different temperatures are fitted bi-exponentially (Figure 5.2b) and the fitted parameters are presented in Table 5.2. It is observed from Table 5.2 that the time constants are in the order of several tens of and several hundreds of picoseconds, respectively. It can be noted that both these components are slower than the subpicosecond solvation time scale reported for bulk water [46]. As has been inferred from steady-state measurements the observed solvation dynamics appear to be due exclusively to the DCM molecules residing at the AOT water interface, a conclusion also supported

Table 5.2. Solvation correlation data for DCM in 18 mM AOT/water vesicle at different temperatures. ^m

Temperature (K)	a ₁ (%)	τ ₁ (ns)	a ₂ (%)	τ ₂ (ns)	<τ _s > (ns)	E _a (kcal mol ⁻¹)
293	32	0.11	68	0.37	0.29	3.7 ± 0.2
303	35	0.10	65	0.36	0.26	
313	49	0.09	51	0.33	0.21	
323	60	0.05	40	0.32	0.16	
333	49	0.05	51	0.22	0.14	
343	41	0.04	59	0.18	0.12	

^m τ_i represents the solvent correlation time constant, a_i represents its relative contribution and <τ_s> the average solvation time constant. Estimated maximum error in determination of τ_i is 6%.

from the fact that DCM in hydrocarbon produces very short lifetime of ~ 50 ps as opposed to the considerably slow decay time constants found in the present study. The observed average solvation time ($\langle \tau_s \rangle = a_1\tau_1 + a_2\tau_2$) of 0.29 ns at 293 K is comparable to that of DCM obtained in the interfacial stern layer of SDS micelle [39]. The two slow time components obtained in the present study have their origin from the relaxation of the interfacial bound type (hydrogen bonded to the polar headgroup, τ₂) and free type water molecules (not directly hydrogen bonded to the headgroup, but hydrogen bonded to the interfacial-bound water, τ₁) present in the interface of AOT vesicles. This observation also provides supports towards the unilamellarity of AOT vesicles as explained below. The entrapped water pool of unilamellar AOT vesicle is considerably bigger (radius ~68.0 nm) than those of the water pool of the reverse micelles (radius < 10 nm). Earlier Bhattacharya *et al.* reported that in AOT microemulsion ([H₂O]/[AOT] = 20), DCM exhibits bimodal solvation dynamics with time components of 0.3 ns and 2.4 ns, respectively having an average time constant of 1.23 ns [44]. This solvation time gets faster as the water pool

radius increases, which in turn is due to the addition of fast moving bulk water into the system [47]. The present study rather exhibits a faster relaxation time scale compared to that in w/o microemulsion systems. Earlier studies by Xie *et al.* [25] reveal that MLVs consist of concentric bilayers (onion like structure) with highly structured water molecules present in between the bilayers and thus are expected to exhibit a relatively slow solvation response as also obtained in microemulsion systems [44]. The absence of any such slow relaxation component in the present study thus reconfirms the formation of ULV only as has been proposed from the DLS measurements.

To further investigate the possible heterogeneity in the positional distribution of DCM at the vesicle interface we follow time-resolved area normalized emission spectroscopy (TRANES), which is a well-established technique [48-50] and is a modified version of TRES. The unique feature of this method is that existence of an isoemissive point in the spectra indicates the presence of two emitting species in the system (i.e., heterogeneity in the residence of the fluorophore). In the present study, we do not find any isoemissive point when we construct TRANES at any of the studied temperatures (Figure 5.3). This observation reconfirms the formation of ULV at the studied AOT concentrations.

Having characterized the uniform size and unilamellarity of the AOT vesicle along with its stability over a range of temperature, it now becomes interesting to study the energetic associated with the dynamical water exchange at the vesicle interface. In this regard, we study the solvation dynamics of AOT vesicle at different temperatures (Figure 5.2b) and the fitted solvation data are presented in Table 5.2. It can be observed from the figure and the table that solvation becomes faster at elevated temperatures, which can be explained with the help of the multishell continuum model proposed by Bagchi *et al.* for reverse micelles and proteins [51-53]. In this model, a dynamic exchange between bound and free water molecules at the interface is assumed. The energetic of the exchange depends upon the strength and the number of hydrogen bonds among the water molecules at the interface. This bound to free type transition of water molecules with temperature has been shown to follow an Arrhenius type of activation energy barrier crossing model [51, 54]. We plot $\ln(1/\langle\tau_s\rangle)$ as a function of $1/T$, and a good linear fit is obtained (Figure 5.4a). From the slope of the straight line, activation energy (E_a) is calculated to be 3.7 ± 0.2 kcal

mol⁻¹, which is of the same order of magnitude to that obtained for the transition from bound type water (hydrogen bonded to polar headgroup) to free type water (not directly hydrogen bonded to headgroup) at RM [55] and micellar [39, 56] interface. This equality is a direct consequence of the dynamic nature of the primary and secondary hydration shell near the cell mimicking AOT vesicle which in turn is largely influenced by temperature.

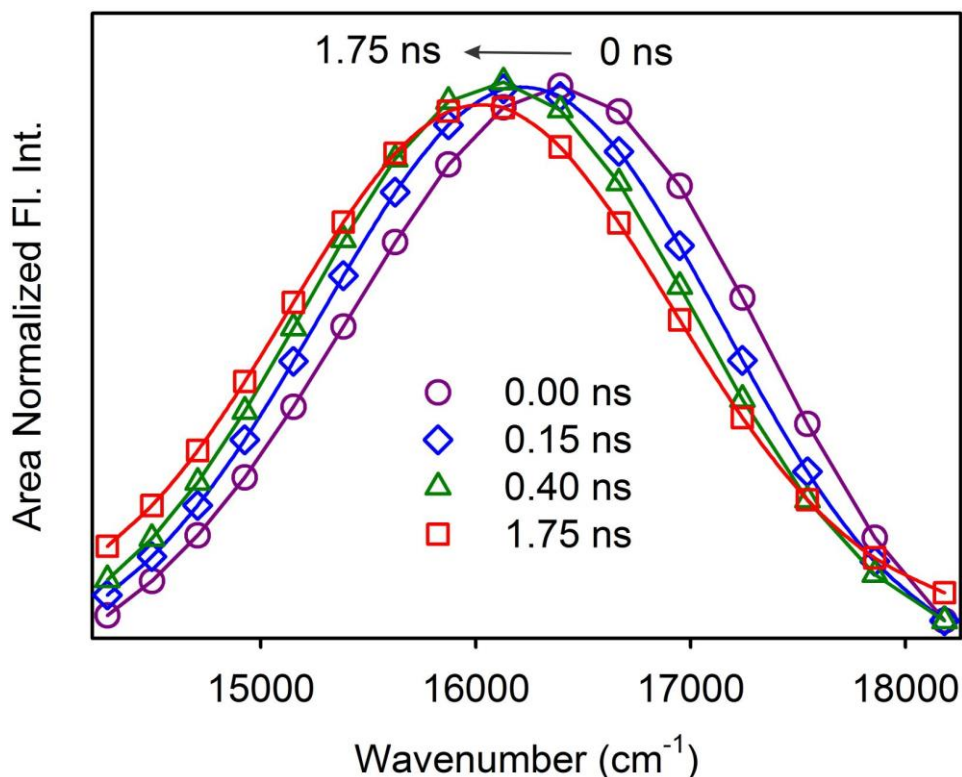


Figure 5.3. Time-resolved area normalized emission spectra of DCM in 18 mM AOT/water vesicle at 293 K.

To have a further idea of the temperature-mediated modification of interfacial water dynamics, we measure the temporal anisotropy decay, $r(t)$, of the probe in AOT vesicle at different temperatures. The inset of Figure 5.4b shows a representative anisotropy decay of DCM in AOT/water vesicles at 293 K. The time components obtained from fluorescence anisotropy decay, $r(t)$, of DCM in AOT vesicles at different temperatures are listed in Table 5.3. The time components obtained in this study are significantly slower than the picosecond time scale reported for conventional hydrophobic dyes in bulk water [40] indicating hindered rotation of the probe. This concludes that the dye experiences much higher viscosity (see later) in AOT vesicles in comparison to that in bulk water, which

concludes the residence of the probe in the interfacial layer of the vesicles at all the

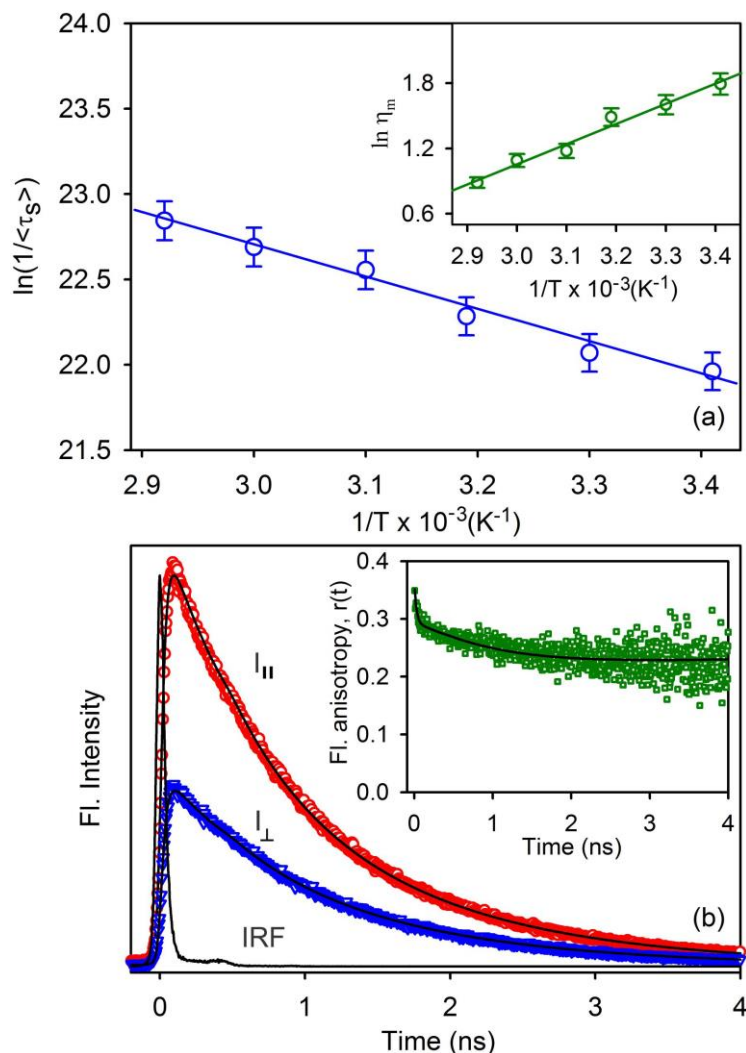


Figure 5.4. (a) Plot of $\ln(1/\langle\tau_s\rangle)$, τ_s expressed in ns, against $1/T$ for 18 mM AOT/water vesicle, with linear fit. A plot of $\ln(\eta_m)$, η_m expressed in cP, against $1/T$ for the same system is shown in the inset with linear fit. (b) Triexponential reconversion analyses of $I_{||}(t)$ and $I_{\perp}(t)$ polarized decays of DCM in AOT/water vesicle at 293 K. The temporal anisotropy decay curve is plotted in the inset.

studied temperatures. Note that the anisotropy decays at low temperatures are biexponential having a major contribution from the fast component (τ_{fast}). At higher temperatures the contribution of the slower component (τ_{slow}) vanishes making the decay transient single-exponential. To account for the effect of temperature on the rotational relaxation process of the probe in the vesicle, the anisotropy decay is analyzed using the two-step wobbling-in-cone model described elsewhere [57-60]. The diffusion coefficient

(D_w) values obtained using this model (Table 5.3) are of the same order of magnitude as reported earlier for micelle [61] and RM systems [55] and increases with temperature. This increase implies that with increasing temperature, the probe experiences less restricted rotation at the vesicle interface which might originate from the faster movement of the trapped water at elevated temperatures. This change is also manifested in the observed faster solvation dynamics at higher temperatures (Table 5.2, Figure 5.2b).

The microviscosity (η_m) values estimated by both simple Stokes-Einstein-Debye equation (SED) (equation (2-39)) and modified SED (equation (2-37)) are presented in Table 5.3. It is evident from the table that the values of microviscosity are ~6 times higher than that of bulk water. Earlier reports suggest that microviscosity in micelle [61] and RM [62] systems are 10-15 and 6-9 times higher than in bulk water, respectively. It is also observed that η_m decreases gradually with increasing temperature revealing that the probe experiences less rotational hindrance at higher temperature which might result from the breaking of water-water hydrogen bond network at the interface. Assuming that η_m changes with temperature following equation (2-41) [63], we plot $\ln(\eta_m)$ against $1/T$

Table 5.3. Fluorescence anisotropy decays and wobbling-in-cone data of DCM in 18 mM AOT /water vesicle at different temperatures. ^m

Temperature (K)	r_0	a_{fast}	τ_{fast} (ns)	a_{slow}	τ_{slow} (ns)	D_w ($\times 10^{-8} s^{-1}$)	η_m (cP) Simple SED	η_m (cP) Modified SED	E_η (kcal mol ⁻¹)
293	0.34	0.26	0.55	0.08	2.18	03.19	7.79	5.99	3.6 \pm 0.2
303	0.34	0.27	0.44	0.07	1.88	04.15	6.45	4.96	
313	0.33	0.33	0.38	-	-	06.57	5.76	4.42	
323	0.33	0.33	0.27	-	-	09.25	4.22	3.24	
333	0.32	0.32	0.24	-	-	10.41	3.87	2.97	
343	0.33	0.33	0.19	-	-	13.15	3.15	2.42	

^m τ_i represents the anisotropy time constant and a_i represents its relative weight in the total anisotropy. Estimated maximum error in determination of τ_i is 5%.

(inset of Figure 5.4a) and a good linear fit is obtained with a calculated energy barrier for the viscous flow (E_η) to be 3.6 ± 0.2 kcal mol⁻¹. The good agreement between the E_η obtained from the rotational anisotropy study and E_a value obtained from solvation dynamics study is notable. The close agreement between these two energy values indicate the cooperatively of the two processes involved. As discussed earlier, the observed

acceleration of the solvation dynamics with temperature has its origin in the transition of the slower moving interfacially bound water to faster moving bulk-type water, which in turn is associated with the decrease in the microviscosity at the vesicle interface.

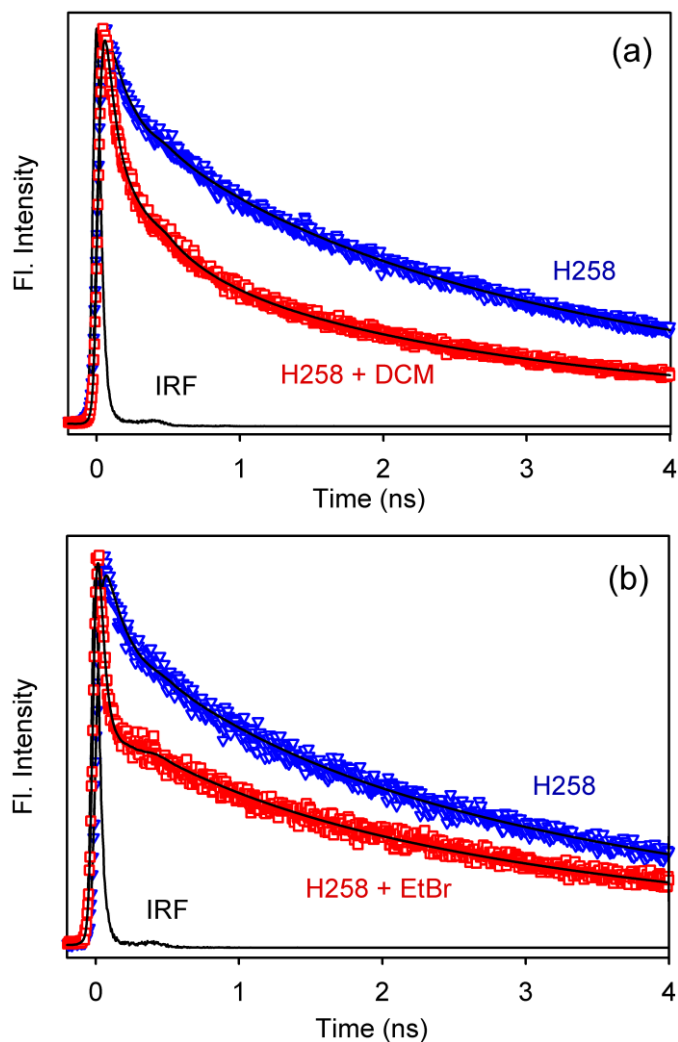


Figure 5.5. (a) The temporal decay of H258 and H258-DCM FRET pair in 18 mM AOT/water vesicles monitored at 490 nm. (b) The temporal decay of H258 and H258-EtBr FRET pair in 18 mM AOT/water vesicles monitored at 490 nm.

To investigate the ability of AOT vesicles to host drugs of various nature (both hydrophobic and charged) simultaneously we study Förster resonance energy transfer (FRET) between the dyes H258 (donor) and DCM (acceptor), and also between H258 (donor) and EtBr (acceptor) in AOT vesicles after solubilizing each donor acceptor pair in AOT vesicles. Figure 5.5 shows that an efficient energy transfer takes place between each

donor-acceptor pair, as indicated by the faster decay of the donor in presence of the acceptor in the vesicles compared to that of the donor itself in the vesicles. The estimated donor-acceptor distances between H258 and DCM pair, and H258 and EtBr pair are calculated to be 4.6 ± 0.05 and 3.0 ± 0.04 nm, respectively (Table 5.4). The observed FRET distances are much smaller than the estimated inter vesicle distance of ~ 120 nm supporting energy transfer between the donor-acceptor pairs hosted simultaneously in the same AOT vesicle. The finding shows the ability of the AOT vesicles to host simultaneously both charged drugs like H258, EtBr and also hydrophobic model drug DCM. This is very crucial for many codelivery applications and supports the strong candidature of AOT vesicles among drug nano carriers.

Table 5.4. Calculated values of parameters obtained from FRET between H258 & EtBr and H258 & DCM pairs at 293K.^a

System	$\langle\tau_D\rangle$ (ns)	$\langle\tau_{DA}\rangle$ (ns)	$J(\lambda)$ ($M^{-1}cm^{-1}nm^4$)	E	R_0 (nm)	R (nm)
H258-EtBr	2.18	0.66	2.50×10^{14}	0.70 ± 0.003	3.4	3.0 ± 0.04
H258-DCM	2.25	1.09	15.2×10^{14}	0.52 ± 0.004	4.7	4.6 ± 0.05

^a where $\langle\tau_D\rangle$ and $\langle\tau_{DA}\rangle$ represents the average fluorescence lifetime of the donor in absence and presence of the acceptor, respectively. Estimated error in determination of τ_D and τ_{DA} is 3%.

An interesting question at this juncture is whether the AOT vesicles produced could evolve as a convenient drug carrier. A good drug nano carrier should prerequisitely be able to release a drug in a controlled manner. To investigate the release profile of AOT vesicle a well-known anti-tuberculosis drug rifampicin [64] is taken as a model. Plot of cumulative percent of drug released against time (Figure 5.6a) shows a typical profile of first order exponential controlled release of the drug (equation (2-63)) [65, 66]. At pH 7.4, 60% of the drug is released from the vesicles in 6.5 hrs whereas 80% of it is released within the first 6.0 hrs in a controlled experiment without AOT vesicle (Figure 5.6a). This clearly indicates that AOT vesicle helps in increasing the dosage time making the drug available for a longer period of time without degradation. The release of rifampicin loaded vesicles is studied further in an acidic pH of 5.8 as rifampicin shows variation in solubility with pH [67] which in turn could affect its bioavailability. As observed from Figure 5.6a an acidic environment not only retards the rate of release but also the extent of rifampicin release. The decrease of drug release at lower pH is also evident from the K (rate constant for the

release) value obtained by fitting the curves with equation (2-63) (Figure 5.6a, Table 5.5). Decreasing pH from 7.4 to 5.8 is manifested in a 3 fold decreases in the rate of rifampicin release from AOT vesicle whereas the change is negligible in the control experiment. It is reported that at various pH medium the dissolution rate depends on the interaction of rifampicin with the acidic excipients like SDS and AOT [68]. In our case also

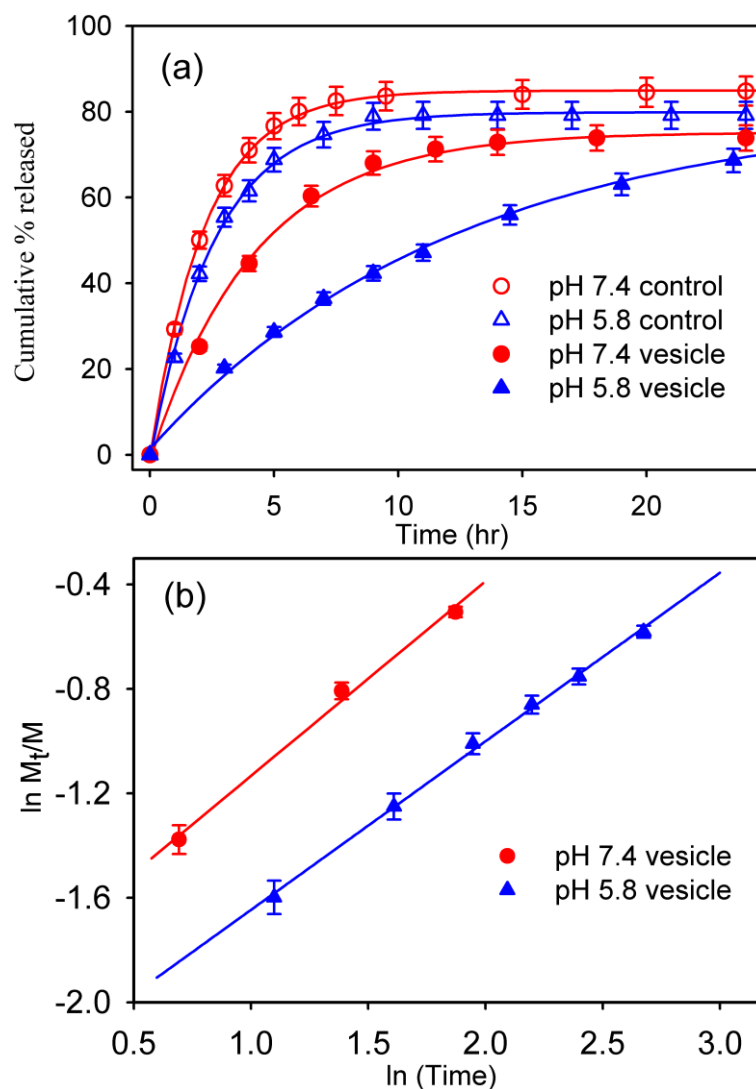


Figure 5.6. (a) Release profile of rifampicin from AOT vesicle at pH 7.4, 5.8. The solid lines are fits according to equation (2-63) (b) Peppas fit (equation (2-64)) at pH 7.4 and 5.8 with time expressed in hours.

the observed retardation might originate from the interaction of rifampicin with AOT, which in turn could modulate rifampicin bioavailability.

The mechanism of drug release can be analyzed by a relationship proposed by Peppas et al. [69] applying equation (2-64), for the first 60 % of the release. We obtain good linear fits (Figure 5.6b) with corresponding n values of 0.79 ± 0.03 at pH 7.4 and 0.65 ± 0.01 at pH 5.8. It should be noted here that for spherical carrier n should be

Table 5.5. Rate constant values using first order exponential equation for the release of rifampicin from AOT vesicles and water.

pH	K (hr ⁻¹)		n
	Control	AOT vesicle	AOT vesicle
7.4	0.45 ± 0.01	0.24 ± 0.01	0.79 ± 0.03
5.8	0.40 ± 0.02	0.08 ± 0.01	0.65 ± 0.01

equal to 0.5 for a pure Fickian release, 1 for zero-order kinetics and $0.5 < n < 1$ for anomalous (non-Fickian) release [69]. In the present system the release of rifampicin from AOT vesicle is found to be non-Fickian in nature.

5.2.2. Nanostructure, Solvation Dynamics and Nanotemplating of Plasmonically Active SERS Substrate in Reverse Vesicles [70]:

To study the effect of adding the o/w ME (micelle, $X_w = 0.37$) in excess of nonpolar oil IPM, we conducted transmission electron microscopy (TEM) study. The TEM images in Figure 5.7 show a number of spherical structures with distinct shells, much like the conventional micrographs of vesicles. Here, ammonium molybdate is used as the aqueous phase of the reverse vesicle (RV) in order to deflect the electron beam, revealing a clear contrast between the peripheral and central areas of the reverse aggregates. Figure 5.7a shows three isolated unilamellar RVs having a prolate shape and the average sizes ranging from 20 to 30 nm. The prolate shape of the RV is also evident in Figure 5.7c; however, the structure is distinctly multilayered with an average size of 400 nm. Formation of prolate aggregates supports the hypothesis of the RVs in the present system [71]. The multilamellar characteristic of the RVs is also evident in Figure 5.7b; however, the shape is spherical with a diameter of 265 nm. The individual bilayers in the multilamellar RVs are well separated from each other, indicating a more repulsive interaction (most likely

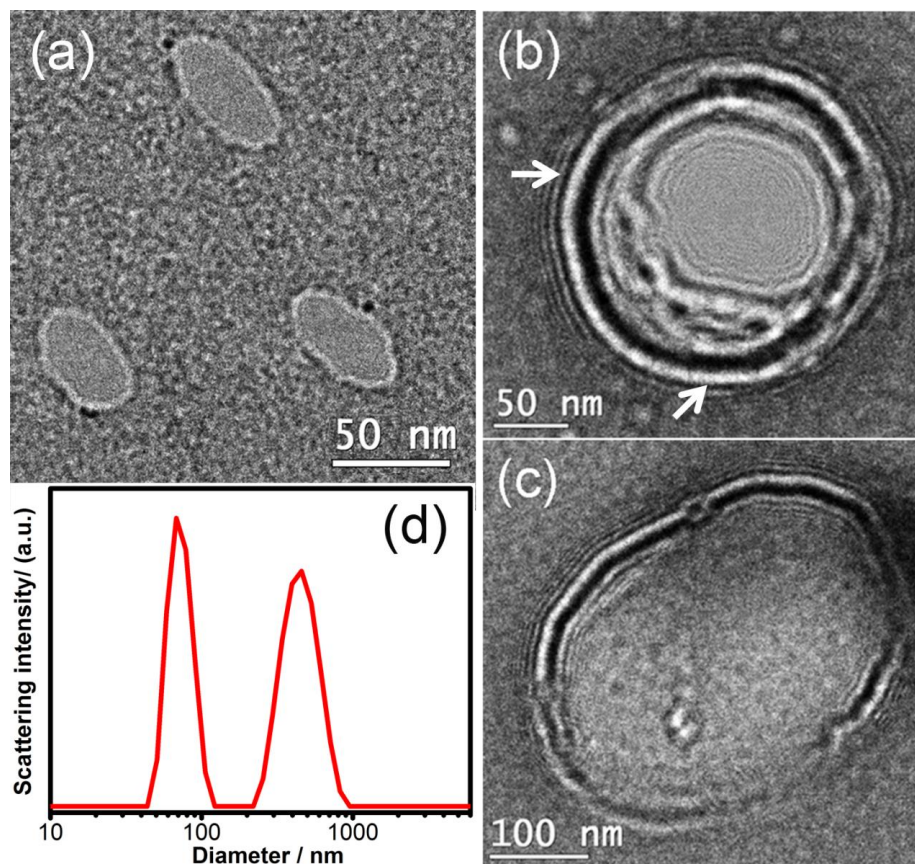


Figure 5.7. Representative TEM images of ammonium molybdate labelled reverse vesicles (RVs). (a) Unilamellar RVs with prolate shape in the size range of 30 nm. (b) A typical structure of multilamellar spherical RV is shown. Arrows indicate different spacing of the lamellar bilayers. (c) The 400 nm RV with ellipsoidal shape is distinctly multilayered. These RVs are formed when 13.3 μl of the microemulsions are added to 2 ml of isopropyl myristate. (d) Shows the DLS signal of the as prepared RVs.

enhanced undulation repulsion [72]) between the bilayers than it is found in the lamellar phase, in which the spacing of the bilayer is about the same as the bilayer thickness [73].

The formation of the RV is further confirmed by DLS technique. Figure 5.7d shows the size distribution of the as prepared reverse aggregates. The DLS signals are found to be polydispersed with $\sim 70\text{-}460$ nm of size distribution. Signature of a larger size distribution of the aggregates in these solutions compared to that in ME (~ 5 nm [74]) provides evidence for RV formation. The observed higher polydispersity in size distribution indicates multilamellarity of the vesicles and is quite in agreement with the TEM data (Figure 5.7) and the data published in previous literature [75]. The RVs formed here are stable and do not revert back to the initial stage on prolonged standing as evidenced by DLS study.

To understand the physical nature of water molecules entrapped in the RV, we carry out Fourier transform infrared spectroscopy (FTIR) to determine the O-H stretching frequency of water in the RVs. In order to avoid the contribution of C-H stretching frequency, the observed spectra at RV has been subtracted from the surfactant system without water, and the differential spectra have been analyzed. A representative result is depicted in Figure 5.8a. It is known that different types of hydrogen bonded water molecules exist in surfactant self-assemblies like RMs, that can broadly be classified into two major classes, namely headgroup bound and bulk-like water molecules [76]. The differential IR spectra obtained in the present study have been deconvoluted into two spectra peaking at ~ 3425 and ~ 3390 cm^{-1} , corresponding to the O-H stretching frequency of the head-group bound and bulk-like water, respectively. To probe the dynamical states of such water confined in the RV, polar solvation dye H258 has been used. Figure 5.8b shows the steady-state excitation and emission spectra of H258 in buffer and RV. In buffer the excitation and emission peaks of H258 are at 366 and 500 nm, respectively. However, these are significantly blue shifted to 355 and 468 nm, respectively in RV. It may be recalled that in hydrophobic environments H258 shows blue shifted absorption and emission peak [77]. Accordingly, the observed blue-shift in the excitation and emission peaks of H258 in RV is consistent with the presence of a considerable fraction of H258 molecules at the surfactant-water interface of the RV where the microenvironment polarity is expected to be lower compared to bulk water.

Figure 5.9a shows the decay transients of H258 in RVs at three selected wavelengths of 430 (at the blue end of the spectrum), 470 (at the peak position), and 530 (at the red end of the spectrum) nm. The transient at 430 nm can be fitted tri-exponentially with time components of 0.09 ns (50%), 0.98 ns (31%) and 2.97 ns (19%). For the extreme red wavelength (530 nm), a distinct rise component of 0.09 ns is obtained along with the decay components of 2.05 and 4.35 ns. The presence of faster decay components at the blue end and a rise component at the red wavelength is indicative of solvation [33] of the probe in RV system within the experimental time window.

Using the decay transients at different wavelengths, we construct TRES of the probe in RV. Figure 5.9b shows the representative TRES for H258 in RV, wherein a

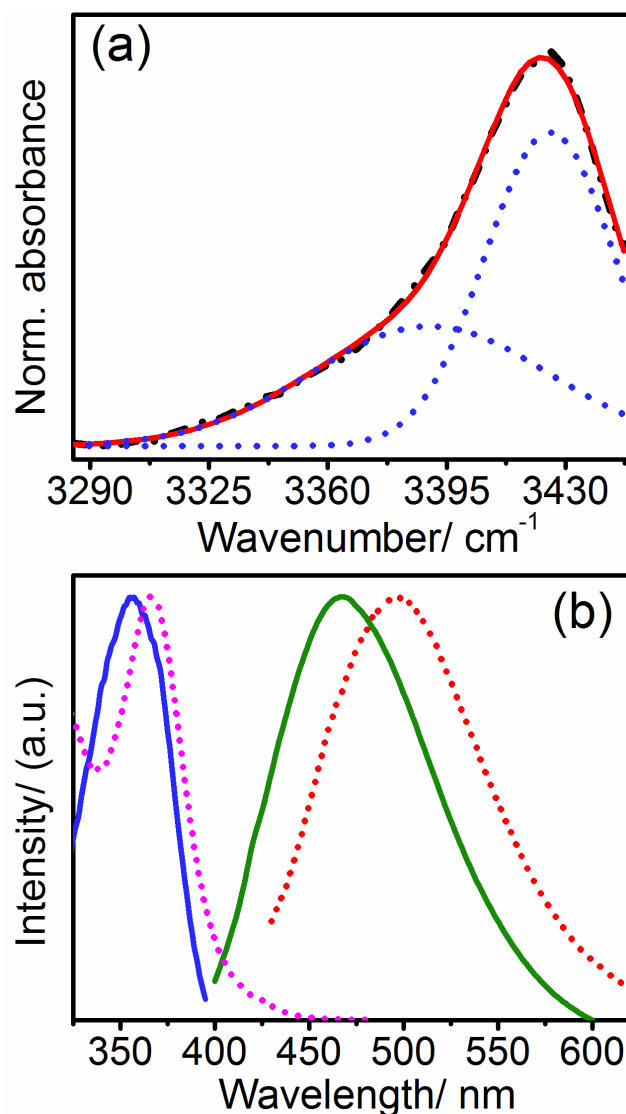


Figure 5.8. (a) FTIR spectra of reverse vesicle (RV). The black (dash dotted) curve is the experimental one, red (solid) curve is the overall fitted data and the blue (dotted) lines are the deconvoluted curves. (b) Excitation and emission spectra of H258 in RV, respectively (solid lines). The dotted lines are the corresponding spectra in buffer.

significant dynamic fluorescence Stokes shift of 1300 cm^{-1} in 9 ns is observed. The solvent correlation function, $C(t)$ obtained are fitted bi-exponentially (Figure 5.9c) based on the core-shell model [78] with time components of 2.26 ns (45%) and 0.12 ns (55%). It can be noted that both these components are slower than the subpicosecond solvation time scale reported for bulk water [46]. As has been inferred from steady-state measurements the observed solvation dynamics appear to be due exclusively to the H258 molecules

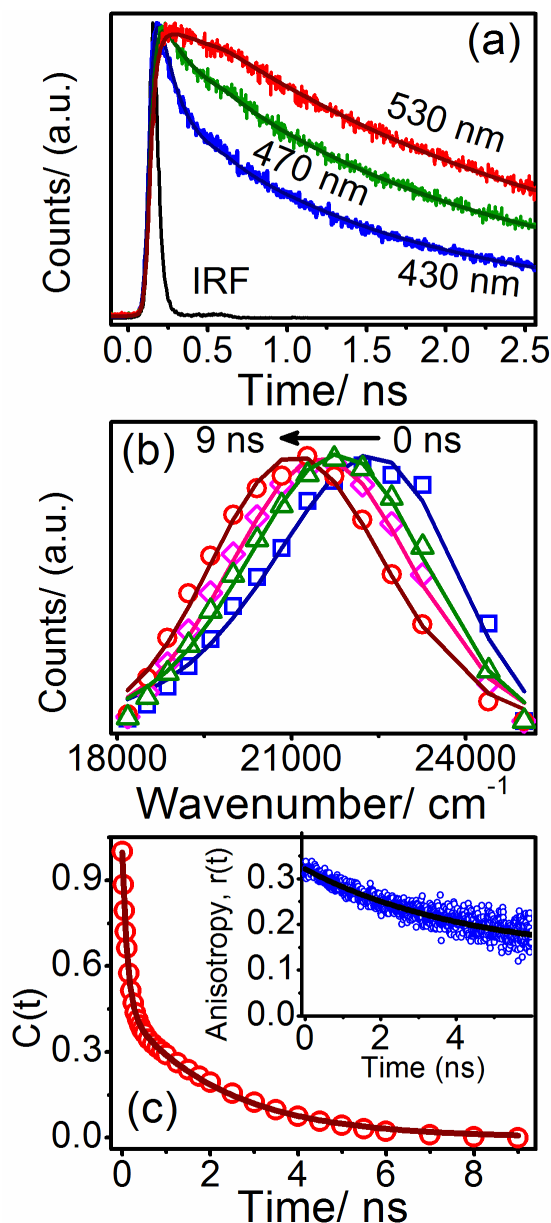


Figure 5.9. (a) Fluorescence decay transients of H258 in reverse vesicle (RV). (b) Time-resolved emission spectra (TRES) of H258 in RV. (c) Solvent correlation function, $C(t)$ of H258 in RV. The solid lines denote the best fit to the biexponential decay. Inset shows the picosecond-resolved fluorescence anisotropy decay of H258 in RV.

residing at the surfactant water interface of the RVs. The observed average solvation time ($\langle\tau_s\rangle = a_1\tau_1 + a_2\tau_2$) of 1.08 ns is comparable to that of H258 molecules located in the hydration shell at the interface of the nanotemplating AOT-RM [77], and essentially corresponds to the dynamical exchange between head group bound and interfacially bound water. Successful probing of interfacial water dynamics is well evident in the restricted rotation of the probe in RV. The rotational anisotropy of the dye in RV is shown in the

inset of Figure 5.9c. It could be noted that H258 in bulk water shows the rotational lifetime, τ_r of 500 ps [79], indicative of the free rotational motion. However, in RV the rotational anisotropy of the probe is significantly slower and even does not complete within the time window of 6 ns (inset of Figure 5.9c). This shows that the dye is experiencing higher microviscosity in RVs in comparison to that in bulk water, and illustrates the residence of the probe in the interfacial layer of the RV.

The water nano-channels present in between the bilayers of RV show dynamic behavior typical of a nanotemplating RM (discussed earlier) and can trap metal ions like MoO_4^{2-} quite efficiently (Figure 5.7). Thus RV water layers are expected to be a potential template for inorganic metal nanoparticle (NP) synthesis. The formation of silver NPs in the RV template is realized in the high resolution TEM (HRTEM) and UV-Vis absorption studies. Figure 5.10a displays the absorption spectrum of the as-obtained silver NPs exhibiting the characteristic surface plasmon bands at 400 nm [80]. The *in situ* formation and inclusion of silver NPs between lamellae is shown in the TEM images of Figure 5.10b, d and f. The HRTEM image in Figure 5.10c shows an isolated spherical silver NP of 9.10 nm size, with clear lattice fringes of interplane distance of 0.20 nm corresponding to the (200) lattice space of metallic silver [81]. The fringe pattern shows the high quality of the nanocrystals. The polydispersed size distribution of the metallic silver (ranging between 4.3 nm and 13 nm), as revealed in Figure 5.10e is quite consistent with variable inter lamellar distance of the RVs (Figure 5.7b). The existence of distinct isolated clusters of silver NPs found in the size range of the RVs suggest that after particle synthesis the overall aggregate structure of the RV is retained. According to the colloidal particle nucleation and growth model proposed by La Mer and Dinegar, particle nucleation occurs when ion concentration reaches supersaturation concentration [82]. This condition is likely to be met when metallic salt (like Ag^+ , here) is already present in the aqueous phase during the formation of RV as has been adopted here. In this condition addition of external reducing agent (like NaBH_4) may lead to the simultaneous nucleation of NPs at many sites of the vesicle walls, and many particles can grow within the bilayers. Importantly, the gradual diffusion of reductant along the RV bilayer is believed to be responsible for particle growth in a controlled manner forming smaller size (4.3-13 nm) NPs. In fact the

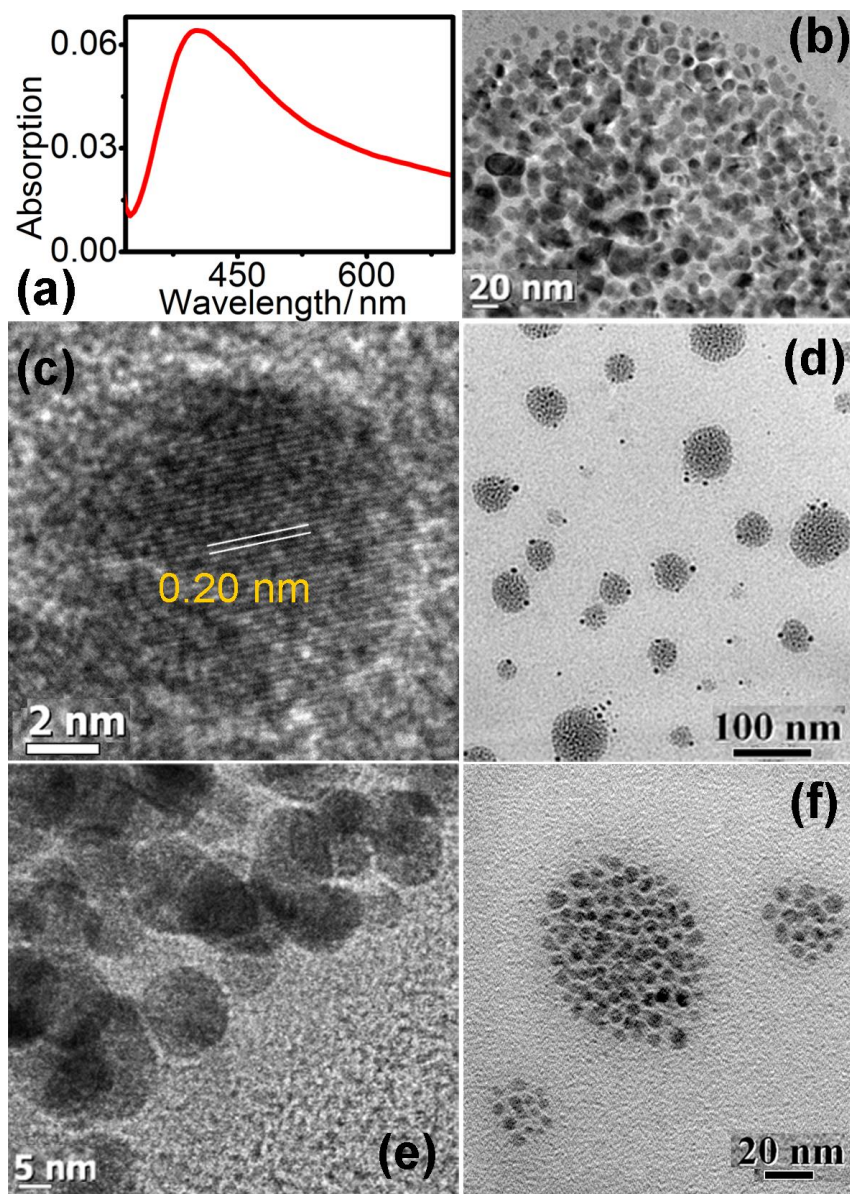


Figure 5.10. (a) UV-Vis absorption spectra of silver nanoparticles (NPs) obtained in the nanotemplate of reverse vesicles (RVs). (b) TEM micrograph of silver NPs loaded RVs. (c) HRTEM image of a spherical silver NP with clear lattice fringes. (d) Silver NPs produced in RVs of different size. (e) HRTEM image of silver NPs produced at the RV oil interface with different particle size. (f) Isolated silver NPs, highly clustered in various RVs.

finite vesicular volume places a restriction on the number of metal ions available for crystal nucleation and growth resulting in particles significantly smaller than those formed in the extravascular phase and additionally can avoid particle aggregation [83]. Significantly, the dispersing media of RV being oil, particle synthesis can occur only in the vesicle water layers, and possibility of bulk synthesis (extravesicular synthesis) as can

occur in normal vesicles is totally eliminated. In this regard the clustering of the NPs (Figure 5.10b and f) strongly suggests templated particle formation and growth indicating complete prevention of extravesicular particle synthesis. Consequently, the prevention of such extravesicular particle synthesis makes RVs much more attractive than unilamellar vesicles or even classical multilamellar vesicles for particle synthesis. Notably, formation of classical vesicles requires sonication or mechanical stirring. In such systems, vesicle components are mixed with an excess solution of metallic salt. Consequently, not only the exact internal concentration of metal remains unknown, but also extravesicular particle synthesis cannot be avoided [84], unless a separation step (either by column chromatography [85] or dialysis [83]) is performed to remove unencapsulated metal ions. Since the continuous medium of RV is oil, polar metal ions are localized only in the aqueous layer of the RVs, which avoids any separation step as required for classical vesicle directed particle synthesis. Thus RV directed particle synthesis is more efficient and is economically advantageous over the classical vesicle mediated synthetic procedure.

The crystal structure of the synthesized silver NPs are analyzed by powder X-ray diffraction (XRD) measurements. Figure 5.11 shows a typical XRD pattern of the as-prepared product. The discernible peaks can be indexed to (111), (200), (220), (311) and (222) crystal planes of face-centered cubic structure of metallic silver [86]. XRD pattern thus clearly illustrates that the silver NPs formed in this present synthesis are crystalline in nature. According to the Debye Scherrer equation, the diameter of the silver NPs is estimated to be ~ 14.5 nm, which is relatively close to the size range of the silver NPs as shown in the TEM images.

The templated synthesis of highly clustered metal NPs in the RV template offers a unique opportunity to use these NP-vesicle hybrid assemblies in various plasmonic applications. Interestingly electromagnetic (EM) field are intensively localized into a nanoscale junction of metal NPs, to create significant field enhancement, referred to as “hotspots” [87-89]. This huge EM field localization resonant coupling with the surface plasmon of metal NPs is crucial for various surface enhanced Raman scattering (SERS) applications like biosensing [90], label-free immunoassays [91] etc. Thus NP clusters of

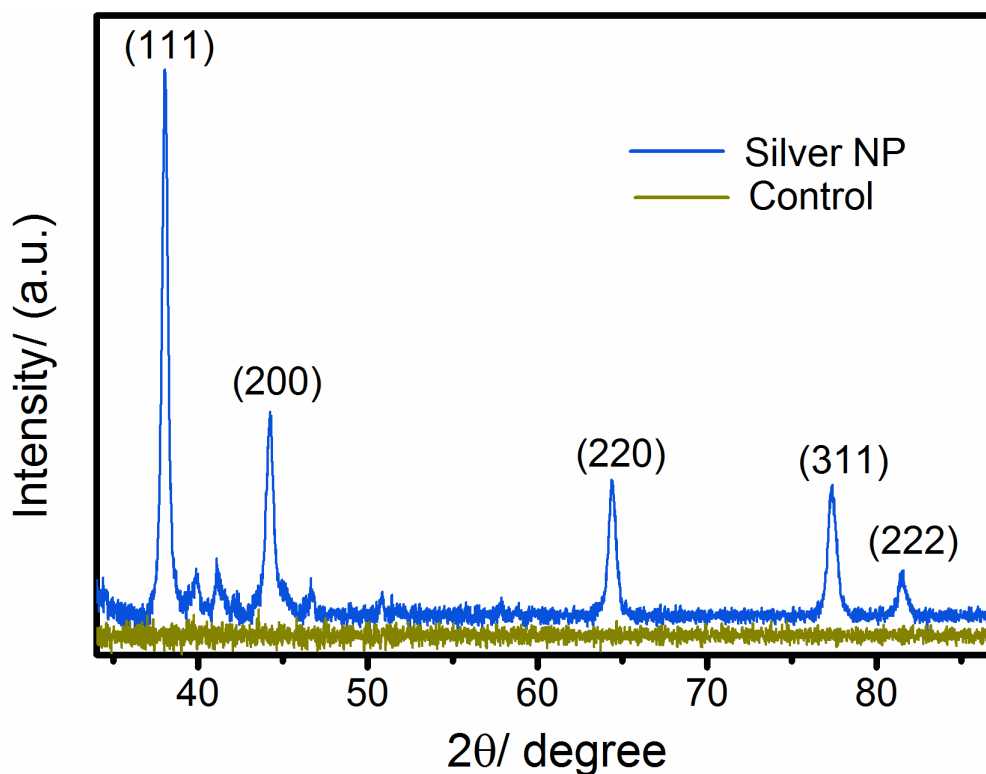


Figure 5.11. XRD pattern of silver nanoparticles (NPs) synthesized from reverse vesicles (RVs). The control set denotes the XRD pattern of the RVs.

nobel metals are attractive for SERS sensors due to the strong EM field enhancements arising at the interparticle junctions upon interaction with visible radiation [92]. To get insight on the SERS detection performance of the highly dense cluster of silver NPs as revealed in Figure 5.10b, d and f, we use crystal violet (CV) as a model analyte. Figure 5.12 shows the SERS spectra of CV at various concentrations adsorbed on the silver NP clusters, measured with an excitation wavelength of 488 nm. The SERS spectra reveal the characteristic peaks of CV (even in trace amounts) with very high intensity, at most of the earlier reported frequencies [93]. Considerable enhancement of the SERS signal at 800, 912, 1170, 1537, 1587 and 1619 cm^{-1} with respect to the bulk Raman spectra of CV can be observed within the scale limit of the diagram. The SERS enhancement factor (EF) estimated from the signal intensities of the ring C-C stretching mode at 1619 cm^{-1} with respect to the bulk Raman spectra of the molecule (193 μM) is in the range of $\sim 10^4$. This superior enhancement of the Raman signal and ultra-sensitivity to the analyte is ascribed due to the high clustering of the silver NPs in the confinement of the RV, which laterally confine the surface plasmons in a very small volume that can efficiently couple to the

incident laser [94]. It is important to note that in EF estimation it was assumed that all CV molecules adsorb with the same efficiency on the silver NP surfaces and/or contribute to the measured signal. However, it is more likely that a small fraction of the molecules will

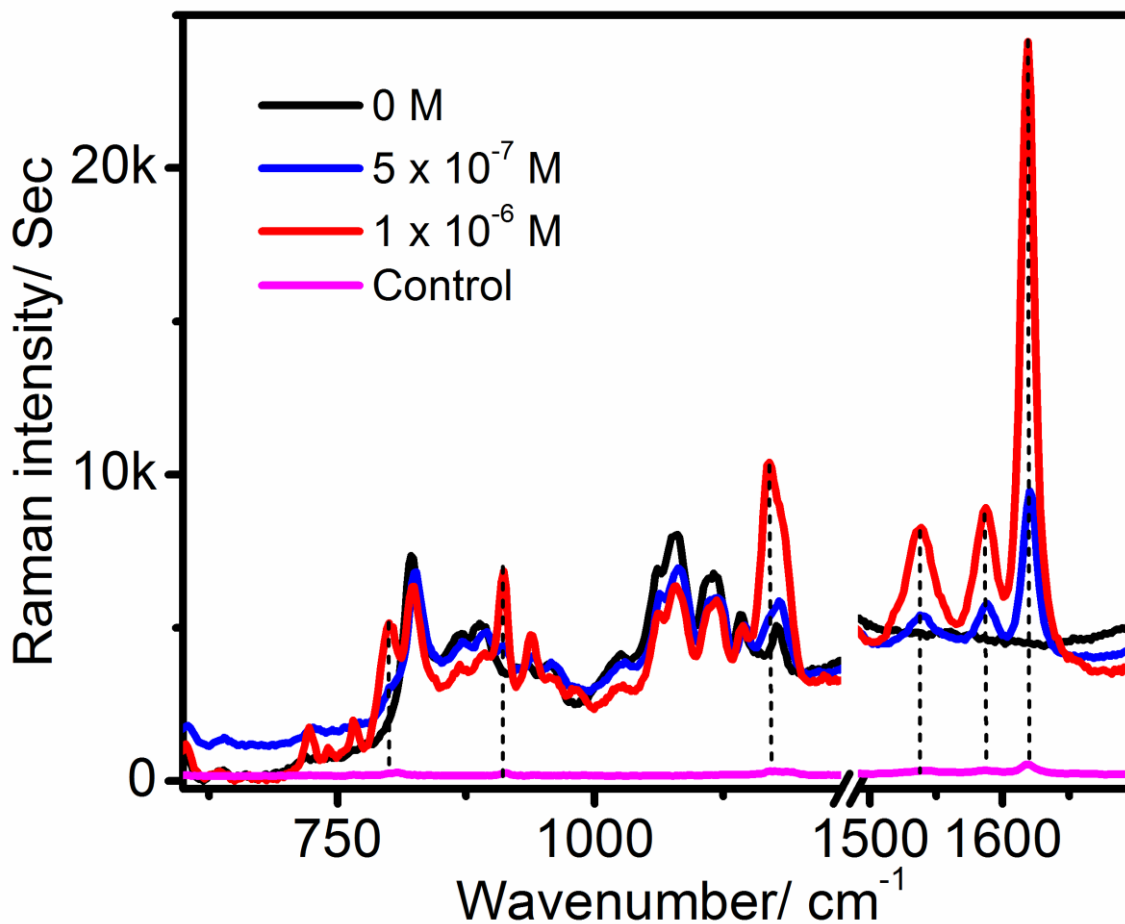


Figure 5.12. SERS spectra of crystal violet at various concentrations for the silver nanoparticle cluster in reverse vesicles (RVs). The control set denotes the bulk Raman spectra of 1.9×10^{-4} M of crystal violet in water. Vertical lines mark positions of some characteristic vibrational bands of crystal violet.

contribute to the observed intensities as CV-ethanol is fairly soluble in IPM. It is again important to note that CV does not exhibit significant absorption band around 488 nm, which excludes the possibility of any resonance Raman effects for the excitation laser employed in our study. Further enhancement of the SERS effect can be achieved by improving the cluster density of the substrate solution, employing probe molecules with resonance effects and by optimizing the laser wavelength employed in the measurements.

5.3. Conclusion:

We have explored the aggregate structure and size of AOT vesicles in dilute aqueous region (9-18 mM AOT), using the combination of spectroscopic and light scattering methods. The size of the AOT vesicles (monodispersed in distribution) is found to be independent of temperature (293-343 K) and surfactant concentration (9, 14 and 18 mM) providing evidence of its unilamellarity. The time independent DLS data further shows its aging stability. Microenvironment of the AOT vesicles is probed through a solvation probe, DCM. Both steady-state and time-resolved fluorescence spectroscopy indicate the residence of the probe DCM at the surfactant water interface and shows the efficacy of the vesicles to host the model drug/ligand DCM. A comparably faster solvation dynamics ($\langle \tau_s \rangle = 0.29$ ns) in AOT vesicle compared to AOT microemulsion ($\langle \tau_s \rangle = 1.23$ ns) rules out the presence of multiple concentric bilayers as has also been evidenced from the DLS study. Absence of an isoemissive point in TRANES further rules out the heterogeneity in the residence of DCM molecules. The residence of the probe in the solvation shell of the AOT vesicle has been confirmed through the increased microviscosity of the probe environment, compared to the bulk viscosity of the solution. The time-resolved FRET studies between various dyes present in the same vesicles show the ability of the AOT vesicles to host model drugs of various natures simultaneously. The drug release from the vesicle is found to be controlled over 24 hr at 37°C at both the studied pH range of the dissolution medium. The release rate changes in acidic pH. All these features hold great promise for the development of AOT vesicle as viable drug delivery systems. The study explores the hydrogen bonded structure and dynamics at the interface of the AOT vesicle, which is similar to the environment around cell. The considerable stability of the nontoxic, monodispersed, unilamellar AOT/water vesicles in wide range of AOT concentration and temperature, with the capability of hosting drugs of various natures simultaneously for many codelivery applications combined with controlled drug release profile may find its application in drug delivery.

We have also prepared a new RV from edible surfactant and oil components. The formation of the RVs has been confirmed by DLS and TEM study. The structures are found to be stable on aging and are of different lamellarity, with diameters ranging from

~70-460 nm. FTIR spectroscopy reveals the signature of different kinds of water molecules in between the RV bilayers. Micropolarity of the water layers are successfully probed by the solvatochromic dye H258. Both steady-state excitation and emission spectra show the dye to reside in the surfactant water interface of the RVs. The significant rotational hindrance of the dye in time-resolved fluorescence anisotropy study, further confirms its presence at the interface. Picosecond time-resolved fluorescence spectroscopy suggests the dynamics of water to be significantly slower compared to bulk water and is very much similar to the nanotemplating water of AOT-RMs. Accordingly, the RVs formed are evaluated as a potential template in controlled growth of highly crystalline silver NPs with high efficiency, and substantial productivity. Powder XRD analyzes the face-centered cubic nature of the silver NPs. TEM study shows high clustering of the NPs in the confinement of the RVs. These NP clusters are evaluated as potential SERS substrates in solution using CV as a reporter molecule. The high quality of the spectra obtained for the model compound demonstrate the efficiency of the prepared substrate for SERS enhancement and its potentiality as a non-toxic SERS detection probe for chemical and biological analysis *in situ*. Notably this study provides the first proof-of-concept data for the ability of RV to be a template of synthesizing metal NPs. Based on the potential of RV for biomimetic nanomaterial preparation demonstrated here, we expect that novel applications based on self-assembled NP-vesicle hybrid assembly would evolve out.

References:

- [1] S.B. Zimmerman, A.P. Minton, Macromolecular crowding: Biochemical, biophysical and physiological consequences, *Annu. Rev. Biophys. Biomol. Struct.* 22 (1993) 27.
- [2] A.P. Minton, The influence of macromolecular crowding and macromolecular confinement on biological reactions in physiological media, *J. Biol. Chem.* 276 (2001) 10577.
- [3] R.J. Ellis, Macromolecular crowding: Obvious but underappreciated, *Trends Biochem. Sci* 26 (2001) 597.
- [4] J.H. Fendler, Self-assembled nanostructured materials, *Chem. Mater.* 8 (1996) 1616.
- [5] G. Gregoriadis, Liposome technology, CRC Press, Florida, 1984.
- [6] H.C. Youn, B. Subhash, J.H. Fendler, Dihexadecyl phosphate, vesicle-stabilized and in situ generated mixed cadmium sulfide and zinc sulfide semiconductor particles: preparation and utilization for photosensitized charge separation and hydrogen generation, *J. Phys. Chem.* 92 (1988) 6320.
- [7] D.D. Lasic, Liposomes, Elsevier, New York, 1993.
- [8] A.M. Carmona-Ribeiro, L.S. Yoshida, A. Sesso, H. Chaimovich, Permeabilities and stabilities of large dihexadecylphosphate and dioctadecyldimethylammonium chloride vesicles, *J. Colloid Interface Sci.* 100 (1984) 433.
- [9] J.E. Brady, D.F. Evans, B. Kachar, B.W. Ninham, Spontaneous vesicles, *J. Am. Chem. Soc.* 106 (1984) 4279.
- [10] Y. Talmon, D.F. Evans, B.W. Ninham, Fast calculation of van der waals volume as a sum of atomic and bond contributions and its application to drug compounds, *Science* 221 (1983) 1047.
- [11] N.E. Gabriel, M.F. Roberts, Spontaneous formation of stable unilamellar vesicles, *Biochemistry* 23 (1984) 4011.
- [12] H. Fukuda, K. Kawata, H. Okuda, S.L. Regen, Bilayer-forming ion pair amphiphiles from single-chain surfactants, *J. Am. Chem. Soc.* 112 (1990) 1635.

- [13] Z. Lin, M. He, L.E. Scriven, H.T. Davis, Vesicle formation in electrolyte solutions of a new cationic siloxane surfactant, *J. Phys. Chem.* 97 (1993) 3571.
- [14] J.C. Hao, H. Hoffmann, K. Horbaschek, A novel cationic/anionic surfactant system from a zwitterionic alkyldimethylamine oxide and dihydroperfluorooctanoic acid, *Langmuir* 17 (2001) 4151.
- [15] M. Mao, J. Huang, B. Zhu, H. Yin, H. Fu, The structural transition of catanionic vesicles induced by toluene, *Langmuir* 18 (2002) 3380.
- [16] H.T. Jung, B. Coldren, J.A. Zasadzinski, D.J. Iampietro, E.W. Kaler, The origins of stability of spontaneous vesicles, *Proc. Natl. Acad. Sci.U.S.A.* 98 (2001) 1353.
- [17] E.F. Marques, Size and stability of catanionic vesicles: Effects of formation path, sonication, and aging, *Langmuir* 16 (2000) 4798.
- [18] A.J. O'Connor, T.A. Hatton, A. Bose, Dynamics of micelle-vesicle transitions in aqueous anionic/cationic surfactant mixtures, *Langmuir* 13 (1997) 6931.
- [19] C. Caillet, M. Hebrant, C. Tondre, Sodium octyl sulfate/cetyltrimethylammonium bromide catanionic vesicles: Aggregate composition and probe encapsulation, *Langmuir* 16 (2000) 9099.
- [20] K.L. Herrington, E.W. Kaler, D.D. Miller, J.A. Zasadzinski, S. Chiruvolu, Phase behavior of aqueous mixtures of dodecyltrimethylammonium bromide (DTAB) and sodium dodecyl sulfate (SDS), *J. Phys. Chem.* 97 (1993) 13792.
- [21] D.J. Iampietro, L.L. Brasher, E.W. Kaler, A. Stradner, O. Glatter, Direct analysis of SANS and SAXS measurements of catanionic surfactant mixtures by Fourier transformation, *J. Phys. Chem. B* 102 (1998) 3105.
- [22] T.K. De, A. Maitra, Solution behavior of aerosol OT in non-polar solvents, *Adv. Colloid Interface Sci.* 59 (1995) 95.
- [23] S.N. Malik, D.H. Canaham, M.W. Gouda, Effect of surfactants on absorption through membranes III: Effects of dioctyl sodium sulfosuccinate and poloxalene on absorption of a poorly absorbable drug, phenolsulfonphthalein, in rats, *J. Pharm. Sci.* 64 (1975) 987.
- [24] M. Varshney, T. Khanna, M. Changez, Effects of AOT micellar systems on the transdermal permeation of glyceryl trinitrate, *Colloids Surf., B* 13 (1999) 1.

- [25] J.-X. Cheng, S. Pautot, D.A. Weitz, X.S. Xie, Ordering of water molecules between phospholipid bilayers visualized by coherent anti-Stokes Raman scattering microscopy, *Proc. Natl. Acad. Sci. U.S.A.* 100 (2003) 9826.
- [26] J. Rogers, P.A. Winsor, Optically positive, isotropic and negative lamellar liquid crystalline solutions *Nature* 216 (1967) 477.
- [27] J. Briz, M.M. Velázquez, Effect of water-soluble polymers on the morphology of aerosol OT vesicles, *J. Colloid Interface Sci.* 247 (2002) 437.
- [28] G.H. Sagar, J.R. Bellare, Estimation of mechanical strength of unilamellar and multilamellar AOT/water vesicles and their rupture using micropipet aspiration, *J. Phys. Chem. B* 113 (2009) 13805.
- [29] S.-H. Tung, H.-Y. Lee, S.R. Raghavan, A facile route for creating “reverse” vesicles: Insights into “reverse” self-assembly in organic liquids, *J. Am. Chem. Soc.* 130 (2008) 8813.
- [30] H. Kunieda, K. Nakamura, U. Olsson, B. Lindman, Spontaneous formation of reverse vesicles, *J. Phys. Chem.* 97 (1993) 9525.
- [31] H. Li, X. Xin, T. Kalwarczyk, E. Kalwarczyk, P. Niton, R. Hołyst, J. Hao, Reverse vesicles from a salt-free catanionic surfactant system: A confocal fluorescence microscopy study, *Langmuir* 26 (2010) 15210.
- [32] S. Rangelov, M. Almgren, K. Edwards, C. Tsvetanov, Formation of normal and reverse bilayer structures by self-assembly of nonionic block copolymers bearing lipid-mimetic units, *J. Phys. Chem. B* 108 (2004) 7542.
- [33] R. Saha, P.K. Verma, R.K. Mitra, S.K. Pal, Structural and dynamical characterization of unilamellar AOT vesicles in aqueous solutions and their efficacy as potential drug delivery vehicle, *Colloids Surf., B* 88 (2011) 345.
- [34] Y.R. Fan, G.G. Yuan, Y.L. Wang, J.B. Wang, C.C. Han, H. Yan, Comparative studies on the micellization of sodium bis(4-phenylbutyl) sulfosuccinate and sodium bis(2-ethylhexyl) sulfosuccinate and their interaction with hydrophobically modified poly(acrylamide), *Langmuir* 21 (2005) 3814.
- [35] I.M. Umlong, K. Ismail, Micellization of AOT in aqueous sodium chloride, sodium acetate, sodium propionate, and sodium butyrate media: A case of two different concentration regions of counterion binding, *J. Colloid Interface Sci.* 291 (2005) 529.

- [36] C. Lin, J. Zhao, R. Jiang, Nile red probing for the micelle-to-vesicle transition of AOT in aqueous solution, *Chem. Phys. Lett.* 464 (2008) 77.
- [37] A. Chatterjee, S.P. Moulik, S.K. Sanyal, B.K. Mishra, P.M. Puri, Thermodynamics of micelle formation of ionic surfactants: A critical assessment for sodium dodecyl sulfate, cetyl pyridinium chloride and dioctyl sulfosuccinate (Na salt) by microcalorimetric, conductometric, and tensiometric measurements, *J. Phys. Chem. B* 105 (2001) 12823.
- [38] T.M. Bayerl, M. Bloom, Physical properties of single phospholipid bilayers adsorbed to micro glass beads. A new vesicular model system studied by ^2H -nuclear magnetic resonance *Biophys. J.* 58 (1990) 357.
- [39] R.K. Mitra, S.S. Sinha, S.K. Pal, Temperature dependent hydration at micellar surface: Activation energy barrier crossing model revisited, *J. Phys. Chem. B* 111 (2007) 7577.
- [40] D. Banerjee, P.K. Verma, S.K. Pal, Temperature-dependent femtosecond-resolved hydration dynamics of water in aqueous guanidinium hydrochloride solution, *Photochem. Photobiol. Sci.* 8 (2009) 1441.
- [41] S.K. Pal, D. Sukul, D. Mandal, S. Sen, K. Bhattacharyya, Solvation dynamics of DCM in micelles, *Chem. Phys. Lett.* 327 (2000) 91.
- [42] Z. Hsing-Kang, M. Ren-Lan, N. Er-pin, G. Chu, Behaviour of the laser dye 4-dicyanomethylene-2-methyl-6-dimethylaminostryryl-4H-pyran in the excited singlet state, *J. Photochem.* 29 (1985) 397.
- [43] M. Meyer, J.C. Mialocq, Ground state and singlet excited state of laser dye DCM: Dipole moments and solvent induced spectral shifts, *Opt. Commun.* 64 (1987) 264.
- [44] S.K. Pal, D. Mandal, D. Sukul, K. Bhattacharyya, Solvation dynamics of 4-(dicyanomethylene)-2-methyl-6-(p-dimethylaminostyryl)-4H-pyran (DCM) in a microemulsion, *Chem. Phys. Lett.* 312 (1999) 178.
- [45] D. C. Easter, A. P. Baronavski, Ultrafast relaxation in the fluorescent state of the laser dye DCM, *Chem. Phys. Lett.* 201 (1993) 153.
- [46] R. Jimenez, G.R. Fleming, P.V. Kumar, M. Maroncelli, Femtosecond solvation dynamics of water, *Nature* 369 (1994) 471.
- [47] P.K. Verma, A. Makhal, R.K. Mitra, S.K. Pal, Role of solvation dynamics in the kinetics of solvolysis reactions in microreactors, *Phys. Chem. Chem. Phys.* 11 (2009) 8467.

- [48] N. Periasamy, A.S.R. Koti, Time resolved fluorescence spectroscopy: TRES and TRANES, *Proc. Indian Natn. Sci. Acad.* 69A (2003) 41.
- [49] A.S.R. Koti, N. Periasamy, TRANES analysis of the fluorescence of Nile red in organized molecular assemblies confirms emission from two species, *Proc. Indian Acad. Sci., (Chem. Sci.)* 113 (2001) 157.
- [50] A.S.R. Koti, M.M.G. Krishna, N. Periasamy, Time-resolved area-normalized emission spectroscopy (TRANES): A novel method for confirming emission from two excited states, *J. Phys. Chem. A* 105 (2001) 1767.
- [51] N. Nandi, B. Bagchi, Dielectric relaxation of biological water, *J. Phys. Chem. B* 101 (1997) 10954.
- [52] N. Nandi, K. Bhattacharyya, B. Bagchi, Dielectric relaxation and solvation dynamics of water in complex chemical and biological systems, *Chem. Rev.* 100 (2000) 2013.
- [53] N. Nandi, B. Bagchi, Anomalous dielectric relaxation of aqueous protein solutions *J. Phys. Chem. A.* 102 (1998) 8217.
- [54] R.K. Mitra, P.K. Verma, D. Banerjee, S.K. Pal, Hydrogen bonding barrier crossing dynamics at bio-mimicking surfaces, K.-L. Han, G.-J. Zhao (Eds.), *Hydrogen bonding and transfer in the excited state*, John Wiley, Chippenham, 2010.
- [55] R.K. Mitra, S.S. Sinha, S.K. Pal, Temperature-dependent solvation dynamics of water in AOT/isooctane reverse micelles, *Langmuir* 24 (2008) 49.
- [56] S. Pal, S. Balasubramanian, B. Bagchi, Identity, energy, and environment of interfacial water molecules in a micellar solution, *J. Phys. Chem. B* 107 (2003) 5194.
- [57] G. Lipari, A. Szabo, Padé approximants to correlation functions for restricted rotational diffusion, *J. Chem. Phys.* 75 (1981) 2971.
- [58] G. Lipari, A. Szabo, Model-free approach to the interpretation of nuclear magnetic resonance relaxation in macromolecules. 1. Theory and range of validity, *J. Am. Chem. Soc.* 104 (1982) 4546.
- [59] G. Lipari, A. Szabo, Effect of librational motion on fluorescence depolarization and nuclear magnetic resonance relaxation in macromolecules and membranes, *Biophys. J.* 30 (1980) 489.

- [60] C.C. Wang, R. Pecora, Time-correlation functions for restricted rotational diffusion, *J. Chem. Phys.* 72 (1980) 5333.
- [61] G.B. Dutt, Are the experimentally determined microviscosities of the micelles probe dependent?, *J. Phys. Chem. B* 108 (2004) 3651.
- [62] E.M. Corbeil, R.E. Riter, N.E. Levinger, Cosurfactant impact on probe molecule in reverse micelles, *J. Phys. Chem. B* 108 (2004) 10777.
- [63] R. Zana, Microviscosity of aqueous surfactant micelles: Effect of various parameters, *J. Phys. Chem. B* 103 (1999) 9117.
- [64] J.W. Long, Essential guide to prescription drugs 1992, HarperCollins Publishers, New York, 1991.
- [65] H. Dai, Q. Chen, H. Qin, Y. Guan, D. Shen, Y. Hua, Y. Tang, J. Xu, A temperature-responsive copolymer hydrogel in controlled drug delivery, *Macromolecules* 39 (2006) 6584.
- [66] L. Zhang, X. Sun, Z.-R. Zhang, An investigation on liver-targeting microemulsions of norcantharidin, *Drug Delivery* 12 (2005) 289.
- [67] T.T. Mariappan, S. Singh, Regional gastrointestinal permeability of rifampicin and isoniazid (alone and their combination) in the rat, *Int. J. Tuberc. Lung Dis.* 7 (2003) 797.
- [68] S. Agrawal, R. Panchagnula, Dissolution test as a surrogate for quality evaluation of rifampicin containing fixed dose combination formulations, *Int. J. Pharm.* 287 (2004) 97.
- [69] P.L. Ritger, N.A. Peppas, A simple equation for description of solute release I. Fickian and non-fickian release from non-swelling devices in the form of slabs, spheres, cylinders or discs, *J. Controlled Release* 5 (1987) 23.
- [70] R. Saha, S. Rakshit, D. Majumdar, A. Singha, R. Mitra, S. Pal, Nanostructure, solvation dynamics, and nanotemplating of plasmonically active SERS substrate in reverse vesicles, *J. Nanopart. Res.* 15 (2013) 1576.
- [71] H. Mays, M. Almgren, A. Dedinaite, P.M. Claesson, Spontaneous formation of reverse vesicles with soybean phosphatidyl ethanolamine in mixture with triglyceride and some water, *Langmuir* 15 (1999) 8072.

- [72] T.J. McIntosh, A.D. Magid, S.A. Simon, Repulsive interactions between uncharged bilayers-hydration and fluctuation pressures for monoglycerides, *Biophys. J.* 55 (1989) 897.
- [73] A. Tardieu, V. Luzzati, F.C. Reman, Structure and polymorphism of the hydrocarbon chains of lipids: A study of lecithin-water phases, *J. Mol. Biol.* 75 (1973) 711.
- [74] R. Saha, S. Rakshit, R.K. Mitra, S.K. Pal, Microstructure, morphology, and ultrafast dynamics of a novel edible microemulsion, *Langmuir* 28 (2012) 8309.
- [75] N. Ushio, C. Solans, N. Azemer, K. H., Formation and stability of reverse vesicles in a sucrose alcanoate system, *J. Jpn. Oil Chem. Soc. (Yukagaku)* 42 (1993) 915.
- [76] R.K. Mitra, S.S. Sinha, P.K. Verma, S.K. Pal, Modulation of dynamics and reactivity of water in reverse micelles of mixed surfactants, *J. Phys. Chem. B* 112 (2008) 12946.
- [77] D. Banerjee, S.S. Sinha, S.K. Pal, Interplay between hydration and electrostatic attraction in ligand binding: Direct observation of hydration barrier at reverse micellar interface, *J. Phys. Chem. B* 111 (2007) 14239.
- [78] I.R. Piletic, D.E. Moilanen, D.B. Spry, N.E. Levinger, M.D. Fayer, Testing the core/shell model of nanoconfined water in reverse micelles using linear and nonlinear IR spectroscopy, *J. Phys. Chem. A* 110 (2006) 4985.
- [79] D. Banerjee, S.K. Pal, Ultrafast charge transfer and solvation of DNA minor groove binder: Hoechst 33258 in restricted environments, *Chem. Phys. Lett.* 432 (2006) 257.
- [80] M.M. Kemp, A. Kumar, S. Mousa, T.-J. Park, P. Ajayan, N. Kubotera, S.A. Mousa, R.J. Linhardt, Synthesis of gold and silver nanoparticles stabilized with glycosaminoglycans having distinctive biological activities, *Biomacromolecules* 10 (2009) 589.
- [81] S. Behrens, J. Wu, W. Habicht, E. Unger, Silver nanoparticle and nanowire formation by microtubule templates, *Chem. Mater.* 16 (2004) 3085.
- [82] V.K. LaMer, R.H. Dinigar, Theory, production and mechanism of formation of monodispersed hydrosols, *J. Am. Chem. Soc.* 72 (1950) 4847.
- [83] F.C. Meldrum, B.R. Heywood, S. Mann, Influence of membrane composition on the intravesicular precipitation of nanophase gold particles, *J. Colloid Interface Sci.* 161 (1993) 66.

- [84] Y.M. Tricot, J.H. Fendler, In situ generated colloidal semiconductor cadmium sulfide particles in dihexadecyl phosphate vesicles: Quantum size and symmetry effects, *J. Phys. Chem.* 90 (1986) 3369.
- [85] S. Mann, J.P. Hannington, R.J.P. Williams, Phospholipid vesicles as a model system for biomineralization, *Nature* 324 (1986) 565.
- [86] M. Chen, W. Ding, Y. Kong, G. Diao, Conversion of the surface property of oleic acid stabilized silver nanoparticles from hydrophobic to hydrophilic based on host-guest binding interaction, *Langmuir* 24 (2008) 3471.
- [87] U. Kreibig, M. Vollmer, Optical properties of metal clusters, Springer, Berlin, 1995.
- [88] D.-F. Zhang, Q. Zhang, L.-Y. Niu, L. Jiang, P.-G. Yin, L. Guo, Self-assembly of gold nanoparticles into chain-like structures and their optical properties, *J. Nanopart. Res.* 13 (2011) 3923.
- [89] M. Muniz-Miranda, C. Gellini, P.R. Salvi, M. Innocenti, M. Pagliai, V. Schettino, Fabrication of nanostructured silver substrates for surface-enhanced Raman spectroscopy, *J. Nanopart. Res.* 13 (2011) 5863.
- [90] Y. Wang, J.L. Seebald, D.P. Szeto, J. Irudayaraj, Biocompatibility and biodistribution of surface-enhanced Raman scattering nanoprobe in Zebrafish embryos: *In vivo* and multiplex imaging, *ACS Nano* 4 (2010) 4039.
- [91] S. Schultz, D.R. Smith, J.J. Mock, D.A. Schultz, Single-target molecule detection with nonbleaching multicolor optical immunolabels, *Proc. Natl. Acad. Sci. U.S.A.* 97 (2000) 996.
- [92] C. Gellini, M. Muniz-Miranda, M. Innocenti, F. Carla, F. Loglio, M.L. Foresti, P.R. Salvi, Nanopatterned Ag substrates for SERS spectroscopy, *Phys. Chem. Chem. Phys.* 10 (2008) 4555.
- [93] M.V. Cañamares, C. Chenal, R.L. Birke, J.R. Lombardi, DFT, SERS, and single-molecule SERS of crystal violet, *J. Phys. Chem. C* 112 (2008) 20295.
- [94] W.J. Cho, Y. Kim, J.K. Kim, Ultrahigh-density array of silver nanoclusters for SERS substrate with high sensitivity and excellent reproducibility, *ACS Nano* 6 (2012) 249.

Chapter 6

Spectroscopic Studies on the Decisive Ultrafast Dynamical Events in Biological Macromolecules

6.1. Introduction:

In the last few decades green fluorescent protein (GFP) and its variants have revolutionized our ability to visualize the key molecular processes occurring in live cells and many other research fields [1]. Recently a new class of photoconvertible fluorescent proteins has been developed whose emission properties can be changed upon illumination of light at specific wavelengths [2-5]. For example, GFP [6], Kaede [7], and EosFP [8] convert irreversibly from green to red (G/R) on irradiation by UV or violet light. This spectral shift caused by irradiation allows the investigation of dynamics in live cells or designing super resolution imaging schemes based on photoactivated localization microscopy [9, 10]. Despite the obvious value of photoconversion of fluorescent proteins, key photoexcited processes such as electron transfer (ET) and proton transfer that underlie significant spectral changes in the chromophore, have remained poorly understood.

GFP from jellyfish *Aequorea victoria* absorbs predominantly at 398 nm. Irradiation with blue light irreversibly transforms this state to red fluorescence state with corresponding excitation-emission maxima at 525 and 600 nm, respectively [6]. The term ‘redding’ is used to describe this photoconversion [11]. The red form of the protein is stable in anaerobic condition, but it disappears after re-oxygenation of the sample [6]. Recently very efficient green to red photoconversion in enhanced GFP (EGFP) was observed upon irradiation with at 488 nm in presence of various electron acceptors including *p*-benzoquinone (BQ), implicating ET in G/R photoconversion of EGFP and other fluorescent proteins (FPs) [11]. However, an understanding of the role of ET and allied processes (proton transfer) can only be obtained from studying the time-resolved dynamics of the excited states of G/R photoconvertible fluorescent proteins (PCFPs). In this chapter, using femtosecond up-conversion technique as well as picosecond-resolved fluorescence spectroscopy, we report the ultrafast excited state dynamics of PCFPs. We

find that while BQ promotes efficient G/R photoconversion in EGFP, by contrast, BQ abolishes G/R photoconversion of mEos2; ultrafast fluorescence spectroscopy provides us clear evidence for the differing roles of ET in the excited states of these PCFPs.

6.2. Results and Discussion:

6.2.1. Light Driven Ultrafast Electron Transfer in Oxidative Redding of Green Fluorescent Proteins [12]:

6.2.1.1. An Ultrafast View of the Photoconversion Process in EGFP: Oxidative photoconversion of EGFP in presence of electron acceptor, BQ, leads to loss of typical EGFP fluorescence emission (compare Figure 6.1a, curves 3 and 4), concomitant with the appearance of red photoconverted protein (Figure 6.1b) with corresponding fluorescence excitation and emission maxima at 575 (Figure 6.1a, 5) and 660 nm (Figure 6.1a, 6), respectively.

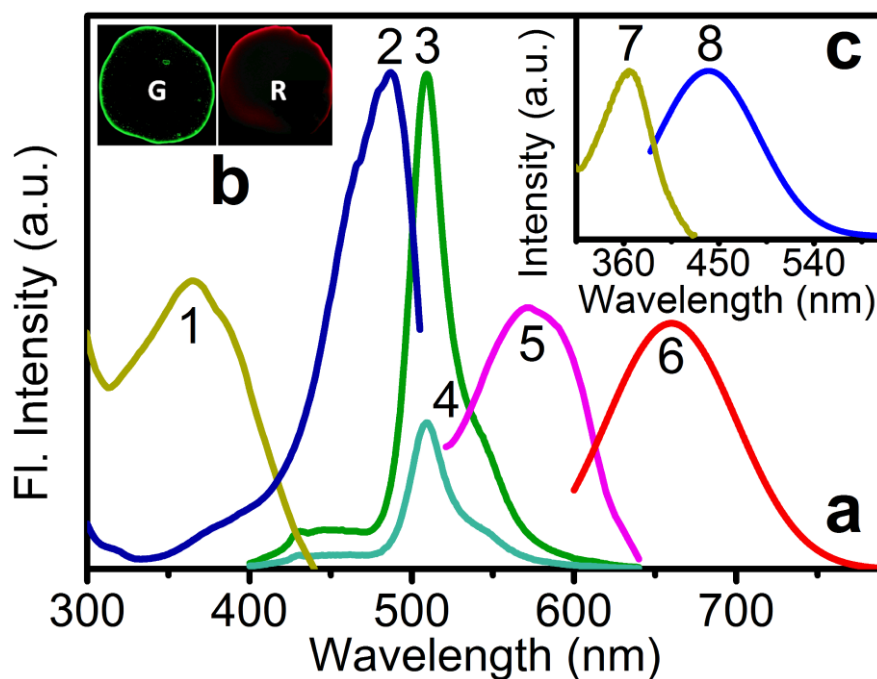


Figure 6.1. (a) Excitation spectrum of EGFP monitored at 440 nm (1) and at 540 nm (2). Emission spectrum of EGFP excited at 375 nm in absence (3) and presence of BQ (4). Excitation spectrum of EGFP in presence of BQ monitored at 660 nm (5). Emission spectrum of EGFP in presence of BQ excited at 575 nm (6). (b) Fluorescence microscopic images of EGFP in absence of BQ excited at blue light (G) and in presence of BQ excited at green light (R). (c) Excitation spectrum of EGFP at pH 3.0 monitored at 440 nm (7). Emission spectrum of EGFP at pH 3.0 excited at 375 nm (8).

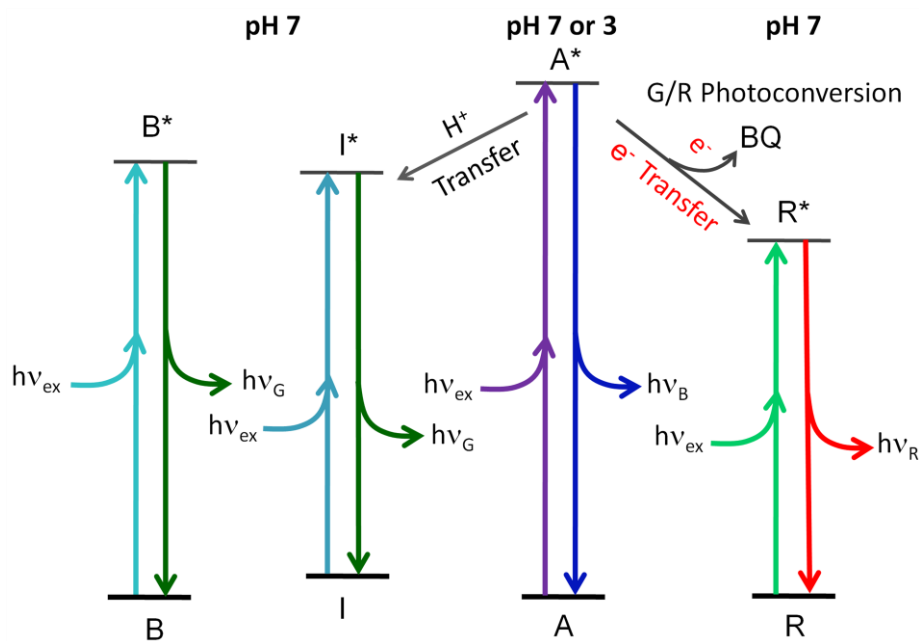


Figure 6.2. Proposed electronic energy-level diagram of the various photoconvertible forms of EGFP. A, protonated form of the chromophore; I and B, deprotonated forms of the chromophore; R is the red photoconverted chromophore. A band excitation produces the excited state species A^* , which can either decay giving blue emission or may undergo excited state proton transfer (ESPT) generating the anionic excited state chromophore I^* . I^* can either depopulate to ground state I giving green emission or may infrequently attain the more relaxed B^* state with the chromophoric environment optimized for green emission. In presence of oxidant BQ, A^* undergoes ultrafast electron transfer (ET) to generate the red emissive species R^* . Both ET and excited state proton transfer (ESPT) are suppressed at lower pH (= 3) of the medium. The energy scheme for the A, B and I form is according to the reference [13]. The model is not accountable for the eventual processes between the ground state chromophoric forms of the protein.

To explore the mechanism of the photoconversion we observe time-resolved (both femtosecond and picosecond) dynamics of the electronic states of EGFP in absence and presence of BQ, using ultrafast spectroscopy. To understand the photochemical reactions taking place during this photoconversion reaction, it is important to appreciate that at neutral pH EGFP may exist in multiple ground states; a neutral (A state) and two deprotonated anionic states (B, and I), appear to dominate the landscape (Figure 6.2). Indeed, the excitation spectrum of EGFP at neutral pH monitored at the emission wavelengths of 440 nm (A state) and 540 nm (B and I states) show evidence for these states (Figure 6.1a, curves 1 and 2); the neutral chromophoric form (A state) has excitation maximum around ~ 365 nm, whereas the excitation maximum near ~ 488 nm can be attributed to the deprotonated anionic chromophores (B and I) [13, 14]. Consistent with this, at acidic pH (pH 3.0) the A state is the predominant chromophore, giving a singular

excitation and emission profiles with maxima at ~ 365 and ~ 440 nm, respectively (Figure 6.1c, curves 7 and 8).

At neutral pH, in the excited state, the neutral chromophore A^* depopulates mainly via an excited state proton transfer (ESPT) reaction to I^* , which can evolve further to a more relaxed state B^* (Figure 6.2). ESPT reaction of EGFP has been studied in detail and occurs via a hydrogen-bond network comprising a water molecule and the side chain of Ser205, with subsequent protonation to the γ -carboxylate group of Glu222 [15, 16]. Consistent with this mechanism, using femtosecond fluorescence up-conversion technique when EGFP is excited at 390 nm, A^* decays rapidly to form excited state species I^* by

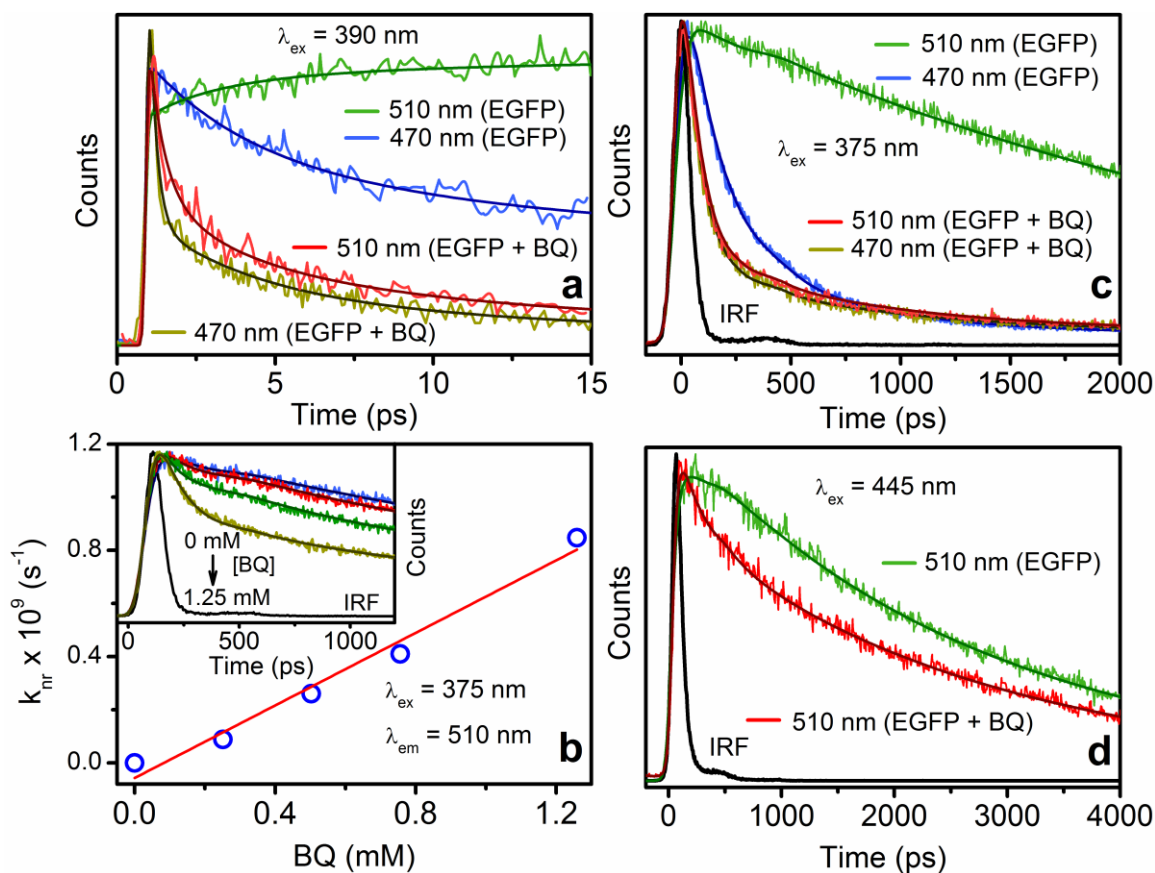


Figure 6.3. (a) Femtosecond-resolved fluorescence decays of EGFP monitored at 470 and 510 nm (excitation wavelength 390 nm) in presence and absence of BQ. (b) Rate constants for nonradiative decay processes at various concentrations of BQ. The inset shows corresponding EGFP fluorescence decays monitored at 510 nm (excitation wavelength 375 nm). (c) Picosecond-resolved fluorescence decays of EGFP monitored at 470 and 510 nm (excitation wavelength 375 nm) in presence and absence of BQ (d) Picosecond-resolved fluorescence decays of EGFP monitored at 510 nm (excitation wavelength 445 nm) in presence and absence of BQ.

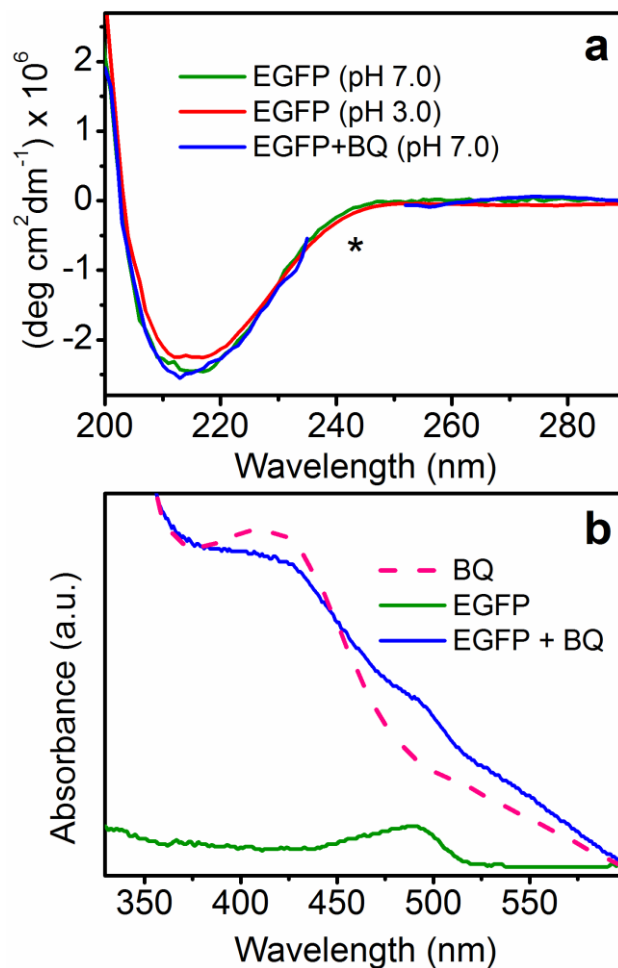


Figure 6.4. (a) CD spectra of EGFP at pH 3 and 7 and in presence of 0.5 mM BQ (asterisks correspond to region where huge rise in voltage due to absorption of BQ masks the CD data). It is to be noted that due to significant absorbance of BQ (0.5 mM BQ and above) around ~240 nm it is not possible to carry out CD measurement at this wavelength. (b) Absorption spectra EGFP in presence and absence of BQ. The dashed line denotes the absorption spectra of BQ.

ESPT due to deprotonation of the neutral chromophore, as seen by the rapid decay (3.51 and 20.13 ps) of blue emission characteristic of A* at 470 nm followed by the corresponding rise (2.12 and 18.39 ps) of the green emission at 510 nm (Figure 6.3a and Table 6.1). At neutral pH, in presence of oxidant BQ, the femtosecond-resolved fluorescence transients characteristic of A* (at 470 nm) shows a major (73%) ultrafast time component of 220 fs in addition to the transients responsible for ESPT (3.40 and 13.46 ps) (Figure 6.3a and Table 6.1). The appearance of the fs time component is unlikely due to any change in the overall structure and ground state property of the fluorophore in the protein, since both the CD and absorbance spectra are respectively unaltered in the

presence of BQ (Figure 6.4). The 220 fs time component is a signature of ET between EGFP and BQ, and indicates that excited neutral chromophore (A*) depopulates mainly via ET process in the presence of BQ (see also Figure 6.3c). Although such fast time scales may also be obtained by ultrafast excitation energy transfer (EET) from A* to BQ, this

Table 6.1. Fluorescence decay parameters of EGFP and mEos2 in presence and absence of BQ. ^m

Sample Name	λ_{ex} (nm)	λ_{em} (nm)	a ₁	τ_1 (ps)	a ₂	τ_2 (ps)	a ₃	τ_3 (ps)	a ₄	τ_4 (ps)
EGFP	390 ^b	470	0.40	3.51	0.20	20.13	0.40	132.46	-	-
		510	-0.09	2.12	-0.15	18.39	0.76	388.78	-	-
EGF+BQ	390 ^b	470	0.73	0.22	0.16	3.40	0.09	13.46	0.02	507
		510	0.57	0.22	0.30	3.40	0.08	13.00	0.05	285
EGFP	375 ^c	470	0.42	31	0.46	198	0.09	578	0.03	4600
		510	-0.10	28	0.16	155	0.14	1469	0.80	3246
EGFP+BQ	375 ^c	470	0.83	68	0.12	398	0.05	3363	-	-
		510	0.83	65	0.12	496	0.05	3471	-	-
EGFP	445 ^c	510	-0.15	35	0.10	178	0.55	2377	0.50	3286
EGFP+BQ		510	0.40	77	0.16	597	0.44	2976	-	-
mEos2	375 ^c	520	0.12	240	0.42	1160	0.46	3450	-	-
		580	0.13	240	0.16	1100	0.71	4420	-	-
mEos2+BQ	375 ^c	520	0.72	60	0.17	240	0.07	1160	0.04	4900
		580	0.71	60	0.19	240	0.08	1160	0.02	4650

^m τ_i represents decay time constant and a_i is its relative contribution. ^bexperiments were conducted on the femtosecond setup. ^cexperiments were conducted on picosecond setup.

could be ruled out by monitoring the rate of nonradiative processes (k_{nr}) obtained by equation (2-62), as a function of BQ concentration. The rate constant k_{nr} exhibits a linear dependence on BQ (Figure 6.3b), whereas non-radiative energy transfer (e.g., via a Förster's mechanism) would have nonlinear dependence on BQ concentration.

When, the detection wavelength is changed from 470 to 510 nm upon excitation of A band with 390 nm light the amplitude of the femtosecond transient decreases from 73% to 57% (Figure 6.3a and Table 6.1) indicating that a fraction of A* is also transferred to I* through ESPT implying a competition between ET process and ESPT. Therefore, monitoring the sub-picosecond components of the rise and fall of fluorescence emission at 470 nm and 510 nm, respectively, provides characteristic information about A* and I* state dynamics. This underscores the use of an “all optical” femtosecond-resolved fluorescence detection system (up-conversion technique) for the exploration of relevant time components associated with ET dynamics.

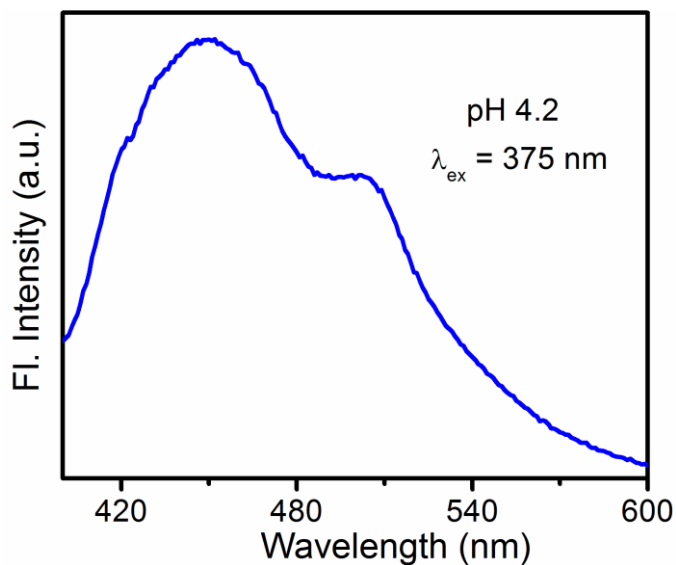


Figure 6.5. Emission spectrum of EGFP at pH 4.2 excited at 375 nm.

As mentioned above, at neutral pH the EGFP ground state also consists of a deprotonated anionic chromophore, the B state. This may be preferentially excited with 445 nm diode laser (instrument response function, IRF ~80 ps) and its characteristic excited states detected by monitoring fluorescence emission decays at 510 nm (Figure 6.3d). The detected fluorescence decay at 510 nm in presence of BQ is only slightly faster compared to that in its absence. This observation suggests that the anionic chromophore does not participate in ET. The reason for the marginally faster decay kinetics is probably due to partial excitation of neutral chromophore ‘A’ by 445 nm laser pulse [17]. Significantly, the detected fluorescence decay of EGFP at 510 nm (excitation wavelength 445 nm) could be fitted with a rise component of 35 ps and three decay components of 0.18, 2.37 and 3.28 ns (Table 6.1). However, in presence of BQ, a faster component of the order of 77 ps (40%) is observed along with the two other decay components of 0.60 and 2.98 ns. This time component (~77 ps) is also present in the decay transients at 470 or 510 nm of EGFP upon 375 nm excitation which is a signature of electron transfer between neutral chromophore A and BQ (Table 6.1). However, the amplitude of this faster time component is much higher in case of 375 nm excitation compared to 445 nm excitation (80% versus 40%; Table 6.1) and this is because 375 nm laser excites mainly neutral chromophore A, whereas 445 nm excites mostly anionic chromophore B along with some population of neutral chromophore A.

6.2.1.2. The Anionic State of Glu222 Facilitates Excited State Proton Transfer in EGFP: In ESPT, the carboxylate side chain of Glu222 acts as the final proton acceptor [18], as proton transfer takes place from the neutral chromophore's tyrosyl hydroxyl group to the γ -carboxylate group of Glu222 via a hydrogen-bond network comprising water molecules and the side chain of Ser205, leading to the deprotonated anionic chromophore (I) from which green emission occurs [16]. At neutral pH, very efficient ESPT occurs as evident from the strong green emission (Figure 6.1a, curve 3). However, at pH 4.2, the emission maximum is at ~ 450 nm (characteristic of neutral chromophore A) with a shoulder at ~ 510 nm (green emission) (Figure 6.5). Thus ESPT is significantly hindered at pH 4.2, and completely blocked at pH 3, with only blue emission is observed at this pH (Figure 6.1c, curve 8).

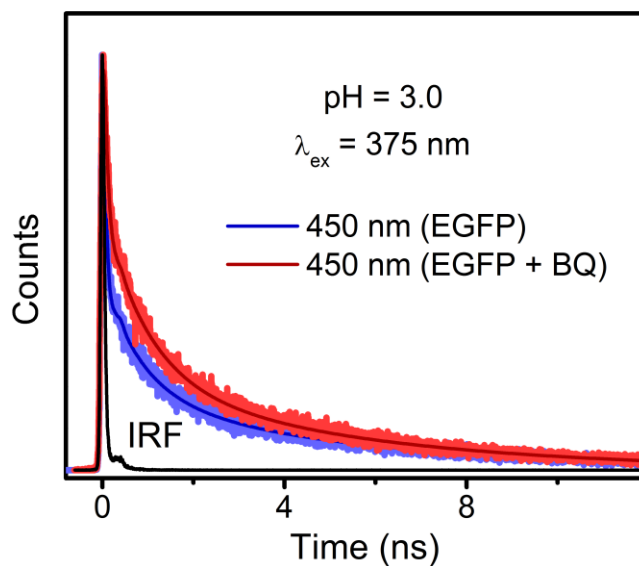


Figure 6.6. Picosecond-resolved fluorescence decays of EGFP in presence and absence of BQ at pH 3.0, excited at 375 nm and emission wavelength being 450 nm (Solid lines are best fit to the experimental data).

This change in ESPT is not accompanied by any gross alteration in the secondary structure of EGFP, since CD measurements (Figure 6.4a) show that the secondary structure remains unperturbed with change in pH. Thus, the observed change in ESPT is likely to be a result of the modification of protonation state of Glu222. The internal proton-binding site in the γ -carboxylate group of Glu222 and the ionization equilibria of GFP-chromophore are mutually dependent. Two acid-base transitions of the chromophore occur at pH values

6.8 and 13.4 [19]; at neutral and basic pH region, the local chromophore environment consists of a proton transfer relay to the bulk solvent through anionic Glu222 (strong proton acceptor) capable of efficient ESPT, resulting in green fluorescence from the anionic chromophore. At low pH, the state neutral Glu222 dominates, since the pK_a of the Glu side chain in solution is 4.07 [20], providing a possible explanation for why Glu222 cannot act as a proton acceptor, resulting in a block of the ESPT pathway at pH 3. A similar explanation has been put forward for the blue emission from a GFP mutant (deGFP1) at low pH [21]. These results presented here also provide a strong rationale for the use of EGFP as a sensitive ratiometric pH sensor.

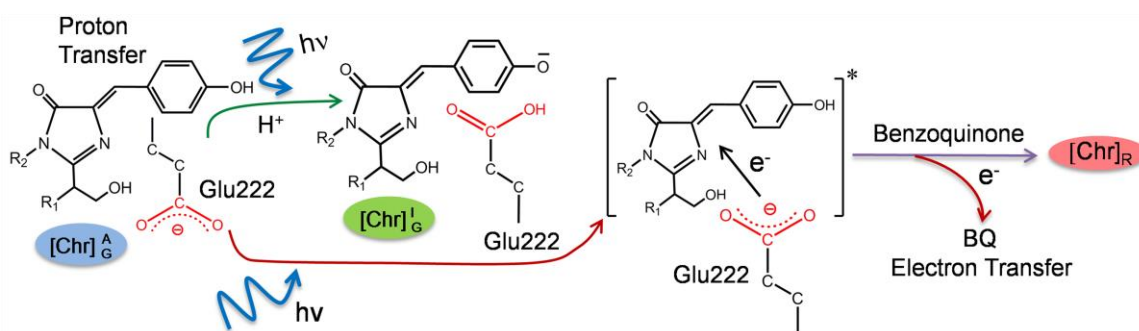


Figure 6.7. Schematic of green to red photoconversion (G/R) of EGFP. Electron transfer during oxidative photoconversion of EGFP competes with excited state proton transfer that initiates the dominant fluorescence photocycle. The ionized Glu222 is the key electron donor to the photoexcited chromophore prior to transfer of electron from the excited chromophore to the electron acceptor BQ. BQ favors G/R photoconversion in EGFP.

6.2.1.3. A Central Role for the Anionic State of Glu222 in Facilitating ET-Dependent Photoconversion in EGFP: Since the ESPT is blocked at acidic pH, we expected that the excited neutral chromophore A^* would depopulate mainly through ET process. However, at pH 3 the decay transients measured at 450 nm in absence of BQ and its presence are almost similar (Figure 6.6), implying that EGFP also does not participate in ET with BQ at pH 3. Consequently, we do not observe any G/R photoconversion in presence of oxidant BQ at low pH. The study at low pH (pH 3) also shows that quenching of the fluorescence by BQ at 450 nm is almost completely suppressed (consistent with the proposed scheme). This observation also argues against ultrafast EET as a possibility of non-radiative energy transfer from A^* to BQ on 390 nm excitation, since EET is expected to occur even at low pH.

The failure of photoconversion at low pH in the presence of oxidant BQ also indicates a role for the anionic state of Glu222. We propose that the excited state of the neutral protonated chromophore acts as an oxidant that will accept electron from the anionic Glu222 residue following which the excited state chromophore donates the electron to the electron acceptor BQ (Figure 6.7). A detailed Stark spectroscopic

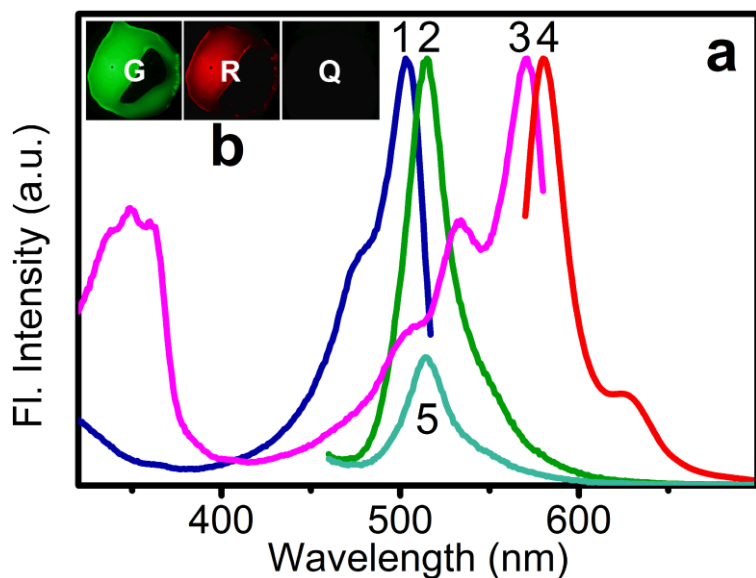


Figure 6.8. (a) Excitation (1; monitored at 540 nm) and emission spectra (2; excited at 390 nm) of green form of mEos2. Excitation (3; monitored at 600 nm) and emission (4; excited at 560 nm) spectra of red form of mEos2 obtained by irradiating mEos2 at 390 nm. Emission spectrum of mEos2 in presence of BQ (without irradiation) excited at 390 nm is marked 5. (b) Fluorescence microscopic images of mEos2 in absence of BQ excited at blue light (G) and green light (R) and in presence of BQ excited at green light (Q).

investigation by Boxer and coworkers suggest that the imidazolidinone ring is certainly electron deficient in the excited state of the neutral, protonated chromophore [22]. Moreover, due to electronic excitation to higher energy states, the split HOMO and LUMO states are occupied by unpaired electrons [23]. In contrast to the ground state of the chromophore, where the molecular orbitals are occupied by paired electrons, the unpaired electron in the HOMO makes the excited state a better electron acceptor, and the lower ionization potential of the lone pair in the LUMO makes the excited state into a better donor. Thus, the excited state of a fluorophore is potentially a better electron acceptor as well as an electron donor. At neutral pH, Glu222 is ionized and thus facilitates the ET

process. On the other hand, at pH 3, Glu222 becomes neutral (protonated) thereby unable to donate electron and hence ET is also shut off.

6.2.1.4. The Role of ET in Other PCFPs: Recent studies suggest that light induced electron donor capacity may be a common feature of many FPs, especially those that have a Tyrosine as a key amino acid in their chromophore [11]. Therefore we investigate the role of ET in a popular photoconvertible fluorescent proteins, mEos2 from the stony coral (*Lobophyllia hemprichii*) which also contains a Tyr in its fluorophore. mEos2 shows

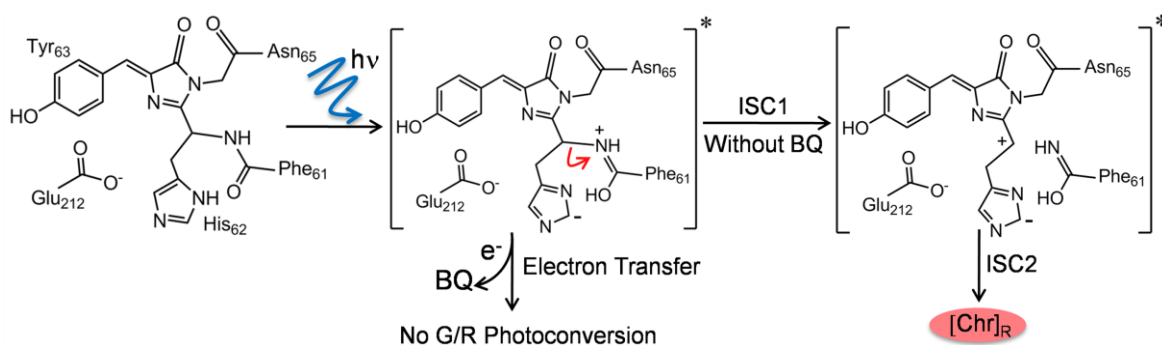


Figure 6.9. Schematic of green to red photoconversion (G/R) of mEos2 in absence and presence of BQ. On irradiation mEos2 undergoes two intersystem crossings (ISCs) to give the red form. However, BQ abolishes such a process by providing an alternative route for the de-excitation of the electron rich chromophore.

highly efficient green emission (Figure 6.8a, curve 2), when excited at 390 nm. The green form of mEos2 arises via autocatalytic maturation in the dark, yielding a cis-coplanar two ring chromophore chemically identical to that found in GFP. Irradiation with near-UV light at ~390 nm causes conversion of the green to the red emitting state (Figure 6.8b) [8]. The red chromophore in mEos2, with excitation and emission maxima at 571 (with a vibronic sideband at 533 nm) and 580 nm (with a vibronic band at 630 nm), respectively (Figure 6.8a, curves 3 and 4), is generated by cleavage of a peptide backbone. The break occurs between His-62 N_α-C_α bond (Figure 6.9) with concomitant extension of the conjugated π electron system in the interior of the β -barrel without disruption of the tertiary structure [24].

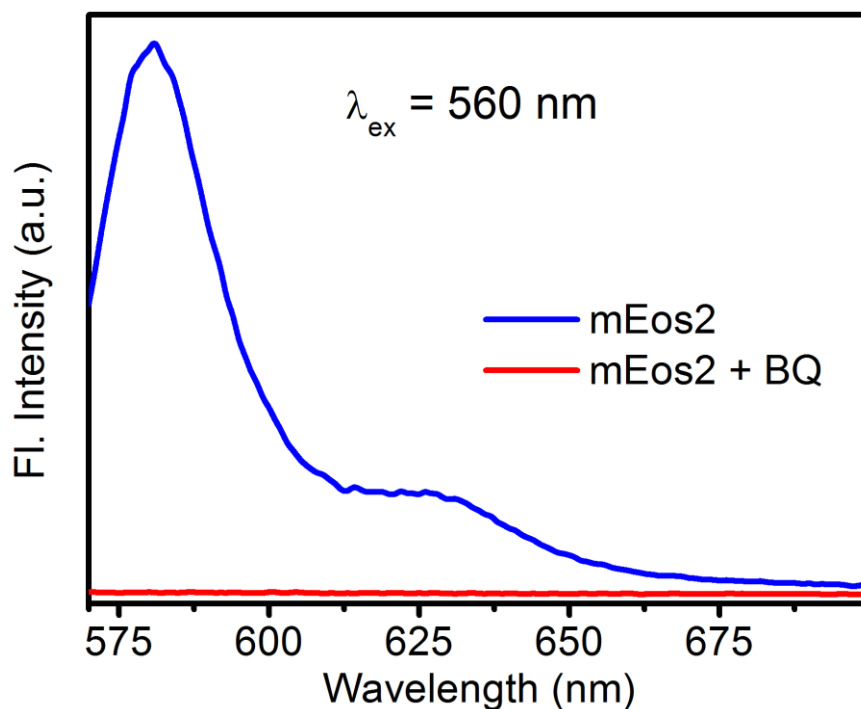


Figure 6.10. Emission spectra of mEos2 irradiated in absence and presence of BQ, excited at 560 nm.

To probe the role of ET in the G/R photoconversion of mEos2, we monitor the emission spectra of the protein treated with BQ. Notably, the fluorescence intensity of mEos2 is substantially quenched in presence of BQ (compare Figure 6.8a, curves 2 and 5), however no prominent emission peak at 580 nm (red state) is generated even after prolonged irradiation (Figure 6.10). Significantly, while BQ has no effect on the ground state of the fluorophore (Figure 6.11), it rapidly photoconverts the excited state into a non-fluorescent species, preventing any further photo-excitation (Figure 6.10). To examine the time scale associated with the excited state quenching phenomenon, we measure picosecond-resolved fluorescence decay of BQ treated protein using 375 nm laser excitation. In absence of BQ, green and red states of partially photoconverted mEos2, have different decay parameters with average lifetimes ($\langle\tau\rangle = \sum a_i\tau_i$) of 2.10 and 3.36 ns, respectively (Figure 6.12a, b). However, fluorescence transients monitored at 520 nm and 580 nm, for BQ treated protein demonstrate similar decay characteristics (Table 6.1 and Figure 6.12a and b) with a major ultrafast time component of 60 ps, consistent with an ET process. The similarity in the decay behavior suggests that, in presence of BQ the emission

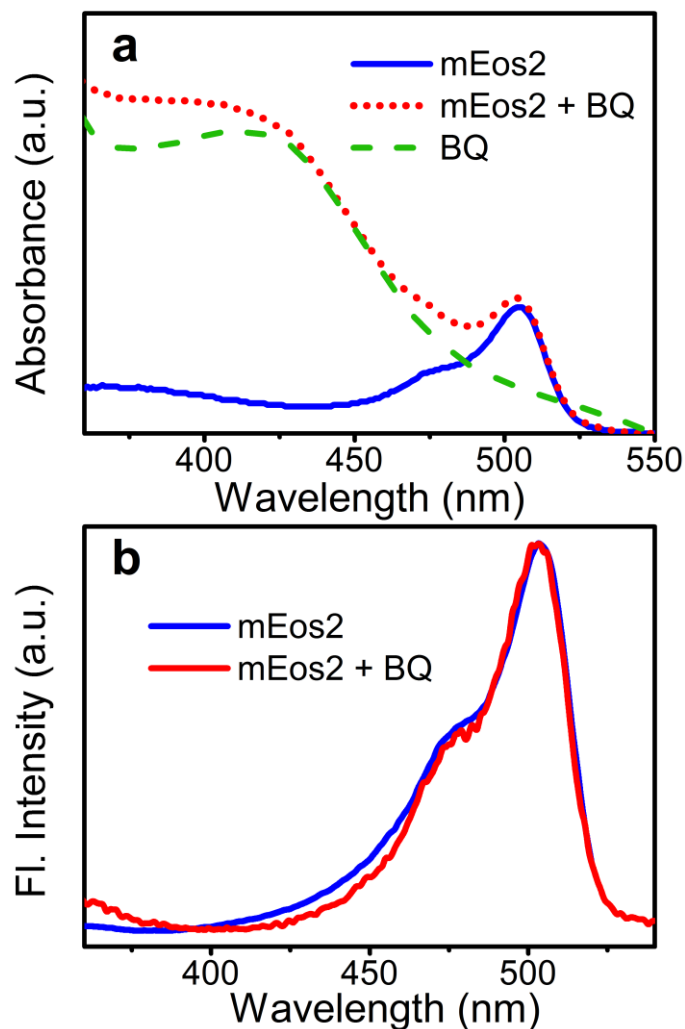


Figure 6.11. (a) Absorption spectra of mEos2 in presence and absence of BQ before irradiation. The green (dashed) line denotes the absorption spectrum of BQ in buffer. Here the peak at ~505 nm (green) is found to be almost unaltered in presence of BQ. Thus insignificant change in the ground state chromophore of mEos2 with BQ is evident. Notably, the shoulder around ~410 nm in BQ treated protein is due to the absorption characteristics of BQ as evident in the absorption spectrum of BQ in buffer. (b) Excitation spectra of mEos2 in presence and absence of BQ before irradiation. The data are also consistent with the lack of perturbation of the chromophore within the protein by BQ.

measured at either wavelength arises predominantly from the same locally excited state species (i.e., green chromophore). Thus, BQ instead of promoting electron mediated G/R photoconversion like observed in EGFP shuts down the photoconversion in mEos2 showing essentially green emission with quenched decay times due to ET (Table 6.1). The observation clearly reveals the role of electron channeling via an alternate path thereby competing with photoconversion.

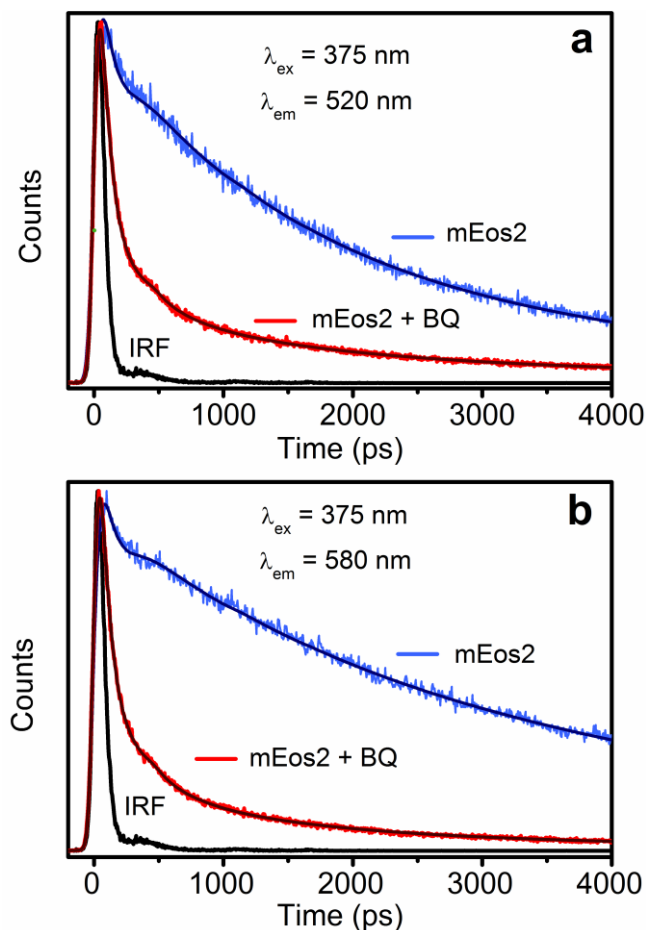


Figure 6.12. (a) Picosecond-resolved fluorescence transients of mEos2 monitored at 520 nm in presence and absence of BQ (excitation wavelength 375 nm). (b) Picosecond-resolved fluorescence transients of mEos2 monitored at 580 nm in presence and absence of BQ (excitation wavelength 375 nm) (Solid lines are best fit to the experimental data).

Recently, computer simulations have been used to understand the photoconversion pathway of mEos2 which involves excitation of the green protonated form to the singlet S_1 state generating a transient imidazolidine anion [25]. Subsequently, the system undergoes intersystem crossing to the triplet state, from which the peptide bond cleavage proceeds to form red emitting species [25]. It is to be noted that the ultrafast ET between mEos2 and BQ takes place on a time scale of 60 ps which is much faster than intersystem crossing of singlet excited state of chromophore to the triplet state, which is of the order of nanosecond [25]. Consequently, presence of electron acceptor (here BQ) provides the photoexcited mEos2 an alternate ultrafast deactivation pathway rather than undergoing slow intersystem crossing (Figure 6.9), inhibiting G/R photoconversion.

6.3. Conclusion:

This ability of electron acceptor (here BQ) to control the G/R photoconversion in EGFP and EGFP like photoconvertible fluorescent proteins (mEos2, Kaede [7], DendFP [26], mcavRFP and rfloRFP [27]) suggests the central role of ET in red chromophore formation in PCFP. In summary, the present work shows an active role of light triggered ET in G/R photoconversion. This strengthens the legitimate use of the photoconversion of EGFP as detectors of electron acceptors as suggested earlier [11]. However, light-induced electron donors can affect the redox balance in the cell by providing reducing equivalents upon photo-excitation, and this may account for some of the photo-toxicity of the fluorescent proteins [28]. For the mEos2 protein, although it has a similar ground state chromophore (Figure 6.9), our experiments suggest that ET causes a depletion of the chromophore itself by channeling the reaction in the excited state towards a different fate, effectively competing with the photoconversion process. This raises a cautionary note about using mEos2 proteins to quantitatively detect intracellular protein distribution and dynamics. The presence of high concentration of electron acceptors in areas such as the mitochondrion, will cause a rapid photochemical conversion of the excited states of these proteins, rendering them of limited applicability. Finally, the femtosecond/picosecond-resolved fluorescent transients presented here provide evidence for the ultrafast time scales associated with ET during the photoconversion process, that unequivocally implicate ET in sculpting spectral changes in emission wavelengths and photochemical changes upon irradiation.

References:

- [1] R.Y. Tsien, The green fluorescence protein, *Annu. Rev. Biochem.* 67 (1998) 509.
- [2] K.A. Lukyanov, D.M. Chudakov, S. Lukyanov, V.V. Verkhusha, Photoactivatable fluorescent proteins, *Nat. Rev. Mol. Cell Biol.* 6 (2005) 885.
- [3] R. Ando, H. Mizuno, A. Miyawaki, Regulated fast nucleocytoplasmic shuttling observed by reversible protein highlighting, *Science* 306 (2004) 1370.
- [4] M. Andresen, M.C. Wahl, A.C. Stiel, F. Gräter, L.V. Schäfer, S. Trowitzsch, G. Weber, C. Eggeling, H. Grubmüller, S.W. Hell, S. Jakobs, Structure and mechanism of the reversible photoswitch of a fluorescent protein, *Proc. Natl. Acad. Sci. U.S.A.* 102 (2005) 13070.
- [5] G.H. Patterson, J. Lippincott-Schwartz, A photoactivatable GFP for selective photolabeling of proteins and cells, *Science* 297 (2002) 1873.
- [6] M.B. Elowitz, M.G. Surette, P.E. Wolf, J. Stock, S. Leibler, Photoactivation turns green fluorescent protein red, *Curr. Biol.* 7 (1997) 809.
- [7] R. Ando, H. Hama, M. Yamamoto-Hino, H. Mizuno, A. Miyawaki, An optical marker based on the UV-induced green-to-red photoconversion of a fluorescent protein, *Proc. Natl. Acad. Sci. U.S.A.* 99 (2002) 12651.
- [8] S.A. McKinney, C.S. Murphy, K.L. Hazelwood, M.W. Davidson, L.L. Looger, A bright and photostable photoconvertible fluorescent protein, *Nat. Methods* 6 (2009) 131.
- [9] E. Betzig, G.H. Patterson, R. Sougrat, O.W. Lindwasser, S. Olenych, J.S. Bonifacino, M.W. Davidson, J. Lippincott-Schwartz, H.F. Hess, Imaging intracellular fluorescent proteins at nanometer resolution, *Science* 313 (2006) 1642.
- [10] J. Wiedenmann, G.U. Nienhaus, Live-cell imaging with EosFP and other photoactivatable marker proteins of the GFP family, *Expert Rev. Proteomics* 3 (2006) 361.
- [11] A.M. Bogdanov, A.S. Mishin, I.V. Yampolsky, V.V. Belousov, D.M. Chudakov, F.V. Subach, V.V. Verkhusha, S. Lukyanov, K.A. Lukyanov, Green fluorescent proteins are light-induced electron donors, *Nat. Chem. Biol.* 5 (2009) 459.
- [12] R. Saha, P.K. Verma, S. Rakshit, S. Saha, S. Mayor, S.K. Pal, Light driven ultrafast electron transfer in oxidative redding of green fluorescent proteins, *Sci. Rep.* 3 (2013) 1580.

- [13] T.M.H. Creemers, A.J. Lock, V. Subramaniam, T.M. Jovin, S. Volker, Three photoconvertible forms of green fluorescent protein identified by spectral hole-burning *Nat. Struct. Mol. Biol.* 6 (1999) 557.
- [14] M. Chattoraj, B.A. King, G.U. Bublitz, S.G. Boxer, Ultra-fast excited state dynamics in green fluorescent protein: Multiple states and proton transfer, *Proc. Natl. Acad. Sci. U.S.A.* 93 (1996) 8362.
- [15] K. Brejc, T.K. Sixma, P.A. Kitts, S.R. Kain, R.Y. Tsien, M. Ormö, S.J. Remington, Structural basis for dual excitation and photoisomerization of the *Aequorea victoria* green fluorescent protein, *Proc. Natl. Acad. Sci. U.S.A.* 94 (1997) 2306.
- [16] D. Stoner-Ma, A.A. Jaye, P. Matousek, M. Towrie, S.R. Meech, P.J. Tonge, Observation of excited-state proton transfer in green fluorescent protein using ultrafast vibrational spectroscopy, *J. Am. Chem. Soc.* 127 (2005) 2864.
- [17] A.F. Bell, D. Stoner-Ma, R.M. Wachter, P.J. Tonge, Light-driven decarboxylation of wild-type green fluorescent protein, *J. Am. Chem. Soc.* 125 (2003) 6919.
- [18] G. Jung, J. Wiehler, A. Zumbusch, The photophysics of green fluorescent protein: Influence of the key amino acids at positions 65, 203, and 222, *Biophys. J.* 88 (2005) 1932.
- [19] C. Scharnagl, R. Raupp-Kossmann, S.F. Fischer, Molecular basis for pH sensitivity and proton transfer in green fluorescent protein: Protonation and conformational substates from electrostatic calculations, *Biophys. J.* 77 (1999) 1839.
- [20] D. Voet, J.G. Voet, *Biochemistry*, J. Wiley & Sons, 2004.
- [21] G.T. Hanson, T.B. McAnaney, E.S. Park, M.E.P. Rendell, D.K. Yarbrough, S. Chu, L. Xi, S.G. Boxer, M.H. Montrose, S.J. Remington, Green fluorescent protein variants as ratiometric dual emission pH sensors. 1. Structural characterization and preliminary application, *Biochemistry* 41 (2002) 15477.
- [22] G. Bublitz, B.A. King, S.G. Boxer, Electronic structure of the chromophore in green fluorescent protein (GFP), *J. Am. Chem. Soc.* 120 (1998) 9370.
- [23] M. Klessinger, J. Michl, *Excited states and photochemistry of organic molecules*, Wiley-VCH, 1995.
- [24] H. Mizuno, T.K. Mal, K.I. Tong, R. Ando, T. Furuta, M. Ikura, A. Miyawaki, Photo-induced peptide cleavage in the green-to-red conversion of a fluorescent protein, *Mol. Cell* 12 (2003) 1051.

- [25] M.I. Lelimosin, V. Adam, G.U. Nienhaus, D. Bourgeois, M.J. Field, Photoconversion of the fluorescent protein EosFP: A hybrid potential simulation study reveals intersystem crossings, *J. Am. Chem. Soc.* 131 (2009) 16814.
- [26] A.A. Pakhomov, N.Y. Martynova, N.G. Gurskaya, T.A. Balashova, V.I. Martynov, Photoconversion of the chromophore of a fluorescent protein from *Dendronephthya* sp., *Biochemistry (Moscow)* 69 (2004) 901.
- [27] D.A. Shagin, E.V. Barsova, Y.G. Yanushevich, A.F. Fradkov, K.A. Lukyanov, Y.A. Labas, T.N. Semenova, J.A. Ugalde, A. Meyers, J.M. Nunez, E.A. Widder, S.A. Lukyanov, M.V. Matz, GFP-like proteins as ubiquitous metazoan superfamily: Evolution of functional features and structural complexity, *Mol. Biol. Evol.* 21 (2004) 841.
- [28] P. Carpentier, S. Violot, L. Blanchoin, D. Bourgeois, Structural basis for the phototoxicity of the fluorescent protein KillerRed, *FEBS Lett.* 583 (2009) 2839.

Chapter 7

Ultrafast Spectroscopic Studies on the Electron Transfer Dynamics in a Protein Under Nanoscopic Confinement of a Biomimetic Self-assembly

7.1. Introduction:

At the cellular interior, biopolymers such as proteins and DNA carry out various biological functions in a small space that can be approximated by nano-sized confinement (or nanocavity). For example, DNA packs in virus capsids [1] and orients in pores [2]; proteins fold in chaperonin cages [3, 4] and ribosomal exit tunnels [5]. Altogether, reactions in such *in vivo* confined environments differ from those processes in a simple aqueous solution, and with recent advances in various computational/experimental methods and resources: investigations of macromolecular crowding and confinement effects on protein conformational changes [6, 7], folding [8-12], thermodynamics and kinetics of protein folding under confinement [13], its association [14-16], and dynamics [17, 18] have deepened our understanding of biopolymer dynamics. Although considerable progress has been made in this direction of protein folding reaction, little is known about biochemical reaction dynamics like ultrafast electron transfer (ET) under cell-like confinement. ET is crucial to life and is ubiquitous in enzymatic catalysis [19-21], especially in enzymes with redox reactions [22]. Flavoproteins with flavin chromophores are examples of such enzymes and are involved in various catalytic processes [23, 24]. The understanding of ET reaction dynamics of flavins in proteins and their redox reactions in cell-like confinement is crucial to the enzyme function.

In this chapter, we report picosecond-resolved ET dynamics of riboflavin (Rf; vitamin B2) in Rf-binding protein (RBP, a flavoprotein) under the confinement, of sodium bis(2-ethylhexyl) sulfosuccinate reverse micelles (AOT-RMs) at various hydration levels ($w_0 = [\text{water}]/[\text{surfactant}]$). Encapsulation limits the available solvent, and the ability to precisely control micellar water pool radius through hydration provides the flexibility to

probe the effects of confinement in a systematic way. RM encapsulation is thus proposed to be an ideal model for crowded cellular confinement studies [25-27]. Recently, it has been suggested that the dominant factors influencing protein behavior *in vivo* are a combination of excluded volume effects and weak attractive forces (like hydrodynamic interactions and electrostatics) [28-32]. Nevertheless, how different electrostatic charge of the confining volumes affects protein cofactor binding and the associated reaction dynamics like ultrafast ET, has not been studied so far. To this end, we also monitor the ET dynamics of Rf in RBP under the confinement of a cationic hexadecyltrimethylammonium bromide (CTAB) RMs with similar water pool size to the anionic AOT-RMs, towards simulating equal restricted volume effect. We have monitored the secondary, tertiary structures and vitamin binding capacity of RBP at different hydration levels (w_0) of the RMs using various spectroscopic techniques like circular dichroism, UV-Vis absorption, steady-state and picosecond-resolved fluorescence studies. The different dynamics of ET observed in such environments has been correlated with the hydration and structure of the protein in the corresponding nano-confining environments.

7.2. Results and Discussion:

7.2.1. Protein-Cofactor Binding and Ultrafast Electron Transfer in Riboflavin Binding Protein under the Spatial Confinement of Nanoscopic Reverse Micelles [33]:

Figure 7.1a shows the absorption spectra of Rf bound to RBP in buffer and AOT-RMs of different degrees of hydration. Isoalloxazine (ISO) ring is known to be responsible for the light absorption and emission of the flavin chromophore in the near-UV and visible regions [34, 35]. Although Rf absorbs approximately at 450 nm, it also shows distinct absorbance in 300 nm region (Figure 7.1a). Complexation of Rf with RBP in buffer is found to quench both the fluorescence of Rf (excited both at 300 nm and 445 nm) and tryptophan (Trp) fluorescence (excited at 300 nm) of protein (Figure 7.1b) compared to the free Rf and RBP in buffer respectively. The observed quenching of Rf upon binding with RBP in buffer is a consequence of ultrafast ET to the flavin chromophore (Rf) in the excited electronic state from nearby tryptophan or tyrosine residues present in RBP [34, 36-38]. Upon confining

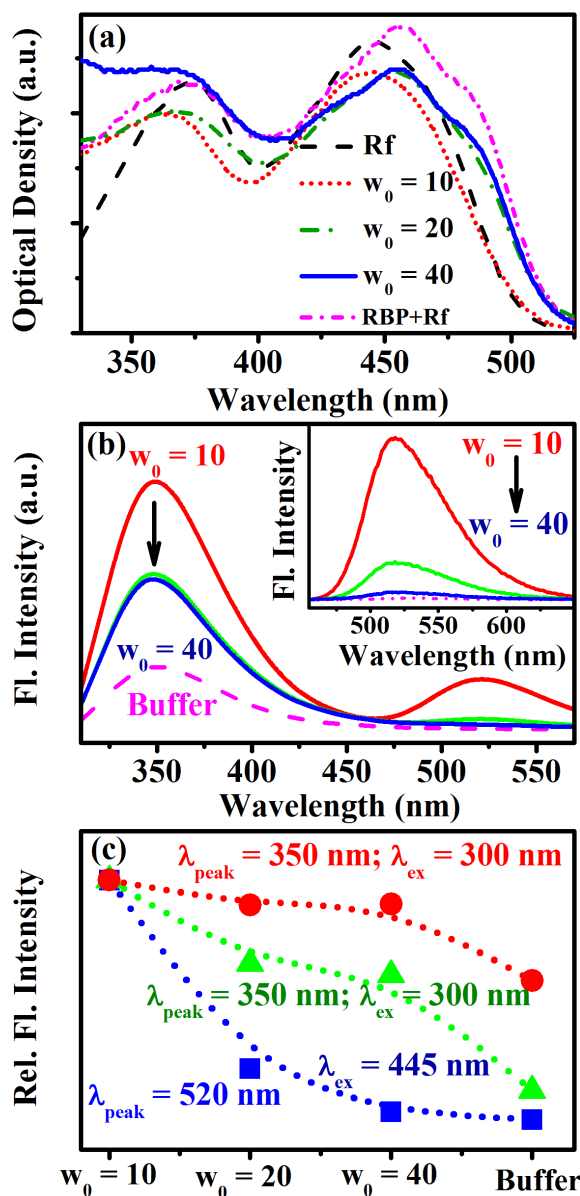


Figure 7. 1. (a) Absorption spectra of RBP-Rf complex in buffer and AOT-RMs of $w_0 = 10, 20,$ and 40 . The black line represents free Rf in buffer. (b) The total emission spectrum of the RBP-Rf complex in buffer and AOT-RMs of $w_0 = 10, 20$ and 40 ($\lambda_{\text{ex}} = 300$ nm). The inset shows emission spectrum of the RBP-Rf complex excited at 445 nm, in buffer (pink dotted line) and AOT-RMs of $w_0 = 10, 20$ and 40 . (c) Relative fluorescence intensity of trp of RBP and RBP-Rf complex, and Rf of RBP-Rf complex in buffer, and AOT-RMs of $w_0 = 10, 20$ and 40 (circle, RBP, $\lambda_{\text{ex}} = 300$ nm; triangle, RBP-Rf with $\lambda_{\text{ex}} = 300$ nm; square, RBP-Rf with $\lambda_{\text{ex}} = 445$ nm).

RBP spatially in AOT-RM of $w_0 = 10$, we find that Rf retains its characteristic fluorescence intensity at 520 nm (excited both at 300 nm and 445 nm, Figure 7.1b and its inset) which is characteristic of free Rf in buffer. However, in AOT-RM of $w_0 = 20,$ and 40 Rf fluorescence is quenched (Figure 7.1b and square symbol of Figure 7.1c), which is only

observed when it binds to RBP and appears to mark the associated ET from RBP to Rf. The binding of Rf to RBP can similarly be concluded from the emission intensity (at 350

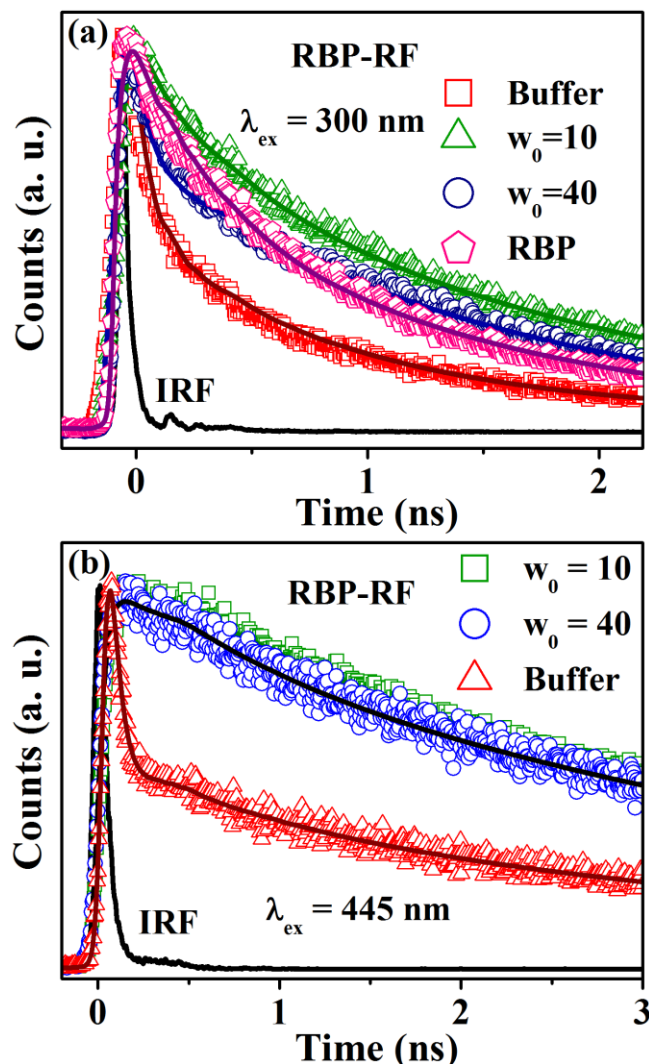


Figure 7.2. (a) Fluorescence decay transients of tryptophan of RBP-Rf complex ($\lambda_{ex} = 300$ nm; decay monitored at 350 nm) in buffer (square) and AOT-RMs of $w_0 = 10$ (triangle), $w_0 = 40$ (circle). The pentagon represents free RBP decay in buffer. (b) Fluorescence decay transient of Rf of RBP-Rf complex ($\lambda_{ex} = 445$ nm; decay monitored at 520 nm) in buffer (triangle) and AOT-RMs of $w_0 = 10$ (square), $w_0 = 40$ (circle).

nm) of tryptophan residue of RBP but this requires more concern. Upon confining RBP in AOT-RM, we find that its fluorescence intensity ($\lambda_{em} = 350$ nm) increases in RM with decreasing w_0 values (Figure 7.1c; circular symbols), which might result from a change in the protein conformation due to confinement. On the other hand, in case of RBP-Rf complex, the fluorescence intensity of tryptophan residue increases in AOT-RM of $w_0 = 10$

followed by substantial decrease in RM of $w_0 = 20$ and 40 (Figure 7.1c; triangular symbol). This quenching in tryptophan fluorescence in RM of $w_0 = 20$, and 40 could be related to Rf-binding in the protein nanospace and is believed to be both static and dynamic quenching discussed later.

To get a better insight into the observed change in fluorescence intensity, time-resolved fluorescence measurements are performed. Figure 7.2a shows the quenched decay transients of RBP-Rf complex (excited at 300 nm) in buffer compared to that of free RBP. The significant quenching of the Trp fluorescence is very much in line with the observed steady-state emission (SSEM) data discussed earlier (Figure 7.1b). Previously, Choi *et al.* suggested that the quenching of RBP fluorescence upon binding of Rf is mainly due to ground-state stacking interaction between a Trp residue at the binding site and the quinoxaline portion [35]. In fact the distinct shift in the absorption peak position of RBP

Table 7.1. Fluorescence lifetime components of RBP, and RBP-Rf complex in buffer and different RMs. ^m

$\lambda_{ex} = 300 \text{ nm}, \lambda_{em} = 350 \text{ nm}$			a_1	τ_1 (ns)	a_2	τ_2 (ns)	a_3	τ_3 (ns)	$\langle \tau \rangle$ (ns)
Buffer	-	RBP	0.49	0.24	0.43	1.18	0.08	3.64	0.92
	-	RBP-Rf	0.71	0.08	0.23	0.76	0.06	3.30	0.43
AOT-RM	$w_0 = 10$	RBP	0.33	0.24	0.54	1.50	0.13	4.44	1.47
	$w_0 = 20$		0.27	0.26	0.58	1.39	0.15	3.98	1.47
	$w_0 = 40$		0.42	0.16	0.47	1.35	0.11	4.23	1.17
	$w_0 = 10$	RBP-Rf	0.37	0.23	0.53	1.53	0.10	4.60	1.35
	$w_0 = 20$		0.37	0.21	0.54	1.42	0.09	4.21	1.22
	$w_0 = 40$		0.58	0.08	0.36	1.34	0.06	4.34	0.79
CTAB-RM	$w_0 = 25$	RBP	0.58	0.23	0.28	0.84	0.14	3.29	0.83
	$w_0 = 33$		0.58	0.21	0.28	0.78	0.14	3.22	0.78
	$w_0 = 25$	RBP-Rf	0.62	0.14	0.24	0.76	0.14	3.24	0.73
	$w_0 = 33$		0.60	0.14	0.27	0.68	0.13	3.33	0.69

^m τ_i represents decay time constant, a_i represents its relative contribution and $\langle \tau \rangle$ is the average lifetime.

bound Rf, compared to free Rf in buffer supports such an explanation (Figure 7.1a). However, significant quenching of Trp fluorescence in the excited state (Table 7.1) suggests that the quenching is dynamic in nature also. It is to be noted that considerable geometrical confinement of RBP (without Rf) in RM of $w_0 = 10$ leads to an increase in the average lifetime ($\langle \tau \rangle = a_1\tau_1 + a_2\tau_2 + a_3\tau_3$) of Trp residue (Table 7.1). However, increase in

the water content of the RM reduces $\langle\tau\rangle$ of Trp to reach a value comparable to that obtained in buffer (Table 7.1). On the other hand, when RBP-Rf complex is confined in RM, the Trp lifetime in RM of $w_0 = 10$ system is found to be more or less comparable to that of RBP itself confined in RM of $w_0 = 10$, which clearly identifies the inability of RBP to bind Rf at this hydration level of RM. However, it is evident from Table 7.1 that for RBP-Rf complex in RM of $w_0 = 20$, and 40, $\langle\tau\rangle$ of Trp is quenched compared to that of RBP in RM with identical hydration indicating that RBP is able to bind Rf in RM of $w_0 = 20$ and onwards.

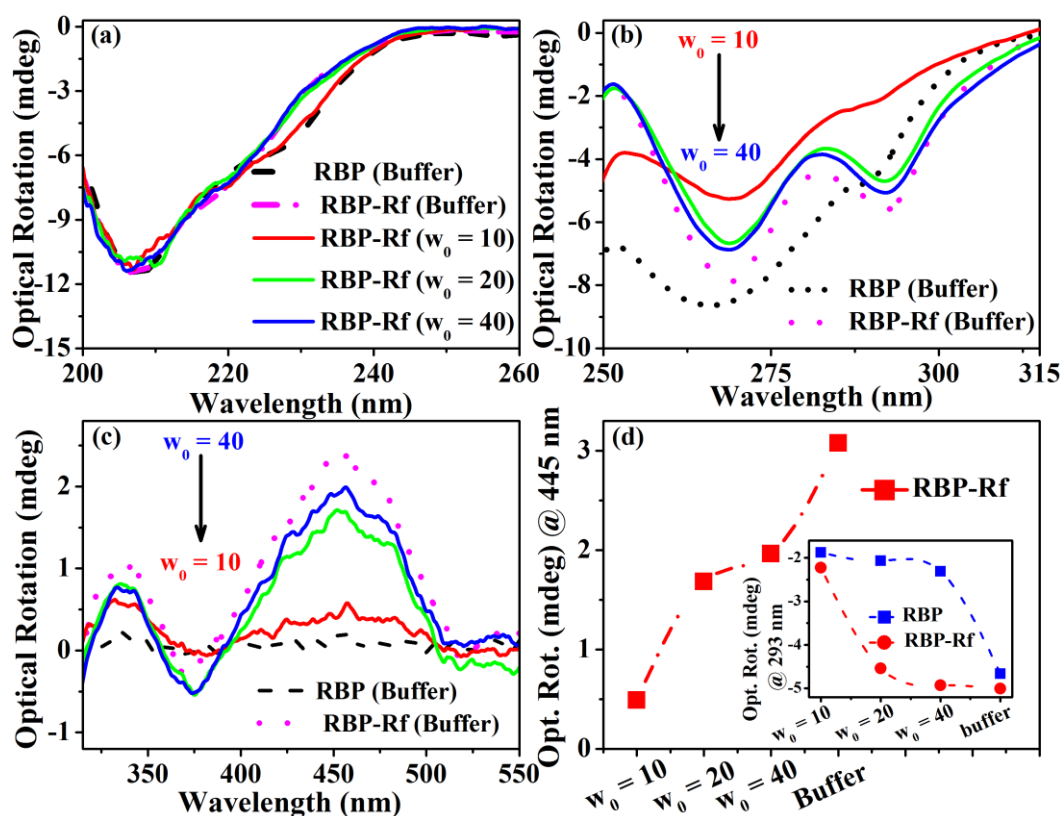


Figure 7.3. (a) Far-UV (b) Near-UV (c) Visible CD spectra of RBP in buffer and RBP-Rf complex in buffer, and AOT-RMs of $w_0 = 10, 20$ and 40. (d) Optical rotation value at 445 nm of RBP-Rf complex in buffer and AOT-RMs of $w_0 = 10, 20$ and 40. The inset shows the Optical rotation value at 293 nm of RBP (square) and RBP-Rf (circle) in buffer and AOT-RMs of $w_0 = 10, 20$ and 40.

The binding of Rf at higher hydration of the protein is also evident in the absorbance (Figure 7.1a) and visible circular dichroism (CD) spectra (Figure 7.3c) of RBP-Rf complex in RM. In Figure 7.1a it is observed that the bathochromic shift (~ 10 nm) in the visible band and a shoulder at ~ 490 nm, which is characteristic of Rf binding to RBP

[35] is absent in $w_0 = 10$ RM and is present in RM of $w_0 \geq 20$ indicating that RBP is able to bind Rf only in RM of $w_0 = 20$ and 40. Similarly, appearance of strong CD bands in the visible region for RBP-Rf complex in RM of $w_0 = 20$, and 40 (Figure 7.3c and d) suggests Rf binding to RBP. Importantly, the band positioned at ~ 445 nm is due to $\pi \rightarrow \pi^*$ transition, whereas those at 370 and 340 nm are attributed to a second $\pi \rightarrow \pi^*$ and $n \rightarrow \pi^*$ transitions, respectively (Figure 7.3c) [39]. These strong CD bands suggest that Rf is rigidly packed in the binding cleft and rotation of the ribose moiety is completely hindered. It is important to mention here that encapsulation of either RBP or RBP-Rf complex does not result in any significant change in the secondary structure (Figure 7.4a and Figure 7.3a, respectively). However, the tertiary structure of the RBP-Rf complex as well as that of the protein itself suffers considerable perturbation upon confinement in $w_0 = 10$ RM system, as concluded from a loss in the intensity of the peaks at 268 and 293 nm (Figure 7.3b). With increased hydration ($w_0 \geq 20$), the near UV CD spectrum considerably recovers its native form for the RBP-Rf complex, however, not for the protein itself (Figure 7.3b and inset of 7.3d). Indeed one can observe that whereas intensity of the CD signal for RBP at 293 nm is almost unaltered, it increases for the RBP-Rf complex with increased hydration of the RM (Figure 7.3d, inset). This behavior affirms that vitamin when bound to the protein indeed plays an important role in providing extra stability to protein in confined environment just like Rf bound RBP has enhanced thermal stability manifested by the increase of denaturation temperature from 60.8°C to 72.8°C [40].

The observations mentioned above might be better understood in terms of confinement and water properties in RM. Water present inside the RM can broadly be distinguished as bound type (water molecules hydrogen bonded to the interface) and bulk type [41, 42]. At very low w_0 , the water molecules in the pool remain very close and strongly attracted to the polar head groups of the surfactants and hence are rather slow moving. As w_0 increases, the size of the water pool increases, and in such large water pools, the mobility of water molecules becomes relatively high. This change in mobility of the entrapped water molecules inside the RM has also been reported to affect the reaction kinetics occurring in the RM [43]. In RM of $w_0 = 10$, RBP retains its secondary structure, although loses its tertiary structure partially as well as its binding capability. It is important to note here that the presence of hydration shell is essential for a macromolecule's

biological activity [44]. Without hydration water, proteins would lack not only their native

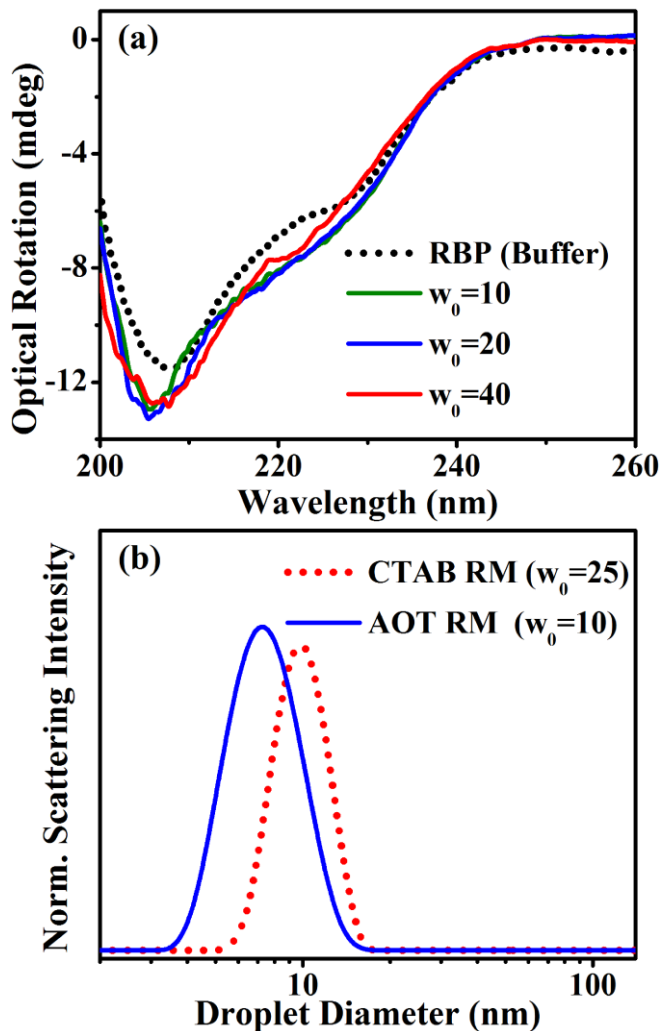


Figure 7.4. (a) Far-UV CD spectra of RBP in buffer, and AOT-RMs of $w_0 = 10, 20$ and 40 . (b) Representative DLS signals for AOT and CTAB-RMs.

folded structure but also the conformational flexibility that allows their biological activity [45]. For proteins with nearly spherical shape, the empirical relationship between its molar mass (M) and the hydration degree of RM is described by the following relation [46],

$$w_0 = (0.083 \pm 0.008) \sqrt{M} \quad (7-1)$$

Equations (7-1) indicates that the maximum degree of hydration for RBP ($M = 30$ kDa) is expected to occur at $w_0 = 13-16$. It seems that in $w_0 = 10$ AOT-RM, RBP is in a lower degree of hydration compared to that in aqueous buffer making the protein relatively rigid and hence not functional. In RMs of $w_0 \geq 20$, abundance of bulk type water compensates

its dehydration and also geometrical confinement is relieved at a higher extent compared to that in $w_0 = 10$ RM bringing in RBP's native tertiary structure and hence its functionality.

Table 7.2. Fluorescence lifetime components of Rf, and RBP-Rf complex in buffer and different RMs. ^m

$\lambda_{\text{ex}} = 445 \text{ nm}, \lambda_{\text{em}} = 520 \text{ nm}$			a₁	τ_1 (ns)	a₂	τ_2 (ns)	a₃	τ_3 (ns)	$\langle\tau\rangle$ (ns)
Buffer	-	Rf	0.00	1.00	0.00	1.00	1.00	4.70	4.70
	-	RBP-Rf	0.83	0.03	0.05	0.80	0.12	4.78	0.64
AOT-RM	$w_0 = 10$	Rf	0.20	1.11	0.00	1.00	0.80	4.84	4.09
	$w_0 = 20$		0.20	0.62	0.00	1.00	0.80	4.69	3.88
	$w_0 = 40$		0.15	0.79	0.00	1.00	0.85	4.72	4.13
	$w_0 = 10$	RBP-Rf	0.21	0.61	0.00	1.00	0.79	4.81	3.93
	$w_0 = 20$		0.20	0.65	0.00	1.00	0.80	4.81	3.98
	$w_0 = 40$		0.18	1.20	0.00	1.00	0.82	4.81	4.16
CTAB-RM	$w_0 = 25$	Rf	0.68	0.21	0.32	0.60	0.00	1.00	0.33
	$w_0 = 33$		0.76	0.27	0.24	0.81	0.00	1.00	0.40
	$w_0 = 25$	RBP-Rf	0.74	0.05	0.24	0.45	0.02	2.45	0.20
	$w_0 = 33$		0.73	0.05	0.24	0.52	0.03	2.44	0.23

^m τ_i represents decay time constant, a_i represents its relative contribution and $\langle\tau\rangle$ is the average lifetime.

Complexation of Rf with RBP in buffer leads to quenching of Rf fluorescence [47] as also observed in Figure 7.1b. Although significant quenching in steady-state fluorescence of Rf is observed upon binding with RBP in $w_0 = 20$, and 40 RM, its lifetime does not change appreciably (Figure 7.2b and Table 7.2). The unchanged fluorescence decay of Rf in RBP rules out the occurrence of ultrafast ET in AOT-RMs ($w_0 \geq 20$). As has been discussed earlier, RBP regains its tertiary structure and binding capacity in RMs of $w_0 \geq 20$. So quenching in lifetime of Rf bound to RBP is expected in RM of $w_0 = 20$, and 40 (Figure 7.2b). Remarkably ET and its rate is dependent on the redox centre distance [48-50] e.g., tunnelling times range from a few nanoseconds (12.2 Å ET in the high-potential iron-sulfur protein from *C. vinosum*) to 10 milliseconds (26 Å ET in *Pseudomonas. aeruginosa azurin*) [49]. For flavin chromophores with various flavoproteins the ET rate is found to be different due to different chromophore-aromatic amino acid residue arrangements in the protein nanospace [34]. The donor-acceptor distance dependence of photoinduced ET in flavoproteins has been revealed by the work of Tanaka *et al.* [51]. In the confinement of AOT-RM ($w_0 \geq 20$), the nonoccurrence of ultrafast ET in the protein nanospace is thus believed to be the improper distance between the donor and acceptor

pair, due to the electrostatic charge interaction of the RM surface as discussed latter. Remarkably, in proper redox distance with aromatic amino acids in RBP the near UV absorption band position of Rf do not undergo any shift [35]. The combination of red shift by complexing with aromatic amino acids at the binding site and blue shift due to nonpolar environment in the protein nanospace results in nearly unshifted band position of Rf in RBP. However, in AOT-RMs of $w_0 \geq 20$ a small blue shift in the near-UV band position coupled with a shoulder at 490 nm (Figure 7.1a) suggests improper complexation of Rf with the aromatic amino acids. In this context, the steady-state quenching of Trp

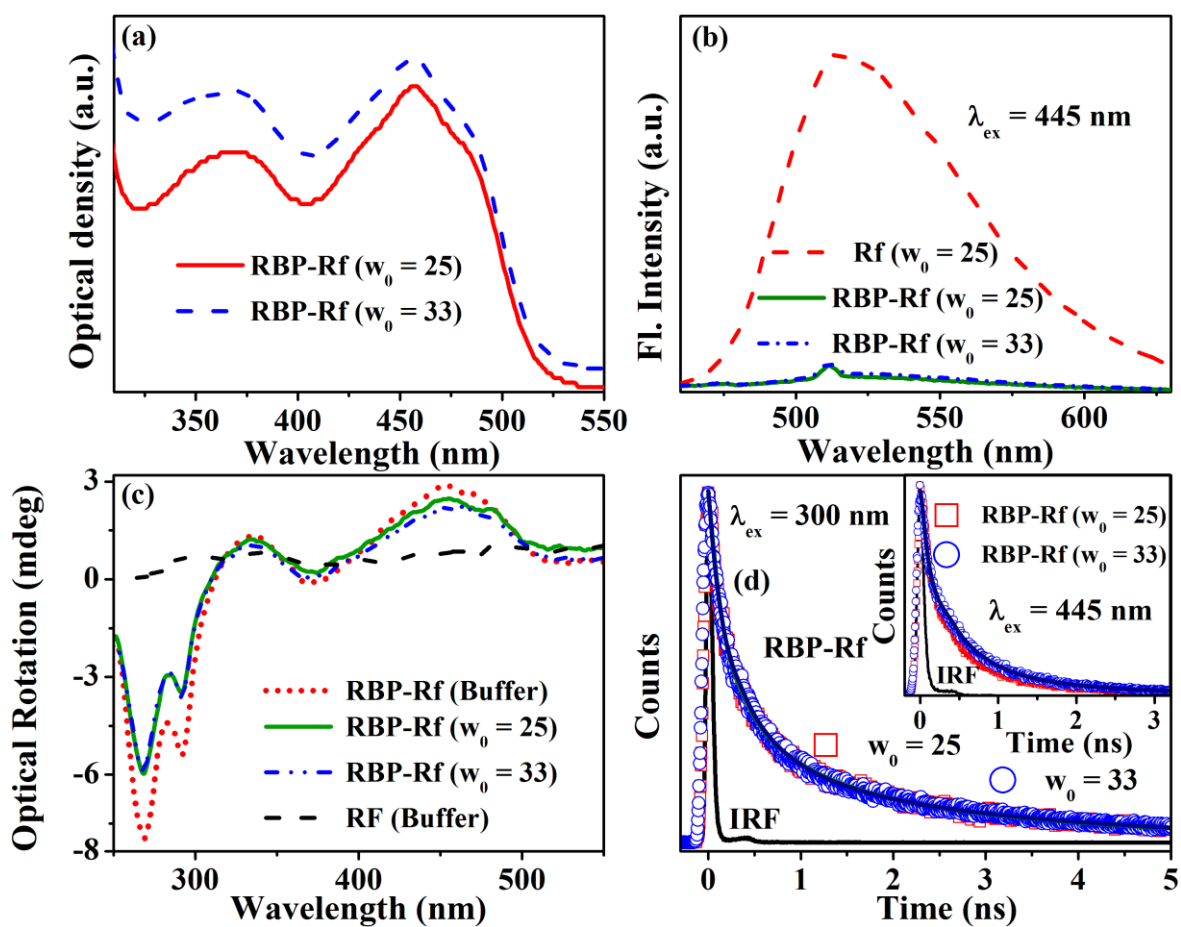


Figure 7.5. (a) Absorption spectra of RBP-Rf complex in CTAB-RMs of $w_0 = 25$ and 33. (b) Emission spectra of free Rf and RBP-Rf complex in CTAB-RMs of various w_0 values ($\lambda_{ex} = 445$ nm). (c) Visible-CD spectra of Rf and RBP-Rf complex in buffer, and CTAB-RMs of $w_0 = 25$, and 33. (d) Fluorescence decay transients of tryptophan of RBP-Rf complex ($\lambda_{ex} = 300$ nm; $\lambda_{em} = 350$ nm) in CTAB-RMs of $w_0 = 25$ (square) and 33 (circle). The inset shows decay transient of Rf of RBP-Rf complex ($\lambda_{ex} = 445$ nm; $\lambda_{em} = 520$ nm) in CTAB-RMs of $w_0 = 25$ (square) and 33 (circle).

fluorescence in AOT-RMs also needs some attention. Previously, the observed substantial quenching of Trp fluorescence ($\sim 65\%$) in buffer was attributed to the presence of 5 out of 6 tryptophans in RBP in the vicinity (< 0.45 nm) of Rf [35]. However, for AOT-RMs of $w_0 \geq 20$ such quenching of Trp fluorescence is found to be only $\sim 40\%$ compared to the free RBP in respective RMs. Thus, both steady-state absorption and emission spectroscopic data suggest the improper complexation of Rf for ET in the RBP interior, and in this condition the observed steady-state quenching of Rf fluorescence in RM of $w_0 = 20$ and 40 systems is believed to be due to the ground state stacking interaction of Rf with RBP.

Table 7.3. Dynamic light scattering (DLS) data of AOT and CTAB-RMs of various w_0 values.

AOT-RM			CTAB-RM		
w_0	Droplet Diameter (nm)	Water Pool Size (nm)	w_0	Droplet Diameter (nm)	Water Pool Size (nm)
5	6.70	4.50	10	6.10	1.90
10	7.56	5.36	20	8.40	4.20
20	10.06	7.86	25	9.90	5.70
40	14.90	12.70	30	14.4	10.2
-	-	-	35	22.2	18.0
-	-	-	40	24.0	20.3

In order to investigate the effect of confinement by a cationic surfactant forming RM, we choose CTAB-RMs with similar water pool size ($w_0 = 25$ and 33) to that of AOT-RM of $w_0 = 10$ and 40 respectively (Table 7.3). Figure 7.4b is the representative DLS signals for each AOT and CTAB-RMs. The DLS signals are indicative of monodispersed RMs and the observed values are quite consistent with previous literature [52, 53]. The fluorescence decay transients of RBP fluorescence in the RBP-Rf complex at different hydration levels of CTAB-RM is shown in Figure 7.5d. The observed quenching in the Trp fluorescence is evident from Table 7.1 and essentially indicates successful binding of Rf to RBP in accordance with the minimum hydration criterion of RBP in a RM (equation (7-1)). In fact the binding of Rf to RBP at these degrees of hydration are very much consistent with the associated absorption and CD spectroscopic data. In Figure 7.5a the shoulder at ~ 490 nm which is characteristic of Rf binding to RBP is distinctly observed in both the hydration levels of CTAB-RM. Similarly, the strong CD bands at 445, 370 and 340 nm

(Figure 7.5c) in the visible region for the RBP-Rf complex further supports the hindered rotation of the ribose moiety in the nanospace of RBP. In this situation one can see significant quenching of Rf fluorescence in both the steady-state and time-resolved fluorescence spectroscopic data of Figure 7.5b and d. The observed quenching of Rf fluorescence is well evident from the decay components of Table 7.2. Notably, confinement of Rf in CTAB-RM itself quenches the Rf fluorescence (Table 7.2) and is found to be the quenching effect of bromide ion. In this respect we monitor the decay transients of Rf in KBr solution and various RMs containing bromide ion, showing quenching of Rf fluorescence compared to that in buffer. It is to be noted that although Rf itself is quenched in the CTAB-RM, the decay time constants of free Rf in CTAB-RM are distinctly different than that present in the protein nanospace (Table 7.2). So we emphasize that under the confinement of CTAB-RM, Rf present in the nanospace of RBP is free from bromide quenching effect and the observed quenching is essentially due to the ultrafast ET in the protein nanospace, which is similar to that in buffer (Table 7.2).

At this juncture it is quite essential to discuss on the different behavior of the flavoprotein under the confinement of RM with different charge types. One can see that although ET of Rf in CTAB-RM occurs in a manner similar to that in buffer, it certainly does not occur under the confinement of anionic AOT-RMs of similar hydration, although hydration of the protein under confinement enables its binding to Rf. Recent simulation has shown that protein folding/unfolding equilibrium largely depends upon the polarity of the confining volume [54]. The simulation by Griffin *et al.* suggests that in addition to the confinement effect, surface interaction plays determining role on the dimerization of an off-lattice β -barrel protein [15]. In the present study the different behavior of the ET in various RMs suggests that electrostatic interaction of the RM surface plays a significant role in determining the feasibility of such a process in flavoproteins. Notably in the RM pH of ~ 7.0 RBP is expected to be negatively charged (pI of RBP is 4.0 [55]). A study by Lucent *et al.*, [56] using an explicit solvent model, showed that a protein is destabilized when confined by a purely repulsive potential together with solvent. So, we emphasize that in the repulsive potential of the confining volume (anionic AOT-RM) the binding site of the protein is so influenced that Rf is unable to complex properly with aromatic amino acids in the protein nanospace. However, under the attractive interaction of the cationic

CTAB-RM the protein conformation is so maintained that Rf can complex properly with aromatic amino acids in the protein nanospace, and ET is feasible with RBP.

7.3. Conclusion:

It has been found that under confinement of anionic AOT-RM, RBP loses its ability to bind with Rf in RM of $w_0 = 10$, however, it regains its binding capacity and tertiary structure in RM of $w_0 \geq 20$. The reason being that maximum degree of hydration for RBP occurs at $w_0 = 13-16$. Thus when there is higher volume accessible to a protein and more bulk type water as in AOT-RM of $w_0 = 20$ and onwards, RBP recovers its tertiary structure as well as binding capacity. Our detailed steady-state and time-resolved spectroscopic data suggest that under the similar size restriction of RM confinement the biochemical function of RBP-Rf system is distinctly different depending upon the hydration and the nature of the RM forming surfactant showing confinement. In anionic AOT-RM, confinement perturbs the ET from RBP to Rf, even at the maximum hydration of the protein. On the other hand the cationic CTAB-RM resumes such a process with similar confining volume. We believe that due to the electrostatic repulsion of the anionic AOT-RM surface the cofactor binding site of RBP is so perturbed that Rf is found unable to complex properly with the aromatic amino acids in protein interior. However, the confinement of cationic CTAB-RM resumes such a process with proper binding of Rf in the nanospace of RBP. Thus both the hydration and surface charge of the confining volume is expected to largely determine the biochemical reaction dynamics like ET in real biological cells. Further studies will expand the present work to a wide range of biochemical reaction systems in different confinements of RMs.

References:

- [1] A.A. Simpson, Y. Tao, P.G. Leiman, M.O. Badasso, Y. He, P.J. Jardine, N.H. Olson, M.C. Morais, S. Grimes, D.L. Anderson, T.S. Baker, M.G. Rossmann, Structure of the bacteriophage ϕ 29 DNA packaging motor, *Nature* 408 (2000) 745.
- [2] J. Mathé, A. Aksimentiev, D.R. Nelson, K. Schulten, A. Meller, Orientation discrimination of single-stranded DNA inside the α -hemolysin membrane channel, *Proc. Natl. Acad. Sci. U.S.A.* 102 (2005) 12377.
- [3] R.J. Ellis, A.P. Minton, Cell biology: Join the crowd, *Nature* 425 (2003) 27.
- [4] A. Brinker, G. Pfeifer, M.J. Kerner, D.J. Naylor, F.U. Hartl, M. Hayer-Hartl, Dual function of protein confinement in chaperonin-assisted protein folding, *Cell* 107 (2001) 223.
- [5] P. Nissen, J. Hansen, N. Ban, P.B. Moore, T.A. Steitz, The structural basis of ribosome activity in peptide bond synthesis, *Science* 289 (2000) 920.
- [6] M.S. Cheung, D. Thirumalai, Effects of crowding and confinement on the structures of the transition state ensemble in proteins, *J. Phys. Chem. B* 111 (2007) 8250.
- [7] D. Homouz, H. Sanabria, M.N. Waxham, M.S. Cheung, Modulation of calmodulin plasticity by the effect of macromolecular crowding, *J. Mol. Biol.* 391 (2009) 933.
- [8] S.-Q. Zhang, M.S. Cheung, Manipulating biopolymer dynamics by anisotropic nanoconfinement, *Nano Lett.* 7 (2007) 3438.
- [9] S. Qin, H.-X. Zhou, Atomistic modeling of macromolecular crowding predicts modest increases in protein folding and binding stability, *Biophys. J.* 97 (2009) 12.
- [10] H.-X. Zhou, Protein folding and binding in confined spaces and in crowded solutions, *J. Mol. Recognit.* 17 (2004) 368.
- [11] L.A. Munishkina, E.M. Cooper, V.N. Uversky, A.L. Fink, The effect of macromolecular crowding on protein aggregation and amyloid fibril formation, *J. Mol. Recognit.* 17 (2004) 456.
- [12] G. Ping, J.-M. Yuan, Z. Sun, Y. Wei, Studies of effects of macromolecular crowding and confinement on protein folding and protein stability, *J. Mol. Recognit.* 17 (2004) 433.

- [13] J. Mittal, R.B. Best, Thermodynamics and kinetics of protein folding under confinement, *Proc. Natl. Acad. Sci. U.S.A.* 105 (2008) 20233.
- [14] W. Wang, W.-X. Xu, Y. Levy, E. Trizac, P.G. Wolynes, Confinement effects on the kinetics and thermodynamics of protein dimerization, *Proc. Natl. Acad. Sci. U.S.A.* 106 (2009) 5517.
- [15] M.A. Griffin, M. Friedel, J.E. Shea, Effects of frustration, confinement, and surface interactions on the dimerization of an off-lattice β -barrel protein, *J. Chem. Phys.* 123 (2005) 174707.
- [16] A.P. Minton, Macromolecular crowding and molecular recognition, *J. Mol. Recognit.* 6 (1993) 211.
- [17] S.R. McGuffee, A.H. Elcock, Atomically detailed simulations of concentrated protein solutions: The effects of salt, pH, point mutations, and protein concentration in simulations of 1000-molecule systems, *J. Am. Chem. Soc.* 128 (2006) 12098.
- [18] P. Bernadó, J.G. de la Torre, M. Pons, Macromolecular crowding in biological systems: Hydrodynamics and NMR methods, *J. Mol. Recognit.* 17 (2004) 397.
- [19] V. Balzani, Electron transfer in chemistry, Wiley-VCH, Weinheim, Germany, 2001.
- [20] D.S. Bendall, Protein electron transfer, Bios Scientific, Oxford, U.K., 1996.
- [21] J. Stubbe, W.A. van der Donk, Protein radicals in enzyme catalysis, *Chem. Rev.* 98 (1998) 705.
- [22] M. Sinnott, Comprehensive biological catalysis: A mechanistic reference, Academic, San Diego, 1998.
- [23] S. Ghisla, P. Kroneck, P. Macheroux, H. Sund, Flavins and flavoproteins, Agency for Scientific Pub, Berlin, 1999.
- [24] F. Müller, Chemistry and biochemistry of flavoenzymes, CRC Press, Boca Raton, Florida, 1991.
- [25] J.H. Tian, A.E. Garcia, Simulations of the confinement of ubiquitin in self-assembled reverse micelles, *J. Chem. Phys.* 134 (2011) 225101.
- [26] W.D. Van Horn, M.E. Ogilvie, P.F. Flynn, Reverse micelle encapsulation as a model for intracellular crowding, *J. Am. Chem. Soc.* 131 (2009) 8030.

- [27] P.S.W. Yeung, P.H. Axelsen, The crowded environment of a reverse micelle induces the formation of β -strand seed structures for nucleating amyloid fibril formation, *J. Am. Chem. Soc.* 134 (2012) 6061.
- [28] M. Feig, Y. Sugita, Variable interactions between protein crowders and biomolecular solutes are important in understanding cellular crowding, *J. Phys. Chem. B* 116 (2011) 599.
- [29] M. Jiao, H.-T. Li, J. Chen, A.P. Minton, Y. Liang, Attractive protein-polymer interactions markedly alter the effect of macromolecular crowding on protein association equilibria, *Biophys. J.* 99 (2010) 914.
- [30] P.B. Crowley, K. Brett, J. Muldoon, NMR spectroscopy reveals cytochrome c-poly(ethylene glycol) interactions, *ChemBioChem* 9 (2008) 685.
- [31] A.P. Minton, The effect of volume occupancy upon the thermodynamic activity of proteins: Some biochemical consequences, *Mol. Cell. Biochem.* 55 (1983) 119.
- [32] C. Li, G.J. Pielak, Using NMR to distinguish viscosity effects from nonspecific protein binding under crowded conditions, *J. Am. Chem. Soc.* 131 (2009) 1368.
- [33] R. Saha, S. Rakshit, P.K. Verma, R.K. Mitra, S.K. Pal, Protein-cofactor binding and ultrafast electron transfer in riboflavin binding protein under the spatial confinement of nanoscopic reverse micelles, *J. Mol. Recognit.* 26 (2013) 59.
- [34] N. Mataga, H. Chosrowjan, Y. Shibata, F. Tanaka, Y. Nishina, K. Shiga, Dynamics and mechanisms of ultrafast fluorescence quenching reactions of flavin chromophores in protein nanospace, *J. Phys. Chem. B* 104 (2000) 10667.
- [35] J.-D. Choi, D.B. McCormick, The interaction of flavins with egg white riboflavin-binding protein, *Arch. Biochem. Biophys.* 204 (1980) 41.
- [36] D. Zhong, A.H. Zewail, Femtosecond dynamics of flavoproteins: Charge separation and recombination in riboflavine (vitamin B₂)-binding protein and in glucose oxidase enzyme, *Proc. Natl. Acad. Sci. U.S.A.* 98 (2001) 11867.
- [37] S. Rakshit, R. Saha, P.K. Verma, R.K. Mitra, S.K. Pal, Ultrafast electron transfer in riboflavin binding protein in macromolecular crowding of nano-sized micelle, *Biochimie* 94 (2012) 2673.
- [38] A. Lukacs, R.-K. Zhao, A. Haigney, R. Brust, G.M. Greetham, M. Towrie, P.J. Tonge, S.R. Meech, Excited state structure and dynamics of the neutral and anionic flavin

radical revealed by ultrafast transient mid-IR to visible spectroscopy, *J. Phys. Chem. B* 116 (2012) 5810.

[39] A. Galat, Interaction of riboflavin binding protein with riboflavin, quinacrine, chlorpromazine and daunomycin, *Int. J. Biochem.* 20 (1988) 1021.

[40] M. Wasylewski, Binding study of riboflavin-binding protein with riboflavin and its analogues by differential scanning calorimetry, *J. Protein Chem.* 19 (2000) 523.

[41] P.K. Verma, R. Saha, R.K. Mitra, S.K. Pal, Slow water dynamics at the surface of macromolecular assemblies of different morphologies, *Soft Matter* 6 (2010) 5971.

[42] R. Saha, S. Rakshit, R.K. Mitra, S.K. Pal, Microstructure, morphology, and ultrafast dynamics of a novel edible microemulsion, *Langmuir* 28 (2012) 8309.

[43] P.K. Verma, A. Makhal, R.K. Mitra, S.K. Pal, Role of solvation dynamics in the kinetics of solvolysis reactions in microreactors, *Phys. Chem. Chem. Phys.* 11 (2009) 8467.

[44] S.K. Pal, A.H. Zewail, Dynamics of water in biological recognition, *Chem. Rev.* 104 (2004) 2099.

[45] J.A. Rupley, G. Careri, Protein hydration and function, *Adv. Prot. Chem.* 41 (1991) 37.

[46] A.N. Eryomin, D.I. Metelitz, Effect of hydration degree of aerosol OT reversed micelles and surfactant concentration in heptane on spectral and catalytic properties of catalase, *Biochemistry (Moscow)* 64 (1999) 1049.

[47] N. Mataga, H. Chosrowjan, S. Taniguchi, F. Tanaka, N. Kido, M. Kitamura, Femtosecond fluorescence dynamics of flavoproteins: Comparative studies on flavodoxin, its site-directed mutants, and riboflavin binding protein regarding ultrafast electron transfer in protein nanospaces, *J. Phys. Chem. B* 106 (2002) 8917.

[48] T. Mondol, S. Batabyal, S.K. Pal, Ultrafast electron transfer in the recognition of different DNA sequences by a DNA-binding protein with different dynamical conformations, *J. Biomol. Struct. Dyn.* 30 (2012) 362.

[49] J.R. Winkler, Long-range electron transfer in biology, John Wiley & Sons, Ltd, 2006.

[50] S.S. Isied, M.Y. Ogawa, J.F. Wishart, Peptide-mediated intramolecular electron transfer: Long-range distance dependence, *Chem. Rev.* 92 (1992) 381.

- [51] F. Tanaka, H. Chosrowjan, S. Taniguchi, N. Mataga, K. Sato, Y. Nishina, K. Shiga, Donor-acceptor distance-dependence of photoinduced electron-transfer rate in flavoproteins, *J. Phys. Chem. B* 111 (2007) 5694.
- [52] R.K. Mitra, S.S. Sinha, S.K. Pal, Temperature-dependent solvation dynamics of water in AOT/isooctane reverse micelles, *Langmuir* 24 (2008) 49.
- [53] E.M. Corbeil, N.E. Levinger, Dynamics of polar solvation in quaternary microemulsions, *Langmuir* 19 (2003) 7264.
- [54] J. Tian, A.E. Garcia, Simulation studies of protein folding/unfolding equilibrium under polar and nonpolar confinement, *J. Am. Chem. Soc.* 133 (2011) 15157.
- [55] G. Massolini, E. De Lorenzi, M.C. Ponci, C. Gandini, G. Caccialanza, H.L. Monaco, Egg yolk riboflavin binding protein as a new chiral stationary phase in high-performance liquid chromatography, *J. Chromatogr., A* 704 (1995) 55.
- [56] D. Lucent, V. Vishal, V.S. Pande, Protein folding under confinement: A role for solvent, *Proc. Natl. Acad. Sci. U.S.A.* 104 (2007) 10430.

Chapter 8

Spectroscopic Studies on the Molecular Recognition of a Fluorescence-modified Protein by a Model Receptor

8.1. Introduction:

Molecular recognition is a fundamental step crucial in any biological processes starting from cellular signaling to enzyme catalysis, and essentially involves the recognition between two or more molecular binding partners, leading either to their association or to their rejection [1]. How and why two molecular binding partners specifically fit together among a plethora of molecular components in the crowded cell environment, and the weak intermolecular forces that act on them, are questions of complementarity of size, shape, and chemical surface [2]. Proteins are important target molecules for recognition by various signaling molecules. Visualization of the *in vitro* complex cellular processes involving proteins requires the use of spectroscopically distinguishable fluorescent reporters. Labelling of proteins using various hydrophobic fluorescent probes is a procedure often followed in biochemical studies involving recognition of molecules. The hydrophobic fluorescent probe dansyl chloride is widely used to modify charged polar side chains of amino acids like lysine and arginine [3, 4]. However, changes in even one amino acid property of a protein due to DNA point mutation may affect the molecular recognition of the protein leading to various diseases [5-9]. For example, creation of hydrophobic spot in hemoglobin due to Glu6Val point mutation causes clumping together (polymerization) of hemoglobin molecules into rigid fibers to cause “sickling” of red blood cells [10]. Nevertheless, labelling of protein using hydrophobic fluorescent probe is a common procedure in biochemical studies, while its effect on molecular recognition process is less attended in the literature. In the present study the lysine side chains of apomyoglobin (Apo-Mb) has been dansylated, to study the effect of hydrophobic surface modification of the protein on the molecular recognition process by cyclodextrins (CyDs) as a model synthetic receptor.

CyDs are cyclic oligosaccharides known to recognize a wide variety of organic, as well as inorganic, guest molecules, forming host-guest inclusion complexes with various guest molecules of suitable size fitting the host CyD cavity [11-15]. Accordingly, CyDs are used as chiral selectors in chromatographic separations [16, 17]. Inclusion complexation of β -CyD can effectively discriminate the L- and D-phenylalanine depending on the stabilization energies and inclusion geometries of the complexes [18]. In some significant recent publications from the group of Harada *et al.*, the macroscopic molecular recognition property of CyDs have been well demonstrated [12, 19, 20]. α -CyD and β -CyD have even been found to discriminate the subtle differences in the structures of human serum albumin and bovine serum albumin [21]. Small changes in the degree of substitution for a given CyD is known to influence the specific molecular recognition and as such the stability on a specific protein [22]. The study by Douhal *et al.*, shows higher association of the drug Milrinone (MIR) with dimethyl- β -CyD, in comparison with β -CyD [23]. The slow solvation dynamics of water molecules in the CyD cavities, captured in picosecond time domain are clear from the work of Fleming [24] and Bhattacharyya *et al.* [25]. Significant effects are exerted by the cavities on reactions (like proton transfer and charge transfer) that may occur in cellular confinement [14]. Accordingly, CyDs are considered as simple biomimetic compounds, and its interaction with proteins are suitable model systems for biological molecular recognition.

This chapter attempts to discuss our study on the molecular recognition of unmodified and dansyl modified Apo-Mb by two CyD (β - and γ -CyD) molecules having different hydrophobic cavity size. Steady-state fluorescence spectroscopy and picosecond-resolved Förster resonance energy transfer (FRET) study reveals the molecular recognition of the protein in a precise way. The thermodynamic free energy change (ΔG) and stoichiometry of the association is estimated using the emission data. The structural alteration of the protein in presence of CyD has been studied using circular dichroism (CD) spectroscopy. CD spectroscopy has also elucidated the effect of CyD binding on the thermal denaturation of the proteins. The molecular modelling studies support the experimentally derived observations quite reasonably.

8.2. Results and Discussion:

8.2.1. Molecular Recognition of a Model Globular Protein Apomyoglobin by Synthetic Receptor Cyclodextrin: Effect of Fluorescence Modification of the Protein and Cavity Size of the Receptor in the Interaction [26]:

In aqueous solution tryptophan residues of Apo-Mb has emission maximum at 342 nm (Figure 8.1a). Gradual addition of β -CyD is associated with a blue shift (24 nm) of the band maxima along with the enhancement of the fluorescence intensity. The blue shift of the emission band is indicative of the reduced local polarity around tryptophan. Consistently, the significant increase in the fluorescence quantum yield indicates the inclusion of tryptophan in more protected hydrophobic interior of the host β -CyD cavity (Scheme 8.1a) [27]. The increase in the fluorescence quantum yield is due to the deactivation of the non-radiative decay channels in the hydrophobic cavity of β -CyD [28].

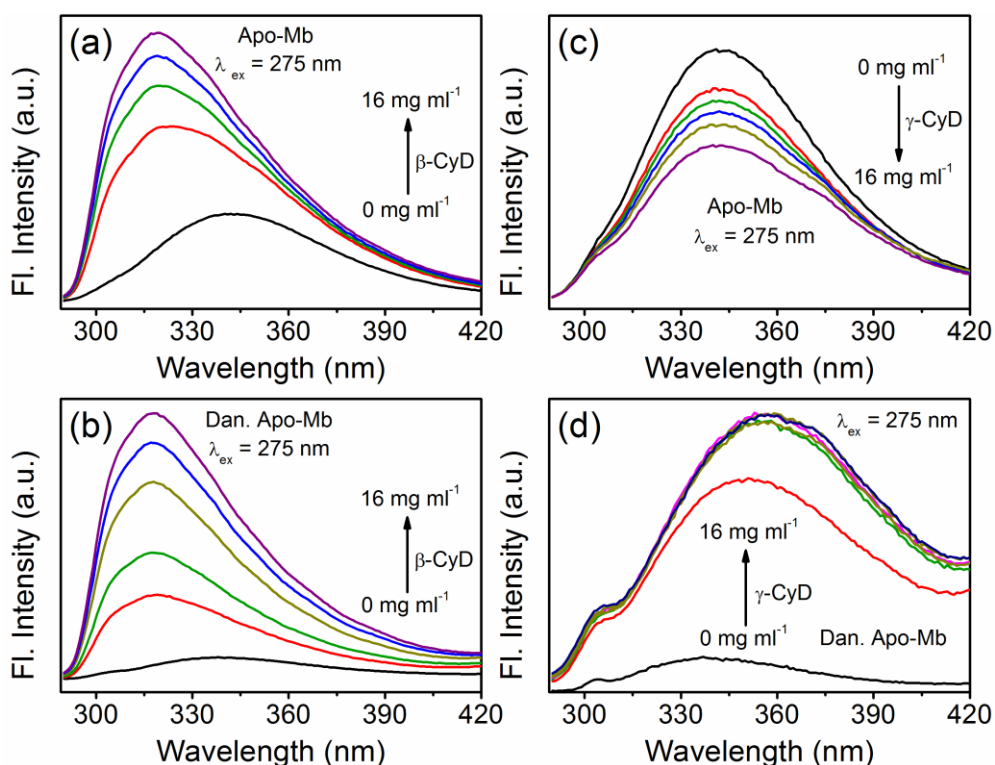
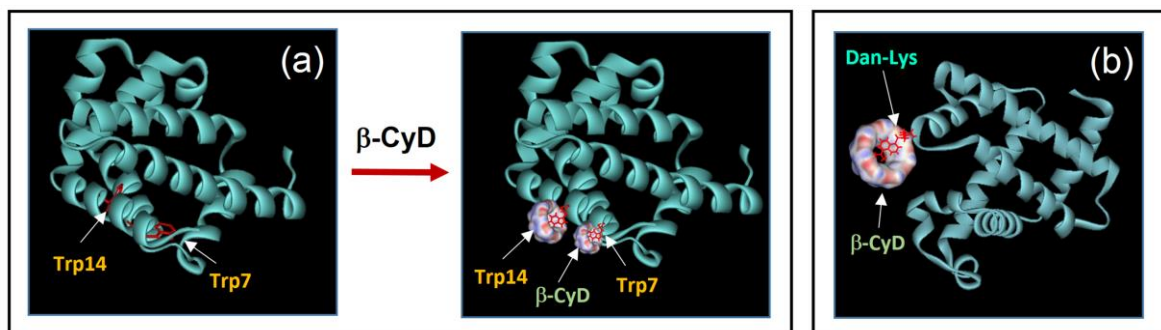


Figure 8.1. Steady-state emission spectra of tryptophan ($\lambda_{ex} = 275$ nm) in dansyl free (a) and dansyl modified (b) apomyoglobin with increasing concentrations of β -cyclodextrin. Steady-state emission spectra of tryptophan ($\lambda_{ex} = 275$ nm) in dansyl free (c) and dansyl modified (d) apomyoglobin with increasing concentrations of γ -cyclodextrin.

The observation is well supported by the molecular modelling studies using free tryptophan, showing effective inclusion of the tryptophan side chain in the β -CyD cavity



Scheme 8.1. (a) Schematic representation of the molecular recognition of apomyoglobin protein by β -cyclodextrin, through tryptophan inclusion in its hydrophobic cavity. The buried tryptophan side chain is surface exposed to form inclusion complex with β -cyclodextrin. (b) The molecular recognition of apomyoglobin through dansyl inclusion in the hydrophobic cavity of β -cyclodextrin is schematically shown.

(Figure 8.2a), with estimated stabilization energy value of -108 kJ mol^{-1} . Similar changes in the tryptophan emission is observed even in the dansylated protein (Figure 8.1b). However, stronger inclusion complexes with β -CyD are formed upon dansylation of the protein (discussed latter).

Molecular recognition in biological systems is specific like “lock and key”. The exact fit of the tryptophan side chains, in the hydrophobic interior of CyD would largely depend upon the size of the molecular cavity. The gradual addition of γ -CyD lowers the emission intensity of tryptophan, without any change in the emission band position (Figure 8.1c). The unchanged band position of tryptophan indicates that side chain of tryptophan is not recognized by γ -CyD cavity. Indeed studies reported so far suggest the insertion of aromatic side chains of peptides into the cavity of natural β -CyD [29-31] and its derivatives [32, 33]. The larger cavity diameter of γ -CyD hardly allows steric fit of aromatic amino acids in an optimal condition, forming deeper and looser inclusion complex between hydrophobic amino acids and γ -CyD [34-36]. The inconsistency in the energy minimization process of free tryptophan with γ -CyD justifies the above observation quite reasonably. The decrease of the tryptophan fluorescence intensity with the gradual addition of γ -CyD is also notable. Remarkably, quantum yield of tryptophan in proteins is determined by its immediate environment. Various side chains of amino acids, as well as

the peptide bond, are efficient quenchers of tryptophan fluorescence through various non-radiative processes like electron and proton transfer [37]. Consequently, the decrease in tryptophan emission intensity is possibly due to the changes in the immediate environment of the protein due to structural alterations in the presence of γ -CyD, as evident from CD studies [38].

The molecular recognition by γ -CyD is also studied with dansyl-modified Apo-Mb. The gradual addition of γ -CyD, enhances the fluorescence intensity of tryptophan with progressive red shift of the band maxima at 355 nm (Figure 8.1d). The observed changes in emission spectra is in sharp contrast to the changes observed on β -CyD addition (Figure 8.1b and d). The emission energy of even a partially buried tryptophan invariably shifts to the red upon surface exposure [38], while the emission spectrum of free tryptophan in water is at 355 nm [38]. Accordingly, the observed spectral change on γ -CyD addition signify the surface exposure of tryptophan residues [39]. The red shift of the band maximum further indicates the non-inclusion of the tryptophan side chain in the γ -CyD cavity (Figure 8.1b and d).

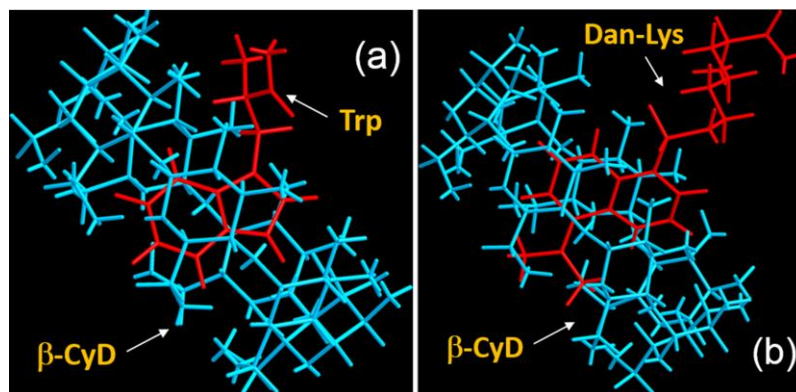


Figure 8.2. (a) The molecular inclusion complex of tryptophan with β -cyclodextrin. (b) The molecular inclusion complex of dansyl-lysine (Dan-Lys) with β -cyclodextrin. Complexes are minimum energy structures optimized using ChemBio3DTM software.

The complexation of Apo-Mb with CyD molecules have also been observed by monitoring the emission spectra of dansyl chromophore. Figure 8.3a shows the emission peak of dansyl (bound to Apo-Mb) ($\lambda_{\text{ex}} = 320$ nm) at 500 nm. The gradual addition of β -CyD progressively changes the emission peak at 484 nm with concomitant enhancement of fluorescence intensity. The blue shift of the emission maxima denotes the lowering of

micropolarity around the probe, indicating the inclusion of the protein bound dansyl molecule in the hydrophobic interior of β -CyD cavity (Scheme 8.1b). The significant enhancement of the dansyl fluorescence is quite similar to the enhancement of tryptophan fluorescence in β -CyD (Figure 8.1a and b), and can be explained due to the deactivation of

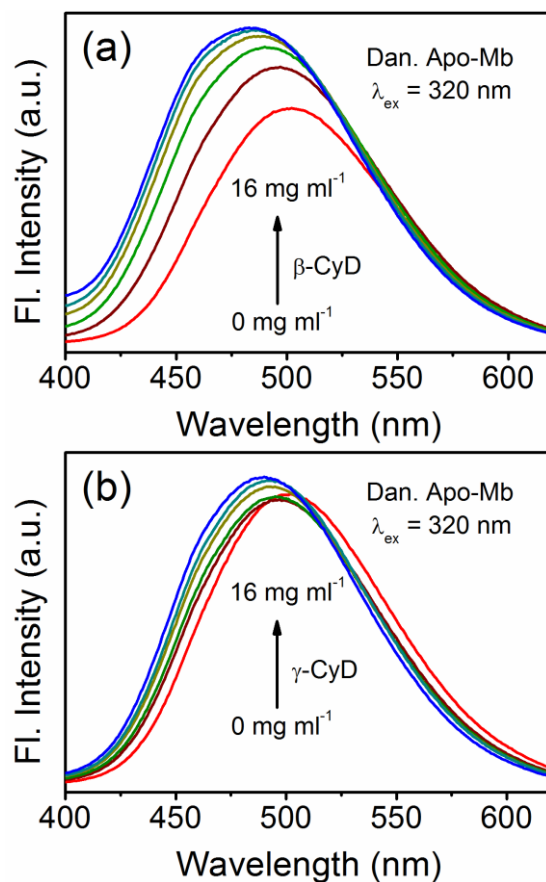


Figure 8.3. Steady-state emission spectra of dansyl ($\lambda_{ex} = 320$ nm) in apomyoglobin in various concentrations of (a) β -cyclodextrin, and (b) γ -cyclodextrin.

non-radiative decay channels in the hydrophobic cavity of β -CyD mentioned earlier [28]. The energy-minimized structures appearing in Figure 8.2b also supports the recognition of dansyl by β -CyD cavity. Using dansylated lysine molecule as a model, the energy-minimized structures in Figure 8.2b indicates effective inclusion of the *N,N*-dimethyl naphthalene moiety of dansyl in β -CyD cavity, with estimated stabilization energy of -156 kJ mol⁻¹.

Changes in the emission spectra of the dansyl (bound to Apo-Mb) is also observed in the presence of γ -CyD molecules (Figure 8.3b). However, inclusion in γ -CyD produces

much smaller blue shift of the emission band maxima, with relatively little changes in the intensity in comparison with β -CyD (Figure 8.3a and b). The difference in the emission behavior of the dansyl molecule (bound to Apo-Mb) suggests the different binding interactions of the protein with CyD molecules of various cavity size. The smaller cavity of β -CyD allows stronger fit of the dansyl molecule, showing significant change of the emission spectra. However, the larger cavity of γ -CyD forms loose complex with dansyl molecule, showing negligible changes in the emission spectra. The inconsistency in the energy optimization process of free dansyl-lysine moiety with γ -CyD also qualifies the above observation quite reasonably.

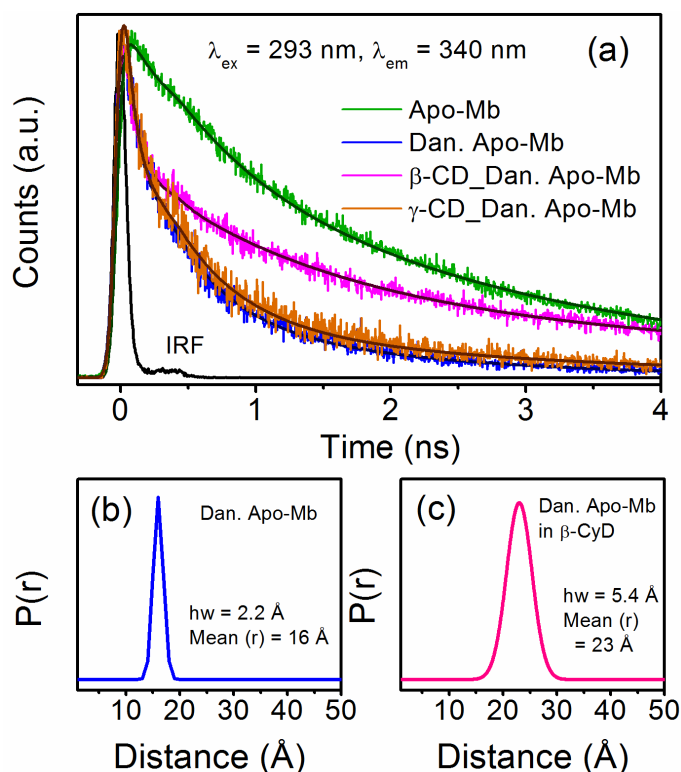


Figure 8.4. (a) Picosecond-resolved fluorescence decay transients of tryptophan in dansyl modified apomyoglobin is shown in the presence of β - and γ -cyclodextrin (16 mg ml^{-1}). The green line is the decay profile of tryptophan in dansyl free apomyoglobin. (b) and (c) show the probability of distance distribution between donor and acceptor pair in absence and presence of β -cyclodextrin, respectively.

We have also applied picosecond-resolved FRET technique, between the probes tryptophan and dansyl, in order to monitor the molecular recognition of the protein by CyD molecules in a more precise way. As evident from Figure 8.4a, the fluorescence decay of

tryptophan residues ($\lambda_{em} = 340$ nm, $\lambda_{ex} = 293$ nm) of the protein becomes faster in dansyl modified Apo-Mb, indicating FRET from tryptophan to dansyl [3]. Significantly, unlike emission in free protein (two longer components), the temporal decay of tryptophan in dansylated Apo-Mb shows three time components, including a faster time component of 45 ps (57%). As a consequence, the average lifetime (τ_{ave}) of tryptophan decreases from 2000 ps to 337 ps, in dansyl modified Apo-Mb (Table 8.1). The Förster distance between the donor-acceptor pair is found to be 16 Å, with estimated possible distribution of, $hw = 2.2$ Å (Figure 8.4b). Upon addition of β -CyD to the dansylated Apo-Mb, the average decay

Table 8.1. Fluorescence decay parameters for apomyoglobin in presence of β - and γ -CyD. ^m

Sample Name	Cyclodextrin	a ₁	τ_1 (ps)	a ₂	τ_2 (ps)	a ₃	τ_3 (ps)	τ_{ave} (ps)
Apo-Mb	-	-	-	0.39	700	0.61	2840	2000
Dan. Apo-Mb	-	0.57	45	0.33	414	0.10	1691	337
Dan. Apo-Mb	γ -CyD	0.65	48	0.28	504	0.07	2621	358
Dan. Apo-Mb	β -CyD	0.58	100	0.28	1398	0.14	6862	1361

^m τ_i represents decay time constants and a_i its relative contribution, $\tau_{ave} = \sum a_i \tau_i$.

time of the tryptophan emission ($\lambda_{em} = 340$ nm, $\lambda_{ex} = 293$ nm) becomes slower, compared to β -CyD free protein (Figure 8.4a, Table 8.1). The Förster distance between the donor-acceptor pair is found to be 23 Å, with $hw = 5.4$ Å (Figure 8.4c). However, insignificant change in the decay profile, attributing no change in the donor-acceptor distance of the dansylated protein is observed upon addition of γ -CyD. The result is quite consistent with the steady-state emission studies of the protein with CyDs. Stronger recognition of the protein (through tryptophan, dansyl) is occurred by the smaller cavity size of β -CyD molecules. Consequently, increase in the donor-acceptor distance is realized in presence of β -CyD. However, insignificant change of the donor-acceptor distance, in presence of γ -CyD, further confirms weak complexation of γ -CyD with Apo-Mb.

The study so far discussed suggests the different molecular recognition of the protein depending on the dimension of the host cavity. In order to establish the stoichiometric compositions of the inclusion complexes of the ligand to its receptor, and to determine the thermodynamic energy parameters associated with the binding, Benesi-Hildebrand method [40] was applied employing following equation (3-17). In β -CyD

solutions, the Benesi-Hildebrand plot for tryptophan emission shows linear behavior in both the dansyl free and bound protein (Figure 8.5a and b). The linearity

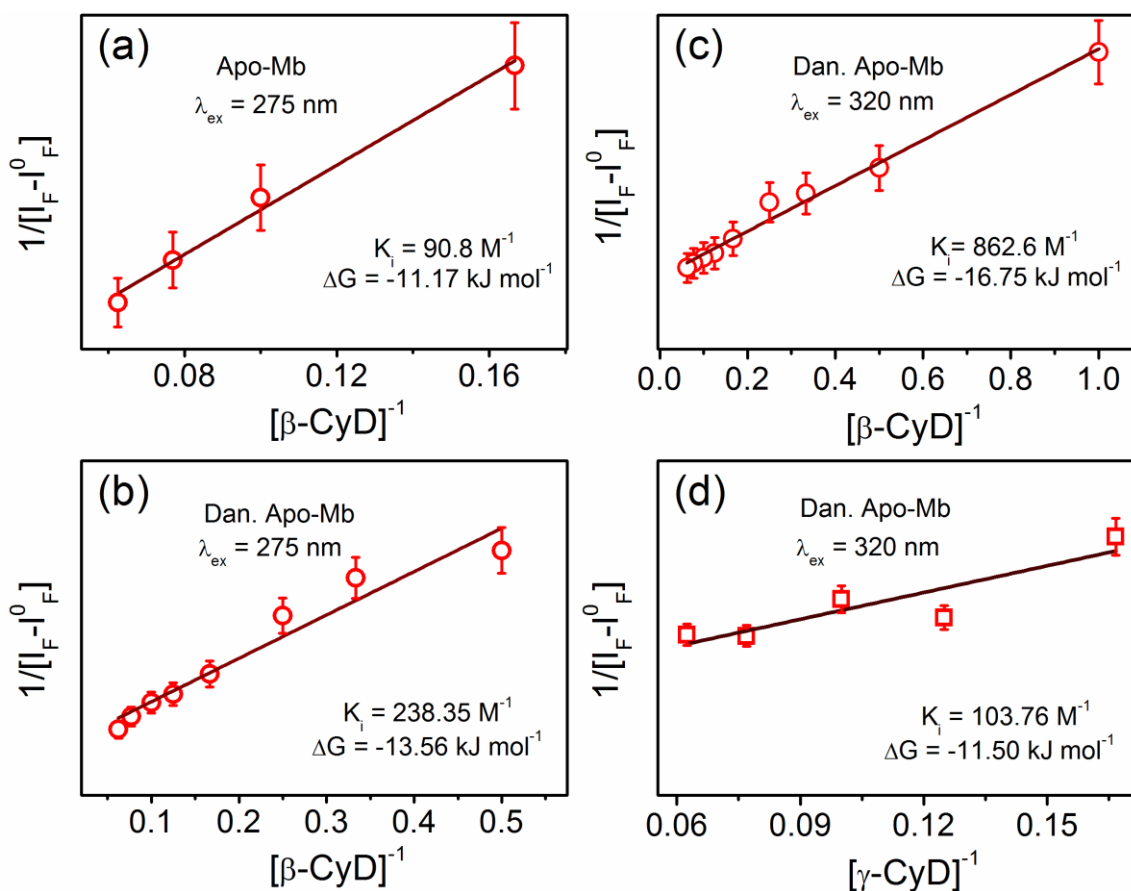


Figure 8.5. Benesi-Hildebrand plot for 1:1 complexation of tryptophan, in dansyl free (a) and dansyl modified (b) apomyoglobin, with β -cyclodextrin are shown. Benesi-Hildebrand plot for 1:1 complexation of dansyl, in apomyoglobin, with β -cyclodextrin (c) and γ -cyclodextrin (d) are shown.

of the plot suggests the formation of 1:1 complex between tryptophan and β -CyD (Scheme 8.1a). From the slope and intercept of the plot the association constant (K_i) for the inclusion complex is estimated to be 90.8 M^{-1} and 238.35 M^{-1} , for dansyl free and dansyl bound protein, respectively. The corresponding standard free energy changes (ΔG°) for the complexes are found to be $-11.17 \text{ kJ mol}^{-1}$ and $-13.56 \text{ kJ mol}^{-1}$, respectively. Significant deviation of the experimental energy value from that of the theoretical data (-108 kJ mol^{-1}) is possibly due to the consideration of free tryptophan moiety in the molecular modelling study. The hydrophobic modification of the protein surface is therefore found to stabilize the tryptophan inclusion of the protein into host β -CyD cavity. The dansylation of the

protein initiates tighter fit of the tryptophan side chain in the β -CyD cavity, which is well reflected in the increased K_i value (by 3 times) and the decrease in the thermodynamic free energy value ($\Delta\Delta G^\circ$) of $-2.39 \text{ kJ mol}^{-1}$ upon dansylation. The increased recognition of the protein is probably associated with the increased localized binding site of the protein due to the conformational modification upon dansylation, discussed latter.

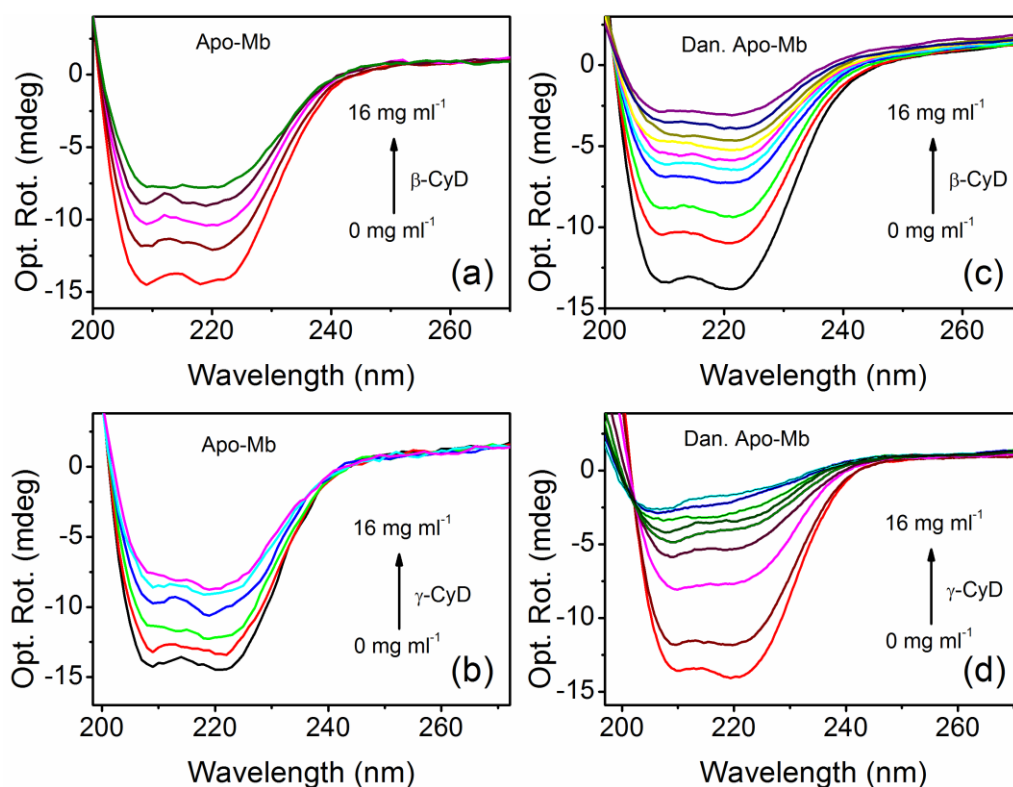


Figure 8.6. Circular dichroism spectra of apomyoglobin as a function of β -cyclodextrin (a) and γ -cyclodextrin (b) concentration. Circular dichroism spectra of dansylated apomyoglobin as a function of β -cyclodextrin (c) and γ -cyclodextrin (d) concentration.

Benesi-Hildebrand plot applying equation (3-17) shows linearity in protein recognition through dansyl molecule, by both the CyD molecules (Figure 8.5c and d). Similar to tryptophan, linearity of the plot suggests the 1:1 stoichiometry of the binding (Scheme 8.1b). The K_i value estimated, for β - and γ -CyD association with the protein are 862.6 M^{-1} and 103.76 M^{-1} , respectively. The corresponding ΔG° value for the association is $-16.75 \text{ kJ mol}^{-1}$ and $-11.50 \text{ kJ mol}^{-1}$, respectively. The higher selectivity of β -CyD ($\Delta\Delta G^\circ = -5.25 \text{ kJ mol}^{-1}$) with greater K_i value of protein association is associated with the smaller cavity size of β -CyD allowing tighter fit of the dansyl molecule to be included. The

deviation of the experimental energy value from that of the theoretical data (-154 kJ mol^{-1}) is possibly due to the consideration of free dansyl-lysine moiety in the molecular modelling study. Applying the multiple equilibria model (equation (3-18)) [41, 42], the overall equilibrium constant (K_{total}) for dan. Apo-Mb association with β -CyD is estimated to be $238.35 \text{ M}^{-1} \times 862.6 \text{ M}^{-1} = 205609 \text{ M}^{-2}$.

We sought evidence of the structural changes of the protein upon CyD addition. CD spectroscopy is an efficient spectroscopic tool to study structural changes in protein. Figure 8.6 shows the CD structure of the protein in dansyl free and bound condition in presence of various concentrations of β - and γ -CyD molecules. The negative band at 208 and 222 nm is indicative of the α -helical content of the protein. In all the cases a gradual decrease of the overall helical content of the protein is observed upon β - and γ - CyD addition (Figure 8.6). Earlier reports suggest the solvent exposure and therefore accessibility of hydrophobic amino acid residues as a prerequisite for CyD-protein interaction [43]. The observed changes in tryptophan emission (Figure 8.1) therefore indicates the surface exposure of the tryptophan side chains on the protein surface (Scheme 8.1a), consistent with CD studies (Figure 8.6). Therefore, changes in the CD structure is quite expected. Similarly, upon dansylation, greater change of the helical content of the protein is consistent with the higher association (K_i) value of the dansylated protein in complexation with CyD (Figure 8.5).

We examine the thermal stability of the protein in the presence of CyD by monitoring the changes in ellipticity at 222 nm. The denaturation temperature (T_m) of Apo-Mb is determined to be 56°C , as the midpoint of the transition curve depicted in Figure 8.7a. Significant decrease in the T_m value (about 13°C) is observed in presence of β -CyD, whereas γ -CyD shows relatively smaller effect (about 8°C) (Figure 8.7a). The higher magnitude of decrease in the T_m value appears to stem from the higher complexation of β -CyD compared to γ -CyD, with the protein (Figure 8.5). The result is quite consistent with previous observation [44], and clearly suggests that the binding of CyD to the exposed hydrophobic side chains of Apo-Mb during heating destabilizes the native conformations of the protein, by shifting the equilibrium in favor of the unfolded state [44, 45].

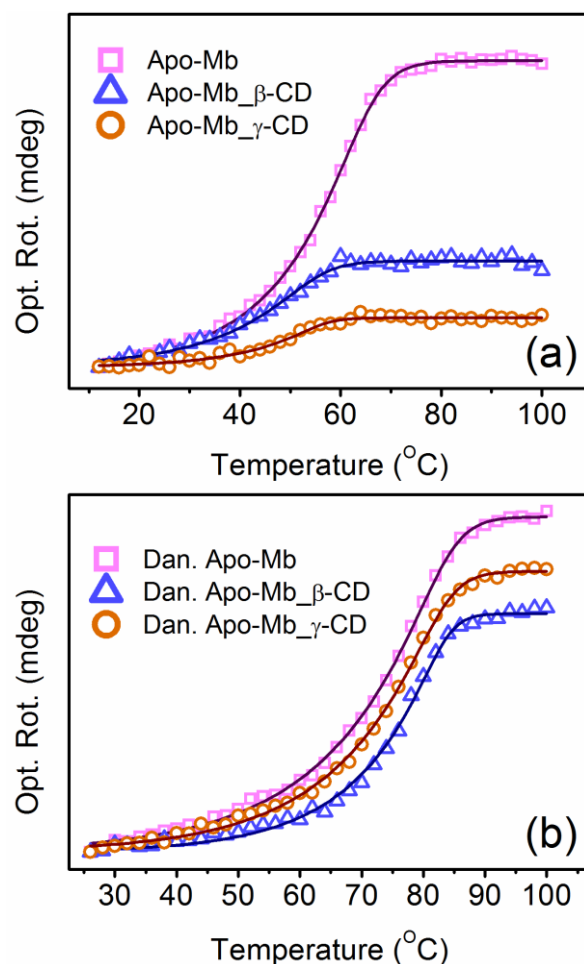


Figure 8.7. Temperature dependent circular dichroism spectra of dansyl free (a) and dansyl modified (b) apomyoglobin, in presence of β -cyclodextrin and γ -cyclodextrin concentration of 16 mg ml^{-1} . (All the curves were base line subtracted for comparison).

Previous report suggests that hydrophobic environment increases the thermal stability of a protein, and is the key factor for the stability of thermophilic proteins, in comparison to other factors like hydrogen bonds, and electrostatic interactions [46]. The study by Georis *et al.* shows that additional aromatic interaction improves the thermostability of family 11 Xylanase [47]. The thermal stability of Apo-Mb has also been evaluated after dansylation of the protein. Considerable enhancement of the T_m ($= 74^\circ\text{C}$) value of the dansylated Apo-Mb is observed in comparison to the dansyl free protein (Figure 8.7a and b). The observed higher thermal stability of the protein appears to stem from the higher surface hydrophobicity of the protein upon dansylation, mentioned above. Remarkably, protein thermal denaturation starts with unfolding of the outer surface leading to the surface exposure of the hydrophobic core [48]. The denaturation can possibly be

prevented by stabilizing the protein surface with hydrophobic interactions. The insignificant change in the thermal denaturation transition of the dansyl modified protein, unaffected by either CyD molecules, is therefore concluded to be due to the increased hydrophobic character of protein surface upon dansylation (Figure 8.7b).

8.3. Conclusion:

We have explored the effect of attachment of a fluoroprobe at the protein surface, in the molecular recognition of Apo-Mb by a synthetic receptor CyD. Significant enhancement of the CyD-protein association is observed upon dansyl labelling of the protein. The recognition of the protein by CyD changes significantly depending on the cavity size of the receptor. The smaller cavity of β -CyD allows steric fit of the hydrophobic residues (like tryptophan and dansyl) of the protein. FRET between the probes tryptophan and dansyl shows increase in the donor-acceptor distance, in presence of β -CyD. However, insignificant change of the donor-acceptor distance in presence of γ -CyD indicates stronger association of the protein with β -CyD over γ -CyD. Molecular modelling studies on the interaction of tryptophan and dansyl probe with β -CyD is found to be consistent with the experimental observations. The unaltered melting behavior of the dansyl-attached protein by CyDs, suggests the stabilization of the protein due to hydrophobic labelling. Thus, both the cavity size of the synthetic receptor and hydrophobic character of the protein surface are found crucial in determining the molecular recognition of a protein by CyD as a synthetic receptor. The study offers a cautionary note on the use of hydrophobic fluorescent labels for proteins in biochemical studies involving recognition of molecules.

References:

- [1] R. Baron, J.A. McCammon, Molecular recognition and ligand association, *Annu. Rev. Phys. Chem.* 64 (2013) 151.
- [2] F. Hof, J. Rebek, Molecules within molecules: Recognition through self-assembly, *Proc. Natl. Acad. Sci. U.S.A.* 99 (2002) 4775.
- [3] T. Mondol, S. Batabyal, A. Mazumder, S. Roy, S.K. Pal, Recognition of different DNA sequences by a DNA-binding protein alters protein dynamics differentially, *FEBS Lett.* 586 (2012) 258.
- [4] U. Banik, N.C. Mandal, B. Bhattacharyya, S. Roy, A fluorescence anisotropy study of tetramer-dimer equilibrium of lambda repressor and its implication for function, *J. Biol. Chem.* 268 (1993) 3938.
- [5] R.F. Warren, A. Henk, P. Mowery, E. Holub, R.W. Innes, A mutation within the leucine-rich repeat domain of the arabidopsis disease resistance gene RPS5 partially suppresses multiple bacterial and downy mildew resistance genes, *Plant Cell* 10 (1998) 1439.
- [6] Y. Ogura, D.K. Bonen, N. Inohara, D.L. Nicolae, F.F. Chen, R. Ramos, H. Britton, T. Moran, R. Karaliuskas, R.H. Duerr, J.P. Achkar, S.R. Brant, T.M. Bayless, B.S. Kirschner, S.B. Hanauer, G. Nunez, J.H. Cho, A frameshift mutation in NOD2 associated with susceptibility to Crohn's disease, *Nature* 411 (2001) 603.
- [7] E.M. Valente, P.M. Abou-Sleiman, V. Caputo, M.M.K. Muqit, K. Harvey, S. Gispert, Z. Ali, D. Del Turco, A.R. Bentivoglio, D.G. Healy, A. Albanese, R. Nussbaum, R. González-Maldonado, T. Deller, S. Salvi, P. Cortelli, W.P. Gilks, D.S. Latchman, R.J. Harvey, B. Dallapiccola, G. Auburger, N.W. Wood, Hereditary early-onset Parkinson's disease caused by mutations in PINK1, *Science* 304 (2004) 1158.
- [8] D.O. Borroto-Escuela, D. Marcellino, M. Narvaez, M. Flajolet, N. Heintz, L. Agnati, F. Ciruela, K. Fuxe, A serine point mutation in the adenosine A2AR C-terminal tail reduces receptor heteromerization and allosteric modulation of the dopamine D2R, *Biochem. Biophys. Res. Commun.* 394 (2010) 222.

- [9] R. Corradini, G. Feriotto, S. Sforza, R. Marchelli, R. Gambari, Enhanced recognition of cystic fibrosis W1282X DNA point mutation by chiral peptide nucleic acid probes by a surface plasmon resonance biosensor, *J. Mol. Recognit.* 17 (2004) 76.
- [10] D. Voet, J.G. Voet, Biochemistry, Wiley, Somerset NJ, 1995.
- [11] A. Hashidzume, A. Harada, Recognition of polymer side chains by cyclodextrins, *Polym. Chem.* 2 (2011) 2146.
- [12] Y. Zheng, A. Hashidzume, Y. Takashima, H. Yamaguchi, A. Harada, Switching of macroscopic molecular recognition selectivity using a mixed solvent system, *Nat. Commun.* 3 (2012) 831.
- [13] H. Dodziuk, Cyclodextrins and their complexes: Chemistry, analytical methods, applications, Wiley-VCH, Weinheim, 2006.
- [14] C. Martín, M. Gil, B. Cohen, A. Douhal, Ultrafast photodynamics of drugs in nanocavities: Cyclodextrins and human serum albumin protein, *Langmuir* 28 (2012) 6746.
- [15] M. El-Kemary, A. Douhal, Chapter 4 - Photochemistry and Photophysics of Cyclodextrin Caged Drugs: Relevance to Their Stability and Efficiency, D. Abderrazzak (Ed.) Cyclodextrin Materials Photochemistry, Photophysics and Photobiology, Elsevier, Amsterdam, 2006, 79.
- [16] S. Li, W.C. Purdy, Cyclodextrins and their applications in analytical chemistry, *Chem. Rev.* 92 (1992) 1457.
- [17] T. Cserhádi, E. Forgács, Cyclodextrins in chromatography, The Royal Society of Chemistry, Cambridge, 2003.
- [18] T. Aree, R. Arunchai, N. Koonrugs, A. Intasiri, Fluorometric and theoretical studies on inclusion complexes of β -cyclodextrin and D-, L-phenylalanine, *Spectrochim. Acta Part A: Mol. Biomol. Spectrosc.* 96 (2012) 736.
- [19] H. Yamaguchi, Y. Kobayashi, R. Kobayashi, Y. Takashima, A. Hashidzume, A. Harada, Photoswitchable gel assembly based on molecular recognition, *Nat. Commun.* 3 (2012) 603.
- [20] Y. Zheng, A. Hashidzume, Y. Takashima, H. Yamaguchi, A. Harada, Macroscopic observations of molecular recognition: Discrimination of the substituted position on the naphthyl group by polyacrylamide gel modified with β -cyclodextrin, *Langmuir* 27 (2011) 13790.

- [21] W. Oi, M. Isobe, A. Hashidzume, A. Harada, Macromolecular recognition: Discrimination between human and bovine serum albumins by cyclodextrins, *Macromol. Rapid Commun.* 32 (2011) 501.
- [22] H.S. Samra, F. He, A. Bhambhani, J.D. Pipkin, R. Zimmerer, S.B. Joshi, C.R. Middaugh, The effects of substituted cyclodextrins on the colloidal and conformational stability of selected proteins, *J. Pharm. Sci.* 99 (2010) 2800.
- [23] M. El-Kemary, J.A. Organero, L. Santos, A. Douhal, Effect of cyclodextrin nanocavity confinement on the photorelaxation of the cardiotoxic drug milrinone, *J. Phys. Chem. B* 110 (2006) 14128.
- [24] S. Vajda, R. Jimenez, S.J. Rosenthal, V. Fidler, G.R. Fleming, E.W. Castner, Femtosecond to nanosecond solvation dynamics in pure water and inside the γ -cyclodextrin cavity, *J. Chem. Soc., Faraday Trans.* 91 (1995) 867.
- [25] K. Bhattacharyya, Nature of biological water: A femtosecond study, *Chem. Commun.* (2008) 2848.
- [26] R. Saha, S. Rakshit, S.K. Pal, Molecular recognition of a model globular protein apomyoglobin by synthetic receptor cyclodextrin: Effect of fluorescence modification of the protein and cavity size of the receptor in the interaction *J. Mol. Recognit.* 26 (2013) 568.
- [27] M. Khajepour, T. Troxler, V. Nanda, J.M. Vanderkooi, Melittin as model system for probing interactions between proteins and cyclodextrins, *Proteins: Struct., Funct., Bioinf.* 55 (2004) 275.
- [28] S. Ghosh, S. Jana, N. Guchhait, Constrained photophysics of partially and fully encapsulated charge transfer probe (E)-3-(4-Methylaminophenyl) acrylic acid methyl ester inside cyclodextrin nano-cavities: Evidence of cyclodextrins cavity dependent complex stoichiometry, *Spectrochim. Acta, Part A* 84 (2011) 249.
- [29] F.L. Aachmann, D.E. Otzen, K.L. Larsen, R. Wimmer, Structural background of cyclodextrin-protein interactions, *Protein Eng.* 16 (2003) 905.
- [30] D.E. Otzen, B.R. Knudsen, F. Aachmann, K.L. Larsen, R. Wimmer, Structural basis for cyclodextrins' suppression of human growth hormone aggregation, *Prot. Sci.* 11 (2002) 1779.

- [31] J. Danielsson, J. Jarvet, P. Damberg, A. Gräslund, Two-site binding of β -cyclodextrin to the alzheimer $A\beta(1-40)$ peptide measured with combined PFG-NMR diffusion and induced chemical shifts, *Biochemistry* 43 (2004) 6261.
- [32] K. Matsubara, T. Irie, K. Uekama, Spectroscopic characterization of the inclusion complex of a luteinizing hormone-releasing hormone agonist, buserelin acetate, with dimethyl-beta-cyclodextrin, *Chem. Pharm. Bull.* 45 (1997) 378.
- [33] S. Tang, L. Kong, J. Ou, Y. Liu, X. Li, H. Zou, Application of cross-linked β -cyclodextrin polymer for adsorption of aromatic amino acids, *J. Mol. Recognit.* 19 (2006) 39.
- [34] M.P. So, T.S.M. Wan, T.W. Dominic Chan, Differentiation of enantiomers using matrix-assisted laser desorption/ionization mass spectrometry, *Rapid Commun. Mass Spectrom.* 14 (2000) 692.
- [35] S. Tavornvipas, S. Tajiri, F. Hirayama, H. Arima, K. Uekama, Effects of hydrophilic cyclodextrins on aggregation of recombinant human growth hormone, *Pharm. Res.* 21 (2004) 2369.
- [36] X.-r. Qin, H. Abe, H. Nakanishi, NMR and CD studies on the interaction of Alzheimer β -amyloid peptide (12–28) with β -cyclodextrin, *Biochem. Biophys. Res. Commun.* 297 (2002) 1011.
- [37] P.D. Adams, Y. Chen, K. Ma, M.G. Zagorski, F.D. Sönnichsen, M.L. McLaughlin, M.D. Barkley, Intramolecular quenching of tryptophan fluorescence by the peptide bond in cyclic hexapeptides, *J. Am. Chem. Soc.* 124 (2002) 9278.
- [38] C.A. Royer, Probing protein folding and conformational transitions with fluorescence, *Chem. Rev.* 106 (2006) 1769.
- [39] C.A. Royer, C.J. Mann, C.R. Matthews, Resolution of the fluorescence equilibrium unfolding profile of trp aporepressor using single tryptophan mutants, *Protein Sci.* 2 (1993) 1844.
- [40] H.A. Benesi, J.H. Hildebrand, A spectrophotometric investigation of the interaction of iodine with aromatic hydrocarbons, *J. Am. Chem. Soc.* 71 (1949) 2703.
- [41] M.T. Beck, I. Nagypál, Chemistry of complex equilibria, Ellis Horwood, 1990.
- [42] E.A. Hoffmann, I. Nagypál, Response reactions: Equilibrium coupling, *J. Phys. Chem. B* 110 (2006) 10581.

- [43] T. Serno, R. Geidobler, G. Winter, Protein stabilization by cyclodextrins in the liquid and dried state, *Adv Drug Deliv Rev.* 63 (2011) 1086.
- [44] S. Tavornvipas, F. Hirayama, S. Takeda, H. Arima, K. Uekama, Effects of cyclodextrins on chemically and thermally induced unfolding and aggregation of lysozyme and basic fibroblast growth factor, *J. Pharm. Sci.* 95 (2006) 2722.
- [45] A. Cooper, Effect of cyclodextrins on the thermal stability of globular proteins, *J. Am. Chem. Soc.* 114 (1992) 9208.
- [46] M.M. Gromiha, M.C. Pathak, K. Saraboji, E.A. Ortlund, E.A. Gaucher, Hydrophobic environment is a key factor for the stability of thermophilic proteins, *Proteins: Struct., Funct., Bioinf.* 81 (2013) 715.
- [47] J. Georis, F.D.L. Esteves, J. Lamotte-Brasseur, V. Bougnet, F. Giannotta, J.-M. Frère, B. Devreese, B. Granier, An additional aromatic interaction improves the thermostability and thermophilicity of a mesophilic family 11 xylanase: Structural basis and molecular study, *Protein Sci.* 9 (2000) 466.
- [48] A. Caflisch, M. Karplus, Molecular dynamics simulation of protein denaturation: Solvation of the hydrophobic cores and secondary structure of barnase, *Proc. Natl. Acad. Sci. U.S.A.* 91 (1994) 1746.

List of Publications

1. **R. Saha**, S. Rakshit and S. K. Pal
“Molecular recognition of a model globular protein apomyoglobin by synthetic receptor cyclodextrin: Effect of fluorescence modification of the protein and cavity size of the receptor in the interaction”, *J. Mol. Recognit.* 26 (2013) 568.
2. **R. Saha**, P. K. Verma, S. Rakshit, S. Saha, S. Mayor and S. K. Pal
“Light driven ultrafast electron transfer in oxidative redding of green fluorescent proteins”, *Sci. Rep.* 3 (2013) 1580.
3. **R. Saha**, S. Rakshit, D. Majumdar, A. Singha, R. K. Mitra, and S. K. Pal
“Nanostructure, solvation dynamics and nanotemplating of plasmonically active SERS substrate in reverse vesicles”, *J. Nanopart. Res.* 15 (2013) 1576.
4. **R. Saha**, S. Rakshit, P. K. Verma, R. K. Mitra and S. K. Pal
“Protein-cofactor binding and ultrafast electron transfer in riboflavin binding protein under the spatial confinement of nanoscopic reverse micelles”, *J. Mol. Recognit.* 26 (2013) 59.
5. **R. Saha**, S. Rakshit, R. K. Mitra and S. K. Pal
“Microstructure, morphology and ultrafast dynamics of a novel edible microemulsion”, *Langmuir* 28 (2012) 8309.
6. **R. Saha**, P. K. Verma, R. K. Mitra and S. K. Pal
“Structural and dynamical characterization of unilamellar AOT vesicles in aqueous solutions and their efficacy as potential drug delivery vehicle”, *Colloids Surf., B.* 88 (2011) 345.
- 7.* S. Rakshit, **R. Saha**, and S. K. Pal
“Modulation of environmental dynamics at the active site and activity of an enzyme under nanoscopic confinement: Subtilisin carlsberg in anionic AOT reverse micelle”, *J. Phys. Chem. B* 117 (2013) 11565.

- 8.* S. Rakshit, **R. Saha**, A. Chakraborty and S. K. Pal
“Effect of hydrophobic interaction on structure, dynamics and reactivity of water”,
Langmuir 29 (2013) 1808.
- 9.* S. Rakshit, **R. Saha**, A. Singha, Z. S. A. Seddigi and S. K. Pal
“Molecular interaction, co-solubilisation of organic pollutants and ecotoxicity of a
potential carcinogenic fuel additive MTBE in water”,
J. Mol. Liq. 180 (2013) 235.
- 10.* S. Rakshit, **R. Saha**, P. K. Verma and S. K. Pal
“Role of solvation dynamics in excited state proton transfer of 1-naphthol in
nanoscopic water clusters formed in a hydrophobic solvent”, *Photochem.*
Photobiol. 88 (2012) 851.
- 11.* S. Rakshit, **R. Saha**, P. K. Verma, R. K. Mitra and S. K. Pal
“Ultrafast electron transfer in riboflavin binding protein in macromolecular
crowding of nano-sized micelle”, *Biochimie* 94 (2012) 2673.
- 12.* N. Goswami, **R. Saha**, S. K. Pal
“Protein-assisted synthesis route of metal nanoparticles: exploration of key
chemistry of the biomolecule”, *J. Nanopart. Res.* 13 (2011) 5485.
- 13.* P. K. Verma, **R. Saha**, R. K. Mitra and S. K. Pal
“Slow water dynamics at the surface of macromolecular assemblies of different
morphologies”, *Soft Matter* 6 (2010) 5971.

* Not included in the thesis.